SPATIAL SCALING OF LARGE-SCALE CIRCULATIONS AND HEAT TRANSPORT IN TURBULENT MIXED CONVECTION

Dissertation
zur Erlangung des mathematisch-naturwissenschaftlichen Doktorgrades
"Doctor rerum naturalium"
der Georg-August-Universität Göttingen

im Promotionsprogramm ProPhys
der Georg-August University School of Science (GAUSS)

vorgelegt von

Andreas Westhoff

aus Alzenau

Göttingen 2012

Betreuungsausschuss

Prof. Dr. rer. nat. Dr. Ing. habil Andreas Dillmann,

Georg-August-Universität Göttingen Fakultät für Physik und Deutsches Zentrum für Luft- und Raumfahrt e.V.

Prof. Dr. Ing. Claus Wagner,

Deutsches Zentrum für Luft- und Raumfahrt, Institut für Aerodynamik und Strömungstechnik

Dr. rer. nat. Johannes Bosbach,

Deutsches Zentrum für Luft- und Raumfahrt, Institut für Aerodynamik und Strömungstechnik

Mitglieder der Prüfungskommission

Referent: **Prof. Dr. rer. nat. Dr. Ing. habil Andreas Dillmann,**

Georg-August-Universität Göttingen, Fakultät für Physik und Deutsches Zentrum für Luft- und Raumfahrt e.V.

Korreferent: **Prof. Dr. Andreas Tilgner,**

Georg-August-Universität Göttingen, Institut für Geophysik

Weitere Mitglieder der Prüfungskommission

Prof. Dr. Wolfram Kollatschny,

Georg-August-Universität Göttingen, Institut für Astrophysik

Prof. Dr. Ulrich Parlitz,

Max-Planck-Institut für Dynamik und Selbstorganisation, Biomedical Physics Group

Prof. Dr. Jürgen Vollmer,

Max-Planck-Institut für Dynamik und Selbstorganisation, Biomedical Physics Group

Prof. Dr. Rein,

Georg-August-Universität Göttingen, Fakultät für Physik und Deutsches Zentrum für Luft- und Raumfahrt e.V.

Tag der mündlichen Prüfung: 14. November 2012

CONTENTS

LIST OF FIGURES

LIST OF TABLES

NOMENCLATURE

GREEK SYMBOLS

α	coefficient of thermal expansion
β	isothermal compressibility
$\Delta\rho$	density variations
$\Delta\Theta$	characteristic temperature difference
η	dynamic viscosity
κ	thermal diffusivity
λ	POD eigenvalue
ν	kinematic viscosity
Ω	vorticity
ω	angular velocity
ω	circuit frequency
$\overline{\Theta}$	mean system temperature
Φ	potential
Ψ	POD eigenfunction
Ψ_i	POD eigenfunction of the i-th mode
Ψ_u, Ψ_v, Ψ_w	POD eigenfunction of the corresponding velocity component
σ	standard deviation
σ_B	Stefan–Boltzmann constant
Θ	temperature
Θ_a	ambient air temperature
Θ_D	mean air temperature in the outlet channel
Θ_D^{end}	air temperature at the end of the outlet channel
Θ_{out}	mean air temperature in the cell outlet port
Υ	scalar function of the vortex detecting algorithm
φ	angle
ρ	density
ρ_0	fluid density
ξ	power of the physical quantities

ζ	POD eigenvector

LATIN SYMBOLS

$\mathcal{A}r$	Archimedes number
$\dot{M}$	mass flow
$\dot{Q}$	enthalpy flux
$\dot{q}$	heat flux density
$\dot{Q}_{FC}$	forced convective enthalpy flux
$\dot{Q}_{TC}$	thermal convective enthalpy flux
$\dot{V}$	volume flow
$\mathcal{G}r$	Grashof number
$\mathbf{C}$	temporal autocorrelation function
$\mathbf{F}$	force per volume
$\mathbf{g}$	gravitational acceleration
$\mathbf{K}$	spatial autocorrelation function
$\mathbf{n}$	unit vector
$\mathbf{R}$	radius vector
$\mathbf{x}(x, y, z)$	spatial coordinates
$\boldsymbol{\nu}$	state variable
$\mathcal{N}u$	Nusselt number
$\mathcal{P}e$	Péclet number
$\mathcal{P}r$	Prandtl number
$\mathcal{R}a$	Rayleigh number
$\mathcal{R}a_{crit}$	critical Rayleigh number
$\mathcal{R}e$	Reynolds number
$\mathcal{R}e_D$	Reynolds number of the outlet channel
s_H	scaling factor for the charateristic height
s_κ	scaling factor for the thermal diffusivity
s_ν	scaling factor for the kinematic viscosity
$\mathbf{u}(u, v, w)$	three component velocity vector
A	area
C_P	specific heat capacity
d	thickness
d_P	particle diameter
E	sum of the POD eigenvalues
f	recording frequency
F_B	buoyancy force
F_F	frictional forces
F_I	inertia forces
F_i	fundamental units
g	gravitational forces

H	characteristic height
H	height of the convection cell
h	heat transfer coefficient
h_a	heat transfer coefficient of the outer channel side
h_{con}	convective heat transfer coefficient
H_{in}	height of the inlet channel
H_{out}	height of the outlet channel
h_{rad}	radiative heat transfer coefficient
k	thermal conductivity
L	characteristic length
L	length of the convection cell
L_{in}	length of the inlet channel
L_{out}	length of the outlet channel
N	number of grid points
N	number of scalar fields
n	POD mode number
P	pressure
R	gas constant
r	radius
R_j	physical quantities
R_{LSC}	radius of the large-scale circulation
S	area of spatial averaging
s_L	scaling factor for the charateristic length
T	period of time
t	time
t_n	discrete time steps
U	characteristic velocity
U_{in}	mean inflow velocity
U_{out}	mean outflow velocity
U_B	buoyancy velocity
U_R	maximal velocity at the boundary of the large-scale circulation
u_ϕ	velocity in rotational direction
u_r	velocity in radial direction
V_{HDG}	air volume of the high pressure wind tunnel
W	width of the convection cell
Z	compressibility factor

MISCELLANEOUS

$(.)$	inner vector product
δ_{ij}	Kronecker delta
Γ	aspect ratio

Γ_{LH}	length to height aspect ratio
Γ_{WH}	width to height aspect ratio
∇^2	Laplace operator
$\langle . \rangle$	time average
$\mathbf{D}$	dimension matrix
∇	differential operator
$^{D}/_{Dt}$	total derivative
Π_i	Π-groups
$\|\|.\|\|$	norm
$\|.\|$	modulus
*	complex conjugate

SUB- and SUPERSCRIPTS

air	air
arc	acrylic glas
b	bottom
core	large-scale circulation core region
c	centre position
in	inlet
outer	large-scale circulation outer region
out	outlet
t	top

ACRONYMS

2C Two Component

3C Three Component

2D Two-Dimensional

3D Three-Dimensional

CFD Computational Fluid Dynamics

DLR Deutsches Zentrum für Luft und Raumfahrt / German Aerospace Center

DIN Deutsche Industrie Norm / German Industry Norms

HDG Hochdruck Windkanal Göttingen / High pressure wind tunnel Göttingen

FC Forced Convection

TC Thermal Convection

MC Mixed Convection

RBC Rayleigh Bénard Convection

LSC Large-Scale Circulations

BL Boundary Layer

PIV Particle Image Velocimetry

PIT Particle Image Thermography

POD Proper Orthogonal Decomposition

CCF Cross-Correlation Function

PRT Platinum Resistance Temperature sensors

LES Large Eddy Simulation

DNS Direct Numerical Simulation

1 MOTIVATION

Convection [lat. *convectum*; to bear together, to collect or to gather] describes the process of heat transport due to the movement of molecules within fluids. The expression is given to the general category of flows, which emerge as a result of density variations. In the literature the term convection is also found as heat transfer, particularly if the focus lies on the transport of heat or as mass transfer, if the flow is governed by concentration variations.

In principle, convection is distinguished in terms of being natural or forced. Natural convection, also referred to as free convection or thermal convection, is determined by an externally induced temperature difference. The resulting variations in density induce buoyancy forces, setting the fluid into motion. On the contrary, forced convection denotes the movement of fluid, which results from external forces like pumps or fans. If further natural convection and forced convection coexist and if they are of the same order of magnitude, the flow is referred to as mixed convection. In mixed convective flows, the formation of flow structures, their dynamics and the transport of heat are determined by the mutual interplay of forced convection and natural convection.

The phenomenon convection is vast and of utmost importance in nature and numerous applications. Often, convective flows occur on large scales, like in the meteorology or the indoor air-conditioning (fig. 1). In meteorology, for example, the restructuring of huge gas masses is driven by convection and determines the clouds' formation or leads to the emergence of hurricanes [90, 114]. Further convective flows on large scales in nature include ocean currents [123, 81], plate tectonics [85] or solar granulation in the outer layer of stars [8, 69]. On cosmological scales convective processes play an important role in the formation and development of galaxies [29]. Additionally, many industrial and technical applications exist where convective flows occur on large scales [12, 46, 98].

Another frequent application, in which the prevailing mechanism of fluid flow and heat transport is mixed convection, is the air conditioning of rooms, entire buildings, vehicles or aircraft. Humans or electronic devices emit heat to the surroundings and as a result air is heated and rises due to buoyancy. In addition, the ventilation induces forced convective flow. As a consequence the flow and heat transfer is determined by the superposition of forced convection and thermal convection. In particular, the use of control electronics and multimedia devices in vehicles, buildings or aircrafts leads to significantly increased heat loads. In addition to the technical need to cool the electronic devices, the higher heat loads influence the climate in a cabin. Nowadays, the climate is a decisive factor for transportation companies in the market of passenger

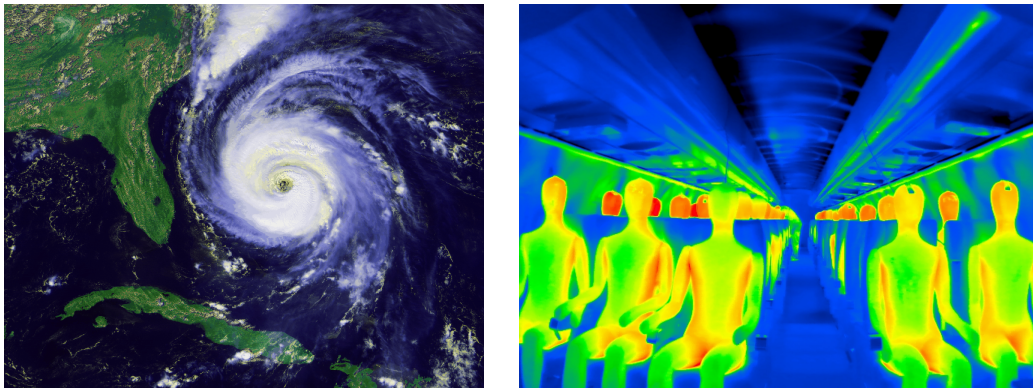

(a) (b)

Figure 1: Convective flow on large scales in nature and technical applications: (1a) Satellite image of a hurricane [87]. (1b) Ventilation of an aircraft cabin: temperature distribution of thermo-dummies simulating the passengers [65].

services. However, air conditioning is energy consuming and leads to considerable emissions of carbon dioxide. As a consequence, indoor climatisation consumes a large proportion of the power-supply [131, 75]. Based on these reasons, many application-related studies [49, 70, 80, 93, 132] as well as fundamental research [57, 58, 18] was performed for dealing with higher heat loads in order to improve the interior thermal comfort, while simultaneously saving energy.

Because mixed convection on large scales is generally turbulent, far from equilibrium or even reveals an almost completely chaotic behaviour, direct experimental investigations, for instance with the objective to optimise the thermal comfort or to develop concepts of energy-saving, on full-scale are complex, costly and time consuming. To overcome that issue, a concept allowing the study of mixed convection on large scales on laboratory scales is highly desirable.

Hence, the motivation of the present study is to examine the feasibility of spatial scaling in mixed convection. Based on a concept of spatial scaling, mixed convective air flow was studied in a small-scale and full-scale configuration. Both containers are geometrically similar and represent a generic configuration, which is frequently encountered in the climatisation of rooms and vehicles. However, due to the prevailing unsteady nature and complexity of mixed convection, the examination and verification of the concept need further analysis. Thus, the first part primarily deals with the questions: how does the flow structure formation depends on the dimensionless parameters and how do coherent flow structures and their trajectory in time influence the transport of heat?

Taken together, the objective of the present investigation is twofold. In the first part, turbulent forced and mixed convective air flow is studied with the aim of extracting the fundamental flow features and to find valid criteria in order to characterise the flow. Based on these criteria in the second part the concept of spatial scaling is examined for mixed convective air flow.

2

MIXED CONVECTIVE FLOWS

2.1 BASIC CONCEPTS

In the following section, the basic concept of convective flows is introduced. The discussion on this topic is restricted to the category of flows with temperature variations, which are introduced through temperature differences between boundaries or between a boundary and the ambient fluid. Flow-induced temperature variations arising from adiabatic expansions or viscous dissipation and heat generation by absorption of thermal radiation, are neglected. Further, the Boussinesq approximation is applied, which considers density variations $\rho = \rho_0 + \Delta\rho$ only, as they give rise to gravitational forces. The criteria for the applicability of the Boussinesq approximation are

$$\begin{aligned} g\rho\beta L &\ll 1 \\ \tfrac{g\alpha L}{C_P} &\ll 1 \\ \tfrac{g\alpha L\Theta}{C_P\Delta\Theta} &\ll 1, \end{aligned} \tag{2.1}$$

where

$$\alpha = -\frac{1}{\rho}\left(\frac{\partial\rho}{\partial\Theta}\right)\Bigg|_{P=\text{const}} \tag{2.2}$$

denotes the coefficient of thermal expansion,

$$\beta = -\frac{1}{V}\left(\frac{\partial V}{\partial P}\right)\Bigg|_{\Theta=\text{const}} \tag{2.3}$$

the isothermal compressibility, L the characteristic length, Θ the absolute temperature, $\Delta\Theta$ the characteristic temperature difference, P the pressure, V the volume and C_P the specific heat capacity [1].

If the Boussinesq approximation is valid the density is assumed to be constant $\partial\rho/\partial t = 0$ and the continuity equation is

$$\nabla\mathbf{u} = 0. \tag{2.4}$$

Further, it is assumed that the gravity $\mathbf{g}$ is uniform, which leads to a potential of $\Phi = gz$ and the forces per volume are

$$\mathbf{F} = -(\rho_0 + \Delta\rho)\nabla\Phi = -\nabla(\rho_0\Phi) - \Delta\rho\mathbf{g}. \tag{2.5}$$

1 For a perfect gas the coefficient of thermal expansion is a function of the absolute temperature $\alpha = 1/\Theta$ only and the isothermal compressibility is $\beta = 1/\rho R\Theta$.

Consequently, the Navier-Stokes equation becomes

$$\rho_0 \frac{D\mathbf{u}}{Dt} = -\nabla P + \eta \nabla^2 \mathbf{u} + \Delta\rho \mathbf{g}, \tag{2.6}$$

where η denotes the dynamic viscosity and $\mathbf{g} = -g\mathbf{n}_z$. According to the Boussinesq approximation $\Delta\rho/\rho_0 \ll 1$ the dependence of the temperature on the density is written in a linearised formula

$$\Delta\rho = -\alpha\rho_0\Delta\Theta \tag{2.7}$$

and the Boussinesq approximated dynamical equation is

$$\frac{D\mathbf{u}}{Dt} = -\frac{1}{\rho_0}\nabla P + \nu\nabla^2\mathbf{u} - \alpha\mathbf{g}\Delta\Theta, \tag{2.8}$$

where $\nu = \eta/\rho$ is the kinematic viscosity. The term $\alpha\mathbf{g}\Delta\Theta$ is the buoyancy force (per mass unit) F_B.

In addition to the continuity equation and the equation of fluid motion, an equation for the temperature is required. In thermal convective flows, the heating is caused by the transfer of heat from neighbouring fluid particles by conduction. The thermal conductive heat flux is given by Fourier's law

$$\dot{\mathbf{q}} = -k\nabla\Theta, \tag{2.9}$$

where k is the thermal conductivity of the fluid, which is taken to be constant in the following. Based on Fourier's law the equation for the heat transfer in incompressible fluids is

$$\frac{\partial\Theta}{\partial t} + \mathbf{u}\nabla\Theta = \kappa\nabla^2\Theta. \tag{2.10}$$

Here $\mathbf{u}$ denotes the velocity and

$$\kappa = \frac{k}{\rho C_P} \tag{2.11}$$

the thermal diffusivity.

The equations (2.4), (2.8) and (2.10) represent a set of basic equations, which describe convective flows. The equations consist of three variables: the velocity $\mathbf{u}$, the pressure P/ρ, the temperature variations $\Delta\Theta$ and two fluid properties ν and κ. However, for the later discussion of similitude just the stationary equations are of interest[2]. By setting all time derivatives zero the equations

$$\mathbf{u}\nabla\Theta = \kappa\nabla^2\Theta \tag{2.12}$$

2 Strictly speaking, in order that convective flow can be stationary it is necessary that the boundaries are isothermal.

and

$$(\mathbf{u}\nabla)\,\mathbf{u} = -\frac{1}{\rho_0}\nabla P + \nu\nabla^2\mathbf{u} - \alpha\mathbf{g}\Delta\Theta \tag{2.13}$$

are obtained.

Depending on the ratio of buoyancy to inertia forces, three classes of convective flows are usually defined. These classes represent the limiting cases in which the inertia forces or buoyancy forces are predominant and an intermediate regime where both have the same order of magnitude. As a rule, the three classes of convective flows are termed forced convection (*FC*), thermal convection (*TC*) and mixed convection (*MC*). In the following, the three categories will be defined. Further, the non-dimensional parameters which are needed to characterise the flows are introduced and examples of practical importance are given.

Forced convection

Convective flow is termed forced convection (*FC*), when the buoyancy forces are negligible small compared to the inertia forces. This is constituted if

$$\frac{\alpha g \Delta\Theta L}{U^2} \ll 1, \tag{2.14}$$

where U represents a characteristic velocity, L a characteristic length and $\Delta\Theta$ a characteristic temperature difference. In such flows, the motion of fluid is determined by externally induced pressure gradients, caused by pumps or fans. The literature on the phenomena *FC* is vast and includes flows at the bottom layer of the atmosphere, the euphotic zone in oceans [77], flows in micro channel, focused on the issue of cooling in various applications, e.g. microprocessors, solar panels or high-energy-laser mirrors [95, 55, 4]. Another frequently studied configuration is the flow and heat transfer along heated or cooled plates and behind obstacles [30, 52] or in two-phase nanofluid flows [63, 61]. Although, this thesis is focused on *MC*, however, some studies of *FC* are related to this work. For instance, Saeidi et al. [107] studied the formation of large-scale flow patterns in *FC*. The numerical investigation was performed in a square cavity with different positions of inlet and outlet ports and is fundamentally related to the configuration that is used in this study.

In *FC* the velocity field is almost unaffected by the temperature field, i.e. the temperature is a passive scalar. Hence, the velocity field can be determined without the knowledge of the temperature field, which is in turn determined by the flow field. However, it does not imply that the transport of heat is negligible. Consequently, there are two equations that have to be taken into account: equation (2.13) with $F_B = \alpha\mathbf{g}\Delta\Theta = 0$ and equation (2.12). The dimensional analysis of these equations

shows that two characteristic numbers are necessary to determine forced convective flow. The Reynolds number

$$\mathcal{R}e = \frac{U\,L}{\nu}, \tag{2.15}$$

which states a measure of the ratio of inertia to viscous forces and the Prandtl number

$$\mathcal{P}r = \frac{\nu}{\kappa} = \frac{c_p \eta}{k}, \tag{2.16}$$

reflecting the thermal similarity of two systems. It is found that $\mathcal{P}r$ is a fluid property and independent of the fluid flow. As a result, the comparability of experiments with different fluids is restricted.

Instead of $\mathcal{P}r$ in literature often the Péclet number

$$\mathcal{P}e = \frac{U\,L}{\kappa}, \tag{2.17}$$

is found as a measure of thermal similitude. The Péclet number is $\mathcal{P}e = \mathcal{R}e \cdot \mathcal{P}r$ and reflects the ratio of advective to conductive heat transfer.

Thermal convection

Thermal convection (*TC*) is a classical problem in fluid dynamics. Since Henri Bénard (1874-1939) published his dissertation "*Les Tourbillons cellulaires dans une nappe liquide propageant de la chaleur par convection en régime permanent*" in 1900 numerous studies have been carried out on this topic. *TC* occurs due to buoyancy forces, which are the result of a density gradient induced by an externally applied temperature difference. Considering a small fluid volume with the dimension l, which is $\delta\Theta$ warmer as the surrounding fluid, two conditions have to be met for the onset of convective flow. On the one hand, the resulting velocity of the fluid element δu must be low enough, so that the frictional forces $F_F = \nu\delta u/l^2$ are small enough compared to the velocity of the fluid element. On the other hand, due to the loss of heat $\delta u \Delta\Theta/H \cdot \kappa\delta\Theta/l^2$ of the rising fluid element, the velocity δu should not be too low. Hence, for the onset of thermal convective flow the following condition has to be met

$$\frac{L}{\Delta\Theta}\frac{\kappa}{l^2}\delta\Theta < \delta u < \frac{l^2}{\nu}\alpha g \delta\Theta. \tag{2.18}$$

A frequently studied type of *TC* is the Rayleigh-Bénard Convection (*RBC*). *RBC* occurs in a horizontal fluid layer uniformly heated from below and cooled from above. It is named after the two physicists who first studied convective flows in a horizontal

layer in detail: Henri Bénard and Lord Rayleigh (John William Strutt, 1842-1919). *RBC* is characterised by the two non-dimensional parameters $\mathcal{P}r$ and the Rayleigh number

$$\mathcal{R}a = \frac{g\alpha\Delta\Theta L^3}{\nu\kappa}, \tag{2.19}$$

which represents the ratio of buoyancy to viscous forces. Further, $\mathcal{R}a$ indicates regimes of thermal convective flow. With increasing $\mathcal{R}a$, the buoyancy forces become predominant. As a consequence, at a critical $\mathcal{R}a$ the fluid at rest becomes unstable and buoyancy-driven flow sets in. The $\mathcal{R}a_{crit}$ can be calculated analytically for several configurations and depends primarily on the boundary conditions. For rigid-rigid boundary conditions the critical Rayleigh number is $\mathcal{R}a_{crit} = 1708$ [104] and for a configuration heated from below and a free surface $\mathcal{R}a_{crit} = 657$ [103]. Later changes in the regimes are associated with the passage of $\mathcal{R}a$ through other critical values [2, 3]. Frequently, in literature instead of $\mathcal{R}a$ as characteristic number the Grashof number

$$\mathcal{G}r = \frac{\mathcal{R}a}{\mathcal{P}r} = \frac{g\alpha\Delta\Theta L^3}{\nu^2}, \tag{2.20}$$

is found, in particular, if the study involves free convection.

RBC is related to many flows in nature or technical applications. Exemplary works on *RBC* in nature were published, by Hartmann et al. for convective processes in the atmosphere [51] or by Sreenivasan and Donnelly [120] outlining a general estimation of $\mathcal{R}a$ in nature. Another reason for the great interest in this topic is that *RBC* is not strictly limited to problems in fluid dynamics. *RBC* is subject of research in the stability theory [38, 112], the pattern formation [35] or the chaos research [92, 71]. The understanding of *RBC* remains a challenging issue in natural science in general and fluid dynamics, in particular.

Mixed convection

Mixed convection (*MC*) is determined by the interaction of buoyancy and forced flow. Hence, the velocity and the temperature field are different from those prevailing at *FC* or *TC*. *MC* is characterised by the non-dimensional numbers $\mathcal{R}a$, $\mathcal{R}e$ and $\mathcal{P}r$ (a detailed derivation of the characteristic numbers for *MC* is given in the next paragraph). In addition, the Archimedes number

$$\mathcal{A}r = \frac{\mathcal{R}a}{\mathcal{R}e^2\mathcal{P}r} = \frac{\Delta\Theta\alpha g L^3}{U^2} \tag{2.21}$$

is another frequently used parameter to characterise *MC*. The non-dimensional parameter represents the ratio of buoyancy to inertia forces. Convective flows with $\mathcal{A}r \ll 1$ are predominated by inertia forces and can be assigned to *FC*. If $\mathcal{A}r \gg 1$ the

flow is governed by buoyancy forces and it is referred to as *TC*. Convective flows with $\mathcal{A}r \approx 1$, where inertia and buoyancy forces have the same order of magnitude apply to the regime of *MC*.

In the early research of convective heat transfer, thermal and forced convective flows were studied separately and the often complex mutual interplay of the two flow conditions was simply ignored. In fact, *TC* and *FC* can be considered as extreme conditions of *MC*. At the beginning of the 1980's a considerable increase of interest in *MC* was observed. The greater interest correlates with the increasing computing power of microprocessors. The rapid progress in the development of electronic devices and the resulting generation of heat necessitates an optimisation of cooling. Hence, many studies of *MC* are related to heat transfer in heat exchangers and cooling devices. Studies on this topic are given, for instance, by Jackson et al. [60] and Biswas et al. [17]. While Jackson presents a summary of the topic *MC* in tubes, the work of Biswas is focused on the design of channels for the enhancement of heat transfer. Another frequently studied configuration is the flow and heat transfer in ventilated boxes. An overview and exemplary works on this topic are given, for instance, by Linden et al. [76, 75]. The objective of these studies was to examine new concepts of natural ventilation of entire buildings. However, the issue of efficient ventilation is not restricted to air conditioning. Due to the rapid expansion of many cities (in particular, in emerging and developing countries) air pollution often exceeds a critical level. Hence, several studies of mixed convective air flow in urban atmospheres were carried out. An overview and the state-of-the-art can be found in the publication of Fernando [40].

2.2 LARGE SCALE CIRCULATION

A key feature in many convective flows is the development of large-scale circulation (*LSC*). An example of *LSC* in a rectangular *RBC* container at $\mathcal{R}a = 1 \times 10^5$, using

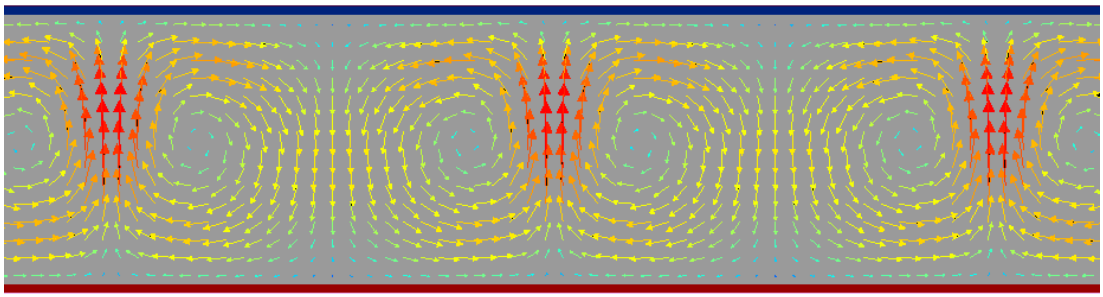

Figure 2: Large-scale circulations in *RBC*. Numerical simulation of *RBC* in a rectangular container with an aspect ratio $\Gamma = \text{width} : \text{depth} : \text{height} = 1 : 1 : 0.15$ at $\mathcal{R}a = 1 \times 10^5$ [50].

air as working fluid, is depicted in figure 2. In *RBC* hot part of the fluid, known as plumes, is emitted from the bottom thermal boundary layer (*BL*) and rises due to buoyancy. Due to the in-compressibility, cold fluid at another position has to sink. As a consequence, descending cold plumes are emitted from the top thermal boundary. In addition, a horizontal flow between the regions of plumes' emission is developed. As a result, an organised roll structure emerges [66, 101]. It is also known as "mean wind" if the diameter of the *LSC* is of the order of the characteristic height [89, 100].

Experimental studies show that the mean wind is found also in strongly turbulent mixed convection $\mathcal{R}a > 1 \times 10^8$, where the wind is strong enough that the bulk becomes turbulent [2, 7]. The details of the mutual interplay of thermal plumes and *LSC* are subject to on going research. Numerous experimental studies of measuring the velocity or the temperature were performed to determine the interaction of plumes and mean wind [129, 53, 33, 99].

In these studies, a time-periodic behaviour in the region of rising and falling plumes within a wide range of $\mathcal{R}a$ is found. For instance, the experiment by Qiu et al. [99] of *RBC* reveals that the velocity oscillation is a response to the periodic thermal plumes' emission between the upper and lower thermal *BL*s. The study shows that the frequencies of the time-periodicity in temperature are similar to those that can be observed for the horizontal velocity component of the mean wind.

Funfschilling and Ahlers [43] presented an experimental study of *RBC* in a cylindrical container with an aspect ratio one, in which the azimuthal orientation of the horizontal component of the plumes' velocity was determined. The time series of the azimuthal orientation reveals a time-periodic behaviour of the *LSC* orientation. Moreover, the oscillation near the ceiling and bottom plate have the same single frequency, but phase shifted by π. Another result of the study is that the measured frequencies in temperature and velocity respond to the plume motion, showing that the flow is much more structured than previously presumed [28, 53, 33]. Additional theoretical and experimental studies on this topic were carried out by Brown et al. and Funfschilling et al. [19, 21, 22, 20, 44] to determine the nature of the time-periodic behaviour.

Another experimental study of the azimuthal motion of *LSC* was conducted by Xi et al. [128]. Like in the study of Funfschilling and Ahlers the experiments were performed in a cylindrical sample with an aspect ratio one. In accordance to Sun et al. [121] and Brown et al. [24], a preferred orientation of the *LSC* in a sample with a rotational symmetry was found. All other states appear as intermediate states.

However, the phenomenon of torsional oscillation is not restricted to laboratory experiments. Torsional movement of *LSC* can be also observed in nature and in technical applications. For instance, it is assumed that the cessations of the convective flow of magma in the outer core of the Earth's mantle control the orientation of the Earth's magnetic field [47, 73]. Moreover, torsional oscillations of the convection rolls are found during the observation of the solar convection zone [34].

Several models were introduced in order to describe the dynamics of the mean wind. Stochastic models are given by e.g. Benzi [15] and Sreenivasan [119]. However, these models are not physically motivated. The parameters are phenomenological and no azimuthal degree of freedom is included. An improved model was given by Fontenele et al. [42]. Similar to the stochastic model lacks it the azimuthal degree of freedom. However, in contrast to the stochastic models, the terms of the differential equations are physically motivated. Another model [23] consists of two coupled stochastic differential equations, which are motivated by the Navier-Stokes equation. The two equations describe the temperature fluctuations and the azimuthal orientation of the *LSC* respectively. Further, the model includes a Gaussian white-noise term representing the small-scale turbulent background fluctuations. However, it simulates the dynamics of the *LSC* only, while other aspects in *TC* such as the heat flux, are not represented by the differential equations.

Many studies were performed with the objective of a better understanding of *LSC* formation and its dynamics. In general, the studies are related to *RBC* in cylindrical geometries. However, the formation of *LSC* and its oscillations are not restricted to *RBC*. Furthermore, in *MC* thermally induced *LSC* is observed, in particular, when the buoyancy forces surpass the inertia forces. Comparable to *TC*, the dynamics of the thermal convection rolls often tends to a time-periodic behaviour in speed and temperature. Nevertheless, due to the additional forced flow in *MC* significant differences in comparison to *RBC* are obtained.

An experimental and numerical study addressing the formation of *LSC* in *MC* within a parameter range of $2472 \leqslant \mathcal{R}a \leqslant 8300$ and $18.1 \leqslant \mathcal{R}e \leqslant 120.2$ is presented by Chiu et al. [32, 31]. Chiu et al. studied the influence of a forced laminar flow in nitrogen on buoyancy induced *RBC* roll patterns. The experimental apparatus consists of a rectangular duct with an aspect ratio of $\Gamma = \mathsf{width}/\mathsf{height} = 10$ heated from below and cooled at the top. Chiu et al. observed *RBC* roll patterns in the region of fully developed flow with the onset of buoyancy flow. The diameter of the buoyancy induced *LSC*s is similar to the height of the duct. Further, with the onset of buoyancy flow a time-periodic modulation of the velocity component in longitudinal direction is found.

Systematic numerical simulations, which are related to the study of Chiu et al. [32, 31], were carried out by Huang et al. [56]. Using air as the working fluid, *MC* was studied in a rectangular cavity with an aspect ratio $\Gamma = \mathsf{width}/\mathsf{height} = 2$ within a wide range of $\mathcal{A}r$, while $\mathcal{R}e$ was kept constant. The study reveals four $\mathcal{A}r$-regimes of thermal *LSC* formation. For $\mathcal{A}r < 4$ the flow is dominated by two steady *LSC*s near the sidewall. As $\mathcal{A}r$ exceeds four, the flow becomes unstable, and four convection rolls, oscillating with a single frequency, and its harmonics are developed. In the regime $19 \leqslant \mathcal{A}r < 25$ the flow is fully unsteady, except a small region near the inlet. For $\mathcal{A}r \geqslant 25$ the flow shows a chaotic behaviour, in particular, within the region close to the exit.

Another investigation of large-scale structure formation in a shear- and buoyancy-driven squared cavity is presented by Aydem [10]. Aydem studied *MC* numerically in the range of $0.01 \leqslant \mathcal{A}r \leqslant 100$, while $\mathcal{R}e = 100$ was kept constant. The study gives a valuable insight into the complexity of flow pattern formation in rectangular cavities. Shear flow is induced by the movement of the left side wall, and the buoyancy forces result from a temperature difference between the vertical walls. Using this configuration buoyancy-aiding and buoyancy-opposing shear flow is produced. For the buoyancy aiding flow case, the change of the flow field topology is nearly negligible, while in case of buoyancy-opposing and $\mathcal{A}r \geqslant 0.5$ a significant impact of the *FC* induced flow is observed. Within this $\mathcal{A}r$-regime a coexistence of a buoyancy and shear induced *LSC*, rotating in opposite directions, was found, while for $\mathcal{A}r \geqslant 10$ the velocity field is almost similar to that at pure *TC*.

An experimental study, which is addressed to the development of *LSC* in mixed convective air flow for low $\mathcal{R}e$ within 9 to 186 and $\mathcal{G}r$ up to 5×10^6, is presented by Lin et al. [74]. The setup consists of a rectangular duct with an aspect ratio $\Gamma = \text{width/height} = 4$ and $\Gamma = \text{length/height} \approx 26.7$. With the onset of a buoyancy induced secondary flow Lin detected four longitudinally arranged roll structures swinging back and forth in the span wise direction. With increasing buoyancy forces at $\mathcal{A}r = 96.1$ a pair of *LSC*s prevailed, which becomes unsteady for $\mathcal{A}r > 110$.

2.3 HEAT TRANSPORT

In convective flows, the heat transfer at a surface within the fluid is determined by the ratio of convection to conduction. The relevant non-dimensional parameter to characterise the convective heat transfer is the Nusselt number

$$\mathcal{N}u = \frac{h\,L}{k}, \tag{2.22}$$

where h denotes the heat transfer coefficient

$$h = \frac{\dot{Q}}{A\Delta\Theta}, \tag{2.23}$$

$\dot{Q}$ is the heat flux and A the area of the heat transfer surface. Depending on the actual flow condition, that is *MC*, *TC* or *FC*, the mechanisms of heat transfer differ. To comprehend the heat transfer at *MC* it is indispensable to know how the transport of heat is realised in *FC* and *TC*.

In *FC*, where buoyancy has no significant impact on the flow, the transport of heat is determined in the *BL*. The heat transport strongly depends on whether the flow in the *BL* is turbulent or laminar. Due to the increased momentum exchange in turbulent *BL*s an increased heat transfer is observed between the boundary and fluid. For flows in ducts or enclosures along an isothermal boundary the thermal

BL thickness increases in flow direction [11]. Hence, the temperature gradient in the thermal *BL* decreases and leads to a detraction of the heat transfer. An overview of the heat transfer correlations in *FC* is given by Whitaker [126], including the analysis of experimental data for laminar and turbulent flows in several tube configurations. Further, in forced convective flows the $\mathcal{N}u_{FC}$ is a function of $\mathcal{R}e$ and $\mathcal{P}r$. Theoretical considerations and empirical studies [11] predict a power law

$$\mathcal{N}u_{FC} \sim \mathcal{R}e^{a}\mathcal{P}r^{b}. \tag{2.24}$$

Due to the great practical importance of *FC* in the development of heat exchangers and cooling devices, a series of parameter studies regarding the heat transfer in *FC* have been performed. Hence, the heat transfer in *FC* is nowadays almost textbook material [11].

The heat transport in thermal convective flows is determined by buoyancy and gravitational forces. Owing to the complexity of this subject, the discussion of the heat transport is limited to *RBC*, which is relevant to this investigation.

Many experiments of heat transfer in turbulent *RBC* were carried out within a wide parameter range of $\mathcal{R}a$ and $\mathcal{P}r$. It was found that the vertical transport of heat is primarily determined by thermal plumes [113, 130]. A schematic sketch (fig. 3a) and a visualisation (3b) of the heat transfer by thermal plumes in a container with aspect ratio one is shown in figure 3, where (🍄) denotes warm rising plumes, which are emitted from the thermal *BL* (▬) at the heated bottom and (🍄) cold plumes emitted from the thermal *BL* (▬) at the cooled ceiling. Thermal plumes originate due to instabilities in the thermal *BL*, which grows from the heat impact by the cooling and heating plate: warm fluid from the bottom is transported by rising plumes and to the same extent, cold fluid is transported by sinking plumes (whereas cold and warm means cold and warm relative to the mean temperature). Experiments of Shang et al. [113] at $\mathcal{R}a = 3.6 \times 10^{9}$ and $\mathcal{P}r = 596$ reveal that the local heat flux is highly intermittent in time and space. Moreover, heat flux fluctuations near the *BL*s and the interior background lead to flow reversals or time-periodic torsional oscillations of *LSC*, which was already discussed in section 2.2.

A frequently studied topic in *RBC* is the $\mathcal{N}u$-dependency on the system relevant characteristic numbers $\mathcal{R}a$ and $\mathcal{P}r$. Older theories predict a unified power law

$$\mathcal{N}u_{RBC} \sim \mathcal{R}a^{a}\mathcal{P}r^{b}, \tag{2.25}$$

which has its origin in the early Malkus marginal-stability theory of 1954 [82]. Several further theories have been developed and introduced. However, with the large amount and high precision of experimental and numerical data, it is found that none of these theories gives a unified view on this topic, in particular, for high $\mathcal{R}a$. Grossmann and Lohse provide a theory within a wide parameter range of $\mathcal{R}a$ and Pr, which is valid also at high $\mathcal{R}a$. A detailed description of the theory is found in [3].

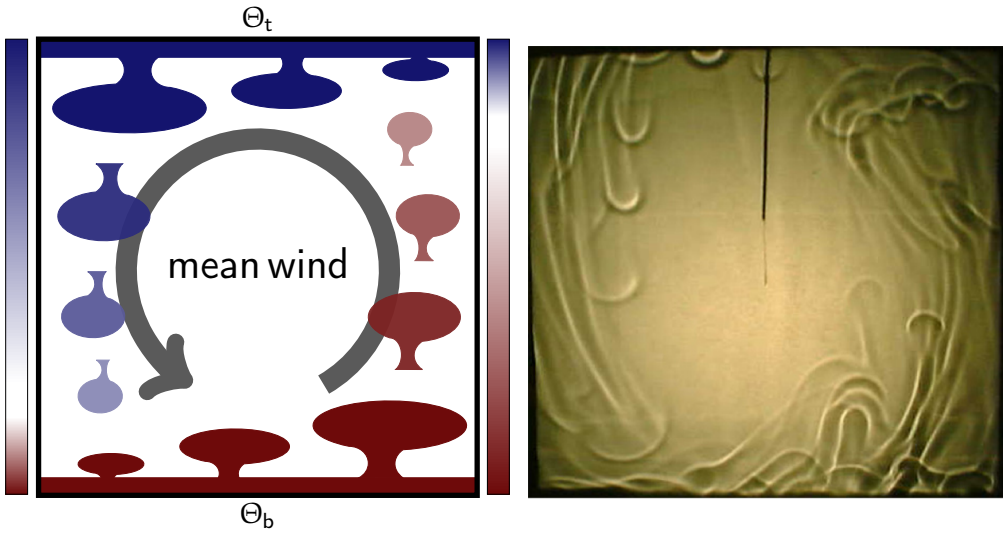

(a) (b)

Figure 3: (3a) Illustration of heat transfer in *RBC*. (3b) Temperature pattern in turbulent *RBC*: Plumes visualisation with a Shadowgraph at $\mathcal{R}a = 6.8 \times 10^8$, $\mathrm{Pr} = 596$ (dipropylene glycol) and aspect ratio one [113].

In *MC*, the transport of heat depends on the ratio of buoyancy forces to inertia forces and on the relative magnitudes of the characteristic numbers $\mathcal{P}r$, $\mathcal{R}a$ and $\mathcal{R}e$. Although heat transfer in mixed convection can be derived analytically through dimensional analysis, an exact solution for these complex flows is often likely to fail. Additional approximate analysis of the energy and momentum transfer in the boundary layers does not offer practical solutions to all problems and configurations. Hence, numerous empirical correlations has been developed to estimate the heat transfer in mixed convective flows for various configurations.

In principle, most studies of *MC* in several configurations report an enhancement of the heat transfer at the boundaries into the fluid for laminar flows with the on-set of secondary buoyancy flow, because the flow in the boundary becomes turbulent. An experimental study in water flows, between two horizontal parallel plates heated from top and below, with a uniform and asymmetric heat flux, was performed by Osborne et al. [91]. The study reveals a clear influence of buoyancy forces on the laminar flow and the heat transfer within $5.2 \times 10^6 \leqslant \mathcal{R}a \leqslant 8.2 \times 10^8$, $650 \leqslant \mathcal{R}e \leqslant 1300$ and $5 \times 10^1 \leqslant \mathcal{R}a^{3/4}/\mathcal{R}e\mathcal{P}r \leqslant 9 \times 10^3$. In addition, Osborne founds that the bottom plate is nearly independent of the conditions at the top plate. However, both are strongly influenced by the buoyancy forces. Moreover, with the onset of buoyancy flows, the impact on the flow in traveling direction leads to an enhanced heat transfer at the bottom plate.

Other studies, which are related to the development and the optimisation of heat exchangers, also report an enhancement of the heat transfer with the onset of a buoyancy flow. Exemplary experimental studies on this topic are given, for instance, by Incropera et al. [59] or Dogan et al. [37]. The studies are focused on *MC* heat transfer in rectangular channels with an array of discrete heat sources at the bottom and top, representing electronic devices. With the onset of the buoyancy flow an enhancement of the heat transfer was found, while a decrease of the heat transfer with increasing channel length was obtained. In addition, Incropera [59] observes that the vertical temperature gradient is much smaller towards the end of the duct than at its beginning.

For *MC*, the dimensional analysis reveals a correlation $\mathcal{N}u = f(\mathcal{R}a, \mathcal{R}e, \mathcal{P}r)$. Experimental studies have disclosed that $\mathcal{N}u$ can be approximated by a superposition of the Nusselt numbers related to the *FC* and *TC*

$$\mathcal{N}u^n = |\mathcal{N}u_{FC}^n \pm \mathcal{N}u_{TC}^n| \,, \tag{2.26}$$

where the exponent n primarily depends on the geometry and the sign, whether the flow of *FC* and *TC* is rectified or opposed [11].

2.4 SPATIAL SCALING OF MIXED CONVECTION

The non-dimensional numbers which are necessary to characterise the process of mixed convective air flow were introduced in section 2.1. Here, the idea and basic concept of the dimensional analysis are introduced and the similarity conditions for *MC* are determined. Furthermore, based on the concept of spatial scaling, it is discussed how the physical properties of a system have to be adjusted, and experiments have to be carried out on the scaled system.

2.4.1 *Dimensional analysis and similarity*

The idea on which the tool of dimensional analysis is based is simple and fundamentally comparable to the problem of similarity in geometry. Its basic principles were already known to Isaac Newton (1686). Newton referred to it as the "Great Principle of Similitude". The dimensional analysis allows the comparison of systems with a high intricacy or tells us under which conditions two systems are comparable. The mathematical theory and technique required for the dimensional analysis, the Buckingham-Π theorem, is textbook material [36, 14]. Edgar Buckingham introduced the key theorem of the dimensional analysis in 1914 [26, 27]. The theorem states that

> "Any physically meaningful relation $\Phi(R_1, ..., R_n) = 0$, with $R_j \neq 0$ is equivalent to a relation of the form $\Psi(\Pi_1, ..., \Pi_{n-m}) = 0$ involving a maximal set of independent dimensionless combinations in terms of m fundamental units."

The set of physical quantities $R_1, ..., R_n$ has to be measured in a consistent system and the fundamental units $F_1, ..., F_m$ of that system have to be independent. Then the new physical quantity referred to as Π by a product of the fundamental physical quantities R_j

$$\Pi = \prod_{j=1}^{n} \{R_j\}^{\xi_j} \quad \text{with} \quad \boldsymbol{\xi} = (\xi_1, ..., \xi_n) \in \mathbb{R}^n, \tag{2.27}$$

where the unit of Π is the product of powers of the fundamental units F_i

$$\{\Pi\} = \prod_{i=1}^{m} F_i^{a_{i1}\xi_1 + ... + a_{in}\xi_n}. \tag{2.28}$$

The combination Π is dimensionless if $\{\Pi\} = 1$, which is equivalent to

$$a_{i1}\xi_1 + ... + a_{in}\xi_n = 0. \tag{2.29}$$

Hence, for a set of physical quantities $R_1, ..., R_n$ a homogeneous system of linear equations

$$\mathbf{D}\boldsymbol{\xi} = \begin{pmatrix} a_{11} & \cdots & a_{1n} \\ \vdots & \ddots & \vdots \\ a_{m1} & \cdots & a_{mn} \end{pmatrix} \begin{pmatrix} \xi_1 \\ \vdots \\ \xi_n \end{pmatrix} = 0 \tag{2.30}$$

is obtained, where $\mathbf{D} \in \mathbb{R}^{m \times n}$ is the so-called dimension matrix. Any column of this matrix represents the dimension vector of the corresponding physical quantity R_j and Π_i is dimensionless if $\boldsymbol{\xi}$ is an element of the null space $\mathcal{N}(\mathbf{D})$. If the rank of $\mathbf{D}$ is m, the dimension of the null space is $n - m$. Hence, for a basis in the null space, $n - m$ linear independent dimensionless combinations $\Pi_1, ..., \Pi_{n-m}$ of the physical quantities $R_1, ..., R_n$ are found. Buckingham referred to these groups as Π-groups. Moreover, any physical relation $\Phi(R_1, ..., R_n) = 0$ is equivalent to the relation $\Psi(\Pi_1, ..., \Pi_{n-m}) = 0$. However, the choice of dimensionless combinations is not unique. The Buckingham-Π theorem describes a method of constructing a set of dimensionless parameters and does not automatically choose the most physical meaningful combination.

Two systems are similar if the corresponding non-dimensional parameters are the same and the physical values differ only in respect of the scale. Hence, two geometrically identical systems with different spatial dimensions are comparable if

$$\Pi_1^{(O)} = \Pi_1^{(S)}, ..., \Pi_{n-m}^{(O)} = \Pi_{n-m}^{(S)}, \tag{2.31}$$

where the superscript O is used for the full-scale size apparatus and S for the down-scaled apparatus.

Knowing under which conditions two apparatuses with the same geometry but scaled by a factor s_L are similar the question has to be answered: what are the governing parameters of mixed convective flow and how do they have to be adjusted to guarantee similitude?

To determine the physical quantities that have to be adjusted, it is necessary to examine the governing equations. *MC* is determined by the equation of heat transfer (2.12), the continuity equation (2.4) and the equation of motion (2.13). The corresponding fluid properties are: dynamic viscosity η, density ρ, heat capacity c_p, thermal conductivity k, thermal expansion coefficient α and the gravitational acceleration g. Due to the Boussinesq approximation, the thermal expansion coefficient α and the gravitational acceleration g do not have to enter the considerations separately. Just the product (αg) has to be taken into account.

To solve the three differential equations, boundary conditions are needed. The variables of relevance are a characteristic length L, a characteristic velocity U and a characteristic temperature difference $\Delta\Theta$. Because the setup of this study is strongly related to a *RBC* setup the characteristic length corresponds to the height H and the

	U	H	η	ρ	k	(αg)	$\Delta\Theta$	C_P
m	1	1	−1	−3	1	1	0	2
s	−1	0	−1	0	−3	−2	0	−2
kg	0	0	1	1	1	0	0	0
K	0	0	0	0	1	−1	1	−1

Table 1: The dimension matrix **D**. The entries represent the power of the fundamental units.

characteristic temperature difference $\Delta\Theta$ is the difference between the top and bottom plate.

The variables and their dimensions of physical quantities in fundamental SI-units are

$$\begin{aligned} &[\eta] : \mathrm{kg\,m^{-1}\,s^{-1}},\ \ [H] : \mathrm{m},\ \ [k] : \mathrm{Kg\,m\,s^{-3}\,K^{-1}},\ [U] : \mathrm{m\,s^{-1}},\\ &[\Delta\Theta] : \mathrm{K},\ \ [(\alpha g)] : \mathrm{m\,K^{-1}\,s^{-2}},\ \ [\rho] : \mathrm{kg\,m^{-3}},\ \ [C_P] : \mathrm{m^2\,s^{-2}\,K^{-1}} \end{aligned} \tag{2.32}$$

and the corresponding dimension matrix is shown in table 1. The rank of the matrix is four and eight columns. Consequently, $n - m = 8 - 4 = 4$ independent dimensionless parameters are necessary to characterise the flow at *MC* sufficiently. The non-dimensional similarity parameters Π_i are for instance

$$\Pi_1 = \frac{\eta\, C_P}{k},\ \ \Pi_2 = \frac{\Delta\Theta\, \alpha\, g\, H}{U^2},\ \ \Pi_3 = \frac{U\, H\, \rho\, C_P}{k},\ \text{ and }\ \Pi_4 = \frac{\alpha\, g\, H}{C_P}. \tag{2.33}$$

In the paragraph of *MC* just three characteristic numbers are introduced. However, four are determined from the dimension analysis. While Π_1, Π_2 and Π_3 can be calculated by the combination of $\mathcal{R}a$, $\mathcal{R}e$ and $\mathcal{P}r$, the non-dimensional parameter Π_4 is a new independent parameter. In this study, convective motion in thin layers is discussed, where the Boussinesq approximation is valid and thus $\Pi_4 \ll 1$. An assessment of a characteristic height $\hat{H} \gg C_P/\alpha\, g$, using air at standard conditions $C_P = 1026\ \mathrm{J\,kg^{-1}\,K^{-1}}$, $\alpha = 3.43 \times 10^{-3}\ \mathrm{K^{-1}}$ results in $\hat{H} \approx 35\,\mathrm{km}$ [67]. Here, with a characteristic length H much less than 35 km, the effect of the similarity parameter Π_4 is neglectable. Furthermore, for many other large-scale mixed convective flows, for example, modelling mixed convective flows in buildings or in meteorology, the characteristic length is mostly small enough. Nevertheless, scaling and modelling of convective flows in the Earth's mantle or in the sun's convection layer, where the Boussinesq approximation fails, needs an additional similarity parameter.

2.4.2 *Concept of spatial scaling for mixed convective air flow*

Convective flows on large scales usually result in high characteristic numbers. In particular, due to $\mathcal{R}a \sim H^3$, the Rayleigh number increases dramatically with increasing

height. Hence, for spatial scaling of *MC* the thermal convective flow is the limiting factor. The question arises: how can full-scale numbers can be obtained on laboratory scales, where the characteristic length is small?

In general high characteristic numbers are received by adjusting the fluid properties ν and κ, which requires an adaptation of the physical properties. This can be obtained by variation of the fluid pressure and the temperature or using a working fluid with a different density. For instance, high $\mathcal{R}a$ up to 10^{11} were obtained by Fleischer et al. [41] using pressurised sulphur hexafluoride (SF_6). The fluid properties of SF_6 are similar to air at atmospheric pressure; however, the density is six times higher. SF_6 is frequently used for spatial scaling in convective air flows, because the similarity condition of $\mathcal{P}r$ is inherently met. Another methodology of spatial scaling in mixed convective air flows is introduced by Linden et al. and Baker ([76], [13]). Their intention was to study the fluid mechanics of ventilation in rooms or entire buildings, without having to perform direct measurements on the full scale. This concept of small-scale modelling uses water as a working fluid and the buoyancy forces are produced by salinity. Due to U scaling with $\sqrt{g\,(\Delta\rho/\rho)\,H}$ the characteristic numbers for the spatial scaling are $\mathcal{R}e = (g'\,H)/\nu$ and $\mathcal{P}e = (g'\,H)/\kappa$. The concept of scaling the spatial dimensions is limited to a scaling factor of $s_H \approx 10$. Further, due to the absence of a thermal *BL* it does not reflect the processes of heat transfer and its dynamics sufficiently well. However, comparisons between small and full-scale measurements by e.g. Lane-Serff [72] showed that the concept accords well for large-scale flow structures.

Frequently, experimental studies combine multiple capabilities of scaling. For instance, Niemela et al. [88] studied the heat transfer in *RBC* up to very high $\mathcal{R}a \sim 10^{17}$ using cryogenic helium gas near the gas-liquid critical point. This very high $\mathcal{R}a$, according to my knowledge, is the highest $\mathcal{R}a$ obtained on laboratory scales. Nevertheless, $\mathcal{R}a$ is still some orders of magnitude smaller than $\mathcal{R}a$ in oceans ($\mathcal{R}a \leqslant 10^{20}$) or in the convective zone of the sun ($\mathcal{R}a \leqslant 10^{23}$).

Using air on both the laboratory scale and the full scale, one has to know how the physical properties in *MC* have to be adjusted and how experiments have to be carried out on the scaled system to obtain full-scale numbers. Based on

$$\frac{\mathcal{R}e^{(O)}}{\mathcal{R}e^{(S)}} = 1,\ \frac{\mathcal{R}a^{(O)}}{\mathcal{R}a^{(S)}} = 1 \text{ and } \frac{\mathcal{P}r^{(O)}}{\mathcal{P}r^{(S)}} = 1 \tag{2.34}$$

similarity in *MC* can be obtained by adjustment of the fluid properties $\Delta\Theta$, ν, κ and α, and U. However, which parameters have to be adjusted depends on the working fluid. Due to the low compressibility of liquids, the concept of spatial scaling and the implementation of the experiment on small-scales differs from the concepts, using a gas as the working fluid.

In this study, the working fluid at the full scale and small scale is air. Here the fluid properties ν, κ, $\Delta\Theta$ and $(g\alpha)$ depend on the physical properties pressure P and

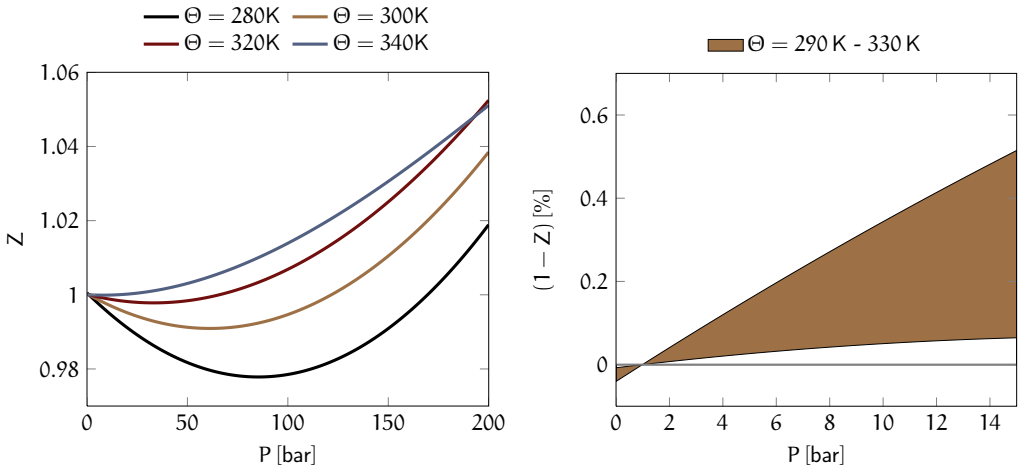

(a) (b)

Figure 4: (4a) Compressibility factor Z as a functions of P for different temperatures. (4b) The deviation of the compressibility factor from the state of perfect gas $Z = 1$ in a pressure range $1\,\text{bar} \leqslant P \leqslant 15\,\text{bar}$ and a temperature range $290\,\text{K} \leqslant \Theta \leqslant 330\,\text{K}$.

temperature Θ. A further parameter for adjusting $\mathcal{R}e$ is the characteristic velocity U. Hence, the spatial dimensions are scalable by varying the pressure, the characteristic velocity and the temperature separately or in combination. For the concept of spatial scaling in *MC*, which will be introduced in the following, the scaling is realised by the adjustment of the fluid pressure and characteristic velocity, while having the same $\Delta\Theta$ on full scale and small scale. Using air as working fluid, a scaling just by pressure and the characteristic velocity involves several benefits, which will be discussed later.

Before the concept is introduced, approximations are proposed for air as working fluid. Figure 4a depicts the compressibility factor

$$Z = \frac{P}{\rho\, R\, \Theta}, \tag{2.35}$$

for air as a function of pressure for different temperatures. The compressibility factor illustrates how much air differs from the behaviour of a perfect gas. Here, P denotes the fluid pressure, ρ the density, R the gas constant and Θ the fluid temperature. The factor is calculated by a third order virial equation given by Smits and Zagarola [118]. The graph clearly reveals that Z deviates of the order of a few per cent from the state of a perfect gas within a wide pressure range. In particular, within the parameter range of this study, the deviation from the state of a perfect gas is less 0.5 % (fig. 4b). Hence, within this pressure and temperature range air can be handled as a perfect gas. As a consequence, the specific heat capacity C_P and the thermal conductivity k can be assumed as constant and the thermal expansion coefficient is given by $\alpha = 1/\Theta$. If the

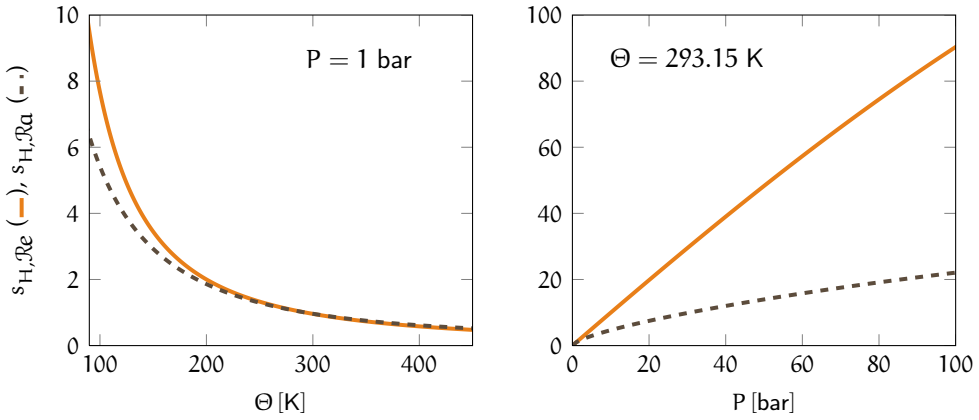

(a) (b)

Figure 5: $s_{H,\mathcal{R}e} = \mathcal{R}e/\mathcal{R}e^*$ and $s_{H,\mathcal{R}a} = \sqrt[3]{\mathcal{R}a/\mathcal{R}a^*}$ as a function pressure P and temperature Θ, where $(*)$ denotes the characteristic numbers at P = 1 bar and Θ = 293.15 K: (5a) $s_{H,\mathcal{R}e}$ and $s_{H,\mathcal{R}a}$ as a function of Θ and (5b) $s_{H,\mathcal{R}e}$ and $s_{H,\mathcal{R}a}$ as a function of P.

temperature difference ΔΘ and the ambient temperature of the full and small-scale configuration are the same, the similarity condition (eq. 2.34) leads to the set of equations

$$\begin{aligned}
\frac{\mathcal{R}e^{(O)}}{\mathcal{R}e^{(S)}} &= \left(\frac{U\,H}{\nu}\right)\left(\frac{s_\nu \nu}{s_U U\, s_H H}\right) = \frac{s_\nu}{s_U\, s_H} = 1 \\
\frac{\mathcal{R}a^{(O)}}{\mathcal{R}a^{(S)}} &= \left(\frac{H^3\,\Delta\Theta\, g\,\alpha}{\nu\,\kappa}\right)\left(\frac{s_\nu \nu\, s_\kappa \kappa}{(s_H H)^3\,\Delta\Theta\, g\,\alpha}\right) = \frac{s_\nu\, s_\kappa}{(s_H)^3} = 1 \\
\frac{\mathcal{P}r^{(O)}}{\mathcal{P}r^{(S)}} &= \left(\frac{\nu}{\kappa}\right)\left(\frac{s_\kappa \kappa}{s_\nu \nu}\right) = \frac{s_\kappa}{s_\nu} = 1,
\end{aligned} \tag{2.36}$$

where s_U, s_ν and s_κ denote the scaling factor of the corresponding properties U, ν and κ respectively. The solution of this set of equations discloses the following relations

$$s_U = \sqrt{s_H}, \quad s_\kappa = (s_H)^{\frac{3}{2}} \quad \text{and} \quad s_\nu = (s_H)^{\frac{3}{2}}. \tag{2.37}$$

To demonstrate the convenience of spatial scaling by adjusting the pressure, the scaling factors $s_{H,\mathcal{R}a} = \sqrt[3]{\mathcal{R}a(P,\Theta)/\mathcal{R}a^*}$ and $s_{H,\mathcal{R}e} = \mathcal{R}e(P,\Theta)/\mathcal{R}e^*$ as a function of P are displayed in figure 5, where $\mathcal{R}a^*$ and $\mathcal{R}e^*$ denote the characteristic numbers at atmospheric conditions (P = 1 bar and Θ = 293.15 K). The spatial scaling factors $s_{H,\mathcal{R}a}$ and $s_{H,\mathcal{R}e}$ reveal the capability of spatial scaling by pressure and temperature separately for $\mathcal{R}a$ and $\mathcal{R}e$. Figure 5a depicts the normalised scaling factors $s_{H,\mathcal{R}a}$ and $s_{H,\mathcal{R}e}$ as a function of the temperature Θ, while P = 1bar. The graph shows the limits

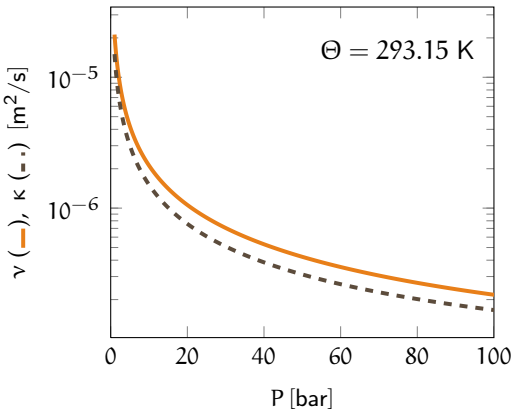

Figure 6: Fluid properties ν and κ as a function of the pressure P.

of spatial scaling by temperature adjustment. For a temperature of $\Theta = 90\text{K}$, which is already below the critical point of nitrogen ($\Theta_{crit} \approx 129\,\text{K}$), the spatial scaling factor $s_{H,\mathcal{R}a}$ is less than 6.3 and $s_{H,\mathcal{R}e}$ less than 9.5. Hence, the possibility of reducing the size of full-scale samples by temperature is limited to $s_H < 6$. On the contrary, figure 5b shows the scaling factors $s_{H,\mathcal{R}a}$ and $s_{H,\mathcal{R}e}$ as a function of P. The corresponding scaling factors already exceed the maximum factor of scaling by temperature at $P \approx 17\,\text{bar}$. Moreover, at $P = 100\,\text{bar}$, which is provided by several high pressure wind tunnels and vessels, a spatial scaling factor of $s_H \approx 22$ is obtainable.

The fluid properties ν and κ scale similar as a function of the pressure (fig. 6). Due to the nearly concurrent scaling of the fluid properties ν and κ it is evident that $\mathcal{P}r$ is approximately unaffected by P. Hence, the similarity condition $\mathcal{P}r^{(O)} = \mathcal{P}r^{(S)}$ is met inherently within a wide pressure and temperature range. However, figure 6 reveals a restriction of scaling by pressure. For $P > 50\,\text{bar}$ an increase of pressure demands a great effort compared with a little change of ν and κ.

In conclusion, spatial scaling in mixed convective air flows is theoretically possible by adjusting pressure and velocity. Moreover, the introduced concept of spatial scaling offers advantages compared to the scaling by temperature. The advantages are straightforward: it is less limited and simplified. Indeed, higher characteristic numbers or an enhanced scaling factor can be achieved by combining temperature and pressure adjustment or using a gas with a higher density. However, this would mean the loss of the simplicity of this concept.

3

EXPERIMENTAL SETUP AND MEASUREMENT METHODS

The examination of the heat transport and the fundamental flow features in mixed convective air flows is strongly affected by the apparatus and experimental setup. A challenging issue is thus the layout and functionality of the setup to obtain well-defined and reproducible mixed convection. In this study, the experiments are performed in a rectangular container with an inlet and an outlet port. The measurements are conducted at atmospheric and high pressure conditions to prove the concept of spatial scaling. In the following chapter, the experimental setup and the adaptations of the applied measurement techniques are introduced and discussed, for the experiments under high pressure and atmospheric pressure conditions.

3.1 EXPERIMENTAL FACILITIES

3.1.1 *Enclosure*

Mixed convective air flow was studied in two geometrically identical containers, while the lengths of the containers are scaled by the factor five. The dimensions of the full-scale and small-scale setup are listed in the table of figure 7, where H denotes the height, L the length, W the width, H_{in} the height of the inlet channel, H_{out} the height of the outlet channel, L_{in} the length of the inlet channel and L_{out} the length of the outlet channel. All dimensions are in mm. The small container was constructed to operate under high pressure conditions and the large container was designed to work at atmospheric pressure.

A sketch of the container's geometry is illustrated in figure 7. The container is formed of two parts. One part is a *RBC* container, consisting of a rectangular box with a quadratic cross-section and the aspect ratios

$$\Gamma_{LH} = \frac{\text{length}}{\text{height}} = 5 \quad \text{and} \quad \Gamma_{WH} = \frac{\text{width}}{\text{height}} = 1.$$

To generate buoyancy flows, the container is isothermally heated from below and cooled from above. In the present geometry, where $\Gamma_{LH} = \frac{\text{length}}{\text{height}} = 5$, the preferred pattern for pure thermal convective flow consists of four counter-rotating *LSC*s in the longitudinal cross-section (fig. 7).

The sketch on the right side of figure 7 depicts the vertical cross-section of the container. At the top, the container is equipped with an inlet slot and at the bottom with an outlet slot. The slots are located on the same side and span over the whole

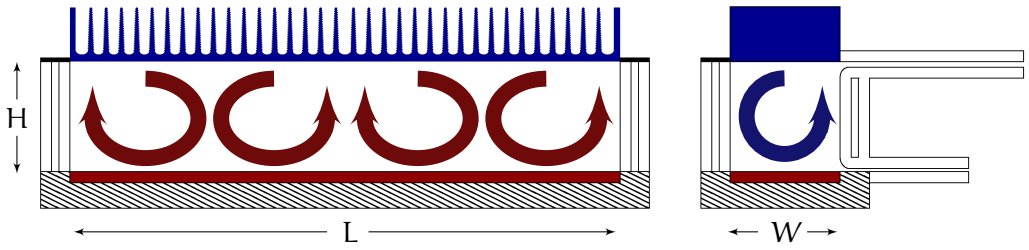

[mm]	H	L	W	H_{in}	H_{out}	L_{in}	L_{out}
small container	100	500	100	5	3	150	110
large container	500	2500	500	25	15	750	450

Figure 7: Sketch of the container's geometry and a table of the lengths in the small container and in the large container. All dimensions are in mm.

length, where the height of the inlet is $H_{in} = 0.05 \times H$ and of the outlet $H_{out} = 0.03 \times H$. To guarantee well-defined and reproducible inflow conditions the container is additionally equipped with an inflow channel, to provide a fully developed velocity profile at the inlet slot. The length of the inflow channel is $L_{in} \approx 30 \times H_{in}$. To provide defined outflow conditions, as well the outlet is equipped with a channel. With this configuration, well-defined forced convective flow is obtained. The air enters the container through the inlet at the top and the incoming wall jet follows the ceiling, detaches, flows downward on the opposite side wall, detaches again, flows over the heating device and splits into two parts. One part of the flow leaves the container through the outlet, while the other part ascends along the right side wall. As a result, a two-dimensional roll structure is developed in the vertical cross-section (fig. 7 right side).

3.1.2 *Thermal boundary conditions*

A major issue for the design of the setup is the thermal boundary condition. Most fundamental studies of convective flows support adiabatic boundary conditions at the lateral walls and isothermal conditions at the top and bottom plates. While these boundary conditions can be easily realised in numerical simulations, an implementation is almost impossible in an experimental setup. Several studies have been performed to determine the influence of finite side wall conduction on the thermal convective flows and the heat transfer. For instance, Brown et al. [25] examined the impact of finite heating and cooling device conductivities on the heat transport in *RBC* using water as the working fluid. Brown et al. studied the effect on the heat

transport in three apertures of different size in a range of $10^8 \leqslant \mathcal{Ra} \leqslant 10^{12}$ for various aspect ratios. Two sets of top and bottom plates with differing conductivities for each sample were used. Both sets of plates are geometrically identical and the plates are made of copper and aluminium. A lower $\mathcal{Nu}$ was observed in the configuration with aluminium plates, when the conductivity is smaller, while $\mathcal{Nu}$ was almost independent of the aspect ratio.

In addition to the impact on the heat transport by finite conductivity of the heating and cooling device, the effect of lateral wall's conductance is at least of same importance. Several theoretical and numerical studies were performed in *RBC*, related to the effect of sidewall conductance on the heat transport, the temperature and the velocity distribution. For the heat transport through the lateral walls, Roche et al. [105] and Ahlers [1] argue that in turbulent *TC* a correction by simple subtraction of the heat flux through the lateral walls, which was determined in an empty container, leads to greater errors. Ahlers shows that the error of $\mathcal{Nu}$, using water as the working fluid, can be 20 % or more for $\mathcal{Ra}$ up to 10^{12}. An accurate correction is only possible with knowledge of the two-dimensional temperature field at the side walls.

A numerical investigation, which studies the effects of finite thermal conductivity at the lateral wall in turbulent *RBC*, was presented by Verzicco [122]. A comparison of the results with adiabatic and non-adiabatic boundary conditions reveals an additional heat flux at a lateral wall leading to a vertical thermal boundary layer. As a result, an elevated buoyancy is obtained and the temperature field and the flow field differ from that with adiabatic boundary conditions.

In conclusion, small differences of the boundary conditions can lead to a significant influence on the heat transport. Moreover, an impact on the velocity and temperature distribution is observed, even though the characteristic numbers are the same. Hence, to examine the scaling in *MC*, the small container and the large container have to provide almost similar boundary conditions. However, despite the greatest efforts, due to technical reasons and cost concerns, differences in the boundary conditions exist.

The lateral walls consist of transparent acrylic glass, in order to perform Particle Image Velocimetry (PIV). Nevertheless, to obtain almost adiabatic boundary conditions, both containers comprise a double-layer system of acrylic glass with an insulating sheath of air between the plates. This configuration allows to obtain almost adiabatic boundary conditions, whith simultaneous optical accessibility. The thickness of the acrylic glass is $d_{acr} = 10\,\mathrm{mm}$ and the air layer between the plates amounts to $d_{air} = 5\,\mathrm{mm}$. For both set-ups, an estimated total thermal transfer coefficient through the lateral walls of

$$h = \left(2 \cdot \frac{d_{acr}}{k_{acr}} + \frac{d_{air}}{k_{air}} + \frac{1}{h_{con}} + \frac{1}{h_{rad}} \right)^{-1} \approx 0.9\,\mathrm{W/m^2\,K}, \tag{3.1}$$

is achieved, where $k_{acr} \approx 0.19\,W/Km$ [39] and $k_{air} \approx 0.034\,W/Km$ [67] denote the thermal conductivities of acrylic glass. The coefficient of the convective heat transfer estimates $h_{con} \approx 6\,W/m^2\,K$ [67] and the radiative heat transfer coefficient is

$$h_{rad} = \sigma_B \epsilon_{acr} \left(\overline{\Theta}^2 + \Theta_a^2\right)\left(\overline{\Theta} + \Theta_a\right) \approx 7\,W/m^2\,K, \tag{3.2}$$

where σ_B denotes the Stefan-Boltzmann constant, $\epsilon_{acr} \approx 0.97$ [86] the emissivity of the acrylic glass, Θ_a the ambient air temperature and $\overline{\Theta}$ the mean system temperature. Because the thermal conductivity and thus the heat transfer coefficient of air is almost constant within a wide pressure range, the assumption applies to high and atmospheric pressure conditions respectively.

The ceiling and the floor of the container are designed to obtain isothermal boundary conditions. In both set-ups, the ceiling is equipped with a passive air to air heat exchanger, which consists of an aluminium body with cooling fins. Accordingly, the temperature of the ceiling approximates the ambient temperature. For technical reasons, the implementation of the heating device is realised differently for both containers. For the measurements under high pressure conditions, the heating of the bottom plate must accomplished electrically. The heating device of the small container consists of a copper plate thermally insulated and heated by a heating pad. In the large container, the bottom consists of an aluminium plate heated via a temperature-controlled water circuit. Further, to obtain a homogeneous temperature distribution, the heating device is divided into five separate sub-circuits.

3.1.3 *Inflow conditions*

Another critical issue is the generation of a homogeneous inflow. Due to the low inflow velocities of $0.140\,m/s < U_{in} < 0.390\,m/s$ in the small container, minor fluctuations or a spatial in-homogeneity of the inflow at the inlet slot lead to different flow structures and dynamics inside the container. To ensure a homogeneous inflow at the inlet, the inflow section is divided into three parts. The first part consists of a box equipped with a speed controlled fan. A tube connects the box to a volume flow meter to determine the mean inflow velocity and before the air enters the inflow channel it is rectified and spatially distributed by a settling chamber. Then the air flows through the inlet channel, which has a length of $L_{in} \approx 30 \times H_{in}$. Consequently, at the inlet slot, a spatially homogeneous and fully developed velocity profile is provided.

In accordance with the concept of spatial scaling, the inflow velocities are higher by a factor $\sqrt{5}$ in the large container. As a result, the speeds are $0.330\,m/s < U_{in} < 0.872\,m/s$. However, a well-defined and a homogeneous inflow condition is of the same importance in the large container. To ensure a homogeneous velocity profile at the inlet slot, the inflow is realised by an external ventilating system. The system consists of a radial fan, a volume flow meter, two settling chambers and an inlet channel. The

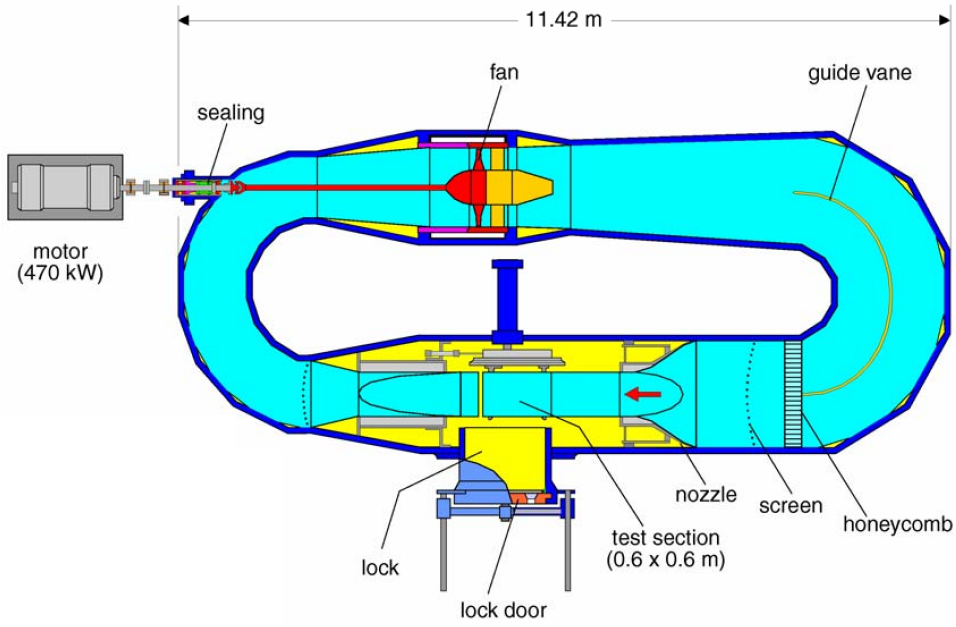

(a)

Figure 8: Sketch of the high pressure wind tunnel Göttingen (HDG) [45].

first settling chamber is located directly at the beginning of the inlet channel to ensure a spatially homogeneously distributed inflow and is divided into three sub systems. To provide a uniform volume flow to each of the three sub systems an additional settling chamber is placed before, in which the volume flow is partitioned into three parts of equal volume flow rate. In addition, the inlet channel is equipped with an array of honeycombs at its beginning to obtain a homogeneous spatial distribution.

3.1.4 *High pressure wind tunnel*

The measurements under high pressure conditions were performed in the High Pressure Wind Tunnel Göttingen (HDG). Figure 8 depicts the wind tunnel. The HDG is a Göttingen-type closed circuit low speed wind tunnel, which can be operated at up to 100 bar. The test section of the HDG has a height of 0.6 m, a width of 0.6 m and a length of 1 m. These dimensions necessitate a compact arrangement of the different measurement components.

The function of the HDG in the experiments is twofold. The HDG allows the adjustment of the fluid pressure and supplies the cooling of the ceiling. For the concept of spatial scaling the HDG provides a scaling factor of $s_H \approx 22$ at 100 bar. For the small container with $H = 0.1\,\mathrm{m}$, $\Delta\Theta \approx 20$ K and a mean temperature of $\Theta \approx 300$ K

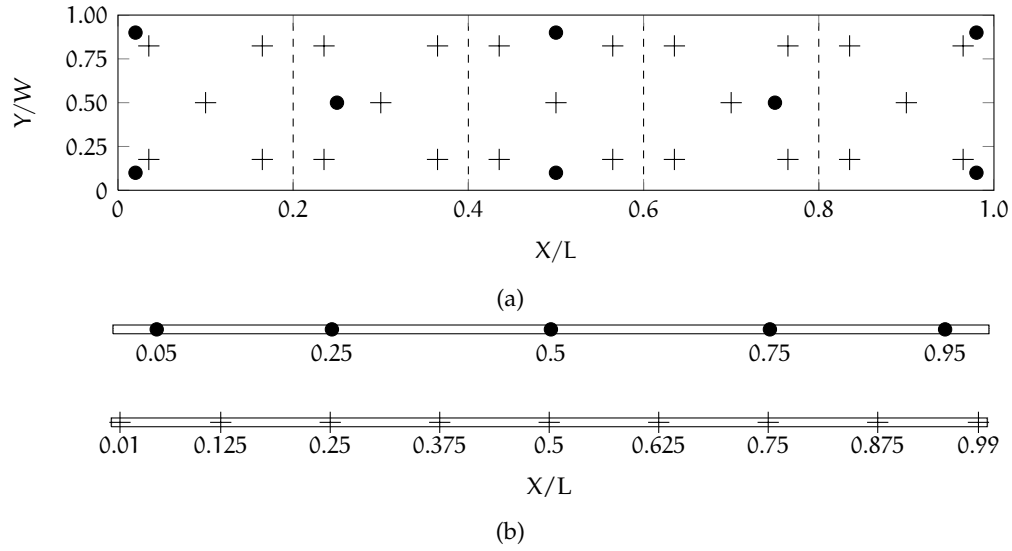

Figure 9: Spatial distribution of the temperature sensors in the top and bottom plate (9a) and at the outlet (9b). Where (+) denotes the sensor positions in the large container and (•) the positions in the small container.

characteristic numbers of $\mathcal{R}a \sim 10^{12}$ and $\mathcal{R}e \sim 10^{6}$ can be obtained. The measurements of this study are performed at $P \approx 11.6\,\mathrm{bar}$, which complies to a spatial scaling factor of five.

In addition, the HDG provides an advantage regarding the thermal boundary conditions. Due to the relative large volume of $V_{HDG} \approx 18\,\mathrm{m}^3$ the heat that dissipates through the heat exchanger at the top and the outlet has no significant effect on the ambient air temperature. Hence, the air temperature in the wind tunnel is constant. On the contrary, in smaller pressure chambers, without additional cooling, the heat flux causes an increase of the ambient temperature, which influences the boundary conditions at the side walls.

3.2 TEMPERATURE MEASUREMENTS

The full-scale and the small-scale setup are equipped with a numerous of temperature sensors. The majority are embedded in the heating and cooling device. In the small container, eight sensors are placed shortly below the surface of the top and bottom plate, while the large container is equipped with 25 sensors respectively. Figure 9a shows the spatial arrangement of the sensor elements. Further, the dashed lines reveal the five sub-circuit systems of the heating plate in the large container. In both containers the temperature sensors, in the top and bottom plate, are Platinum Resistance Thermometers (PRT) and the resistances were recorded by a Keithley

7 1/2-Digit multimeter [64]. The advantages of the PRTs are their high accuracy, low drift, linear characteristic within a wide operating range and suitability for precision applications. The PRTs which were used are Pt100 and Pt1000 1/3 DIN B. The measurement error of the sensors is $\delta\Theta_{Pt100} = \pm 1/3\ (0.3 + 0.005\ \Theta/^{\circ}C)\ K$, while the total error consists of a temperature independent and temperature-dependent error. However, to determine $\mathcal{R}a$ the temperature difference between the top and bottom plate is of interest. Hence, the temperature independent error can easily be disposed of by calibrating the sensors to a reference sensor.

In the large container, three PRTs are placed at the beginning of the inlet channel and nine sensors at the end of the outlet channel (fig. 9b). The sensors are located at the end of the outlet channel in order to avoid disturbance of the flow into the container. However, due to the mixing in the outlet channel, characteristic temperature fluctuations are not measurable. Consequently, in the large container just the spatial temperature distribution is determined. Moreover, the temperature at the end of the outlet channel, does not correspond to the temperature directly at the outlet slot. To obtain the temperature at the outlet slot a correction of the outlet temperature is needed. The loss of heat in the outlet channel is calculated based on the $\mathcal{N}u$-relation for turbulent pipe flow [11]

$$\mathcal{N}u = 0.023\,\mathcal{R}e_D^{4/5}\,\mathcal{P}r^{1/3}, \tag{3.3}$$

where $\mathcal{R}e_D$ denotes the Reynolds number of the flow in the outlet channel. The characteristic length L_D corresponds to the hydraulic diameter of the rectangular duct $L_D = H_{out}\,W/(H_{out} + W)$, where H_{out} is the outlet height and W the corresponding width of the outlet channel. Hence, by equation (2.22) the heat transfer coefficient h_D at the inner duct walls is calculated. Further, the heat transfer through the side walls of acrylic glass is given by d_{acr}/k_{acr}, where $d_{acr} = 0.01\,m$ is the thickness of the channel walls and $h_{acr} = 0.19\,W/m\,K$ a heat transfer coefficient of acrylic glass. Consequently, the heat-transfer coefficient is

$$h = \left(\frac{d_{acr}}{h_{acr}} + \frac{1}{h_{out}} + \frac{1}{h_D}\right)^{-1},$$

while the heat transfer coefficient at the outer side walls is estimated to be $6\,W/m\,K$. The corresponding equation of the enthalpy flux is

$$\dot{Q} = c_p\,\dot{M}\,\frac{d\Theta_D}{dL}\,L = -hA_D(\Theta_D - \Theta_a), \tag{3.4}$$

where $\dot{M}$ denotes the mass flow, Θ_a the ambient temperature, Θ_D the mean air temperature in the outlet channel, A_D the area of the channel walls and L the position in length direction. By solving the differential equation 3.4 the following relation

$$\Theta_{out} = \Theta_a + \left(\Theta_D^{end} - \Theta_a\right)\exp\left(\frac{h\,(2\,H_{out} + 2\,W)}{c_p\,\rho\,H_{out}\,W\,U_{out}}\right) \tag{3.5}$$

is obtained, where Θ_D^{end} represents the temperatures at the end of the outlet channel and $U_{out} = 5/3\,U$ is the mean velocity in the outlet channel. Based on equation 3.5 the outlet temperatures were adapted to estimate the temperatures at the outlet slot.

3.3 PARTICLE IMAGE VELOCIMETRY

Instantaneous velocity fields are determined by Particle Image Velocimetry (PIV) for *FC* and *MC* in the large container under ambient pressure conditions and in the small container under high pressure conditions. PIV is an optical measurement technique, based on the recording of homogeneously distributed tracer particles, which are illuminated, usually by a short pulsed high-energy laser, and recorded twice each measurement. The delay between the two exposures has to be small enough that most of the particles in the first frame are present in the second frame. On the contrary, the delay must not be chosen to be so small, that the particle shift is insufficiently large to be detected. A velocity field is calculated by the displacement of the particles. Therefore, the frames are divided into a large number of interrogation windows. By a spatial cross-correlation a locally averaged displacement vector is calculated for each interrogation window. The particle images are converted to a velocity using the time between two frames and the magnification factor. For further details of this measurement technique, the reader is referred to Raffel et al. [102].

With the objective to identify large-scale flow structures and their low-frequency dynamics, series of instantaneous velocity fields were acquired at a repetition rate of $f = 2/3\,Hz$. For each series, 500 - 800 instantaneous velocity fields for *FC* and $3200 - 4800$ in case of *MC* were recorded in a vertical and a longitudinal measurement plane. In both containers two-dimensional and two-component (2D2C) PIV was performed in the vertical cross-section at $X = 0.5 \times L$ for the whole cross-section. In the longitudinal plane at $Y = 0.5 \times W$ PIV was applied to the cross-section segment $0.43 \times L < X < 0.82 \times L$ in the large container, while in the small container, the PIV was accomplished for the whole cross-section.

A critical component of PIV in the HDG was the generation and injection of the seeding particles into the fluid. At ambient conditions usually oil droplets with a mean diameter of $d_P \approx 2\,\mu m$ are used as tracer particles. Details about the generation of the seeding particles can be found in Raffel et al. [102]. However, for several reasons, including danger of explosions, the usage of oil droplets in the HDG is not allowed. Hence, a challenging issue was the selection and generation of tracer particles for usage under high pressure conditions in the HDG and their homogeneously distributed injection into the flow.

For PIV under high pressure condition, aluminiumoxid Al_2O_3 powder (Matroxid MR-70 [83]) was used. The particles are introduced into the HDG using a pressurised fluidised-bed particle dispenser. The seeding generator produces monodisperse tracer particles with a mean diameter of $d_P = 1\mu m$. The dispenser is additionally equipped

with a sonic flow orifice, where strong shear stresses break up clumps of the material to avoid larger agglomerations. Details on the design and operation of a fluidised-bed seeding generator can be found in the publications of Willert [127] and Kähler [62]. To provide a homogeneous distribution of tracer particles; the particles were seeded into the wind of the HDG. As a result, after a few circulations, the tracer particles are homogeneously distributed and larger agglomerations either sinking to the bottom under the influence of gravity or collided with the wind-tunnel walls due to their mass inertia.

Another restriction of PIV in the HDG is the optical accessibility. Since the HDG was originally not designed for the application of PIV, the wind tunnel provides only five small windows, where the laser light sheet is coupled into the wind tunnel and the camera are placed. Two windows are on the front door and three on the ceiling of the test section. At ambient pressure and under high pressure conditions, the particles were illuminated by a dual cavity Nd:YAG laser. The light pulses were shaped into a sheet of $2-5\,\mathrm{mm}$ thickness and the images were recorded by a pco.4000 [94] camera with a resolution of $4008 \times 2672\,\mathrm{pixel}$ and $12\,\mathrm{bits}$ grayscale. The instantaneous velocity vector fields were calculated using the software PIVview by PIVTEC GmbH [96]. The PIV data processing parameters are listed in appendix A.

3.4 MEASUREMENT PARAMETERS

In the following the calculation of the characteristic numbers is introduced. For $\mathcal{R}e$ and $\mathcal{R}a$ the height of the container represents the characteristic height H and the characteristic velocity U corresponds to the spatial mean of the time-averaged inflow velocity U_{in}. The system temperature

$$\overline{\Theta} = 0.5 \cdot (\Theta_t + \Theta_b) \tag{3.6}$$

is determined by the mean value between top and bottom plate temperature and the characteristic temperature difference $\Delta\Theta$ is given by

$$\Delta\Theta = \overline{\Theta}_b - \overline{\Theta}_t. \tag{3.7}$$

Here, the mean temperature $\overline{\Theta}_t$ and $\overline{\Theta}_b$ corresponds to the spatial mean of the time-averaged temperatures of the top and bottom plate respectively.

The fluid properties ν, κ and α were calculated by a third order virial equation given by Smits and Zagarola [118] as a function of the time-averaged pressure P and system temperature $\overline{\Theta}$. All measurements are performed in a time period of almost thermal equilibrium, which was indicated by a stable oscillation of the temperature at the outlet for the small container and a constant temperature at the end of the outlet channel for the large container. The period to obtain thermal equilibrium is, in particular for higher $\mathcal{A}r$, several hours for the small container and almost one day for the full-scale setup.

4

LARGE-SCALE STRUCTURE ANALYSIS

Turbulent convective flows are usually three-dimensional, unsteady or even reveal a chaotic behaviour. Statistics like the time averaged velocity field or the corresponding velocity fluctuations are insufficient to characterise such complex flows. Hence, to prove the concept of spatial scaling valid characteristics have to be determined to examine similarty of the flows in the two containers with different size. Therefore, the analysis of the velocity vector fields have the two main objectives: identification of the topology of the predominant coherent structures and determination of their dynamics. Here, the prevailing structures are mainly large-scale circulation (*LSC*).

In the following a pattern is termed as *LSC* if the velocity field is normal to both, the symmetry and radial axis. If the velocity is further proportional to the radius r, the rotational plane is characterised by

$$\mathbf{u} = \begin{cases} u_r &= U_0 \\ u_\varphi &= U_R \frac{r}{R_{LSC}} \quad \text{with} \quad 0 \leqslant r \leqslant R_{LSC} \end{cases}, \tag{4.1}$$

where U_R denotes the maximal velocity at the boundary of the *LSC*, R_{LSC} the radius of the *LSC*, u_r the velocity parallel to r and u_φ the velocity orthogonal to r.

For these structures, the usual identification criteria are based on local quantities like velocity, velocity gradients or vorticity. However, due to the intermittant small-scale turbulence a localisation or a derivation of the *LSC* from an instantaneous velocity field is often likely to fail. To cope with this issue, a scalar function is used, which is derived from a velocity vector field [84]. This function provides the detection of the centre position and the boundary of large-scale vortexes by considering only the topology of the velocity field, but not its magnitude. A detailed description of this scalar function is introduced in section 4.1.

Further, for the analysis of the velocity fields, a Proper Orthogonal Decomposition (POD) was applied. The POD was initially introduced to detect and analyse bifurcation of spatiotemporal dynamical systems and was applied to the field of hydrodynamics in the sixties when there was a fundamental need of mathematical definitions of coherent structures in turbulent flows [79, 78]. Despite the initial scepticism (the main criticism was that the extracted features are characteristics of second-order statistics) by parts of the fluid dynamics community with respect to the POD procedure, the POD is now a popular and powerful tool for the analysis of turbulent flows [9].

No overall framework is currently available to incorporate coherent structures into the turbulent theory. The application of POD to the field of fluid dynamics allows a better understanding of complex flow problems in general and of large-scale energetic

flow structures, in particular. Indeed, the POD is an important tool for the analysis of intricate turbulent convective flows with its often chaotic dynamics [117]. Its properties, as optimal convergence or space-time symmetry [54, 6], suggest that it is a preferred basis to use for various applications. Thus, the POD was applied to many other disciplines beside hydrodynamics, for instance: signal analysis [6], data compression [5], image processing [106] or oceanography [97]. The mathematical framework of the POD algorithm and its adaptation to a set of instantaneous velocity fields is described in section 4.2.

In the present study, both analysis methods were applied to two-dimensional velocity vector fields determined by PIV. Nowadays, PIV systems enable the measurment of thousands of instantaneous velocity fields over a large field of view. Each consists of tens of thousands velocity vectors. An analysis of this highly resolved data requires sufficient computing power. In regard to the POD procedure in 1987, Sirovich [115] notices, that large number of snapshots with a high spatial resolution exceeds the machine capacity of the moment. However, the rapidly growing computing power enables the computational analysis of even a large quantity of data in a timely manner. Nevertheless, this huge quantity of data remains a challenging task for robustness and efficiency of the applied analysis algorithms. Both algorithms were proven to be robust dealing with large sets of highly resolved velocity vector fields [124, 48].

4.1 VORTEX IDENTIFICATION ALGORITHM

Due to intermitting small-scale vortexes in turbulent convective flows a clear identification of the roll structure's characteristics like its centre position or its diameter is often difficult or even impossible. To overcome this issue Michard et al. [84] introduced a dimensionless scalar function Υ. The function is directly calculated from a two-dimensional velocity vector field by

$$\Upsilon(\mathbf{x}) = \frac{1}{S}\int_{\mathbf{x}'\in S} \frac{(\mathbf{R}(\mathbf{x}')\times\mathbf{u}(\mathbf{x}'))\cdot\mathbf{n}_z}{|\mathbf{R}(\mathbf{x}')|\cdot|\mathbf{u}(\mathbf{x}')|}\,dS = \frac{1}{S}\int_{\mathbf{x}'\in S} \frac{((\mathbf{x}'-\mathbf{x})\times\mathbf{u}(\mathbf{x}'))\cdot\mathbf{n}_z}{|\mathbf{x}'-\mathbf{x}|\cdot|\mathbf{u}(\mathbf{x}')|}\,dS, \quad (4.2)$$

where S is an area surrounding the point $\mathbf{x}$, $\mathbf{x}'$ is an element of the area S, $\mathbf{R}(\mathbf{x}') = \mathbf{x}'-\mathbf{x}$ a radius vector with the origin at $\mathbf{x}$, $\mathbf{n}_z$ the unit vector normal to the plane S and $\mathbf{u}(\mathbf{x}')$ the in-plane velocity vector at the position $\mathbf{x}'$. According to its definition Υ is a dimensionless scalar function with $-1 \leqslant \Upsilon \leqslant 1$, where $|\Upsilon|$ has the local maximum at the vortex centre position. In addition, the sign indicates the rotation direction of the vortex. The function Υ provides a systematic and explicit procedure to detect the location of the vortex centre position and the topology.

Another feature of Υ is the capacity to remove small-scale turbulent intermittency. The averaging over the area S is a spatial low-pass filter and with a skillful choice of S, small-scale structures are removed without having a strong effect on the location of the maximum of Υ. This feature almost predestines Υ to extract *LSC* from the

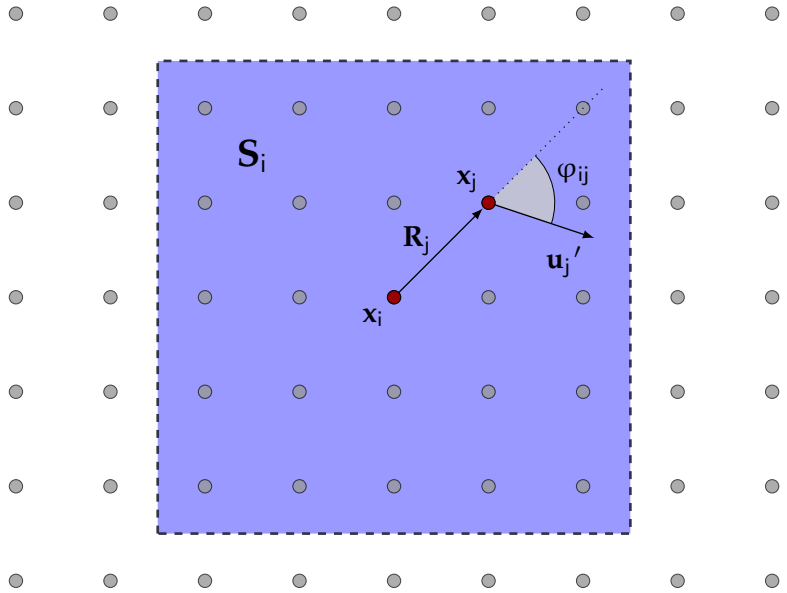

Figure 10: Definition sketch for the computation of the scalar function Υ.

small-scale turbulent background in turbulent convective flows. Furthermore, to make the function Υ Galilean invariant the mean local velocity in the vicinity of the point $\mathbf{x}$

$$\tilde{\mathbf{u}}(\mathbf{x}) = \frac{1}{S'} \int_{\mathbf{u} \in S'} \mathbf{u}'(\mathbf{x}') \, dS \tag{4.3}$$

is subtracted prior the evaluation of Υ. Hence, the local velocity is given by $\mathbf{u}'(\mathbf{x}') = \mathbf{u}(\mathbf{x}') - \tilde{\mathbf{u}}(\mathbf{x})$, where for the present data the calculation was performed with $S = S'$.

For the adaptation to the velocity vector field, a field is divided into discrete quadratic sub domains S_i of unique size. Then, Υ is written in a discrete form

$$\Upsilon(\mathbf{x}_i) = \frac{1}{N-1} \sum_{\mathbf{x}_j \in S_i} \frac{\left((\mathbf{x}_j - \mathbf{x}_i) \times \mathbf{u}_j' \right) \cdot \mathbf{n}}{|\mathbf{x}_j - \mathbf{x}_i| \cdot |\mathbf{u}_j'|} = \left| \frac{1}{N-1} \sum_{\mathbf{x}_j \in S_i} \sin(\varphi_{ij}) \right|, \tag{4.4}$$

where N is the number of grid points in the domain S_i and φ_{ij} the angle between the radius vector $\mathbf{R}_j = \mathbf{x}_i - \mathbf{x}_j$ and the velocity vector $\mathbf{u}_j'$. Additionally, a sketch of the corresponding variables required for the computation of Υ is depicted in figure 10.

To demonstrate the pertinence of Υ, in order to extract and detect *LSC*, an example is illustrated in figure 11. The plots show an instantaneous velocity vector field (fig. 11a), the corresponding Υ function (fig. 11b) and the vorticity (fig. 11c). The two-dimensional velocity vector field of mixed convective air flow was measured in the longitudinal cross-section $Y = 0.5 \times W$ at $\mathcal{R}a = 2.39 \times 10^8$, $\mathcal{R}e = 1.01 \times 10^4$ and $\mathcal{A}r = 3.3$ and reveals four *LSC*s arranged in the longitudinal direction. While

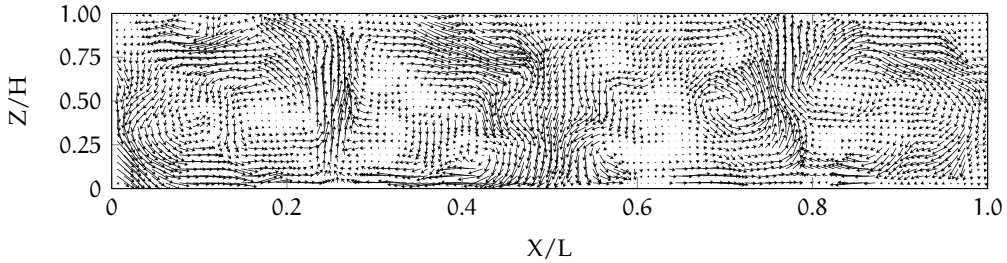

(a)

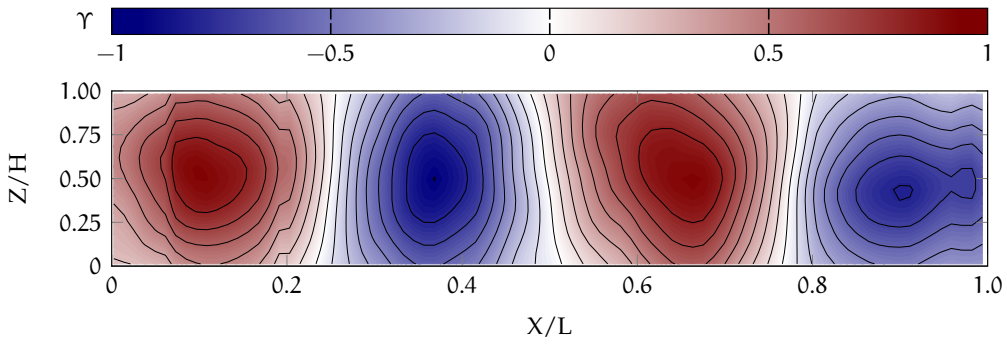

(b)

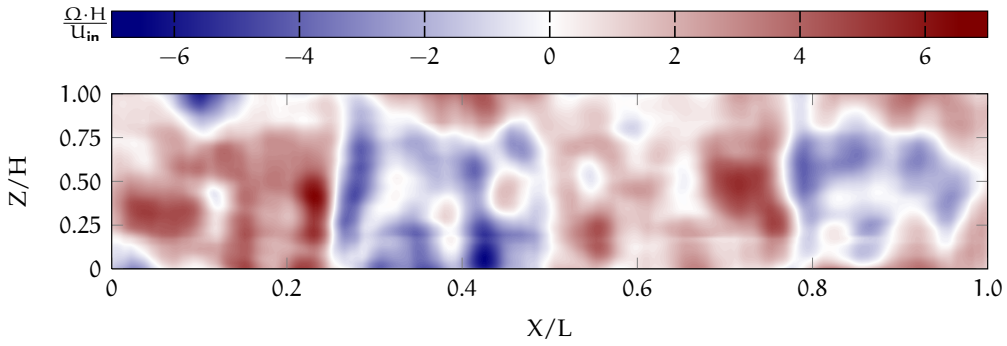

(c)

Figure 11: Detection of large-scale roll structures: (11a) instantaneous velocity vector field of mixed convective air flow in the longitudinal measurement plane $Y = 0.5 \times W$ at $\mathcal{R}a = 2.39 \times 10^8$, $\mathcal{R}e = 1.01 \times 10^4$ and $\mathcal{A}r = 3.33$, (11c) corresponding locally spatial averaged vorticity Ω normalised by H/u_{in} and (11b) scalar field Υ.

the *LSC* is approximately visible in the velocity vector field, a direct and automatic identification of *LSC* characteristics is unsuitable.

On the contrary, the contour plot of Υ clearly depicts the topology and the centre positions of the four longitudinally arranged *LSC*s. Once, the optimal size of S is determined, the algorithm provides a convenient process to calculate of *LSC* characteristics. For comparison, the vorticity $\Omega = (\partial u_y/\partial x) - (\partial u_x/\partial y)$ is displayed in figure 11c to reveal the great accurateness of Υ. The figure illustrates the corresponding in-plane vorticity, normalised by H/u_{in}. Furthermore, the vorticity is spatially averaged over an area S to remove small-scale vorticity. The figure discloses four regions with alternating rotational direction (blue signifies clockwise and red counter clockwise rotation), representing the four *LSC*s. However, an automatic identification of *LSC* characteristics based on the Ω distribution is not currently available.

4.2 PROPER ORTHOGONAL DECOMPOSITION

The POD was applied to the present data to extract the topology of predominant large-scale coherent flow structures and their trajectories in time from a set of instantaneous velocity vector fields. For practical applications in literature basically two methods of the POD exist: the direct method introduced by Berkooz et al. [16] and the snapshot method by Sirovic [115, 116]. For the analysis of the present data, the latter method was used. However, both are well proven and no significant difference was found [54, 9].

Basic concept

In principle, the POD is based on the Karhunen-Loéve theorem, which represents a stochastic process as an infinite linear combination of orthogonal functions, analogous to a Fourier series. However, the coefficients in the Karhunen–Loève theorem are uncorrelated random variables, in contrast to a Fourier series where the expansion basis consists of sinusoidal functions. The orthogonal basis functions are determined by calculus of variations to produce the optimal basis for its expansion.

Suppose, we have an ensemble of scalar fields $\{u^{(n)}\}$ and $u = u(\mathbf{x})$, where $\mathbf{x}$ denotes the spatial coordinates (u can also be a vector, but for simplicity, the fundamentals of the POD are introduced in the context of a scalar field). To project $u^{(n)}$ onto a new basis of orthonormal functions it is assumed that these functions belong to the Hilbert space $\mathbb{L}^2$, with an inner product

$$(f, g) = \int f(\mathbf{x}) g^*(\mathbf{x}) \, d\mathbf{x}. \tag{4.5}$$

Here, $(^*)$ indicates the complex conjugation. The basic objective of the POD procedure is to find a new basis of orthonormal functions, as a linear combination

$$u^{(n)}(\mathbf{x}, t_n) = \sum_{k=1}^{n} a_k \Phi_k(\mathbf{x}). \tag{4.6}$$

Therefore, a set of basis functions $\Phi_j(x)$ have to be calculated by maximising the time averaged projection of u onto Φ

$$\max_{\Phi \in \mathbb{L}^2} \frac{\left\langle |(u, \Phi)|^2 \right\rangle}{||\Phi||^2}, \tag{4.7}$$

where $|\cdot|$ denotes the modulus, $< \cdot >$ the time averaging operation and $||\cdot||$ represents the $\mathbb{L}^2$-norm. To find the maximum by calculus of variations, $\left\langle |(u, \Phi)|^2 \right\rangle$ has to maximise, while $||\Phi||^2 = 1$. This problem is equivalent to the eigenvalue equation

$$\int \left\langle u(\mathbf{x}) u^*(\mathbf{x}') \right\rangle \Phi(\mathbf{x}') \, d\mathbf{x}' = \lambda \Phi(\mathbf{x}), \tag{4.8}$$

whose null space is a two-point autocorrelation function

$$\mathbf{K}(\mathbf{x}, \mathbf{x}') = \left\langle u(\mathbf{x}) u^*(\mathbf{x}') \right\rangle. \tag{4.9}$$

Finally, a set of eigenmodes with the corresponding eigenfunctions, eigenvectors Φ_i and real eigenvalues

$$\lambda_n = \delta_{nm} \left\langle \zeta_n \zeta_m^* \right\rangle \tag{4.10}$$

is received, where all eigenvalues $\lambda_n > 0$, because $\mathbf{K}$ is positive definite.

In the case of PIV we have an ensemble of two-dimensional velocity vector fields $\mathbf{u}^{(n)} = \mathbf{u}(\mathbf{x}, n\tau)$ consisting of a set of N «snapshots» sampled at discrete time and space with a repetition rate τ. Based on this ensemble, a state variable for each snapshot

$$\boldsymbol{\nu}(\mathbf{u}) = (u_1, ..., u_M, v_1, ..., v_M, w_1, ..., w_M)^T$$

is defined, where u, v, w represent the velocity components and $M = i \times j$ are the number of grid points (the state variable can include other physical properties, for instance, pressure or temperature). The autocorrelation function of the state variables has a non-trivial null space and eigenfunctions of the form

$$\Psi = \sum_{n=1}^{N} \zeta_n \boldsymbol{\nu}^n, \tag{4.11}$$

where the constants ζ_n remain to be found. To calculate the constants, a state matrix

$$\boldsymbol{V} = \left[\boldsymbol{\nu}^{(1)}, ..., \boldsymbol{\nu}^{(N)} \right]$$

is defined and thus the autocorrelation matrix is

$$\mathbf{C} = \frac{1}{N}\boldsymbol{V}^T\boldsymbol{V}. \tag{4.12}$$

The matrix $\mathbf{C}$ is of the order $N \times N$. Based on equation (4.12) and equation (4.8) the eigenvalue equation is

$$\mathbf{C}\,\zeta = \lambda\zeta. \tag{4.13}$$

Because $\mathbf{C}$ is a squared matrix and all entries are positive, the eigenvectors are linearly independent and the matrix is positive definite, thus the eigenvalue problem can be written as

$$\mathbf{C} = \mathbf{P}\boldsymbol{\Sigma}\mathbf{P}^{-1}, \tag{4.14}$$

where $\boldsymbol{\Sigma}$ is a diagonal matrix with the eigenvalues $\lambda_1, ..., \lambda_N$ on the diagonal and $P = (\zeta_1, ..., \zeta_N)$ a matrix with the eigenvectors ζ on the columns. Solving the equation by an eigenvalue decomposition a set of eigenvectors $\{\zeta_i\}$ with the corresponding eigenvalues $\{\lambda_i\}$ and eigenfunctions

$$\boldsymbol{\Psi} = \mathbf{VP} \tag{4.15}$$

is obtained, where the columns of $\boldsymbol{\Psi}$ contains the eigenfunctions Ψ_i.

Physical interpretation

Basically, the POD is a mathematical framework for decomposing a set of spatial temporal functions via a statistical analysis, which have no inherent physical meaning. An interpretation of the eigenmodes as a relevant coherent flow structure has to be based on fluid dynamical aspects and on intuition.

Since the eigenfunctions $\{\Psi_i(\mathbf{x})\}$ are linearly independent, the eigenfunctions $\{\Psi_n\}$ are commonly termed as coherent structures and the corresponding eigenvalues are

$$\lambda_n = \left\langle |(\boldsymbol{\Psi}^n, \mathbf{v}^n)|^2 \right\rangle. \tag{4.16}$$

Thus, the eigenvalues λ_n have an interpretation of an energy and the total energy is the sum of the eigenvalues

$$E = \sum_{n=1}^{N} \lambda_n. \tag{4.17}$$

Moreover, in the present application $\mathbf{u}^n$ is a function of velocity components, hence the entries of the autocorrelation matrix $\mathbf{C}$ are the sum of squared velocity components

(eq. 4.12) comparable to a kinetic energy. In this case, the eigenfunctions $\{\boldsymbol{\Psi}_n\}$ have the interpretation of a kinetic energy distribution.

In practice, the POD is applied to identify coherent flow patterns, which are important for the dynamics. But what are the eigenmodes, respectively the flow pattern, of interest? For the analysis of turbulent flow this question is of vital importance. Commonly, POD provides eigenvalues, which are sorted in a descending order, such that the mode with the highest eigenvalue represents the most dominant coherent flow structure in terms of energy. With the aim of identifying the eigenmodes of importance, a frequently used criterion is to take the first m eigenmodes whose commutative sum of the normalised eigenvalue exceeds a threshold

$$\tilde{E} \geqslant \sum_{n=1}^{m} \tilde{\lambda}_n. \tag{4.18}$$

In principle, higher eigenvalues are obtained for eigenfunctions, which consists of large structures. Thus, the eigenmodes with the largest eigenvalues commonly represent large-scale coherent structures. Because we are interested in the topology and dynamic of large-scale structure, the eigenvalues is a valid indicator to identify the eigenmodes of interest.

By equation 4.6 it is found, that the eigenvector $\zeta_n(t)$ is a function of time. Hence, $\zeta_n(t)$ is often termed as time developing coefficient, representing the trajectory in time of the corresponding eigenfunction. In agreement with the physical interpretation of the POD eigenmodes, in the following the eigenfunctions are also termed as coherent structures, the eigenvectors as the time developing coefficient and the eigenvalues as energy eigenvalues.

5

MIXED CONVECTIVE AIR FLOWS IN A RECTANGULAR CONTAINER

Within the scope of verifying the concept of spatial scaling, it is indispensable to determine the characteristic features of mixed convective air flow. Hence, the subject of the following chapter is a rather general discussion of the large-scale structure formation in turbulent *MC* to identify and verify the prominent flow features. However, due to the diversity of the flow states and their complex dynamics, the identification of the flow characteristics needs further analysis.

In the present geometry, a key feature is the formation of large-scale circulation (*LSC*), often with a diameter of the order of the characteristic height H. With the objective of identifying the topology and dynamics of these large-scale roll structures, a *LSC* detecting algorithm (sec. 4.1) and a proper orthogonal decomposition (sec. 4.2) was utilised separately and in combination. By these analysing methods, in combination with temperature measurements, the spatio-temporal characteristics of the flow are extracted, quantified and discussed as a function of $\mathcal{R}e$ and $\mathcal{A}r$.

In the following, the magnitude of the time-averaged velocity vector fields and the standard deviations are calculated from the in-plane velocity components. Further, for the sake of comparability, all velocities are normalised by the characteristic velocity U and the velocity vectors are scaled to unity. In regard to the POD coherent structures, the eigenfunctions $\Psi_i^{(n)}$ and the magnitude Ψ_n of the eigenfunctions are normalised as well. Here n denotes the mode number and i indicates the velocity component u, v and w. For the illustration of the coherent structure, the vectors are scaled to unity and consist of the corresponding eigenfunctions $\Psi_i^{(n)}$.

5.1 LARGE-SCALE FLOW STRUCTURES

In turbulent *MC*, the formation of flow pattern is determined by the mutual interplay of *TC* and *FC*. Depending on the ratio of inertia to buoyancy forces, numerous coherent flow states are developed. It is almost impossible to capture all the states of flow. However, with the objective to examine the formation and dynamics of the large-scale coherent structures in mixed convective air flow, *MC* was studied at four different Archimedes numbers, while $\mathcal{R}a$ is almost constant and $\mathcal{R}e$ varies. The flow case with the lowest $\mathcal{A}r$ is related to *FC* and the highest $\mathcal{A}r$ reflects the regime where the flow is dominated by *TC*.

In this chapter, the results of the measurement under high fluid pressure conditions $P \approx 11.6$ are analysed and discussed only. The findings of the measurement in the

	$\mathcal{R}e =$	1.01×10^4	1.22×10^4	1.40×10^4	2.67×10^4
$\mathcal{P}r$		0.69	0.69	0.68	0.68
U	[m/s]	0.137(1)	0.163(1)	0.183(1)	0.355(2)
$\overline{\rho}_{air}$	[kg/m^3]	13.85(3)	13.84(2)	13.84(2)	13.88(4)
$\overline{\Theta}$	[K]	295.50(1)	295.43(1)	295.34(1)	295.65(3)
$\overline{\Theta}_{in}$	[K]	295.35(1)	295.34(1)	295.36(1)	295.69(3)

Table 2: List of measurement parameters, fluid properties and characteristic numbers of PIV in the vertical cross-section at $X = 0.5 \times L$ for *FC* at a fluid pressure $P \approx 11.6$.

large container under atmospheric pressure conditions are presented and reviewed in terms of spatial scaling in chapter 6.

5.1.1 *Isothermal flow*

In general, the term *FC* is related to convective flows where the inertia forces clearly exceed the buoyancy forces $F_B \ll F_I$, while here the term is used more narrowly. In the following section the term *FC* denotes isothermal flows without the presence of *TC*.

The time-averaged measurement parameters, the corresponding fluctuations (values in brackets) and the characteristic numbers of PIV in the vertical cross-section at $X = 0.5 \times L$ are itemised in table 2, whereas the fluctuations correspond to the standard deviation. In addition, the PIV data processing parameters are listed in table 9 (appendix A).

The formation of large-scale structures in *FC* is studied within the parameter range of $1.01 \times 10^4 \leqslant \mathcal{R}e \leqslant 2.67 \times 10^4$, where the time-averaged velocity fields (fig. 12a - 12d) are calculated from 500 instantaneous velocity fields recorded at a repetition rate of 2/3 Hz corresponding to a time period of 750 s. For the sake of visibility only every 9th - 12th velocity vector is drawn.

On the upper right side, a jet of air enters the cell through the inlet. The inflow drives a nearly two-dimensional and stationary rotating mean wind, where the core is located close to the centre position of the cross-section. The two-dimensional and stationary nature of the mean wind is identified by the corresponding velocity fluctuations (fig. 13). The contour plots depict the normalised standard deviation of the velocity magnitude $\overline{\sigma}_{(v,w)} = \sqrt{\sigma_v^2 + \sigma_w^2}/U$ as a function of $\mathcal{R}e$. Except for the region of the wall jet at the ceiling, the contour plots reveal a rather homogeneous distribution of low $\overline{\sigma}_{(v,w)}$-values, indicating the stationary nature of the mean wind. However, for the region of the wall jet stronger fluctuations are found. At the ceiling, the wall jet detaches and starts to oscillate as a result of the free shear layer instability,

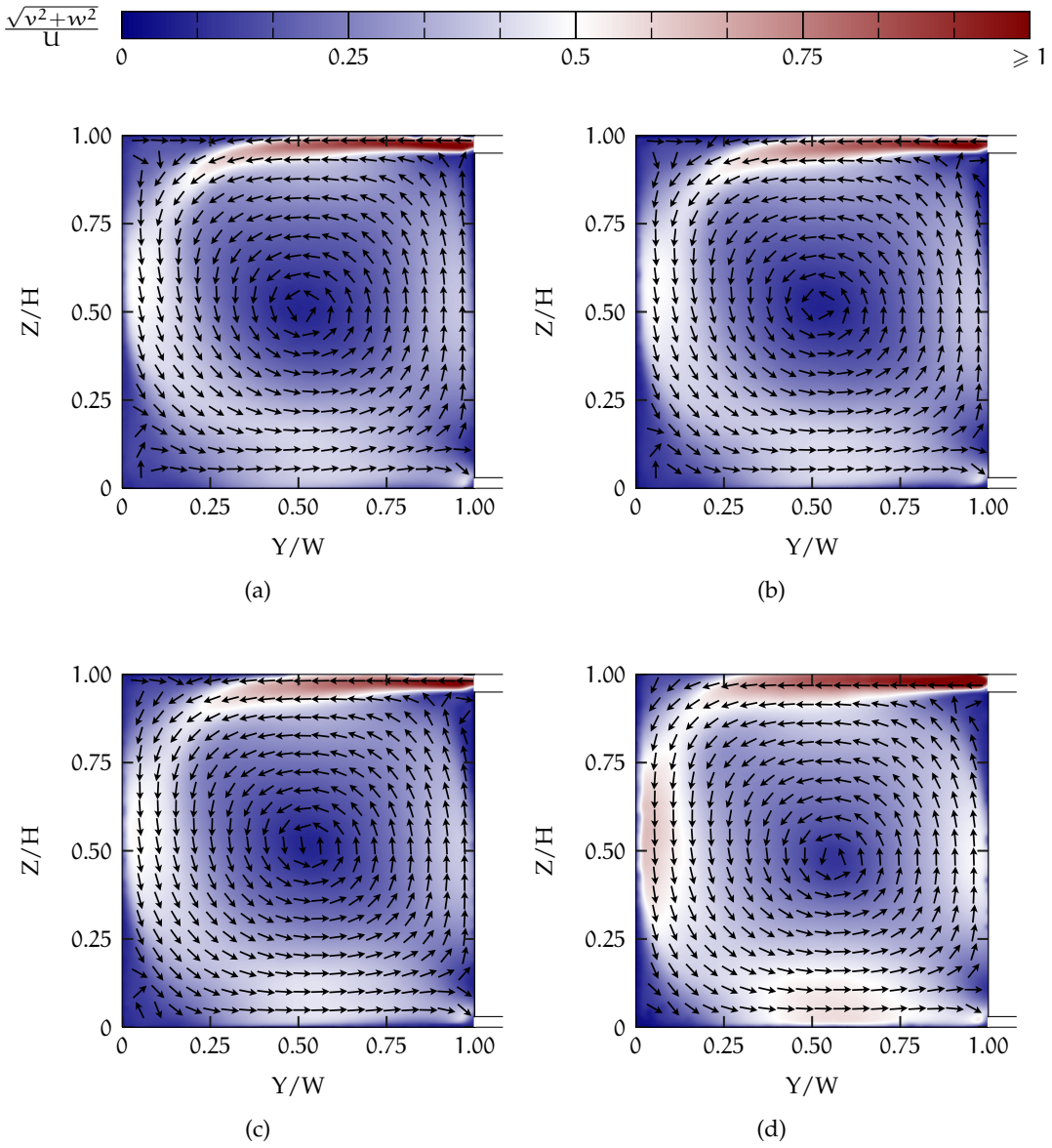

Figure 12: Mean wind in the vertical cross-section $X = 0.5 \times L$ at four different $\mathcal{R}e$. Figure (12a) - (12d): time-averaged in-plane velocity vector fields of *FC* at $\mathcal{R}e = 1.01 \times 10^4$, $\mathcal{R}e = 1.22 \times 10^4$, $\mathcal{R}e = 1.40 \times 10^4$ and $\mathcal{R}e = 2.67 \times 10^4$ respectively.

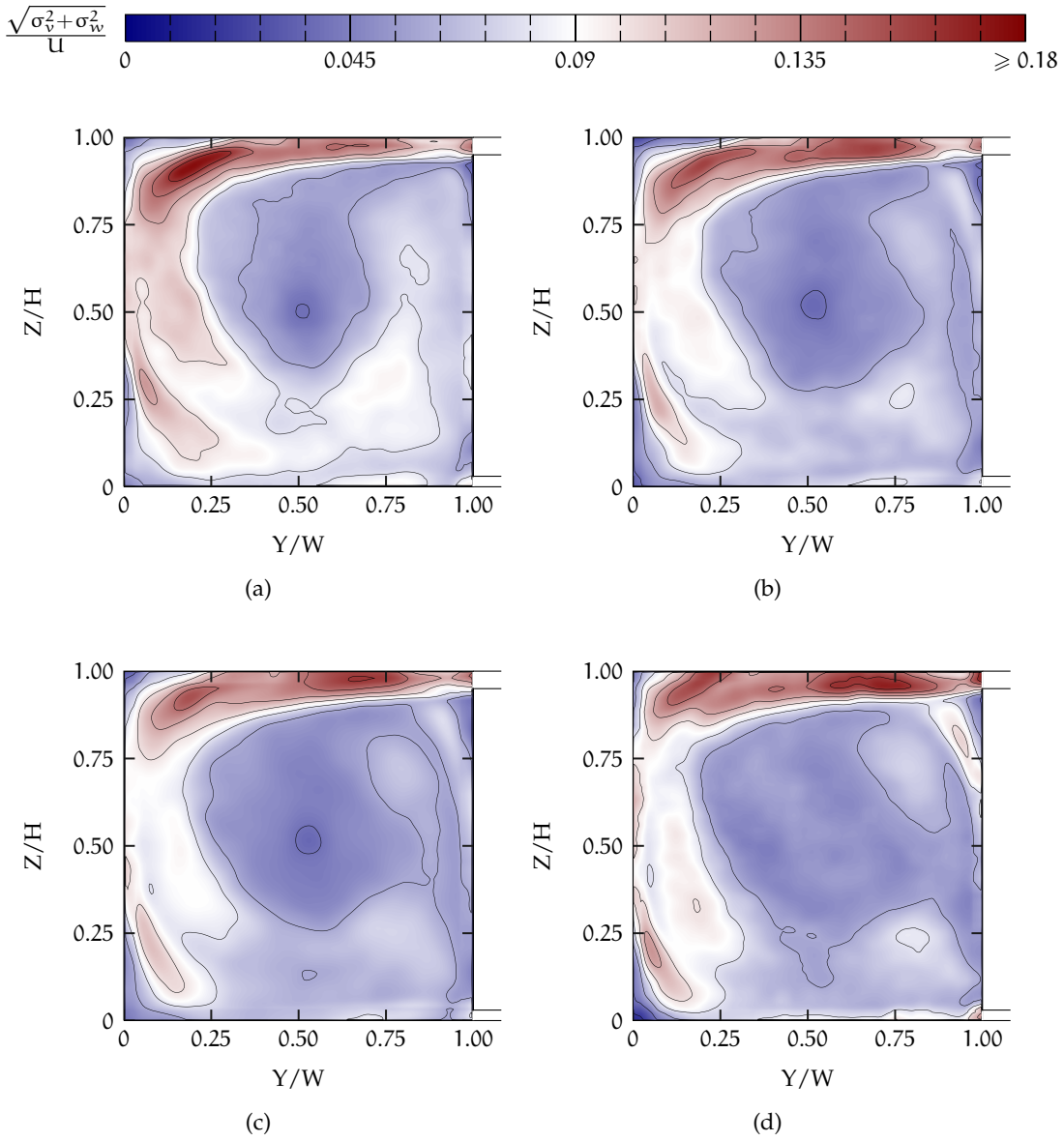

Figure 13: Velocity fluctuations in the vertical cross-section X = 0.5 × L as a function of $\mathcal{R}e$. Figure (13a) - (13d): normalised standard deviation of the velocity magnitude at $\mathcal{R}e = 1.01 \times 10^4$, $\mathcal{R}e = 1.22 \times 10^4$, $\mathcal{R}e = 1.40 \times 10^4$ and $\mathcal{R}e = 2.67 \times 10^4$ respectively.

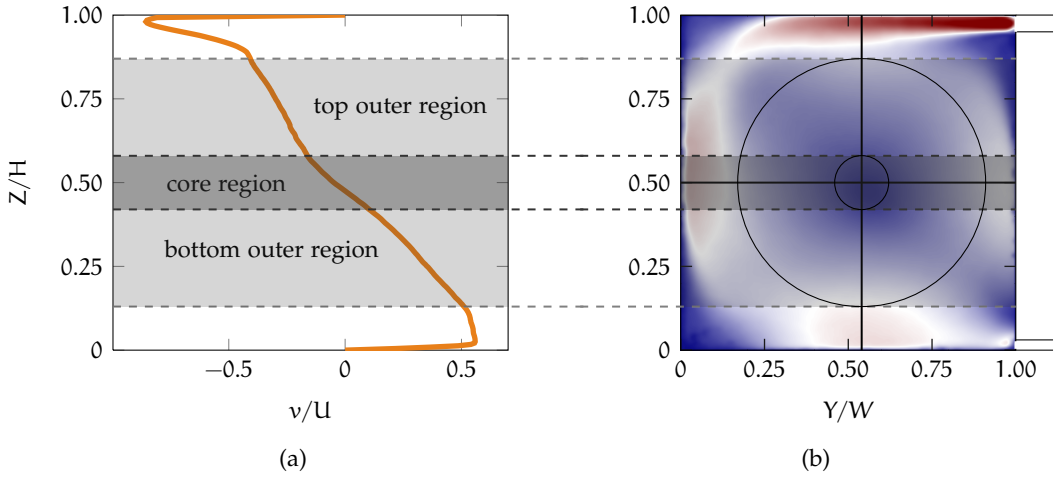

Figure 14: Characterisation of the roll structure topology at *FC* in the vertical cross-section. (14a) Vertical velocity profile of the v-component in the cross-section $X = 0.5 \times L$ at $Y = Y_c$. (14b) Corresponding in-plane velocity magnitude.

which is developed between the incoming air jet and the mean wind. As a result, these oscillations lead to elevated $\overline{\sigma}_{(v,w)}$-values at the ceiling. A comparison of the velocity fields at $\mathcal{R}e = 1.0 \times 10^4$, $\mathcal{R}e = 1.22 \times 10^4$ and $\mathcal{R}e = 1.40 \times 10^4$ further reveals an almost congruent topology of the velocity magnitude and its fluctuations. On the contrary, due to the higher inflow velocity, in case of $\mathcal{R}e = 2.67 \times 10^4$ the wall jet detaches further down-wind. Consequently, the centre position of the mean wind is shifted towards the right side wall.

Characteristic features of the mean wind are calculated from the time-averaged velocity vector fields. The horizontal velocity profile $w(y)$ is cut along the y-axis at $Z = Z_c$, where the subscript c denotes the corresponding *LSC* centre position and the vertical velocity profile $v(z)$ is cut along the z-axis at $Y = Y_c$. The centre positions Z_c and Y_c are determined by the *LSC* identification algorithm.

Figure 14a shows the vertical velocity profile $v(z)$ for $\mathcal{R}e = 2.67 \times 10^4$. The profile is segmented into four regions: the region of the wall jet, the outer region at bottom, the outer region at the top and the core region. Moreover, the partly linear slopes of the profile depict that the core region and the outer regions rotate rigid-body-like, whereas the angular velocity for each segment differs. In addition, the contour plot of figure 14b depicts the spatial distribution of the in-plane velocity magnitude in the cross-section $X = 0.5 \times L$, where the centre position of the mean wind corresponds to the intersection of the horizontal line and vertical line. The lines corresponds to the positions of the line cuts and the rings represent the *LSC* outer region and the

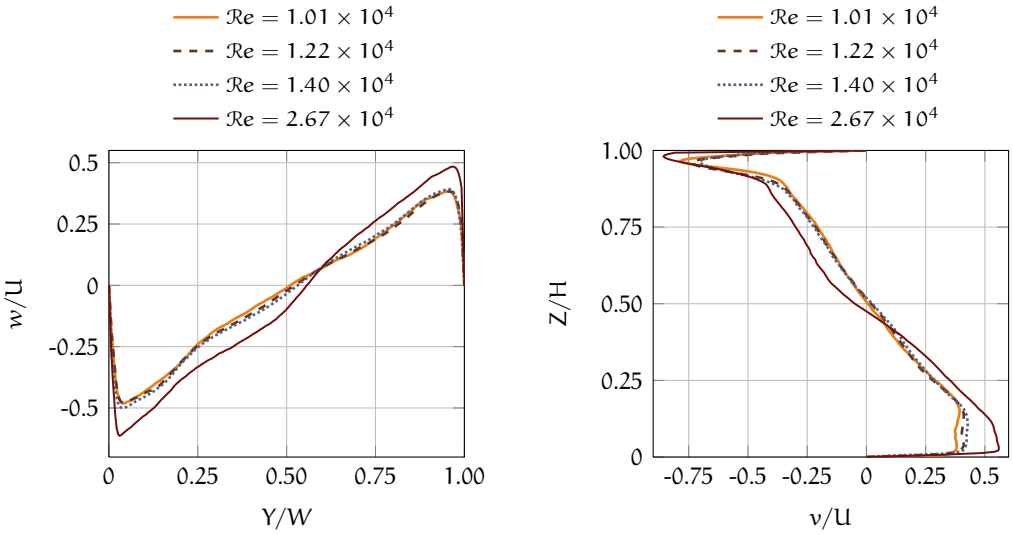

Figure 15: Velocity profiles at Y_c and Z_c for the different $\mathcal{R}e$. (15a) Normalised w-component profile at $X = 0.5 \times L$ and Y_c. (15b) Normalised v-component profile at $X = 0.5 \times L$ and Z_c.

core region. Based on these attributes, the characteristics of the forced mean wind are determined.

The line cuts disclose differences between the normalised velocity profiles at $\mathcal{R}e = 2.67 \times 10^4$ and the profile at lower $\mathcal{R}e$. With the objective to verify the differences between the *LSC*'s topology at high and lower $\mathcal{R}e$ the angular velocities of the core region, outer region and the whole *LSC* are calculated by

$$\omega = \frac{1}{N} \sum_{\mathbf{x}_j \in S_i} \frac{(\mathbf{x}_c - \mathbf{x}_j) \times \mathbf{u}_j}{|\mathbf{x}_c - \mathbf{x}_j|^2} \mathbf{n}, \tag{5.1}$$

where S_i denotes the areas of the *LSC* core region, outer region or the entire *LSC*, $(\mathbf{x}_c - \mathbf{x}_j)$ the radius vector, $\mathbf{u}_j$ the velocity, $\mathbf{n}$ the unit normal vector in x-direction and N the number of points. The corresponding spatially averaged angular velocity, the radius, the centre position of the *LSC* and the *LSC* sub regions are listed in table 3 as a function of $\mathcal{R}e$, where the radius of the core region and outer region is estimated by eye and corresponds to the length of the segments with linear slopes.

For the three flow cases with the lower inflow velocity, the normalised horizontal velocity profiles and vertical velocity profiles (fig. 15) are similar. On the contrary, at $\mathcal{R}e = 2.67 \times 10^4$ the profiles clearly differ due to the further down-wind detaching wall jet. Moreover, it is found that in all cases the outer regions have a slightly higher angular velocity in comparison to the core region. This higher angular velocity

$\mathcal{R}e =$	1.01×10^4	1.22×10^4	1.40×10^4	2.67×10^4
$(Y_c/H, Z_c/H)$	$(0.50, 0.51)$	$(0.50, 0.52)$	$(0.49, 0.51)$	$(0.54, 0.50)$
R_{core}/H	0.20	0.19	0.19	0.08
R_{LSC}/H	0.36	0.36	0.35	0.35
ω_{LSC} [rad/s]	1.10	1.32	1.46	4.00
ω_{core} [rad/s]	1.07	1.21	1.40	3.96
ω_{outer} [rad/s]	1.11	1.35	1.51	4.17

Table 3: List of the mean wind flow features: angular velocities, normalised radius and the centre position of the forced induced *LSC* as a function of $\mathcal{R}e$.

indicates that the innermost region of the *LSC* appears to be unable to follow the fluid motion of the outer region, which is driven by the incoming wall jet. Further, the radius of the core is almost the same for lower $\mathcal{R}e$, while for $\mathcal{R}e = 2.67 \times 10^4$ a smaller radius of the core is observed. However, the radius of the whole *LSC* is similar in all four cases of $\mathcal{R}e$.

In conclusion, for the given geometry and the parameter range $1.01 \times 10^4 \leqslant \mathcal{R}e \leqslant 2.67 \times 10^4$ an two-dimensional roll structure is developed. The mean wind is divided into two regions: the jet region and the *LSC*. The *LSC* itself is divided into two regions: the core region and the outer region. Both regions behave rigid-body-like, however, with different angular velocities, while the outer region rotates with a higher angular velocity than the core region. In addition, the delayed detachment of the incoming wall jet at the highest $\mathcal{R}e$ results in a broader jet region at the left side wall and a shift of the *LSC* centre position is discerned, relative to the centre position at lower $\mathcal{R}e$. Based on these findings, in the following the impact of the buoyancy flow on the forced mean wind is discussed.

5.1.2 *Mixed convection*

Mixed convective air flow is studied for the Archimedes numbers $\mathcal{A}r = 3.33$, $\mathcal{A}r = 2.29$, $\mathcal{A}r = 1.81$ and $\mathcal{A}r = 0.48$ and $\mathcal{R}a \approx 2.40 \times 10^8$, while $\mathcal{R}e$ corresponds to the numbers which have been examined at *FC*. The measurement parameters, fluid properties and characteristic numbers of PIV in the vertical cross-section at $X = 0.5 \times L$ are listed in table 4. The PIV data processing parameters are itemised in table 10 (appendix A). All time-averaged velocity fields of *MC* are calculated from a set of 4800 instantaneous velocity fields. The measurement time is 7200 s, expecting the flow at $\mathcal{A}r = 0.48$. At $\mathcal{A}r = 0.48$ just 3000 instantaneous velocity fields were recorded within a period of 9000 s.

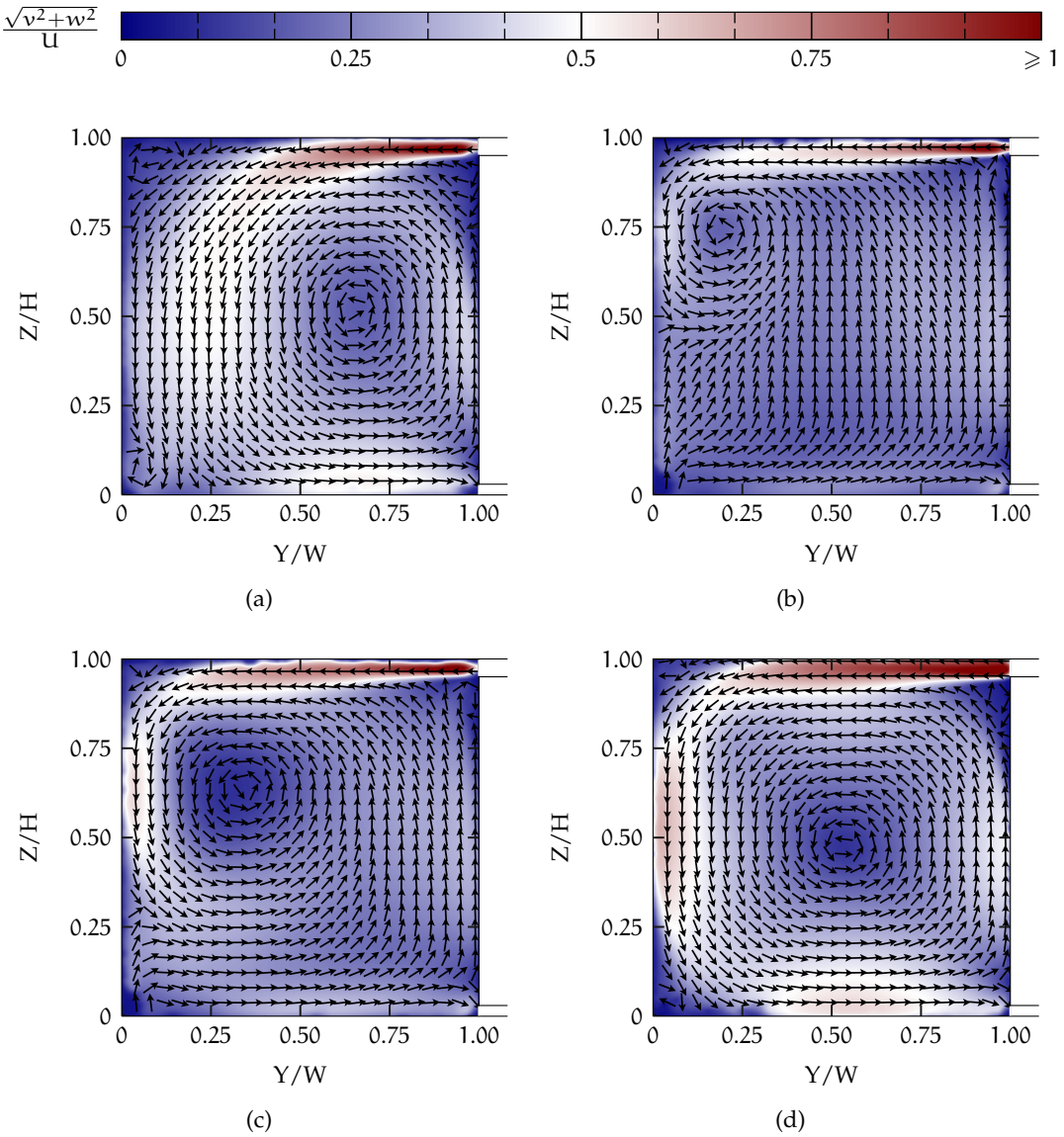

Figure 16: *MC* in the vertical cross-section X = 0.5 × L as a function of $\mathcal{A}r$. (16a) - (16d) time-averaged in-plane velocity vector field at $\mathcal{A}r = 3.33$, $\mathcal{A}r = 2.29$, $\mathcal{A}r = 1.81$ and $\mathcal{A}r = 0.48$ respectively.

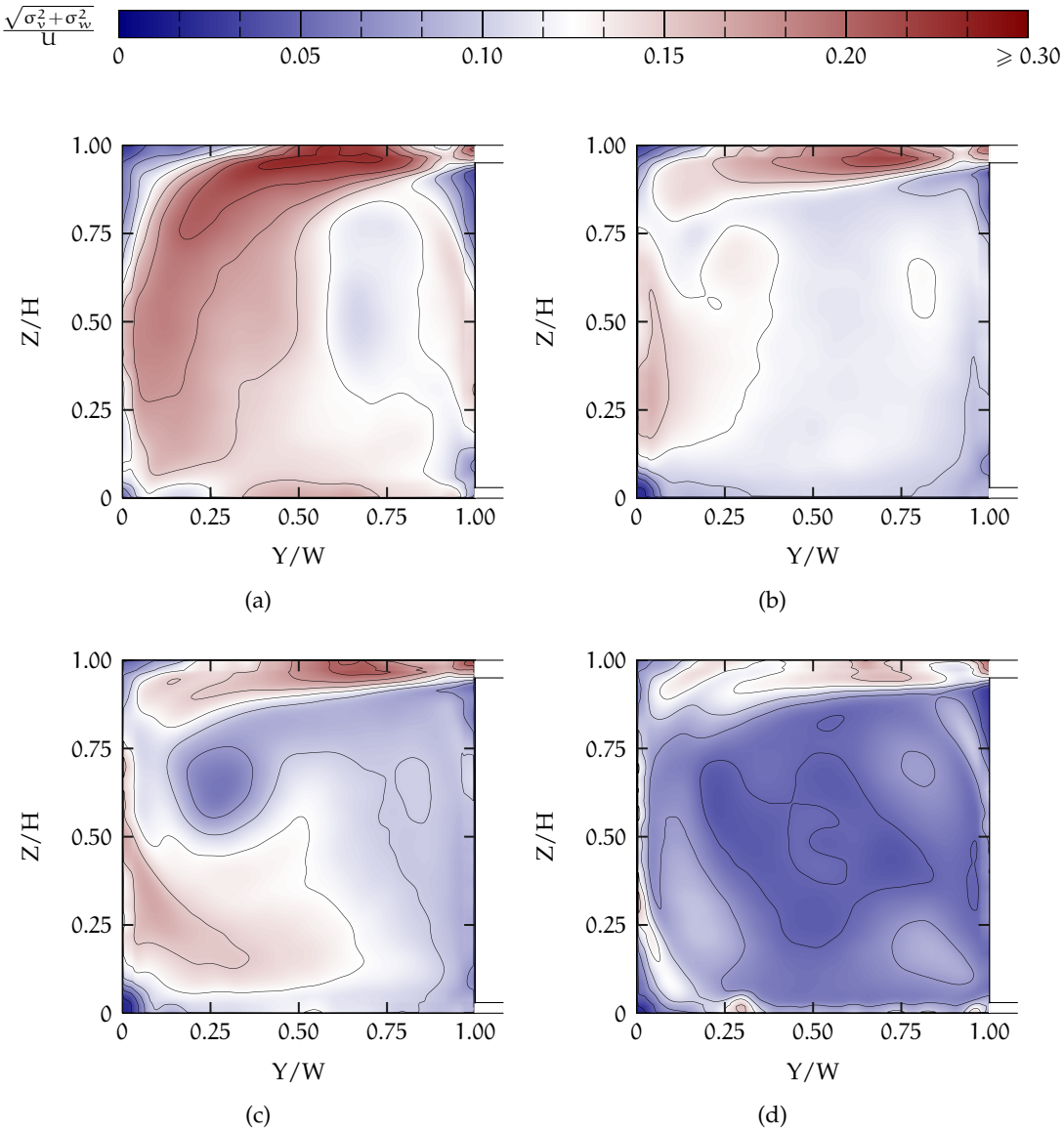

Figure 17: Standard deviation of the velocity magnitude as a function of Ar in the vertical cross-section at $X = 0.5 \times L$. (17a) - (17d) normalised standard deviation $\sqrt{\sigma_v^2 + \sigma_w^2}/U$ at $Ar = 3.33$, $Ar = 2.29$, $Ar = 1.81$ and $Ar = 0.48$ respectively.

		$\mathcal{A}r = 3.33$	$\mathcal{A}r = 2.29$	$\mathcal{A}r = 1.81$	$\mathcal{A}r = 0.48$
$\mathcal{R}e$		1.01×10^4	1.22×10^4	1.37×10^4	2.70×10^4
$\mathcal{R}a$		2.40×10^8	2.41×10^8	2.39×10^8	2.47×10^8
$\mathcal{P}r$		0.71	0.71	0.71	0.70
$\overline{\rho}_{air}$	[kg/m^3]	13.83(1)	13.84(4)	13.83(7)	13.98(5)
U	[m/s]	0.143(1)	0.172(1)	0.200(1)	0.377(3)
$\Delta\Theta$	[K]	21.20(10)	21.25(17)	21.17(16)	21.23(15)
$\overline{\Theta}_b$	[K]	316.78(10)	316.68(17)	316.79(16)	315.01(14)
$\overline{\Theta}_t$	[K]	295.58(3)	295.43(4)	295.62(3)	293.78(4)
$\overline{\Theta}_{in}$	[K]	295.31(1)	295.25(5)	295.54(7)	293.73(5)

Table 4: Measurement parameters, fluid properties and characteristic numbers of PIV in the vertical cross-section at $X = 0.5 \times L$ for *MC* in the small container under high pressure conditions.

The corresponding time-averaged velocity vector fields in the vertical cross-section at $X = 0.5 \times L$ are shown in figure 17. For the sake of visibility every 7th - 9th velocity vector is drawn. The velocity fields in the vertical cross-section for the three highest $\mathcal{A}r$ (fig. 16a - 16c) strongly deviate from those found at *FC* (fig. 12). With the onset of *TC*, rising hot plumes or falling cold plumes, which are emitted from the thermal *BL* at the floor or the ceiling of the container, lead to a break-up of the almost two-dimensional forced mean wind. Consequently, the incoming wall jet and the topology of the former two-dimensional roll structure are significantly modified.

For $\mathcal{A}r = 3.33$ the incoming wall jet detaches further down-wind in relation to the corresponding *FC* case, while for $\mathcal{A}r = 2.29$ and $\mathcal{A}r = 1.81$ a delayed detachment is found. Depending on whether hot rising plumes or cold falling plumes are prevailing in the cross-section $X = 0.5 \times L$ a later or earlier detachment of the wall jet is observed.

For instance, in case of $\mathcal{A}r = 3.33$ falling cold air is predominant in the cross-section $X = 0.5 \times L$. As a consequence, the cold plumes, emitted from the top thermal *BL*, are convected by the incoming wall jet towards the left side and cold air descends close to the left lateral wall. Moreover, the interaction of the cold plumes with the incoming wall jet causes a broadening of the jet and the downward flow close to the left lateral wall. Consequently, the *LSC* core is shifted towards the right side (fig. 16a). For the flow cases of preferred hot plume emission at the bottom, the plumes are convected by the forced flow towards the right side wall. As a result, the hot plumes interacts with the ascending forced flow at the right side wall and the flow becomes wider. As a consequence, the *LSC* core shifts towards the upper left corner of the cross-section

		$\mathcal{A}r = 3.33$	$\mathcal{A}r = 2.28$	$\mathcal{A}r = 1.81$	$\mathcal{A}r = 0.48$
$\mathcal{R}e$		1.01×10^4	1.26×10^4	1.37×10^4	2.69×10^4
$\mathcal{R}a$		2.39×10^8	2.39×10^8	2.39×10^8	2.42×10^8
$\mathcal{P}r$		0.71	0.71	0.71	0.71
$\overline{\rho}_{air}$	[kg/m^3]	13.83(2)	13.82(4)	13.83(3)	13.90(2)
U	[m/s]	0.143(1)	0.173(1)	0.199(1)	0.378(2)
$\Delta\Theta$	[K]	21.19(7)	21.19(15)	21.18(16)	21.19(18)
$\overline{\Theta}_b$	[K]	316.79(6)	316.72(15)	316.76(16)	316.53(17)
$\overline{\Theta}_t$	[K]	295.60(2)	295.53(4)	295.58(4)	295.35(5)
$\overline{\Theta}_{in}$	[K]	295.415(9)	295.457(26)	295.600(18)	295.354(10)

Table 5: Measurement parameters, fluid properties and characteristic numbers of PIV in the longitudinal cross-section at $Y = 0.5 \times W$ for *MC*.

and a detachment of the incoming wall jet further down-wind is observed (fig. 16b and 16c).

The interaction of *TC* with the forced mean wind leads to higher fluctuations of the velocity magnitude $\overline{\sigma}_{(v,w)}$ in the whole measuring plane. The contour maps in figure 17 clearly disclose elevated $\overline{\sigma}_{(v,w)}$-values. Moreover, in comparison to the flow at *FC*, a structural change of the standard deviation's topology is found.

In particular, for $\mathcal{A}r = 3.33$ (fig. 17a) significant differences are observed. At $\mathcal{A}r = 3.33$, the standard deviation in the bulk of the measuring plane is $\sigma \geqslant 0.12 \times U$, while in the corresponding case at *FC* comparable values were obtained in the region of the incoming wall jet only. The increased velocity fluctuations seem to be the result of the mutual interplay of hot rising air and cold falling air with the forced mean wind. In addition, elevated fluctuations are found close to the bottom. Over the heating plate, the increased $\overline{\sigma}_{(v,w)}$-values are caused by the interaction between the hot plumes emitted from the bottom thermal boundary layer and the forced flow towards the outlet slot.

With decreasing $\mathcal{A}r$ lower velocity fluctuations are detected in the bulk of the measuring plane. In particular, for $\mathcal{A}r = 0.48$, where the flow is determined by the forced convective flow, the topology and magnitude of σ are almost similar to those found at *FC*, excepting the core region of the forced *LSC*. There, conspicuously higher fluctuations are emerged in comparison to the flow at *FC*. Moreover, for $\mathcal{A}r = 0.48$, the topology of the forced mean wind is almost unaffected by the buoyancy flow and the roll structure in the vertical cross-section (fig. 16d) is similar to the corresponding flow case at *FC* (fig. 13d).

In addition, PIV was performed in a longitudinal cross-section at $Y = 0.5 \times L$. The measurement parameters, fluid properties and characteristic numbers during the PIV in the longitudinal cross-section are listed in a table 5. The corresponding PIV data processing parameters are given in table 11 (appendix A). Further, the results of PIV in the longitudinal cross-section do not cover the full extent of the container reliably. Due to reflections of the laser light, the top and bottom areas become partly inaccessible to the measurements, particularly on the right side.

For $Ar = 3.33$ the formation of flow structures in the longitudinal cross-section is primarily governed by the buoyancy forces. The time-averaged velocity vector field in the cross-section at $Y = 0.5 \times W$ (fig. 18a) discloses large-scale flow structures with a comparable topology on the left side ($X < 0.5 \times L$) and right side ($X > 0.5 \times L$). However, former studies [124, 110] of *MC* at the same characteristic numbers reveals almost symmetrically arranged *LSC*s in the longitudinal cross-section.

To find out why the time-averaged velocity field differs from that of the former studies a POD was performed on the in-plane velocity components of the instantaneous velocity fields. Figure 18b reveals the topology of the eigenfunction Ψ_1 representing the POD mode with the highest eigenvalue. The eigenfunction has the interpreted of the predominant coherent structure, which contains 46.1 % of the total energy $E = \sum_i^N \lambda_i$.

The coherent structure discloses four almost symmetrically arranged counter-rotating *LSC*s with a preferred location of rising hot air in the centre region $X \approx 0.5 \times L$ and at the lateral walls. Accordingly, descending cold air is located at $X \approx 0.25 \times L$ and $X \approx 0.75 \times L$. A closer inspection of the coherent structure reveals that the *LSC*s centre is shifted towards the region of rising hot air. Moreover, a significant broadening of the horizontal flow at the top, relative to the flow over the heating plate, is observed. Both effects result from the interplay of the forced mean wind with thermal convection rolls. The broadening of the horizontal flow at the top is directly caused by the incoming wall jet, where the main flow direction of the forced mean wind is almost orthogonal to the longitudinal arranged thermal convection rolls. As a consequence, the interaction of the oscillating wall jet and the vertical flow of the thermal convection rolls at the ceiling leads to a broadening of the vertical flow. Furthermore, near the bottom plate a cross-flow between the forced mean wind and the thermally induced *LSC*s is developed. However, there the momentum of the forced mean wind is too small to affect the vertical flow as strong as at the top.

In addition, the incoming wall jet convects cold plumes at the ceiling further downwind and hot plumes at the bottom are convected towards the outlet. As a result, the preferred regions of ascending air are shifted towards the side wall with the inlet and outlet. Accordingly, cold descending air is placed on the opposite side. Hence, the rotational plane of the *LSC* is tilted with respect to the measuring plane and the *LSC* centre positions of the rotational plane are not the centre observed from the topology

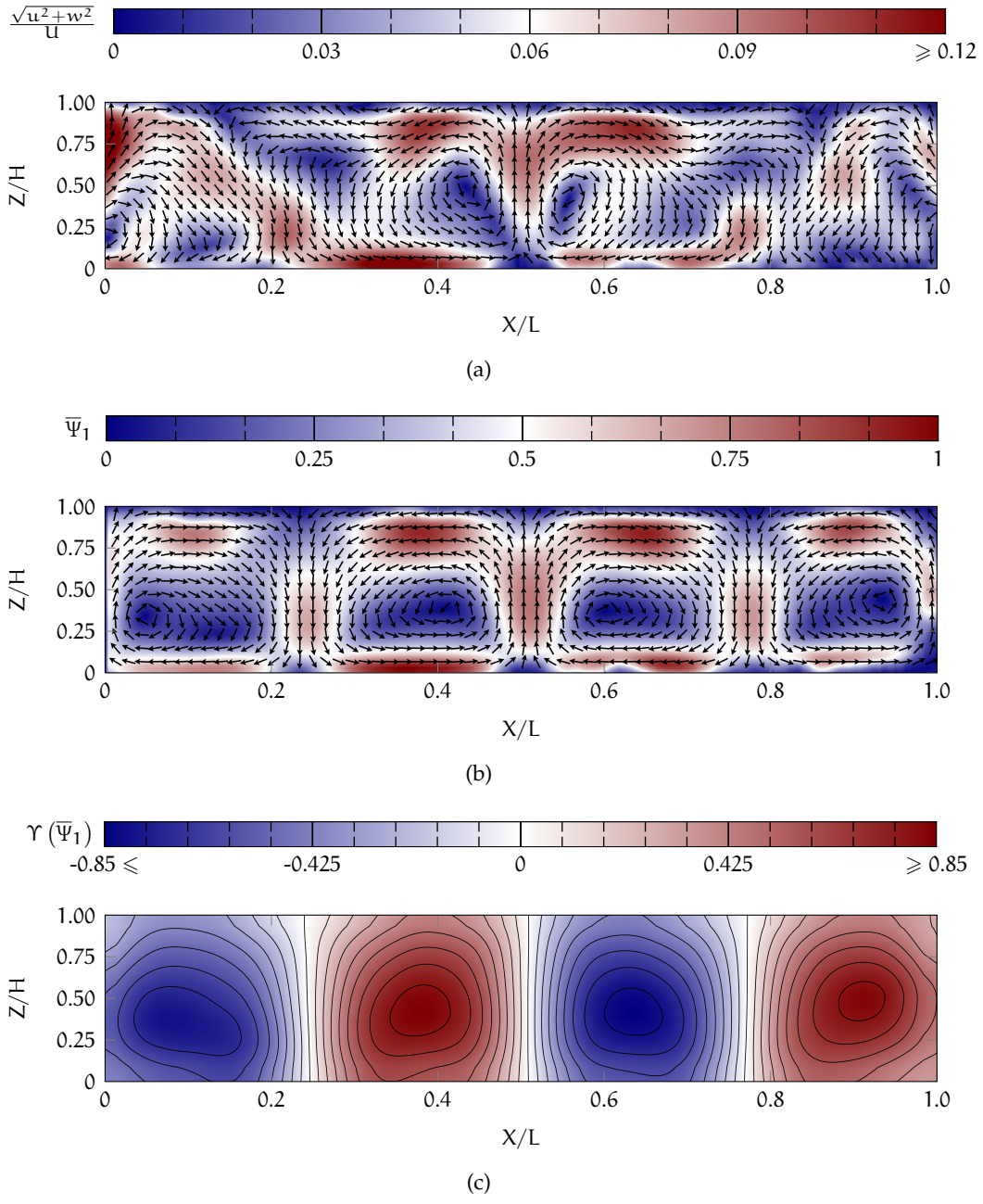

Figure 18: Thermal convective roll structures in the longitudinal cross-section $Y = 0.5 \times W$ at $\mathcal{A}r = 3.33$, $\mathcal{R}e = 1.01 \times 10^4$ and $\mathcal{R}a = 2.39 \times 10^8$. (18a) Time-averaged in-plane velocity vector field. (18b) The topology of Ψ_1. (18c) Υ-distribution calculated Ψ_1, where blue denotes clockwise and red counter-clockwise rotating *LSC*.

of $\overline{\Psi}_1$. As a consequence, a shift of the centre position of the thermal convection rolls towards the region of rising plumes is observed in the cross-section $Y = 0.5 \times W$.

The Υ-distribution (fig. 18c) was calculated from the coherent structure Ψ_1. Here the centre position of the *LSC*s is identified by the local maxima of $|\Upsilon|$, while the regions of vertical flow are charaterised by $\Upsilon \approx 0$. A closer inspection of the Υ-distribution discloses that the centre positions differ from the centre position, which were found from the coherent structure Ψ_1.

Besides the structure of four longitudinally arranged *LSC*s the POD brings to light another coherent structure, consisting of large-scale roll structures. The eigenfunction Ψ_2 has an eigenvalue of $\lambda_2 = 0.08 \times E$ and represents a pattern which consists of three counter-rotating *LSC*s (fig. 19). For a further analysis, the *LSC* detecting algorithm was performed on the eigenfunction Ψ_2 (fig. 19b). The Υ-distribution reveals an almost rotational symmetric topology for the central *LSC*, while the left and right sided *LSC*s are elliptically shaped. Although, the dynamics of the *LSC* will be discussed in detail later, I like to note that in this study, due to the long-time evolution of the large-scale structures at $Ar = 3.33$, just two re-organisations of coherent flow patterns were observed. Hence, further measurements over an extended period of time are necessary to determine whether the coherent structure of three counter-rotating *LSC* represents a transitional or metastable state.

Regarding the large-scale flow pattern at $Ar = 3.33$, the results are in good agreement with the findings of Sergent et al. [111]. Sergent et al. studied the long-time evolution of coherent flow structures in *RBC* in a rectangular container at similar Ra by Large Eddy Simulation (LES). The container has the same aspect ratio, however, no inlet or outlet slots. Although the study is related to *RBC*, it reveals several flow features that are found in *MC* at $Ar = 3.33$ as well. The study of Sergent et al. uncovers three different coherent flow conditions at $Ra = 6 \times 10^8$. The predominant structure corresponds to a steady-state solution of four counter-rotating *LSC*s, comparable to the topology of the coherent structure Ψ_1 at $Ar = 3.33$. However, due to the additional forced flow in *MC* also differences between the flow in *RBC* and *MC* are found. In *RBC* the convection rolls are rotational symmetric. Further, the *LSC*s are arranged side by side in the longitudinal direction, while in case of *MC* the roll structures are stretched and tilted. The topology of the second flow condition reflects three counter-rotating *LSC*s, comparable to the topology of the second mode eigenfunction Ψ_2. However, as well here clear differences are found in symmetry and orientation of the *LSC*s. Furthermore, the study uncovers a third coherent flow state which consists of two counter-rotating rolls. For *MC* a flow state, consisting of two *LSC*s, was not observed. Sergent et al. assume that the second and third flow states are transitional states before a physical solution is established.

The second flow case, which will be discussed in detail, is *MC* at $Ar = 0.48$. The flow at this low Ar represents the other extreme condition of this study, where the flow is primeraly governed by *FC*.

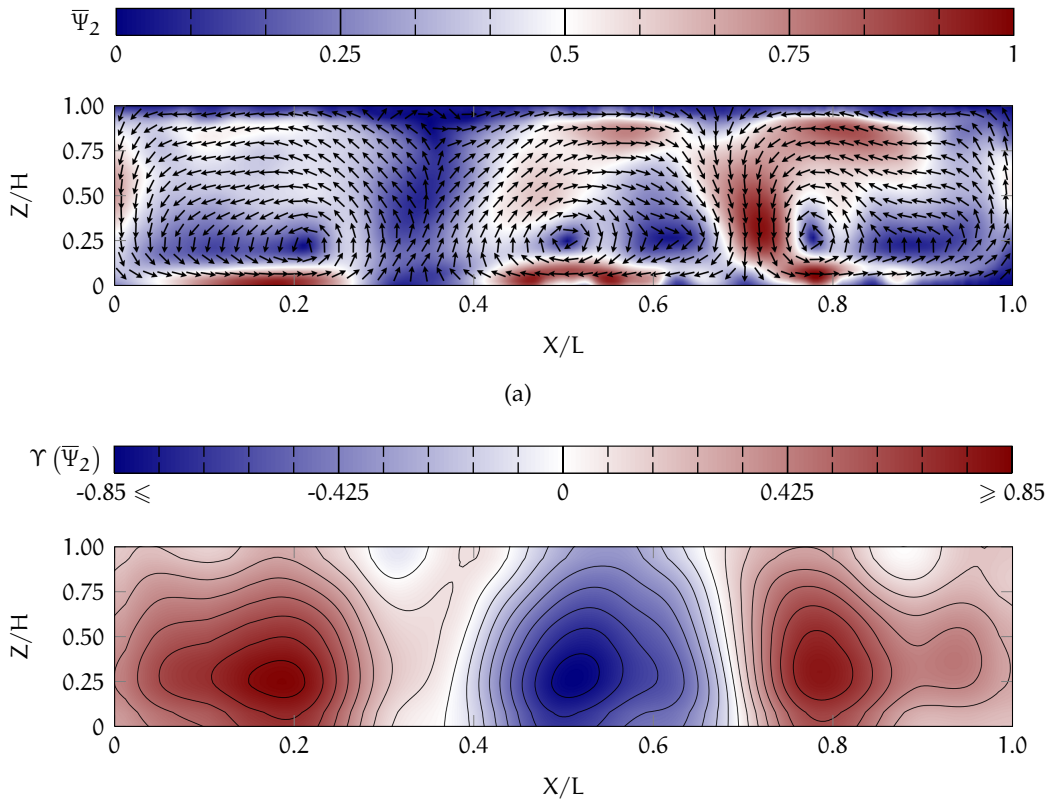

Figure 19: Coherent structure of the second POD mode and the corresponding Υ-distribution for $\mathcal{A}r = 3.33$, $\mathcal{R}e = 1.01 \times 10^4$ and $\mathcal{R}a = 2.39 \times 10^8$. (19a) Topology of $\overline{\Psi}_2$. (19b) Υ-distribution of Ψ_2, where blue denotes clockwise and red counter-clockwise rotating *LSC*.

Figure 20a depicts the time-averaged velocity vector field. A striking feature are the blank regions close to the top, bottom and side walls. At $\mathcal{A}r = 0.48$ the out of plane velocity component on the top and bottom is several times higher than the buoyancy induced in-plane velocities. Hence, no valid results were obtained in these areas by PIV. Furthermore, the large out of plane velocity requires a broadening of the laser light sheet to gain results by PIV. Consequently, augmented reflections are received from the boundaries and close to the side walls no valid results were obtained.

Nevertheless, the time-averaged velocity vector field (fig. 20a) shows a considerable influence of the buoyancy flow on the predominant forced flow, while the velocity field in the vertical measurement plane at $X = 0.5 \times L$ (fig. 16d) was almost unaffected by the buoyancy forces. The pattern in the longitudinal cross-section consists of roll

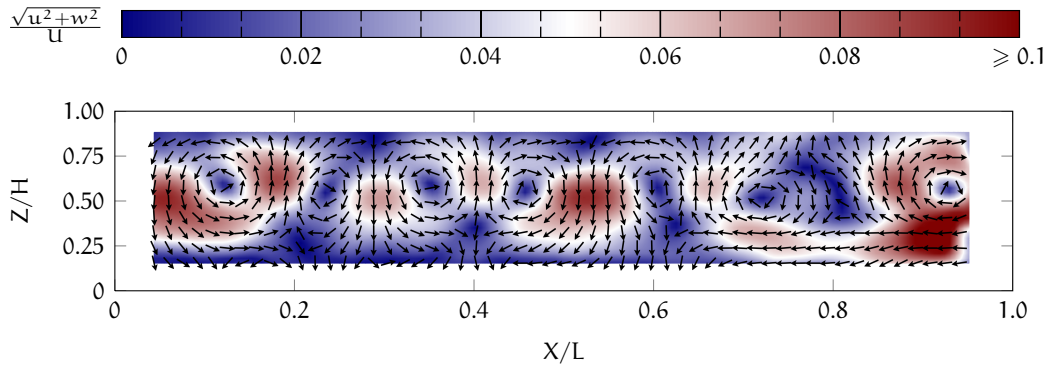

(a)

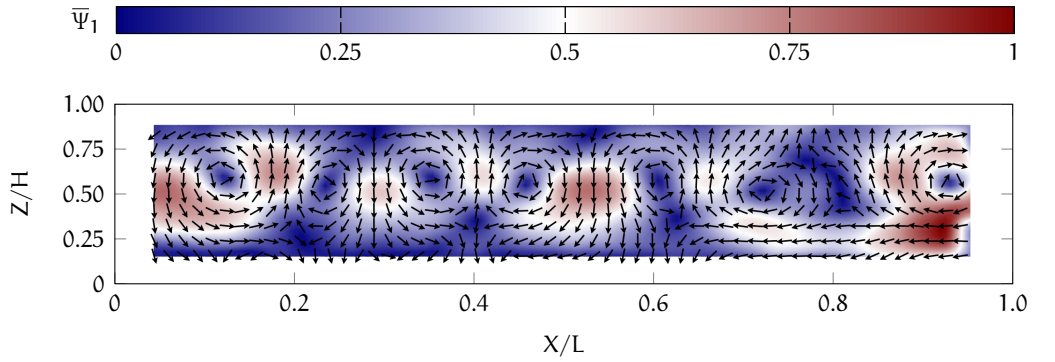

(b)

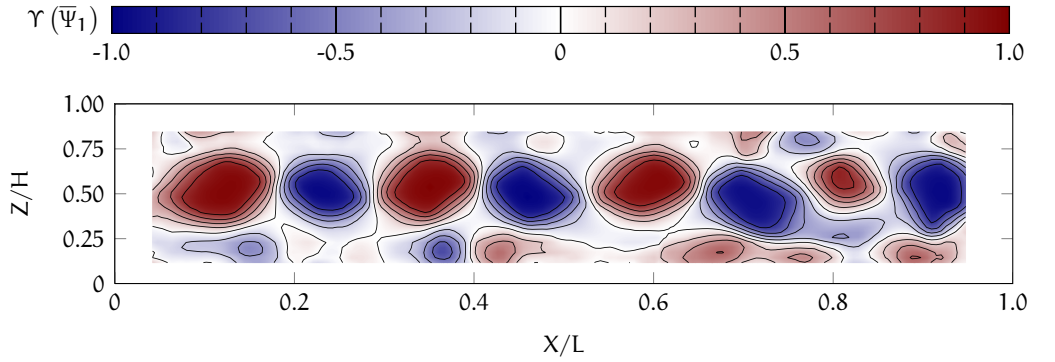

(c)

Figure 20: Coherent flow structure in the longitudinal cross-section $Y = 0.5 \times W$ at $\mathcal{A}r = 0.48$, $\mathcal{R}e = 2.75 \times 10^4$ and $\mathcal{R}a = 2.42 \times 10^8$. (20a) Time-averaged in-plane velocity vector field. (20b) Topology of the normalised first mode coherent structure. (20c) The Υ-distribution calculated from the first mode Ψ_1 coherent structure. Red denotes clockwise and blue counter-clockwise rotating circulation.

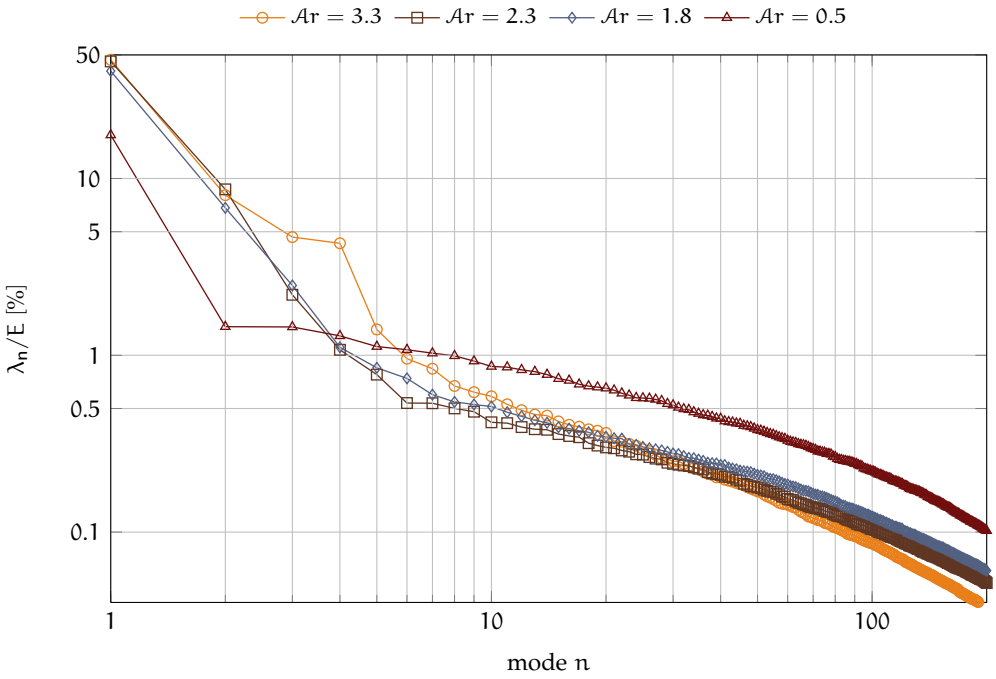

Figure 21: Eigenvalue distribution as a function of the mode number n of the first 200 POD modes in the longitudinal cross-section. The eigenvalues are normalised with respect to the sum of the first 200 eigenvalues.

structures with a diameter of approximately $H/2$, which are located in the core region of the forced mean wind.

The corresponding coherent structure of the first mode Ψ_1 (fig. 20b) is similar to the time-averaged velocity field, while at $\mathcal{A}r = 3.33$ clear differences between the time-averaged velocity field and Ψ_1 are found. The correlation of Ψ_1 and the time-averaged velocity field at $\mathcal{A}r = 0.48$ indicates that the pattern of eight roll structures represents a stable state. However, the energy eigenvalue of the first POD mode at $\mathcal{A}r = 0.48$ contains only 18 % of the total energy. Since the topology of the time-averaged velocity field is nearly congruent with Ψ_1, a much higher eigenvalue is expected for the first mode. I ascribe this unexpected low first eigenvalue to the low signal noise ratio, as a result of the large out of plane velocity component.

The analysis of the eigenvalue distribution as a function of the mode number n (fig. 21) substantiates this assumption. The figure shows the normalised eigenvalues as a function of the first 200 POD modes. The eigenvalues were normalised by the sum of the first 200 eigenvalues in order to make the eigenvalue distributions comparable.

The first mode eigenvalue of the three flow cases $\mathcal{A}r \geqslant 1.81$ contains almost 50 % of the total energy. In case of $\mathcal{A}r = 3.33$ three additional eigenvalues are obtained,

which are significantly elevated, while within the intermediate Ar-regime two higher eigenvalues are found. All other eigenvalues contain 1 % or less of the total energy. The majority of these lower eigenvalues represent small-scale turbulence, statistical noise and measurement noise. In case of $Ar = 0.48$ the eigenvalue distribution differs from those of the other three flow cases. The eigenvalues for the modes $n > 6$ are significantly higher than the eigenvalues for $Ar \geqslant 1.81$. For instance, these elevated eigenvalues could be the result of higher velocity fluctuations caused by small-scale turbulence. In such a case, higher values of the standard deviation have to be found in the vertical cross-section $X = 0.5 \times L$ (fig. 17). However, the standard deviation in the vertical cross-section is significantly lower than the fluctuations in case of $Ar \geqslant 1.81$. Hence, the elevated eigenvalues at $Ar = 0.48$ seems to be measurement noise, resulting from the low signal noise ratio.

In addition, figure 20c depicts the corresponding Υ-distribution of Ψ_1. While the time-averaged velocity field and the first mode coherent structure uncover only seven *LSC*s, the Υ-distribution reveals eight counter-rotating roll structures. At $Ar = 0.48$ the momentum of the incoming wall jet and the flow along the heating device towards the outlet is several times higher than the buoyancy velocities. Consequently, most of the plumes are convected by the forced flow and the vertical movement of plumes at the bottom and the top is less developed. However, in the core region of the forced mean wind, the inertia forces are small and a buoyancy induced flow is developed. Moreover, a such kind of a reduced height for the thermal convective flow part of $H/2$ is obtained and the effective aspect ratio for the thermal convective flow almost doubles. As a result, instead of an aspect ratio $L/H = 5$, a ratio $L/H \approx 10$ is obtained. The diameter of the roll structures is halved and twice as many thermal convective roll structures are developed. Moreover, this finding explains the elevated fluctuations in the core region of the forced mean wind (fig. 17) at $Ar = 0.48$.

So far, the formation of large-scale coherent structures for two extreme conditions of *MC* were discussed. Besides these coherent structures, further large-scale structures can be observed in the intermediate Ar-regime. The formation of coherent structure within the intermediate Ar-regime is vast and depends on the ratio of buoyancy to inertia forces. However, in principle, the predominant coherent patterns in the longitudinal direction consist of four *LSC*s, whereas with decreasing Ar the thermal convective roll structures become more and more stretched and tilted. In figure 22 the predominant coherent structures at $Ar = 2.28$ (fig. 22a) and $Ar = 1.81$ (22b) are depicted. These coherent structures will be discussed in detail later in chapter 6 with the focus on the examination of the concept of spatial scaling.

The discussion on the formation of large-scale flow structures in the longitudinal cross-section $Y = 0.5 \times W$ was restricted to the topology of coherent flow pattern. Besides the time-averaged velocity fields and POD analysis, the velocity fluctuations uncover further details about the thermal convection rolls. In the following the velocity fluctuations in the longitudinal cross-section are discussed as a function of

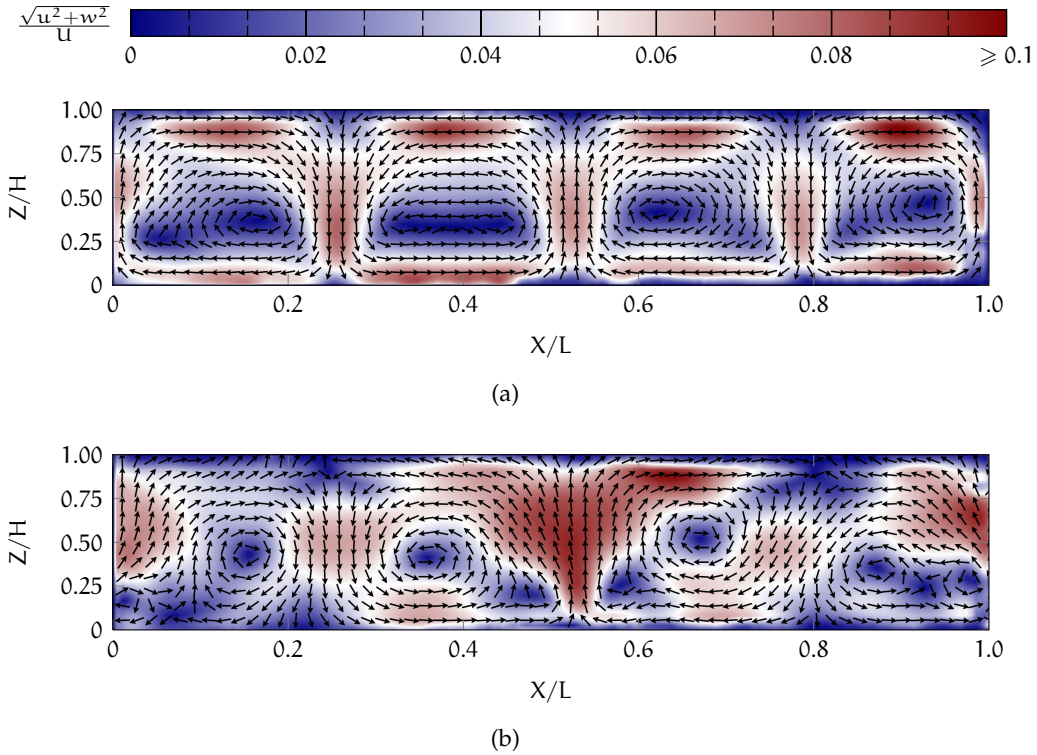

Figure 22: Topology of the first mode coherent structure in the longitudinal cross-section for $Ar = 2.28$ (22a) and $Ar = 1.81$ (22b). The vectors consist of the corresponding eigenfunctions Ψ^1_u and Ψ^1_w and scaled to unity.

Ar, excepting the flow case $Ar = 0.48$. Due to the low signal noise ratio at $Ar = 0.48$, the standard deviation allows no reliable interpretation.

The normalised standard deviation of the velocity component u (fig. 23) reveals elevated fluctuations in the region close to the top and bottom plate. The fluctuations are the result of the cross flow between the horizontal flow of the thermal convection rolls and the forced flow coming from the inlet at the ceiling and the flow towards the outlet at the bottom. For $Ar = 3.33$ (fig. 23a) and $Ar = 2.28$ (fig. 23b) elevated fluctuations are located close to the top and bottom plate. Moreover, the velocity of the incoming wall jet at the top is significantly higher than the flow towards the outlet at the bottom. Consequently, higher shear stresses are obtained at the ceiling. This higher shear stresses cause in a broaden region with elevated σ_u/U-values at the top of the container (fig. 23c), while near the bottom, the region of elevated fluctuations is considerably smaller.

For $Ar = 1.81$ (fig. 23c) the magnitude and the distribution of the velocity fluctuation of the u-component differs from those found at $Ar = 3.33$ and $Ar = 2.28$. Elevated σ_u/U-values are found in the region, where the incoming wall jet and the flow towards

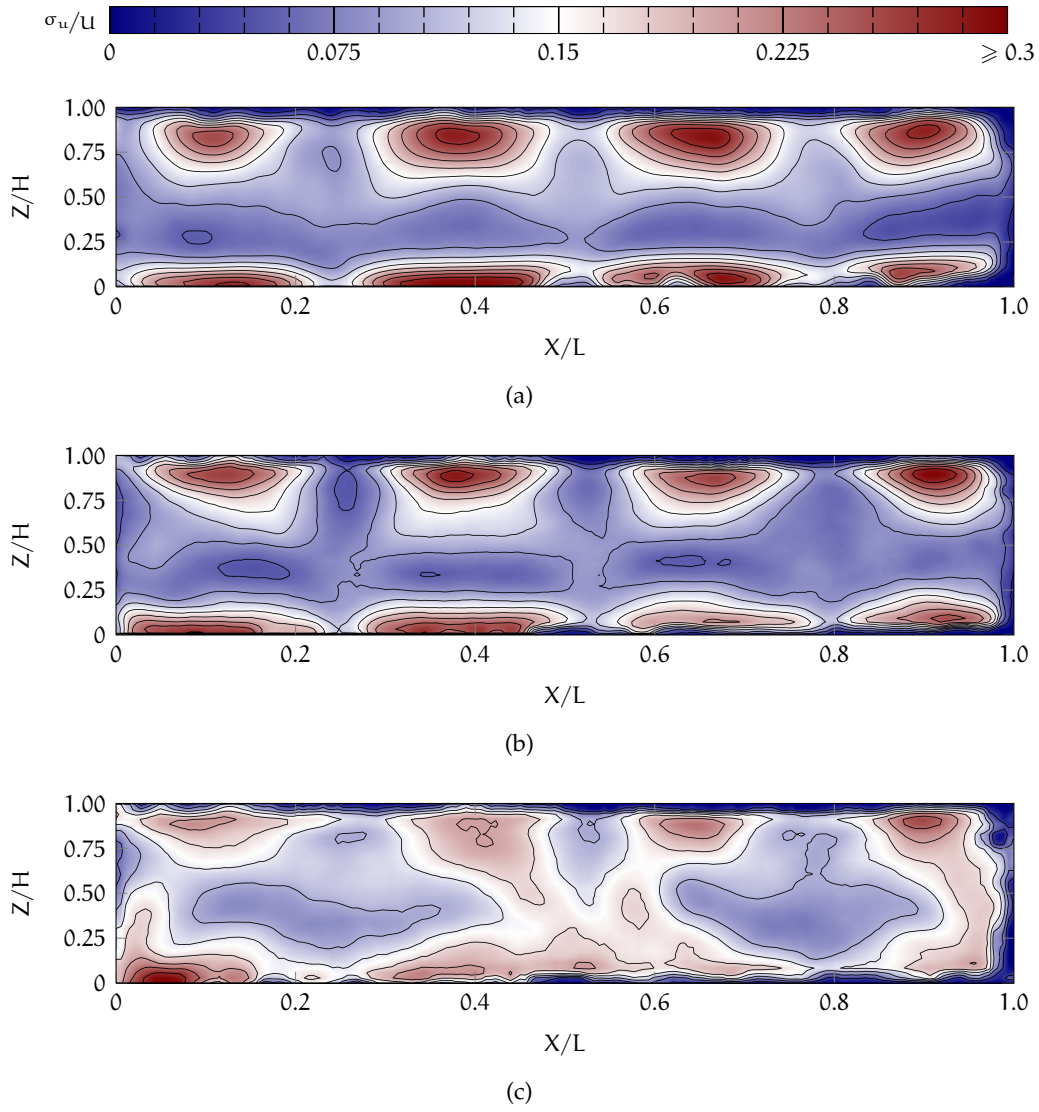

Figure 23: Velocity fluctuations of the u-component as a function of Ar in the longitudinal cross-section at $Y = 0.5 \times W$. (23a) - (23c) Normalised standard deviation σ_u for $Ar = 3.33$, $Ar = 2.28$ and $Ar = 1.81$ respectively.

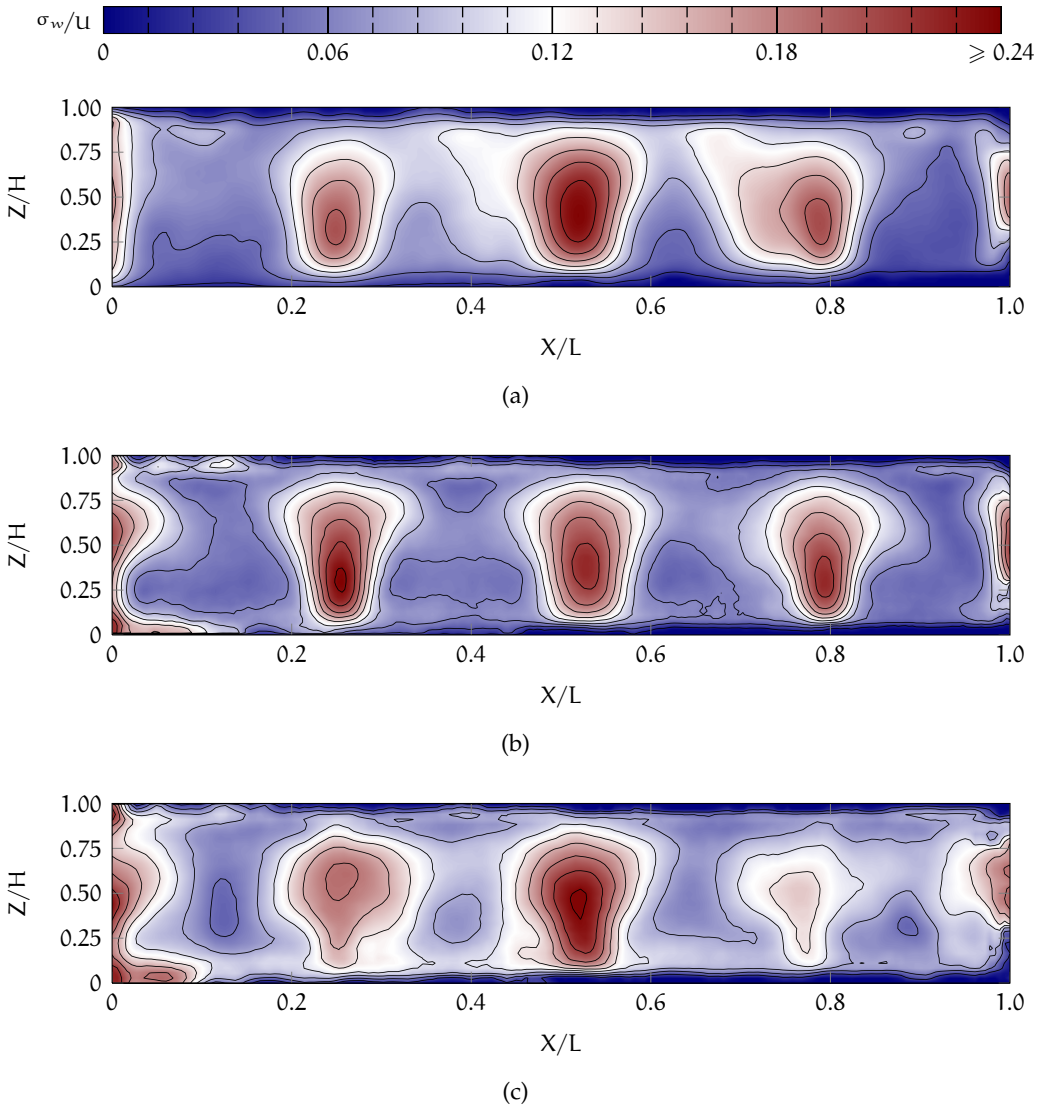

Figure 24: Velocity fluctuations of the w-component as a function of Ar in the longitudinal cross-section at $Y = 0.5 \times W$. (24a) - (24c) Normalised standard deviation σ_w for $\mathcal{A}r = 3.33$, $\mathcal{A}r = 2.28$ and $\mathcal{A}r = 1.81$ respectively.

the outlet interacts with the horizontal flow of the thermal convection rolls. However, the higher inflow velocity leads to a enhanced interaction of *FC* and *TC*. Due to the increased inertia forces, more plumes are convected by the forced mean wind and this leads to an increase of the velocity fluctuations in the bulk of the cross-section. In particular, in the bluk of the regions $0.4 \times L < X < 0.6 \times L$ and close to the lateral walls higher fluctuations are found. A closer inspection of the corresponding first mode coherent structure (fig. 22b) reveals that at these positions, smaller roll structures are developed.

The distribution of the w-component fluctuations (fig. 24) is almost similar for the three flow cases. Elevated fluctuations are obtained in the region of preferred ascending and descending air. Moreover, an increase of σ_w in the bulk of the cross-section is found with decreasing Ar. In particular, at $Ar = 1.81$, where buoyancy and inertia forces have almost the same order of magnitude, the mutual interplay leads to higher σ_w-values.

5.2 LOW FREQUENCY DYNAMICS AND HEAT TRANSPORT

The following section is divided into three paragraphs, including the dynamics of the large-scale coherent structures, the characteristics of the temperature signal at the outlet slot and an overview of the characteristic frequencies, which were identified from the POD time developing coefficient and the temperature time series at the outlet.

5.2.1 *Dynamics of large-scale circulation*

With the objective to uncover the dynamics of the large-scale roll structures, like sudden break-ups of the roll structures or flow reversals, the vortex detecting algorithm (sec. 4.1) is utilised on the set of instantaneous velocity field. The centre positions of the thermal convection rolls are determined in order to obtain the trajectories of the centre positions of the *LSC*s and the rotational directions.

Because the predominant coherent structure in the longitudinal direction at $Ar = 3.33$ consists of four side by side arranged *LSC*s (fig. 18b), the cross-section is subdivided into four regions, where each region contains one *LSC*. The trajectory of the x-coordinates of the centre positions X_c in the longitudinal direction is shown in figure 25. Two intervals consisting of four counter-rotating *LSC*s in the periods $1250\,s \lesssim t \lesssim 2750\,s$ and $3600\,s \lesssim t \lesssim 7200\,s$ are identified, however, with reversed rotational directions respectively. These two periods are interrupted by an intermediate regime $2750\,s \lesssim t \lesssim 3600\,s$. This period is featured by a spontaneous break-up of the *LSC* placed on the right side. As a consequence the other three *LSC*s shift to right and

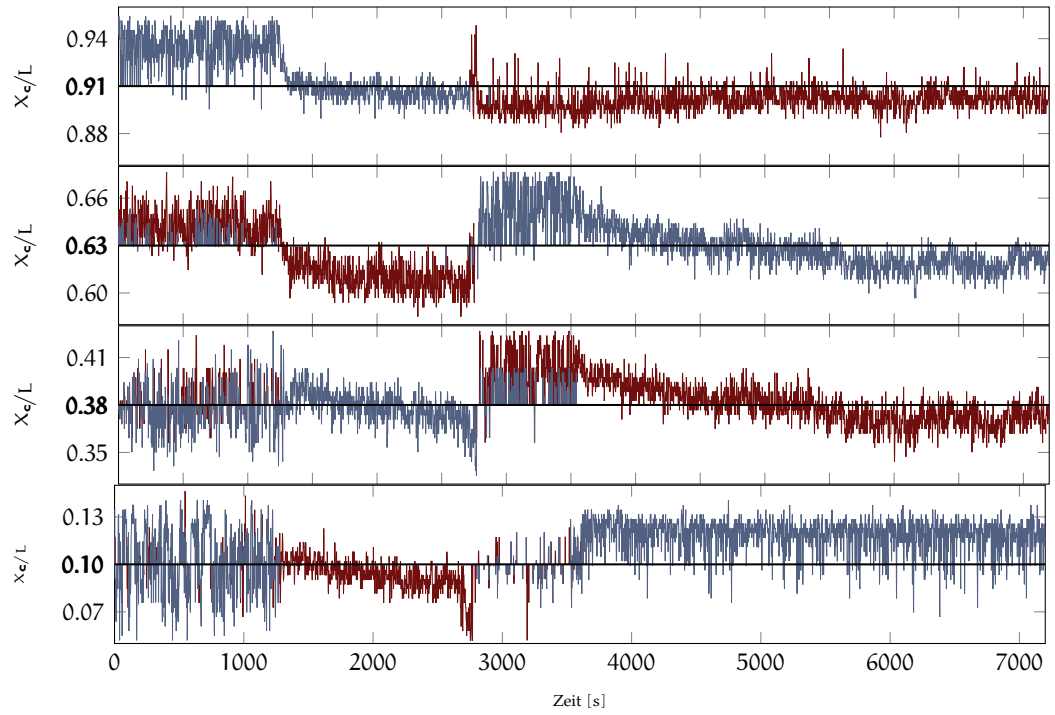

Figure 25: Time series of the *LSC* centre position X_c/L for $\mathcal{A}r = 3.33$, $\mathcal{R}e = 1.01 \times 10^4$ and $\mathcal{R}a = 2.39 \times 10^8$. The bold y-tick labels denote the normalised time averaged X-centre position $\overline{X}_c/L$ and the rotational direction of the *LSC* is colour-coded, where (•) signifies clockwise and (•) counter-clockwise rotating *LSC*.

erratic fluctuations on the left side are found. At $t = 3600\,s$ a coherent state of four counter-rotating *LSC*s is evolved again.

Moreover, within the periods $1450 \lesssim t \lesssim 2600$ and $3600 \lesssim t \lesssim 4600$ a movement of the two middle *LSC*s towards the left is found. These shift could be the result of a torsional movement of the *LSC*s, similar to that observed by Lin et al. [74]. For the present setup, the motion of the *LSC*s is bounded by the lateral walls. This means, if the torsional orientation of the *LSC* reaches a critical point, several options for the dynamics of the thermal roll structures exist. In principle, the options are: a break-up of one or more roll structure and a resulting re-orientation of *LSC*, a sudden reversal of the *LSC* rotational direction or the *LSC* swings back.

The corresponding trajectories of the centre position Z_c (fig. 26) reveal fluctuations as well, but less strong compared to the fluctuations of X_c. At $\mathcal{A}r = 3.33$ the large-scale roll structures have a diameter of the container's height H. As a consequence, the mean position of Z_c is inherently located close to $Z_c = 0.5 \times H$. Nevertheless, a shift of the mean centre position Z_c towards the bottom is found. This shift results from the forced flow. Due to the higher speed of the incoming wall jet, as well as its oscillation,

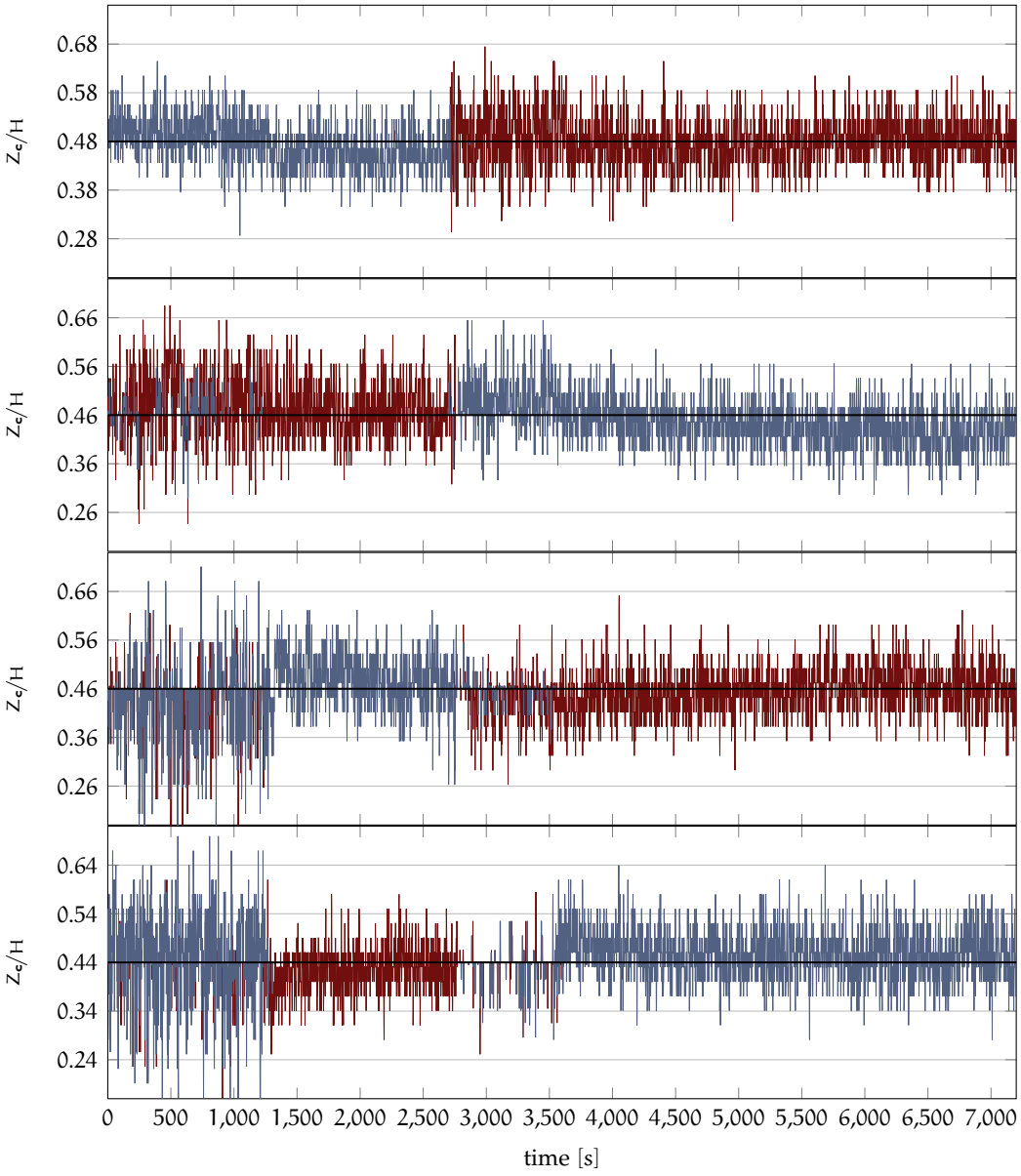

Figure 26: Time series of the *LSC* centre position Z_c/H for $\mathcal{A}r = 3.33$, $\mathcal{R}e = 1.01 \times 10^4$ and $\mathcal{R}a = 2.39 \times 10^8$. The bold y-tick labels denote the normalised time averaged Z-centre position $\overline{Z}_c/H$ and the rotational direction of the *LSC* is colour-coded, where (●) signifies clockwise and (●) counter-clockwise rotating *LSC*.

a broader flow at the ceiling is obtained relative to the flow at the bottom towards the outlet. The forced flow from the inlet and towards the outlet interacts with the horizontal flow of the thermal convection rolls. Due to the broader flow and the higher speed of the forced flow at the ceiling the horizontal thermal convective flow at the top is widened. As a consequence the centre position Z_c is shifted to the bottom.

However, the time series of the centre positions indicates that at the beginning, a period exists, where another flow state is present. Based on the finding of a coherent structure, which consists of three counter-rotating *LSC*s (fig. 19a), I presume that within $0\,s < t < 1250\,s$ this coherent structure is predominant. With the aim to determine the dynamics of the predominant coherent structures, the corresponding time developing coefficients are analysed.

Figure 27 displays the time series of the eigenvectors ζ_1 and ζ_2 for $Ar = 3.33$. The two eigenvectors represent the time developing coefficient of the predominant coherent structures, whose eigenvalues together contain 52 % of the total energy. The eigenvector of the first mode (fig. 27 (top)) corresponds to the coherent structure consisting of four *LSC*s (fig. 18). The eigenvector ζ_1 reveals two periods $1250\,s \lesssim t \lesssim 2750\,s$ and $3600\,s \lesssim t \lesssim 7200\,s$ in which the structure is predominant. Further, the change of the *LSC* rotational direction is indicated by the change of the sign. On the contrary, within the period at the beginning $0\,s \lesssim t \lesssim 1250\,s$ and during the transitional state $2750\,s \lesssim t \lesssim 3600\,s$, the eigenvector is approximately zero. Moreover, this finding corresponds to those determined from the trajectory of the *LSC* centre positions.

Figure 27 (bottom) depicts the time series of the second mode eigenvector ζ_2. The eigenvector represents the time developing coefficient of the coherent structure Ψ_2, consisting of three counter-rotating *LSC*s (fig. 19a), which is predominant in the period at the beginning $0\,s \lesssim t \lesssim 1250\,s$. At $t \approx 1250\,s$ the coherent structure Ψ_1 becomes prevailing and a sudden break-up of Ψ_2 is found. In the following a continuous increase of ζ_2 is observed, while the maximum is reached during the period of the transitional state, where the coherent structures Ψ_2 and Ψ_1 coexist. Further, with the predominance of the coherent structure Ψ_1 at $t \approx 3600\,s$ the magnitude of the eigenvector ζ_2 decreases and becomes approximately zero at $t \approx 5000\,s$.

A key feature of *MC* in the present setup is the low-frequency dynamics of the *LSC*. This characteristic is observed, in particular, within the regime of *MC*, where the flow is primarily governed by *TC* [124, 125]. As well, in the present study, low-frequency oscillations of the predominant coherent roll structures are obtained (fig. 28). The Power Spectral Density (*PSD*) of the eigenvectors reveals a couple of characteristic frequencies. In case of the longitudinal cross-section, the characteristic frequency of the first mode is $\omega = 2\pi f \approx 0.008\,s^{-1}$ (fig. 28a) and in case of the second mode is $\omega \approx 0.007\,s^{-1}$ (fig. 28b). The physical process, which underlies these low-frequency oscillations cannot fully be disclosed with the present data. However, due to studies

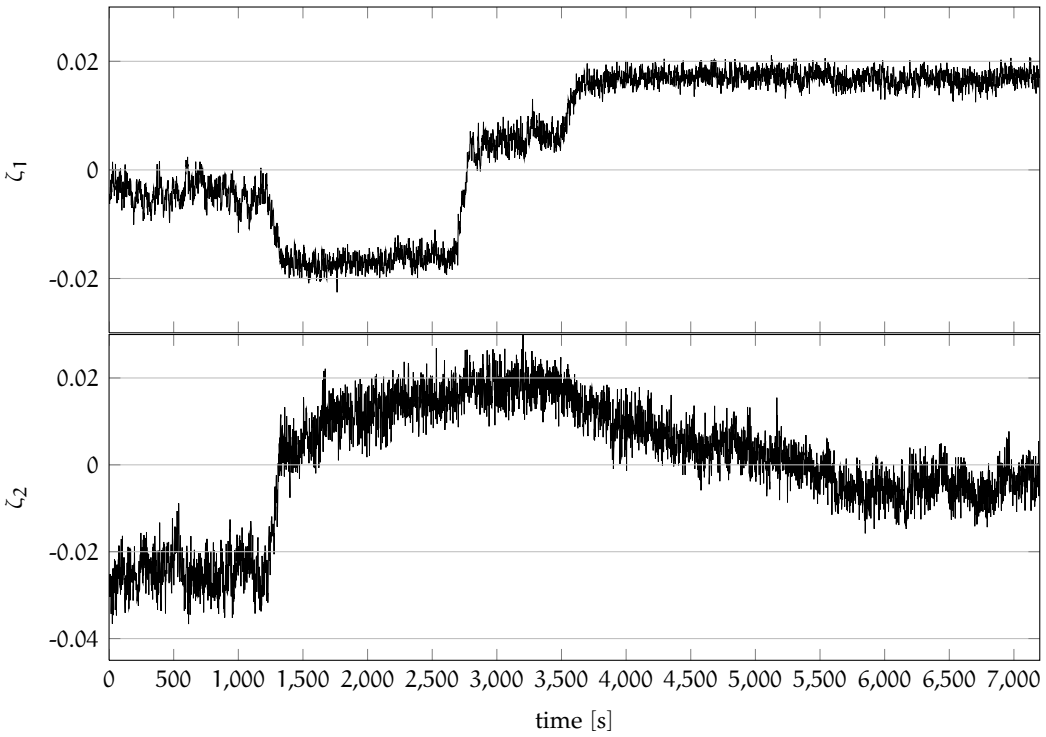

Figure 27: Time series of the eigenvectors ζ_1 and ζ_2 in the cross-section $Y = 0.5 \times L$ at $\mathcal{A}r = 3.33$, $\mathcal{R}e = 1.01 \times 10^4$ and $\mathcal{R}a = 2.39 \times 10^8$.

of *LSC* in *RBC* and in *MC* (details see sec. 2.2) it seems reasonable to assume that the dynamics have the origin in a torsional movement of the *LSC*s.

The frequency analysis of eigenvectors, which are related to the POD of the velocity vector fields in vertical cross-section, reveals characteristic frequencies (fig. 28c and 28d) as well. The eigenvalues of the first two modes are $\lambda_1 = 72.6\,\%$ and $\lambda_2 = 3.7\,\%$ of the total energy. Characteristic frequencies are found at $\omega \approx 0.011\,s^{-1}$, $\omega \approx 0.31\,s^{-1}$ and $\omega \approx 0.62\,s^{-1}$. The characteristic frequency $\omega \approx 0.62\,s^{-1}$ corresponds to the angular velocity of the thermal convective rolls $\omega_{LSC}^{(TC)} \approx 0.63 s^{-1}$ for the flow state of four counter-rotating *LSC*s. However, due to the correlation between the plumes and *LSC* dynamics, one cannot rule out the possibility that these frequencies are even related to a periodic plume emission. In addition, the frequency, which is related to the angular velocity of the *LSC*s, indicates that the thermal convection rolls rotate with a single frequency over hundreds of cycles, although the bulk is turbulent.

Besides the two first modes, several other modes are found, including characteristic frequencies. A detailed discussion and analysis of all these frequencies would go beyond the scope of the discussion in this paragraph. However, in the last paragraph

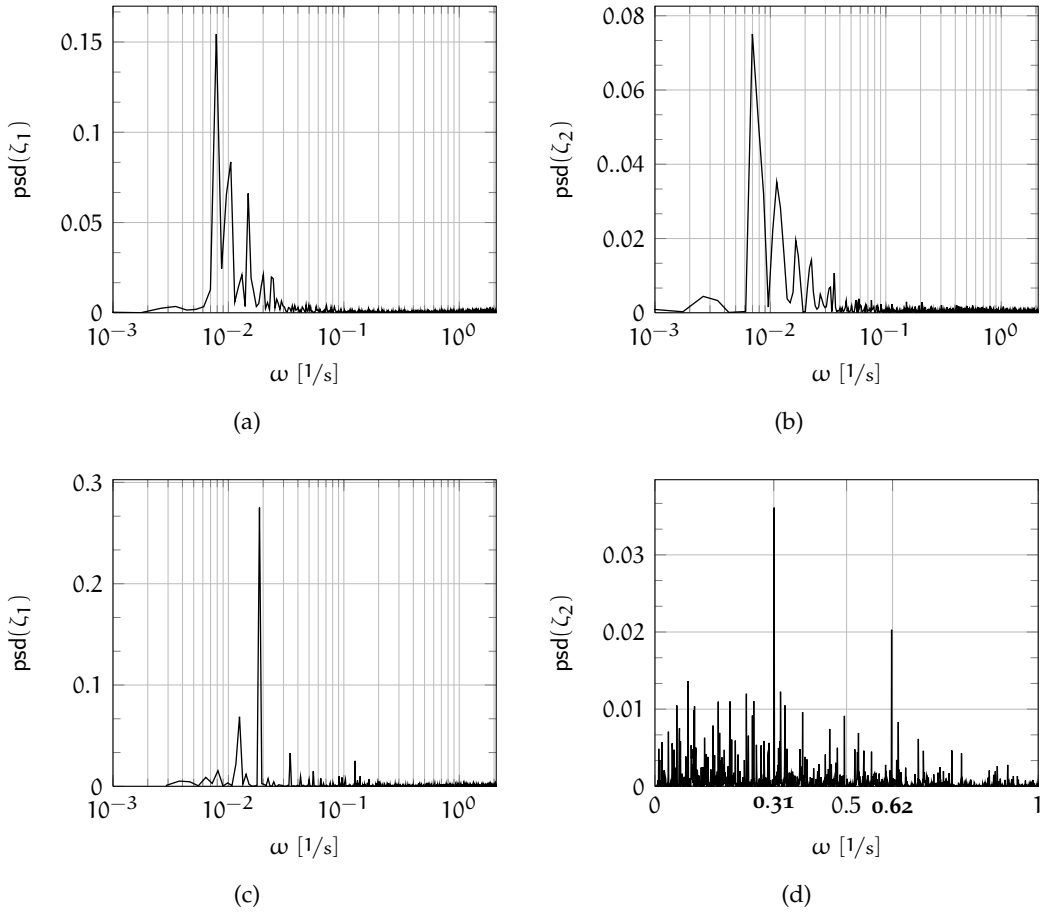

Figure 28: *PSD* of the POD eigenvectors in the longitudinal (28a and 28b) and vertical cross-section (28c and 28d) at $\mathcal{A}r = 3.33$.

of this section, an overview of the characteristic frequencies of the first six POD modes in the vertical and longitudinal cross-section is outlined as a function of $\mathcal{A}r$.

The flow cases $\mathcal{A}r = 2.28$ and $\mathcal{A}r = 1.81$ represent *MC* in the intermediate $\mathcal{A}r$-regime. Here, the eigenfunctions represent a coherent structure consisting of four counter-rotating roll structures (fig. 22). The modes have eigenvalues containing 46 % for $\mathcal{A}r = 2.28$ and 40 % for $\mathcal{A}r = 1.81$ of the total energy. However, in contrast to $\mathcal{A}r = 3.33$ no higher modes are found, disclosing eigenfunctions representing large-scale structures. For $\mathcal{A}r = 2.28$ the coherent structure of the first mode is almost similar to Ψ_1 at $\mathcal{A}r = 3.33$ (fig. 22a). Four almost symmetrically arranged counter-rotating *LSC*s are found, while at $\mathcal{A}r = 1.81$ (fig. 22b) the *LSC*s are already strongly influenced by the forced flow.

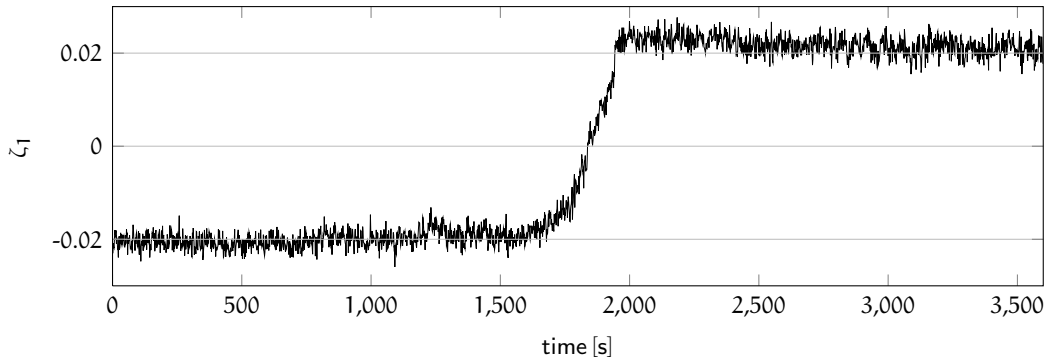

(a)

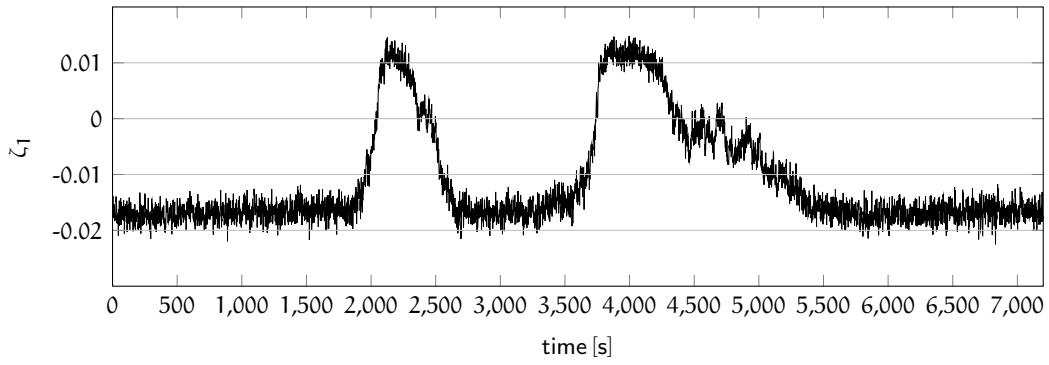

(b)

Figure 29: Time series of the first POD mode eigenvectors ζ_1 in the longitudinal cross-section at $\mathcal{A}r = 2.28$ (29a) and $\mathcal{A}r = 1.81$ (29b).

For the first mode at $\mathcal{A}r = 2.28$, the trajectory of the time developing coefficient (fig. 29a) reveals two stable states. Within these periods, the predominant coherent structure consists of four counter-rotating *LSC*s, but with an opposed rotational direction respectively. Both states persist over tenth of *LSC* rotations and in contrast to $\mathcal{A}r = 3.33$, where a transitional state emerges, the flow reversal occurs suddenly. For $\mathcal{A}r = 1.81$, the time series of the first mode eigenvector (fig. 29b) discloses a preferred stable state, which is interrupted by two periods. Within these periods a change of sign for the eigenvector is observed. These intervals seem to be related to the same coherent structure, however, with an opposed rotational direction. Moreover, within the interval $4500\,\mathrm{s} \lesssim t \lesssim 5500\,\mathrm{s}$ a transitional state is found.

Figure 30 illustrates the *PSD* of the first mode eigenvectors ζ_1 for $\mathcal{A}r = 2.28$ (fig. 30a) and $\mathcal{A}r = 1.81$ (fig. 30b). At $\mathcal{A}r = 2.28$, once again a very-low characteristic frequency of $\omega \approx 0.008\,\mathrm{s}^{-1}$ is found, which was already identified at $\mathcal{A}r = 3.33$. Because the predominant coherent structures are nearly identical and the impact of the forced flow

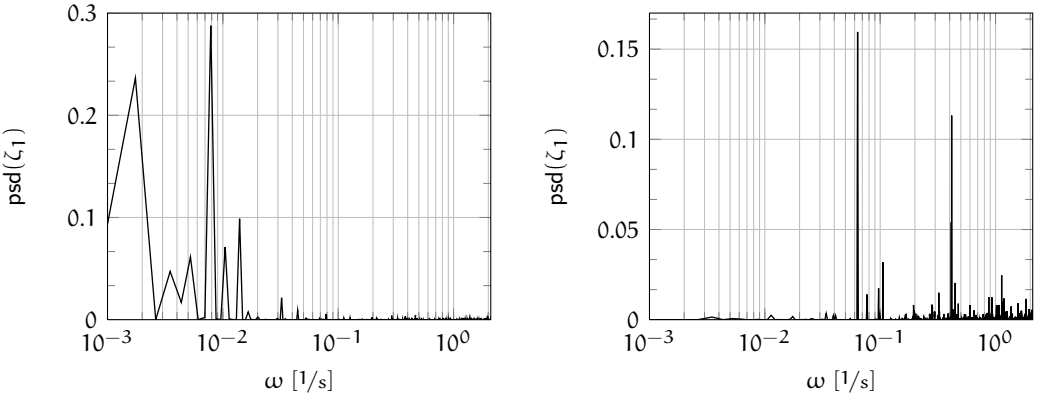

Figure 30: *PSD* of the first mode eigenvector ζ_1 in the longitudinal cross-section at $Ar = 2.28$ (30a) and $Ar = 1.81$ (30b).

on the thermal convection rolls is still small, I assume that the time-periodic dynamics of the thermal convection rolls is almost similar. Furthermore, another very-low characteristic frequency is found at $\omega \approx 1.8 \times 10^{-3}$. This frequency corresponds to a period of $T \approx 3500\,s$, which is the period of the measurement time. This frequency is the result of the flow reversal, which randomly appeared at almost $T/2$, and does not show a periodic dynamics of the roll structures.

For $Ar = 1.81$ the *PSD* of the first mode eigenvector does not reveal a very-low frequency $\omega < 0.01\,s^{-1}$. The impact of the forced flow on the thermal convection roll leads to a significant influence on the dynamics of the thermal convection rolls. Nevertheless, the *PSD* discloses another low frequency, but a magnitude higher in relation to the very-low frequencies, which were found at $Ar = 2.28$ and $Ar = 3.33$.

Besides the characteristic frequency $\omega \approx 0.06\,s^{-1}$ the *PSD* possesses another peak at $\omega \approx 0.4\,s^{-1}$. Due to the mutual interplay of the *TC* and *FC* flow structures, an interpretation or an assumption of the frequencies' origin is difficult. At $Ar = 1.81$, the mixing and the interleaving between forced flow and thermal flow are too strong. However, because $\omega \approx 0.4\,s^{-1}$ is close to the angular velocity of the thermal convection rolls at $Ar = 3.33$, I assume that this frequency represents the angular velocity of the thermal convection rolls. The lower angular velocity, in relation to $Ar = 3.33$, could be the result of the increased impact of the forced flow. At $Ar = 1.81$ significantly more plumes are convected by the forced convective mean wind and thus a reduced buoyancy velocity is obtained. [116]

At $Ar = 0.48$ the formation of large-scale flow structures and its dynamics are governed by *FC*. In the paragraph 5.1.2 it was shown that the predominant flow pattern in the longitudinal cross-section consists of eight counter-rotating roll structures with

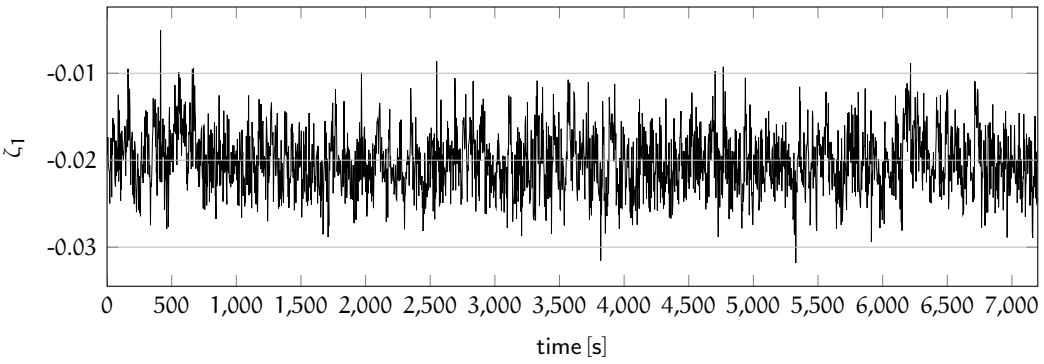

Figure 31: Time series of the eigenvector ζ_1 in the longitudinal cross-section at $Ar = 0.48$.

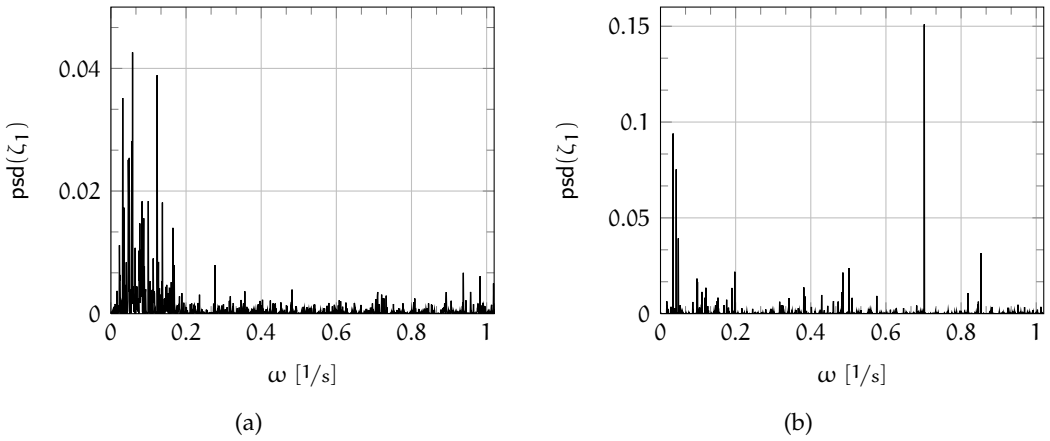

Figure 32: *PSD* of the first mode eigenvectors in the longitudinal cross-section (32a) and the vertical cross-section (32b) in case of $Ar = 0.48$.

a diameter of approximately $H/2$. The time series of the corresponding first mode eigenvector (fig. 32a) discloses the existence of one predominant flow pattern. In contrast to the flow at $Ar \geqslant 1.8$ the time series does not reveal flow reversals or intermediate states. The corresponding *PSD* of the first mode eigenvector ζ_1 in the longitudinal cross-section (fig. 22a) illustrates a frequency band $0.02\,s^{-1} \leqslant \omega \leqslant 0.18\,s^{-1}$ including several peaks, while a periodic dynamics with a single frequency does not exist. However, the *PSD* of the first mode eigenvector in the vertical cross-section (fig. 32b) reveals a dominant peak at $\omega = 0.69\,s^{-1}$. An assignment of the frequencies to the underlying roll structure dynamics is difficult, since at $Ar = 0.48$ the mutual interaction is too complex. Nevertheless, an assumption of the angular velocity for the smaller roll structures in the core of the *FC* mean wind by the time-averaged velocity vector field (fig. 20a) results in an angular velocity of $\omega \approx 0.72\,s^{-1}$ for the

two middle *LSC*s. Hence, it is likely that the characteristic frequency $\omega = 0.69\,s^{-1}$ is related to the rotational dynamics of the small roll structures.

Indeed, the eigenvectors of the first two modes disclose time-periodic behaviour of the large-scale coherent structures. However, one can criticise that POD is only a statistical tool, and the eigenvectors of the predominant coherent structures are without any profound meaning. Thus, it is essential to prove the relevance of these frequencies. To verify if the characteristic frequencies reveal flow features, the temperature time series (*TTS*) at the container's outlet are analysed as a function of $\mathcal{A}r$ for time-periodic behaviour.

5.2.2 *Temperature fluctuations*

Figure 33 shows the temperature fluctuations at the outlet recorded within the PIV measurement in the longitudinal cross-section at $\mathcal{A}r = 3.33$, where Θ_x^{out} are the temperatures at the outlet position $X = 0.05 \times L$, $X = 0.25 \times L$, $X = 0.5 \times L$ and $X = 0.75 \times L$ and $\overline{\Theta}^{out}$ denotes the corresponding time-averaged outlet temperature. However, due to the limited number of temperature sensors at the outlet, the spatial temperature distribution and thus the heat transport is not fully uncovered. Nevertheless, already the temperature data at these distinctive points allow to draw conclusions about the formation of large-scale structures and their dynamics.

In case of $\mathcal{A}r = 3.3$, the POD analysis of the velocity fields in the longitudinal cross-section discloses for $t \lesssim 1250\,s$ a predominant structure, which consists of three counter-rotating *LSC*s. Within this period cold descending air is located on the left side and at $X \approx 2/3 \times L$, while hot ascending air is observed at $X \approx 1/3 \times L$ and on the right side. Consequently, the sensors which are located to the region of descending cold air reveals lower temperatures within this period (fig. 33a and 33d). Moreover, lower temperatures are observed at the sensor position $X \approx 0.5 \times L$ (fig. 33b). Here, the advective flow of the middle *LSC* at the bottom transports the cold air, which descends at $X \approx 2/3 \times L$. On the contrary, the sensor which is located close to the region of rising warm air $X \approx 1/3 \times L$, shows elevated temperatures (fig. 33c).

Within the periods $1250\,s \lesssim t \lesssim 2750\,s$ and $3700\,s \lesssim t \lesssim 7200\,s$ the predominant coherent structure consists of four counter-rotating *LSC*s. Here, the temperature sensor positions in the outlet slot correspond to the regions of rising hot air and descending cold air. Hence, alternating elevated and lowly temperatures are found. Within $1250\,s \lesssim t \lesssim 2750\,s$ falling cold air is located to $X = 0.5 \times L$ (fig. 33c) and close to the lateral wall (fig. 33d). Accordingly, elevated temperatures are found at the sensor positions $X = 0.25 \times L$ and $X = 0.75 \times L$. At $t \approx 2750$ the *TTS* of the sensor at $X \approx 0.5 \times L$ discloses a sudden breakup of the downward oriented flow in the region of $X = 0.5 \times L$. As soon as the stable state of four *LSC*s is re-evolved, a structured distribution of elevated and lowly temperatures are developed at the outlet slot once again. Within the interval $3700\,s \lesssim t \lesssim 7200\,s$ elevated temperatures are found at $X =$

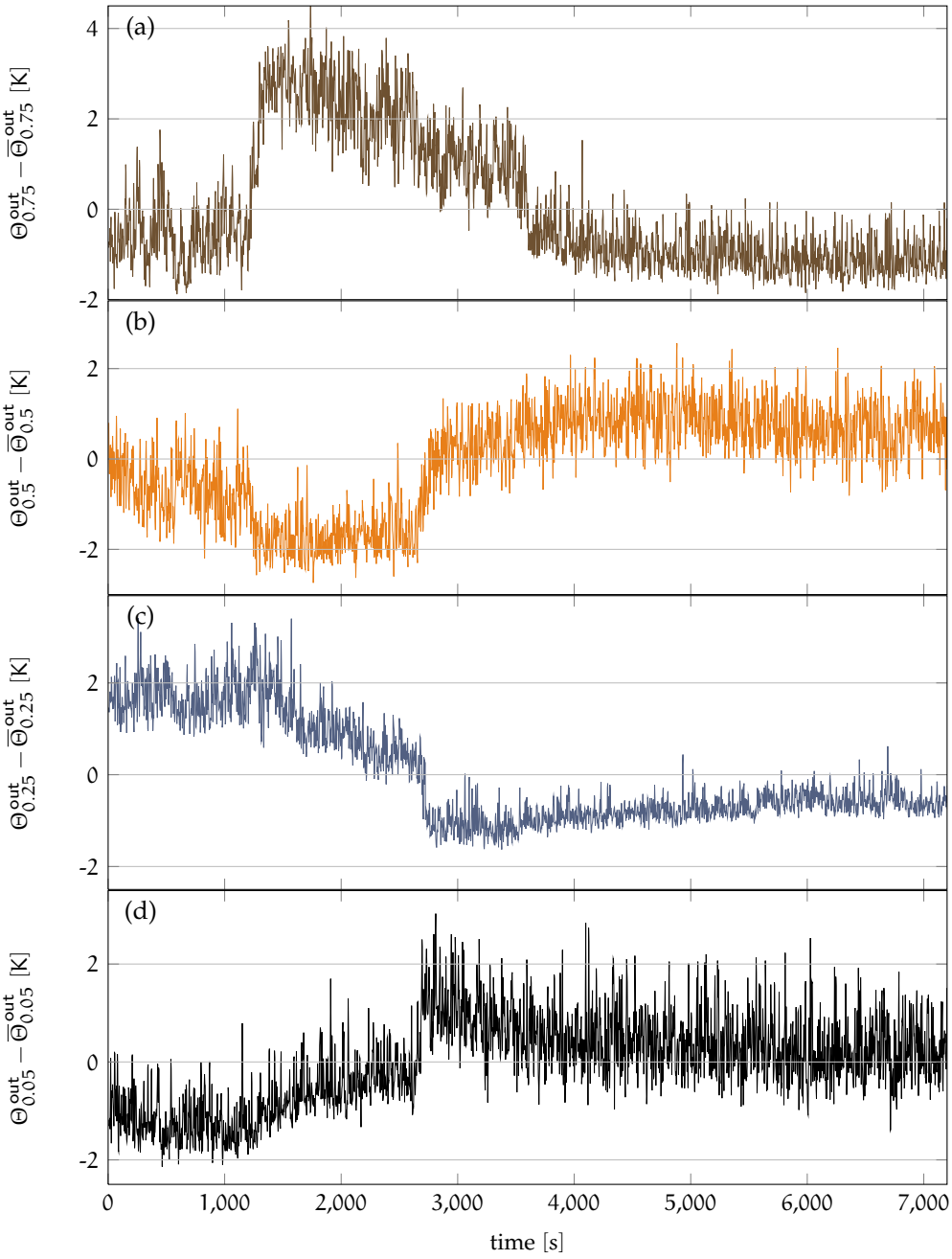

Figure 33: *TTS* for $Ar = 3.33$ at the outlet positions $X = 0.05 \times L$ (●), $X = 0.25 \times L$ (●), $X = 0.5 \times L$ (●) and $X = 0.75 \times L$ (●).

$0.5 \times L$. Accordingly, lower temperatures are obtained at $X = 0.25 \times L$ and $X = 0.75 \times L$. Besides the spatial distribution of regions with preferred ascending and descending air, the *TTS* uncover additional information about the temporal-characteristics of the predominant flow structures. For instance, the sudden temperature shift at $t \approx 2750\,s$ (fig. 33b, 33c and 33d) discloses the flow reversal of the thermal convection rolls.

In addition, a long-time *TTS* of $T = 9294\,s$ at $Ar = 3.33$ is additionally analysed. The *TTS* represents a steady-state of the predominant pattern of four counter-rotating *LSC*s. The time-averaged temperatures at the sensor positions are $\overline{\Theta}^{out}_{0.05} = 303.18\,K$, $\overline{\Theta}^{out}_{0.25} = 299.51\,K$, $\overline{\Theta}^{out}_{0.50} = 302.79\,K$ and $\overline{\Theta}^{out}_{0.75} = 299.75\,K$. In the longitudinal cross-section hot rising air is placed at $X = 0.5 \times L$ and close to the lateral walls, while cold descending air is located to the region of $X = 0.25 \times L$ and $X = 0.75 \times L$.

The corresponding *TTS* at the outlet slot are depicted in figure 34 and show fluctuations around a mean temperature with an amplitude of approximately 1.5 K. Moreover, the *PSD* the *TTS* at $X = 0.05 \times L$, $X = 0.25 \times L$ and $X = 0.5 \times L$ (fig. 35) reveals characteristic frequencies. Moroever, frequencies are found, which correlates to the frequencies of the POD eigenvectores. In particular $\omega \approx 0.009\,s^{-1}$ and $\omega \approx 0.30\,s^{-1}$ are almost similar to the characteristic frequencies, which were found in the *PSD* of the POD eigenvectors (fig. 28). That finding is important for the analysis of *MC*. It allows to draw conclusions about the topology and the dynamics of the large-scale flow structures from the temperature signal at the outlet of the container. Furthermore, the result of this study is in good agreement with measurements of *MC* under high pressure conditions $P = 10.0\,bar$ in the same geometry and similar characteristic numbers [124].

Besides the low frequencies, the *PSD* reveals further peaks at $\omega \approx 1.0\,s^{-1}$ (fig. 35a and fig. 35c). These frequencies are almost similar to the angular velocity $\omega = 1.1\,s^{-1}$ of the forced mean wind in the vertical cross-section $X = 0.5 \times L$ (tab. 3). Hence, these frequencies are assigned to the dynamics of the forced mean wind. The finding of these frequencies shows a clear influence of the forced convective flow on the heat transfer, although the flow is primarily governed by *TC*.

In addition, the cross-correlation functions (*CCF*)

$$R_{ij}(\tau) = \frac{\overline{\Theta_i(t) \cdot \Theta_j(t+\tau)}}{\sqrt{\overline{\Theta}_i^2(t) \cdot \overline{\Theta}_j^2(t+\tau)}} \tag{5.2}$$

are calculated, where Θ_i and Θ_j denotes the *TTS* of the different sensor positions and $\overline{(\cdot)}$ indicates the corresponding time averaged temperature. The figures 36a - 36c depict the *CCF* of the *TTS* at $X = 0.5 \times L$ to the sensor positions $X = 0.75 \times L$, $X = 0.25 \times L$ and $X = 0.05 \times L$. The *CCF* discloses that the *TTS* at $X = 0.5 \times L$ is anti-correlated to all other sensor positions, indicating that the vertical motion of plumes is out of phase. This finding is comparable to the result of Funfschilling and Ahlers [43]. They determined a phase shift of π for the regions of hot and cold plumes in *RBC*. Although

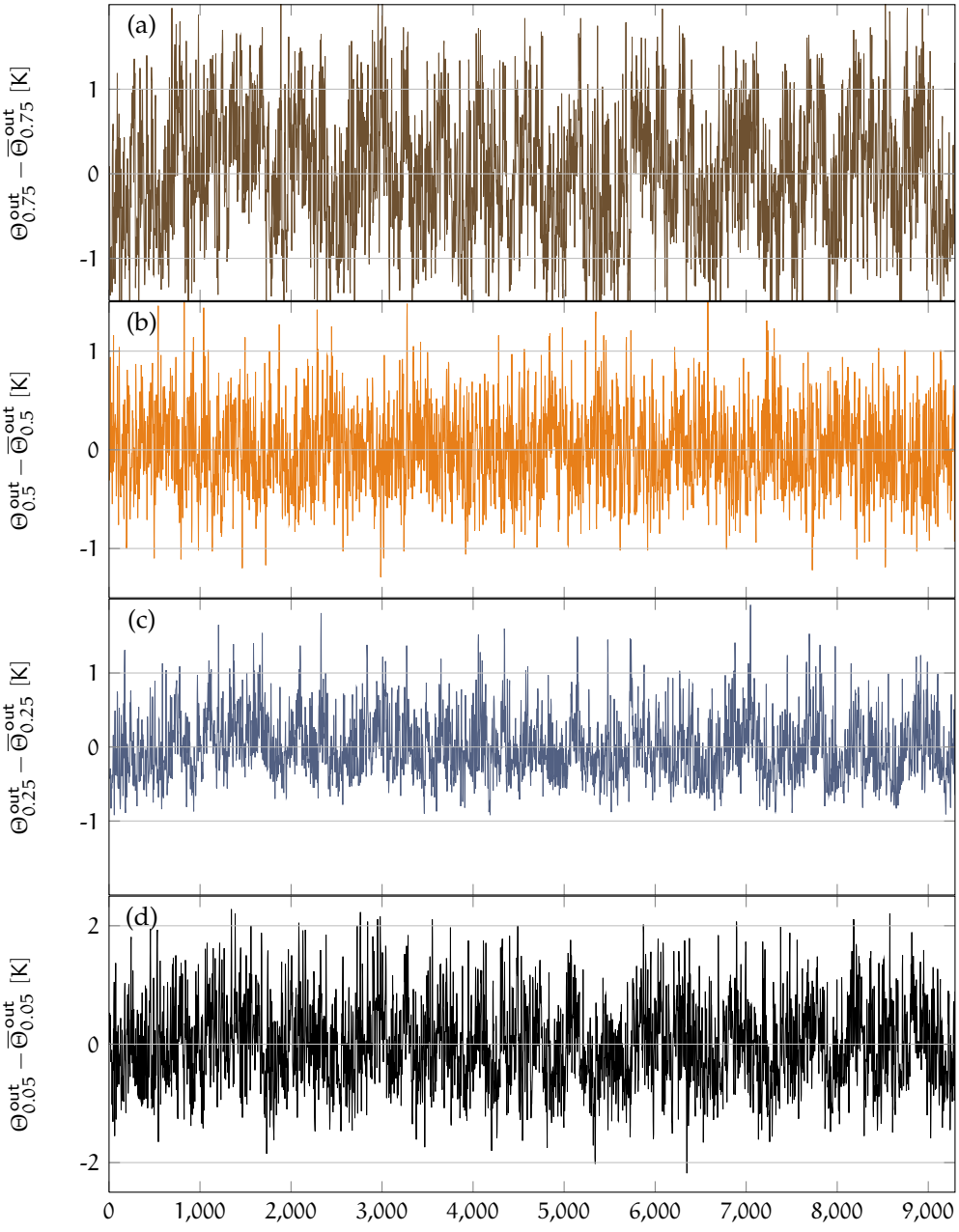

Figure 34: Long time outlet *TTS* for $\mathcal{A}r = 3.33$. Temperature fluctuations at the outlet positions $X = 0.05 \times L$ (●), $X = 0.25 \times L$ (●), $X = 0.5 \times L$ (●) and $X = 0.75 \times L$ (●).

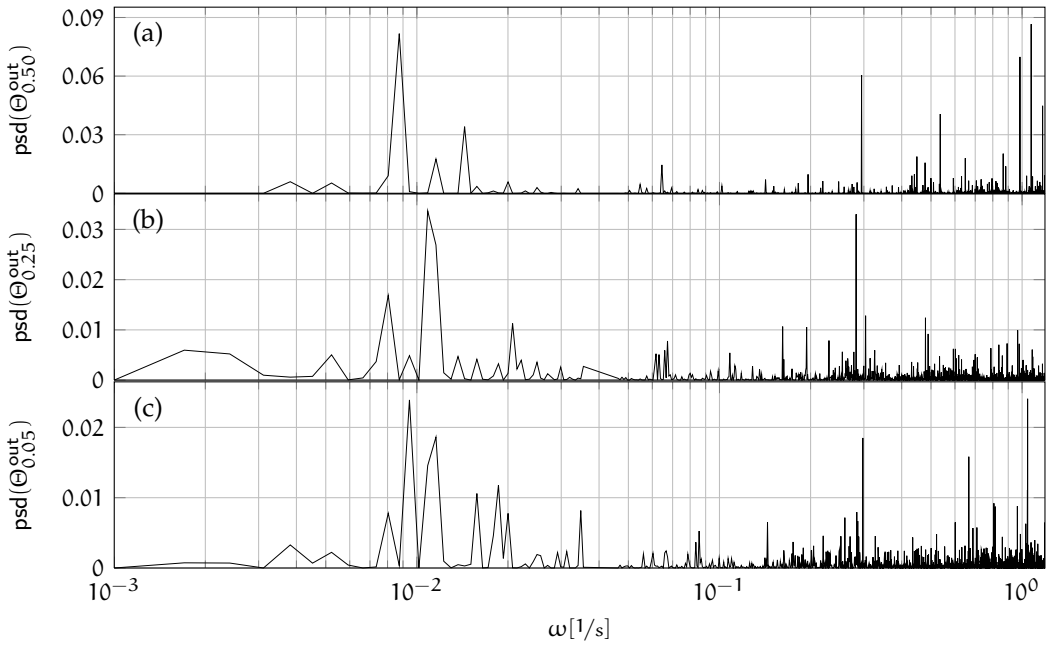

Figure 35: *PSD* of the *TTS* at $X = 0.05 \times L$, $X = 0.25 \times L$ and $X = 0.5 \times L$ for $\mathcal{A}r = 3.33$.

here *MC* is studied, the flow at $\mathcal{A}r = 3.33$ reveals characteristics, which are usually found in the dynamics of *LSC* in *RBC*, indicating that the flow is primarily governed by the thermal convective flow.

On the contrary, the *CCF* of the *TTS* between $X = 0.25 \times L$ and $X = 0.05 \times L$ (fig. 36d) are positive correlated. Why the vertical flow is in phase at this position is not clear to say. For instance, this phenomenon results from side wall effects, like an additional heat transfer through the lateral walls or the influence of the forced flow.

Furthermore, the analysis of the other three flow cases discloses characteristic frequencies. Figure 37 depicts the temperature fluctuations of two independent *TTS* at the outlet for $\mathcal{A}r \approx 1.8$. Both were recorded at $X = 0.5 \times L$. The figure 37a shows the *TTS*, which was measured during PIV in the longitudinal cross-section, while figure 37b reveals an additional temperature measurement, representing a steady-state. The temperature signal (fig. 37a) scatters around the time-averaged value, interrupted for a period at $t \approx 2250$ and $t \approx 4100$. Within this period significantly lower temperatures are observed. Moreover, the temperature signal correlates with the corresponding first mode POD eigenvector (fig. 22b).

The *PSD* of the long-time measurement (fig. 38a) reveals two significant peaks at $\omega = 0.65\,s^{-1}$ and $\omega = 0.90\,s^{-1}$. These frequencies are similar to the frequencies found in the first mode eigenvector in the cross-section $X = 0.5 \times L$. Further, due to the absence of lower characteristic frequencies, it follows that the heat transport is mainly

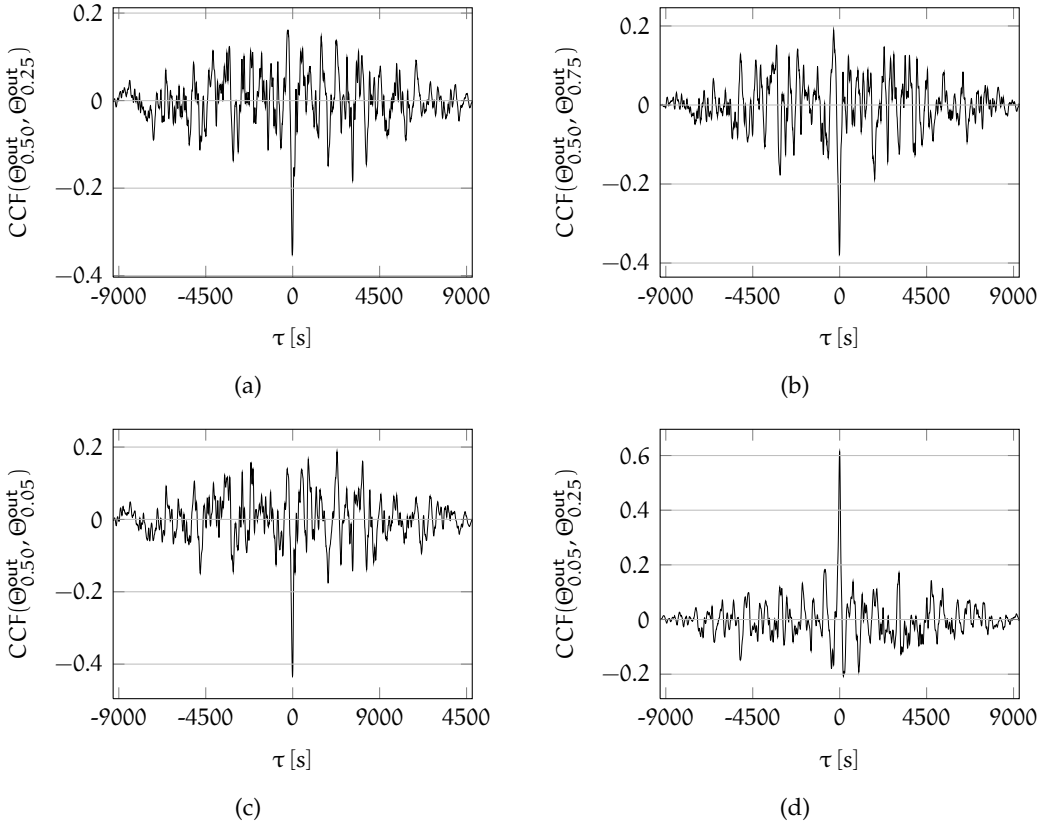

Figure 36: Cross-correlation function (*CCF*) of the outlet *TTS* at $\mathcal{A}r = 3.33$ for $X = 0.5 \times L$ and $X = 0.25 \times L$ (36a), $X = 0.5 \times L$ and $X = 0.75 \times L$ (36b), $X = 0.5 \times L$ and $X = 0.75 \times L$ (36c) and $X = 0.25 \times L$ and $X = 0.05 \times L$ (36d).

determined by the dynamics of forced mean wind. At $\mathcal{A}r \approx 1.8$ most of the plumes are entrained by the forced flow and transported into the bulk region or towards the outlet. Consequently, an increased intermingling of the plumes with the forced flow is obtained. As a result, the buoyancy induced flow is less developed and the vertical flow in the regions of ascending and descending air is broadened (fig. 22b). Further, in contrast to $\mathcal{A}r \approx 3.3$, no clear correlation or a phase-shift exists between the regions of cold and warm air (fig. 38b and 38c), indicating that the transport of plumes is primarily governed by the forced convective flow. However, the buoyancy forces are strong enough to form thermal convective roll structures in the longitudinal cross-section (fig. 22b), even though the *LSC*s are strongly deformed.

At $\mathcal{A}r = 0.48$, the transport of heat is primarily governed by the forced flow. Figure 39 reveals the spatial distribution, the time series and the *PSD* of the outlet temperatures, where Θ_{out} denotes the time-averaged temperatures of each sensor and

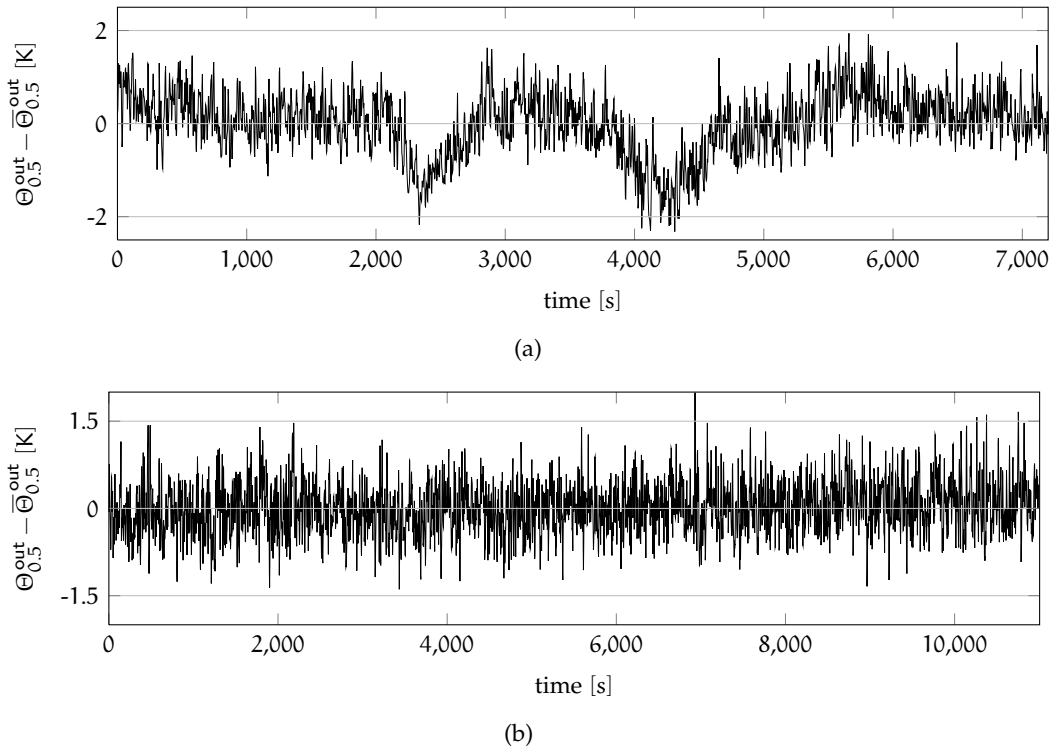

Figure 37: *TTS* at $X = 0.5 \times L$ for $\mathcal{A}r \approx 1.8$: (37a) *TTS* within PIV and (37b) long-time temperature measurement.

$\overline{\Theta}_{out}$ the spatial mean of the time-averaged temperatures. The temperatures were recorded during PIV in the longitudinal (red) and the vertical (black) cross-section. The error bars represent the standard deviation of the corresponding *TTS*. Due to a defect of the temperature sensor at $X = 0.9 \times L$, which was directly located in the outlet slot, the temperatures of a control sensor (located at the end of the outlet channel) is plotted. Of course, due to the mixing in the outlet channel, the sensor at the outlet channel reveals a lower temperature, as well as, significantly lower fluctuations relative to the sensor close to the left side ($X = 0.1 \times L$). Nevertheless, still elevated temperatures are found at the end of the outlet channel at $X = 0.9 \times L$.

In case of $\mathcal{A}r = 0.48$, most of the plumes, emitted at the ceiling or bottom, are entrained by the forced mean wind. As a consequence, the forced mean wind in the vertical cross-section $X = 0.5 \times L$ is almost unaffected by the thermal convective flow. Further, the enhanced mixing leads to a breakup of the thermal large-scale convection rolls with a diameter of H and eight smaller roll structure with a diameter $H/2$ are formed in the core region of the forced mean wind (fig. 20a). Nevertheless, a spatial temperature distribution at the outlet (fig. 39a) with alternating lower and

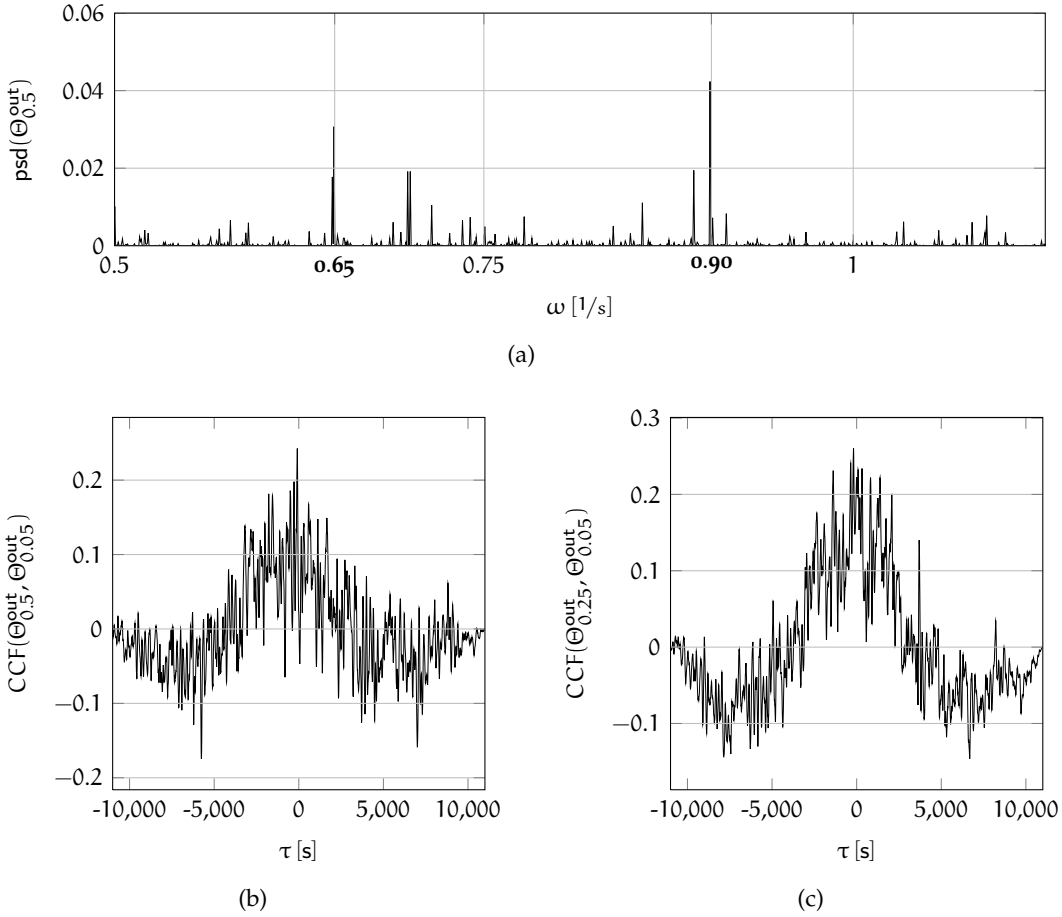

Figure 38: *PSD* and *CCF* of the *TTS* for $\mathcal{A}r \approx 1.8$: (38a) *PSD* of the *TTS* at $X = 0.5 \times L$ and (38b) *CCF* between the outlet *TTS* at $X = 0.5 \times L$ and $X = 0.25 \times L$. (38c) *CCF* between the outlet *TTS* at $X = 0.25 \times L$ and $X = 0.05 \times L$.

elevated temperatures are found. Although a breakup of large-scale flow pattern with a diameter of H is obtained, preferred regions of hot and cold plumes, emission exists.

A closer analysis of the predominant flow pattern in the longitudinal cross-section at $Y = 0.5 \times W$ (fig. 20a) reveals that the regions of cold descending air in the longitudinal cross-section correspond to the position of elevated temperatures at the outlet. Otherwise, the positions of lower temperature correlate with the regions of ascending air. This contradictory result discloses that at $\mathcal{A}r = 0.48$ the regions of hot or cold plume emission not necessarily corresponds to the position of ascending or descending air in the core of the forced mean wind. Further, this finding indicates

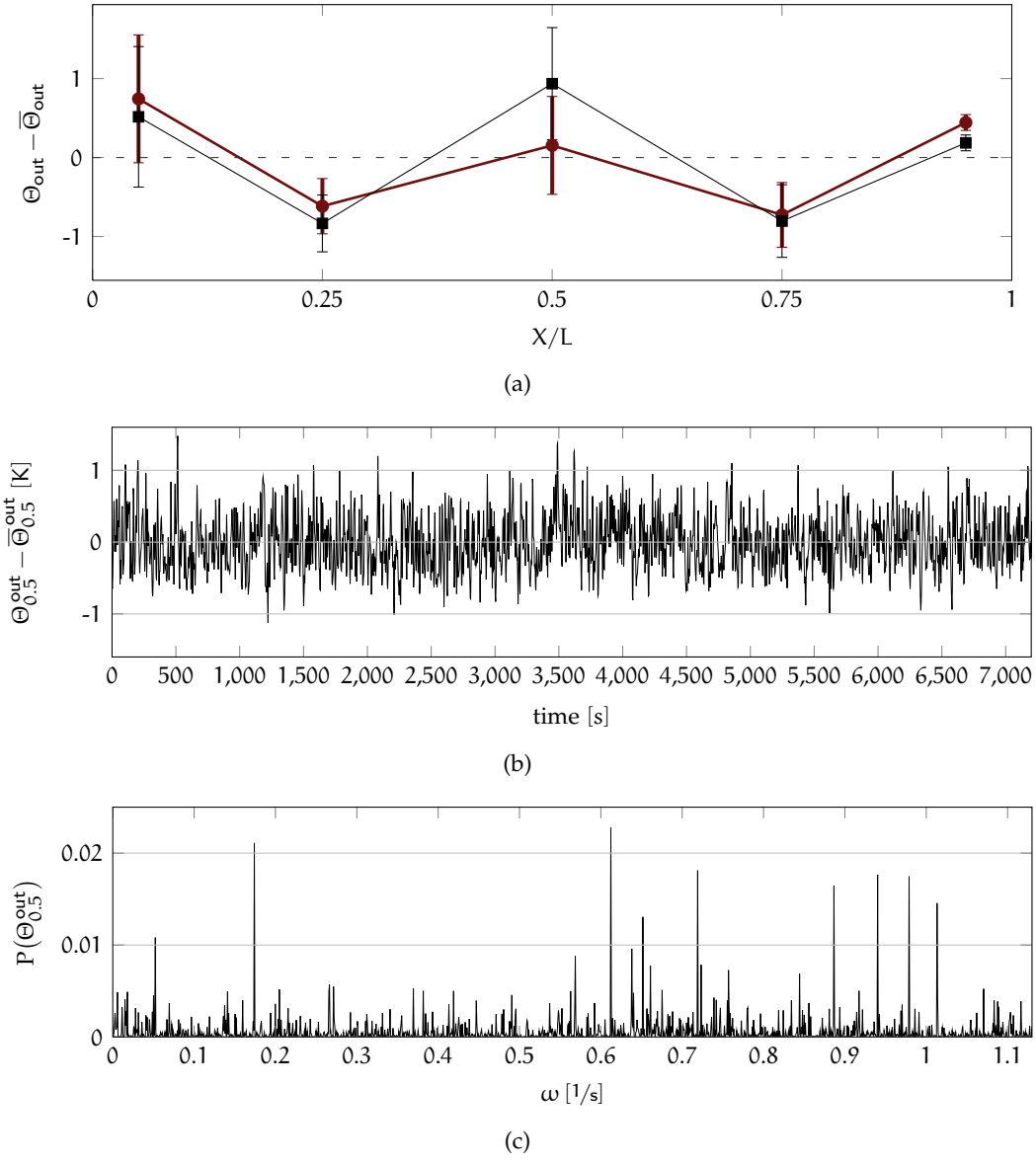

Figure 39: Spatial distribution (39a), time series (39b) and *PSD* of the temperatures at the outlet (39c) for $\mathcal{A}r = 0.48$.

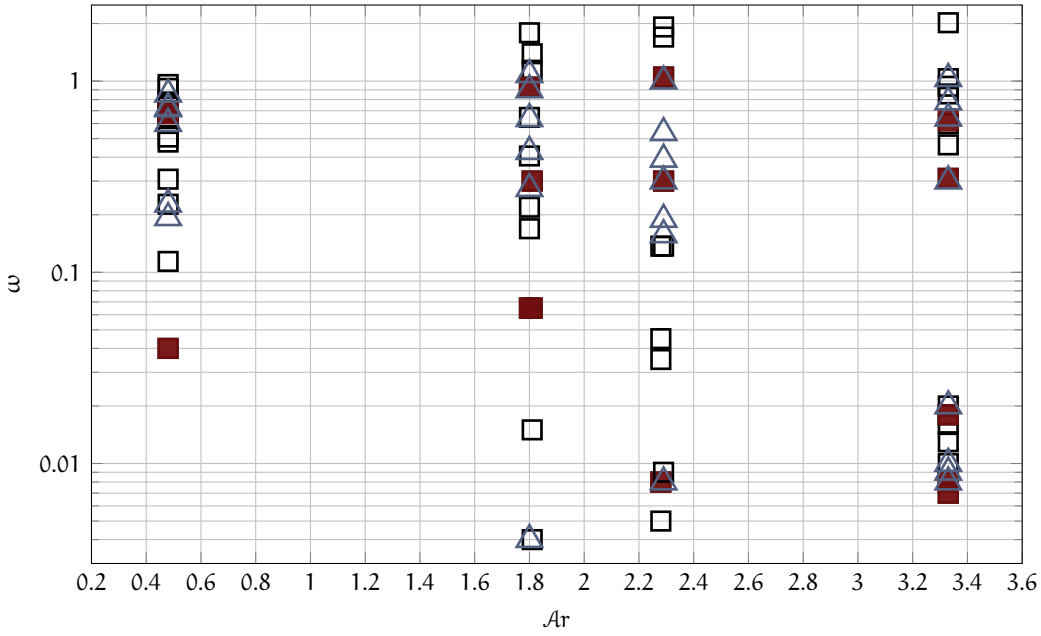

Figure 40: Characteristic frequencies ω of the first six eigenvectors ζ_n and the *TTS* at the outlet as a function of Ar. The squares denote the frequencies determined from the POD eigenvectors, while the modes with eigenvalues $\lambda > 5\%$ are coloured red and the blue triangles represent the frequencies found in the *TTS*.

the three-dimensional and complex nature of the flow in the core region of the forced mean wind.

A further result is the marked temperature fluctuations at the outlet, in particular, at the sensor positions with elevated temperatures. At the position $X = 0.5 \times L$ (fig. 39b) fluctuations with an amplitude of almost 1.0 K are found, although the forced flow determines the heat transport. In addition, time-periodic oscillations of the *TTS* are found. The *PSD* of the temperature signal at $X = 0.5 \times L$ (fig. 39c) reveals several peaks, in particular, within $0.6\,s^{-1} < \omega < 1.1\,s^{-1}$.

5.2.3 *Characteristic frequencies*

The frequency analysis of the temperature signals at the outlet and the POD eigenvectors of the predominant coherent structures brought to light a couple of characteristic frequencies. Figure 40 displays a survey of these frequencies as a function of Ar. On the one hand, the characteristic frequencies of the six eigenvectors with the highest energy eigenvalues (squares) are plotted, where the modes with eigenvalues $\lambda > 5\%$ are coloured red. On the other hand, the characteristic frequencies of the *TTS* at the outlet are depicted (blue triangles).

For $\mathcal{A}r = 3.33$ frequencies within $0.008\,s^{-1} \leqslant \omega \leqslant 0.02\,s^{-1}$ and $0.3\,s^{-1} \leqslant \omega \leqslant 2.0\,s^{-1}$ are determined. The higher frequencies primarily represent periodic features of the forced mean wind (in particular, the angular velocity), excluding $\omega \approx 0.3\,s^{-1}$ and $\omega \approx 0.6\,s^{-1}$. These frequencies are related to the dynamics of thermal convection rolls.

At $\mathcal{A}r \approx 2.3$ and $\mathcal{A}r \approx 1.8$ further frequencies in the intermediate regime of ω are found. However, several of these frequencies are determined from the *PSD* of the eigenvectors, which eigenvalues contains less than 1 % of the total energy. It is difficult to say whether these modes represent flow features or only coherence in terms of statistics. Nevertheless, for the sake of completeness, these frequencies are illustrated. At $\mathcal{A}r = 0.48$ primarily higher frequencies are found.

In all cases of *MC*, frequencies are found in the *TTS* and the eigenvectors which are similar. The correlating frequencies are, in particular, the frequencies which are found in the first two modes eigenvector (red squares) with eigenvalues $\lambda > 5\%$. This frequencies represents the periodic dynamics of the predominant large-scale coherent structures. Due to the reproducibility of these frequencies, the frequencies provide a good measure to examine the concept of spatial scaling for kinematic similitude.

5.3 CONCLUSIONS

Turbulent mixed convective air flow was experimentally studied in a rectangular container with an aspect ratio of $1:1:5$ under high pressure conditions ($P = 11.6$) as a function of $\mathcal{A}r$. In all cases $\mathcal{R}a \approx 2.4 \times 10^8$ is almost constant, while $\mathcal{R}e$ was varied to achieve $\mathcal{A}r \approx 0.5$, $\mathcal{A}r \approx 1.8$, $\mathcal{A}r \approx 2.3$ and $\mathcal{A}r \approx 3.3$. PIV was performed in a vertical cross-section at $X = 0.5 \times L$ and longitudinal cross-section at $Y = 0.5 \times W$ to determine coherent flow patterns and their dynamics. Further, measurements of the temperature at the outlet port were conducted.

In the first paragraph, the time-averaged velocity vector fields in the vertical cross-section at $X = 0.5 \times L$ as a function of $\mathcal{R}e$ were analysed. It was found that at $X = 0.5 \times L$, the forced flow develops an almost rotational symmetric and stationary mean wind with a rotational plane which is congruent to the vertical cross-section, excluding the regions close to the side walls. There the flow is governed by the incoming wall jet. A key feature of the forced mean wind is that it behaves piecewise like a solid body rotation, however, with a different angular velocity in the core region and outer regions.

In the second paragraph, the results of the corresponding mixed convective flow cases were analysed and discussed. In case of the three highest $\mathcal{A}r$ a clear modification of the time averaged velocity fields in the vertical cross-section $X = 0.5 \times L$ was found. Depending on whether rising or falling plumes are predominant in the cross-section a shift of the forced mean wind centre position towards the upper left corner or towards the outlet was observed. For $\mathcal{A}r = 0.48$ the buoyancy forces are too small, in relation to

the inertia forces, to affect the forced mean wind significantly. Furthermore, with the onset of buoyancy flow, the dynamics of the mean wind are modified as well. For the three highest $\mathcal{A}r$ an increase of the velocity fluctuations in the whole measuring plane was found. At $\mathcal{A}r = 0.48$, however, the fluctuations have the same order of magnitude like in the corresponding *FC* case, except for the core region. The increased velocity fluctuations in this region are the result of thermally induced roll structures formed in the core of the forced mean wind.

The POD analysis of the velocity fields in the cross-section $Y = 0.5 \times W$ for $\mathcal{A}r = 2.28$ and $\mathcal{A}r = 3.33$ disclosed a preferred coherent structure, which consists of four counter-rotating *LSC*s longitudinally arranged side by side. In contrast to pure *RBC*, the thermal convection rolls are not fully symmetrically arranged. Due to the additional forced flow, the *LSC*s are stretched and tilted. Moreover, the first mode coherent structure discloses a shifted of the centre position towards the regions of ascending flow. However, the vortex detecting algorithm discloses a rotational symmetry of the *LSC*s. In addition, the POD of the velocity fields for $\mathcal{A}r = 3.33$ uncovers a second mode eigenfunction, which consists of three counter-rotating *LSC*s representing a transitional or metastable state. For $\mathcal{A}r = 1.81$, the predominant coherent structure in the longitudinal cross-section consists of four large-scale roll structures as well, while here a conspicuous modification of the topology by the forced flow was obtained. As a consequence the *LSC*s are not rotational symmetric anymore and strongly deformed. For $\mathcal{A}r = 0.48$ the inertia forces are dominant so that *LSC* with a diameter of H is developed. Nevertheless, in the core region of the forced *LSC*, where the inertia and buoyancy forces have the same order of magnitude, eight counter-rotating smaller roll structures with a diameter of approximate H/2 were found.

Regarding the dynamics of the thermal convection rolls, this study brings to light several interesting effects. In case of $\mathcal{A}r \geqslant 1.81$ flow reveals, sudden breakups and spontaneous re-organisation were detected. Moreover, indications for a torsional oscillation of the thermal convection rolls were found. The frequency analysis of the POD eigenvectors and the *TTS* at the outlet discloses numerous characteristic frequencies, where several frequencies of the *TTS* and the POD eigenvectors are similar. Some of these frequencies could be ascribed to the dynamics of the thermal and forced *LSC*s. The angular velocities of the convection rolls were found in the *PSD* of the time developing coefficient of the coherent structures with the highest energy eigenvalues. In particular, the characteristic frequencies from the first mode eigenvector correspond to the frequencies which were found in the temperature signal at the outlet. As well in case of $\mathcal{A}r = 0.48$, the *PSD* of the eigenvectors and the *TTS* reveal characteristic frequencies. Since the flow is primarily governed by forced convective flow, the frequencies are assigned to the dynamics of the forced mean wind.

However, due to the long-time dynamics of the predominant coherent structures, the results reveal only a period in the dynamics of the *LSC*. In particular, for higher

Ar, measurements have to be performed over a longer time scale in order to uncover the full dynamics of the large-scale flow pattern. Nevertheless, it is possible to extract the prominent flow features from these relative short measurement periods by POD.

For the examination of the concept of spatial scaling, the analysis brings out two criteria. On the one hand, the large-scale coherent structures and on the other hand, the characteristic frequencies. Both will be used to examine the similitude of the flow in the large container and the small container.

6

SPATIAL SCALING OF MIXED CONVECTIVE AIR FLOWS

With the objective to examine the concept of spatial scaling (sec. 2.4.2), mixed convective air flow was studied in two containers. Both enclosures have the same geometry and the spatial dimensions are scaled by a factor five. The measurements were performed in the large container at atmospheric pressure and in the small container at high pressure conditions $P \approx 11.6\,\mathrm{bar}$. For the small container, the pressure and inflow velocity were adjusted in accordance with the concept of scaling to obtain the same characteristic numbers for both setups. Based on the characteristic flow features: coherent structures, their dynamics and the heat transfer, mixed convective air flow is examined for similitude.

6.1 SIMILITUDE OF LARGE-SCALE COHERENT STRUCTURES

To examine the similarity of the predominant coherent structures at $Ar \approx 3.3$, the POD eigenfunctions $\overline{\Psi}_1$ with the highest eigenvalue (fig. 41) are compared. Both eigenfunctions were calculated from a set of 4800 instantaneous velocity fields recorded at a frequency of $2/3\,\mathrm{Hz}$ by PIV in the longitudinal cross-section $Y = 0.5 \times W$. The characteristic numbers and parameters for the measurements in the large container and the small container are listed in table 6. Due to the restricted measuring plane in the large container the coherent structure reveals just one *LSC* completely (fig. 41, bottom). However, the corresponding temperature measurements [110, 124] suggest that a stable-state of four counter-rotating *LSC*s is developed in the longitudinal cross-section.

Both eigenfunctions reveal *LSC*s with a diameter of approximate H, however, with reverse rotational directions. Apart from the differing preferred rotational directions, the topology of the coherent structures is nearly identical. Further, both structures reveal an apparent shift of the *LSC* centre position towards the region of ascending air. Due to the findings in chapter 5 we know that this shift is the result of the tilted orientation of the *LSC*s with respect to the measurement plane.

In addition, the coherent structures of the velocity components Ψ^1_u (fig. 42a) and Ψ^1_w (fig. 42b) are examined for similitude. Both coherent structures reveal a similar topology, while in the region of rising hot air smaller differences are disclosed. In relation to the small container, the region of rising air in the large container is broadened. This broadening could result from a slightly varying orientation of the laser light-sheet or a different orientation of the thermal convection roll.

		$P \approx 1$ bar	$P = 11.553(3)$ bar
H	[m]	$0.50(1)$	$0.100(2)$
Ar		$Ar = 3.31(20)$	$Ar = 3.33(2)$
Re		$1.00(2) \times 10^4$	$1.01(1) \times 10^4$
Ra		$2.40(18) \times 10^8$	$2.39(7) \times 10^8$
Pr		$0.72(1)$	$0.707(2)$
U	[m/s]	$0.32(1)$	$0.143(1)$
$\Delta\Theta$	[K]	$21.15(22)$	$21.25(17)$
$\overline{\Theta}_b$	[K]	$317.68(21)$	$316.68(17)$
$\overline{\Theta}_t$	[K]	$296.53(24)$	$295.43(4)$
$\overline{\Theta}_{in}$	[K]	$295.87(9)$	$295.25(5)$
$\overline{\Theta}$	[K]	$307.11(22)$	$306.20(9)$

Table 6: List of measurement parameters, fluid properties and characteristic numbers for PIV in the longitudinal cross-section at $Y = 0.5 \times W$ at $Ar \approx 3.3$.

In addition, line cuts of the normalised eigenfunction Ψ^1_w are extracted at the middle position of the vertical flow. Figure 43a depicts the Ψ^1_w-profiles at the position of ascending air as a function of Z. Due to the different rotational directions of the *LSC*s, the line cuts are placed at $X = 0.78 \times L$ in the large container and at $X = 0.50 \times L$ in the small container. For the ascending flow, the curves of the Ψ^1_w-profiles are nearly congruent. The profiles slightly deviate near to the vertex, while both have the same position of maximum. The line cuts at the middle position of descending air (fig. 43b) are similar as well. Here, the profiles are congruent in the regions close to the bottom, while the profile differs with increasing height. At the ceiling, the profiles are similar again.

Apart from the good correlation of the predominant coherent structure, differences are disclosed. For the measurements in the small container, a second eigenfunction was identified, which reveals three *LSC*s (fig. 19a). In the large container just one coherent pattern is found, which consists of large-scale roll structures. This is additionally identified by the eigenvalue distribution (fig. 44). The eigenvalue of the first mode contains 48 % of the total energy in the small container, while the eigenvalue in the large container contains 73 % of the total energy. In particular, the high eigenvalue $\lambda_1 = 73$ % relative to the second mode eigenvalue $\lambda_2 = 0.6$ % shows that Ψ_1 represents the sole eigenfunction in the large container, which consists of large-scale structures. Moreover, this relative small second eigenvalue additionally indicates that the coherent structure Ψ_1 seems to be a long-time steady-state.

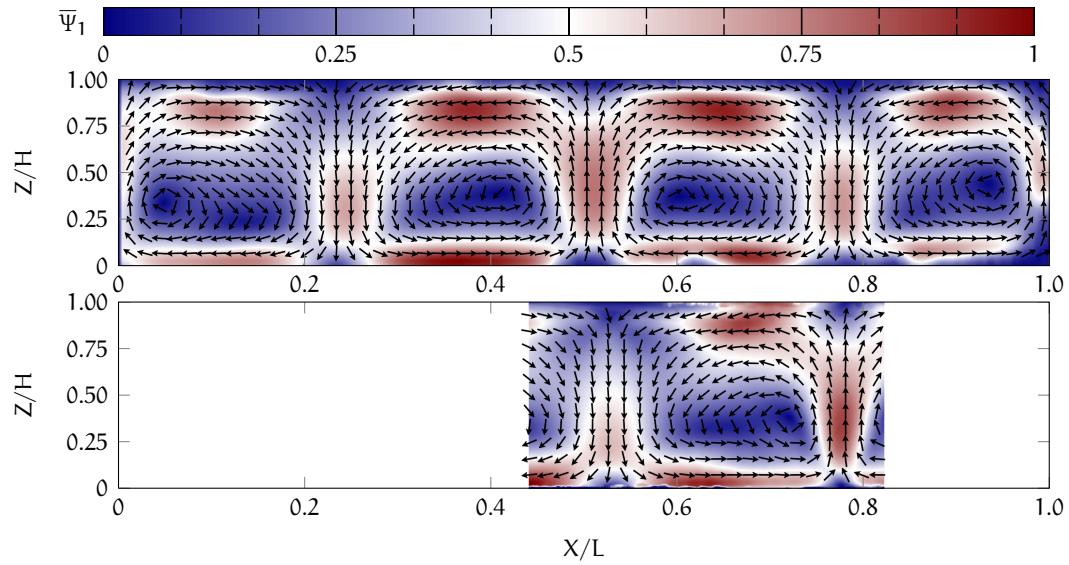

Figure 41: POD eigenfunctions $\overline{\Psi}_1$ at $\mathcal{A}r = 3.31$: large container (bottom) and small container (top). The vectors are composed by the eigenfunctions Ψ^1_u and Ψ^1_w. Further, the vectors are scaled to unity and the magnitude is normalised.

One reason for the absence of additional coherent flow states and the steady-state of the predominant structure in the large container could be that the measurement was randomly performed within a period where the flow was featured by one coherent structure only, without any flow reversals or other erratic flow features. First results of temperature measurements in the large container at almost similar characteristic numbers, with measuring times over several days substantiate this assumption. The study reveals flow reversals and sudden break-ups of the *LSC* also in the large container [109]. However, there is another argument for the steady-state nature of the flow in the large container. In the small container the inflow, the ambient and the mean temperature of the ceiling differ just a few tenths of Kelvin, while the temperature difference between the inflow and ambient air in the large container amounts more than one Kelvin. The difference between inflow and ambient temperature leads to an enhanced heat flux through the lateral walls. As a result, an additional vertical thermal boundary layer is developed at the lateral walls, which may force a preferred vertical flow direction and thus, a prevailing orientation of the thermal convection rolls.

Taken together, at $\mathcal{A}r \approx 3.3$ a good correlation of the predominant coherent structure in the longitudinal measuring plane is found. In both cases, the first mode eigenfunction reveals *LSC*s with a diameter of H. Although the *LSC*s have a preferred reverse rotational direction the topology of the *LSC*s is similar. An examination of the line cuts for the regions with preferred rising air and falling air discloses an almost congruent

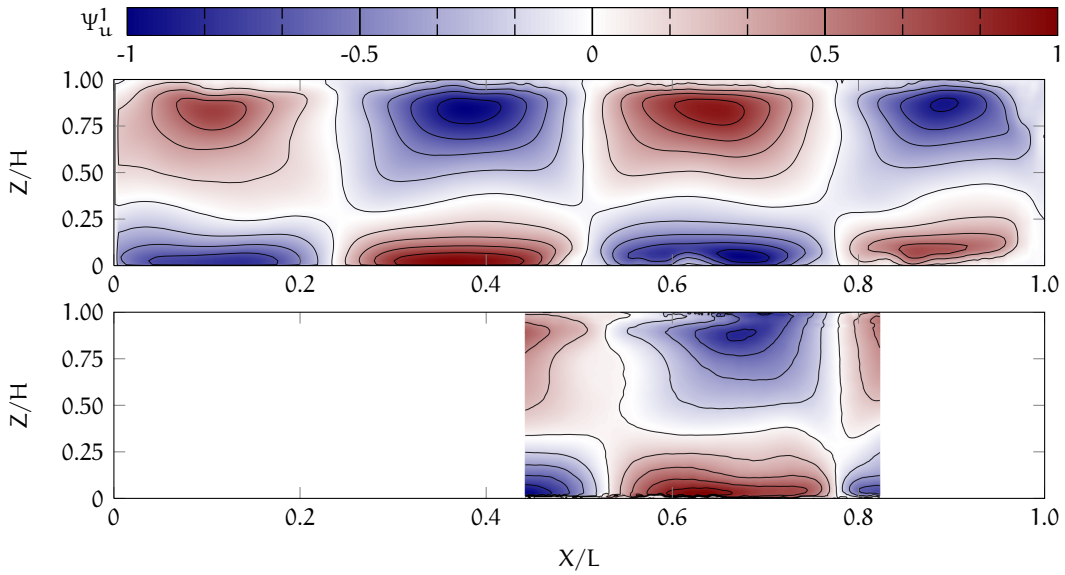

(a)

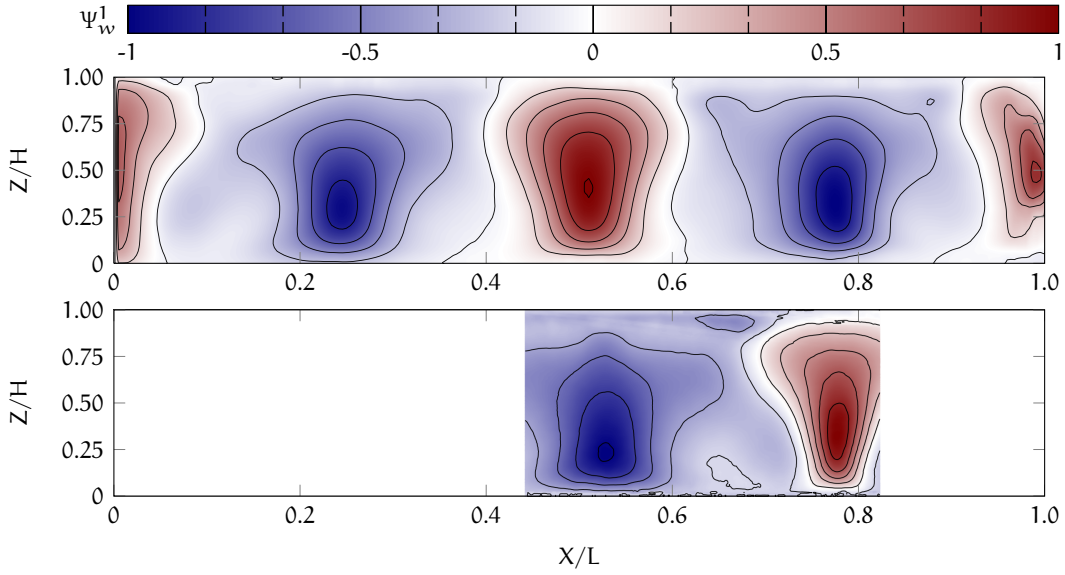

(b)

Figure 42: First mode eigenfunctions of the in-plane velocity components at $Ar \approx 3.3$: (42a) Ψ_u^1 and (42b) Ψ_w^1.

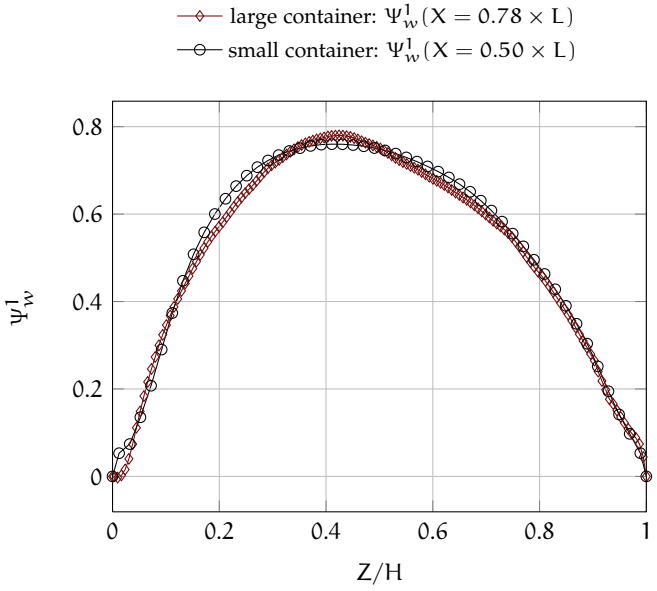

(a)

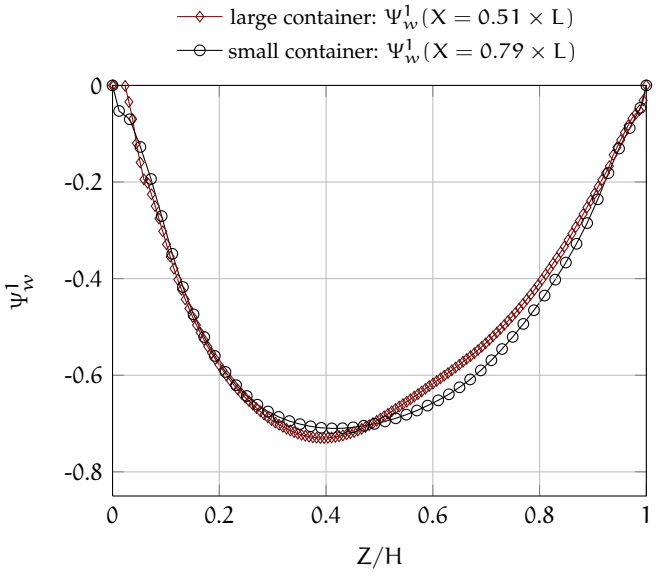

(b)

Figure 43: Profiles of Ψ_w^1 at the positions of ascending and descending air for $Ar \approx 3.3$: (43a) profiles at the position of ascending air. (43b) profiles at the position of descending air.

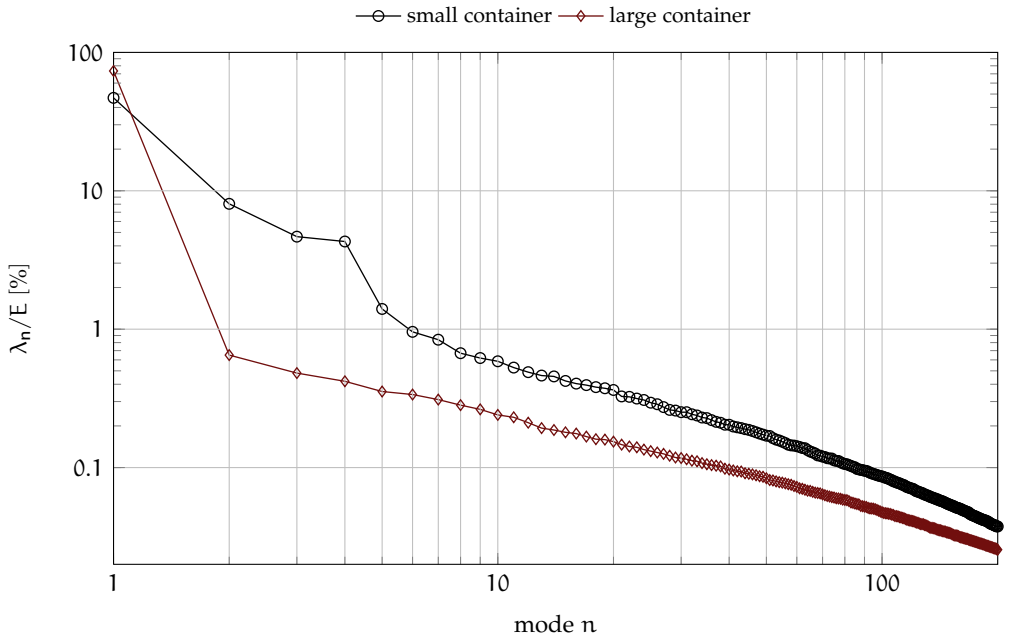

Figure 44: Eigenvalue distribution as a function of the mode number n at $Ar = 3.3$ in the longitudinal cross-section at ambient and high pressure conditions. The eigenvalues are normalised in respect to the cumulative sum E of all eigenvalues.

velocity profile. Nevertheless, smaller differences are found regarding the topology and the magnitude of the first mode coherent structure Ψ_1. Furthermore, in the large container one predominant pattern is found, while an additional coherent structure is obtained in the small container.

At $Ar \approx 2.25$ the eigenfunctions of the first mode in the small container (fig. 45a) and large container (fig. 45c) have a completely different structure, although Ar just differs by 0.05 (tab. 7). The only similarity is that both coherent structures consist of four roll structures, however, with a total different topology. The predominant coherent structure in the small container at $Ar = 2.28$, shows four side by side counter-rotating *LSC*s, indicating that the flow is primarily governed by buoyancy forces. Moreover, the coherent structure correlates with the first mode eigenfunction in the large container at $Ar = 3.31$. On the contrary, the coherent structure of the first mode at $Ar = 2.23$ in the large container (fig. 45c) discloses a clear impact of the forced flow on the thermal convection rolls. Close to the bottom plate, in the region of ascending air ($X \approx 0.5 \times L$), vortexes are developed as the result of the shear stresses between the forced and buoyancy induced flow. A comparable topology is obtained in the small container at $Ar = 1.81$ (fig. 45c). Even when the topologies are not fully congruent,

		$P \approx 1$ bar	$P = 11.553(3)$ bar	$P = 11.553(2)$ bar
H	[m]	0.50(1)	0.100(2)	0.100(2)
$\mathcal{A}r$		2.23(14)	2.28(2)	1.81(1)
$\mathcal{R}e$		$1.22(2) \times 10^4$	$1.22(2) \times 10^4$	$1.38(2) \times 10^4$
$\mathcal{R}a$		$2.40(18) \times 10^8$	$2.41(7) \times 10^8$	$2.39(7) \times 10^8$
$\mathcal{P}r$		0.72(1)	0.707(1)	0.707(1)
U	[m/s]	0.39(2)	0.32(1)	0.200(1)
$\Delta\Theta$	[K]	21.22(33)	21.25(17)	21.17(16)
$\overline{\Theta}_b$	[K]	318.18(25)	316.68(17)	316.79(16)
$\overline{\Theta}_t$	[K]	296.96(23)	295.43(4)	295.62(3)
$\overline{\Theta}_{in}$	[K]	294.82(6)	295.25(5)	295.54(7)
$\overline{\Theta}$	[K]	307.57(25)	306.06(17)	306.21(16)

Table 7: List of measurement parameters and characteristic numbers of PIV in the longitudinal cross-section at $Y = 0.5 \times W$ for $\mathcal{A}r = 2.23$, $\mathcal{A}r = 2.28$ and $\mathcal{A}r = 1.81$.

the flow pattern reveals similar flow features, like the two vortexes close to the bottom plate at $X \approx 0.5 \times L$.

A closer inspection of the coherent structures in the large container at $\mathcal{A}r = 2.23$ and the small container at $\mathcal{A}r = 1.81$ discloses additional similarities. In particular, the coherent structure of the w-velocity component Ψ^1_w reveals a similar topology (fig. 46). In both cases, the eigenfunction Ψ^1_w depicts a mushroom-shaped large-scale structure in the region of ascending air; however, the magnitude of Ψ^1_w significantly differs. The lower magnitude of Ψ^1_w could result from an already enhanced impact of the forced flow. As a result, a different orientation of the *LSC* is obtained and thus, the regions of rising air differ for both containers. The topology of the eigenfunction Ψ^1_w in the region of descending cold air is almost similar as well. In both cases, a coherent structure with a nearly circular topology is found at $0.63 \times L \leqslant X \leqslant 0.83$. However, the coherent structure Ψ^1_u (fig. 46a) reveals rudimentary analogies only.

In conclusion, the eigenfunctions at $\mathcal{A}r \approx 2.25$ disclose significant different coherent structures, although the characteristic numbers $\mathcal{R}a$, $\mathcal{R}e$ and $\mathcal{P}r$ are almost the same. Instead, comparable coherent structures are found at $\mathcal{A}r = 1.81$ (small container) and $\mathcal{A}r = 2.23$ (large container) in the longitudinal cross-section. That brings us to the question if the concept of spatial scaling is incorrect or the Boussinesq approximation fails at high pressure and the scaling at mixed convective air flows needs to consider

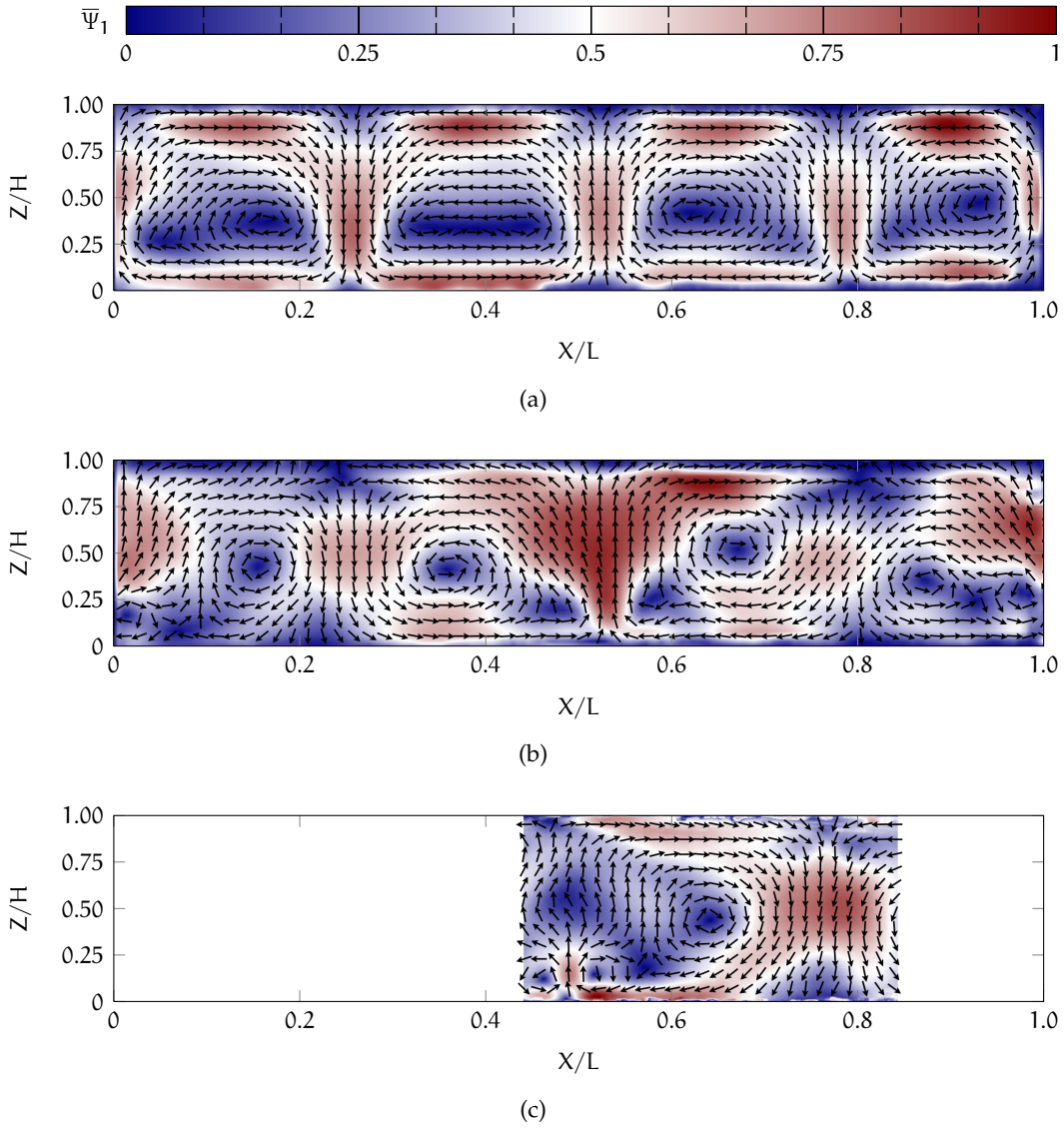

Figure 45: First mode coherent structure $\overline{\Psi}_1$ in the longitudinal cross-section at $\mathcal{A}r = 2.28$ and $\mathcal{A}r = 1.81$ for the small container and $\mathcal{A}r = 2.23$ for the large container. The vectors are composed by the eigenfunctions Ψ^1_u and Ψ^1_w and the magnitude is colour-coded. The vectors are scaled to unity and the magnitude is normalised.

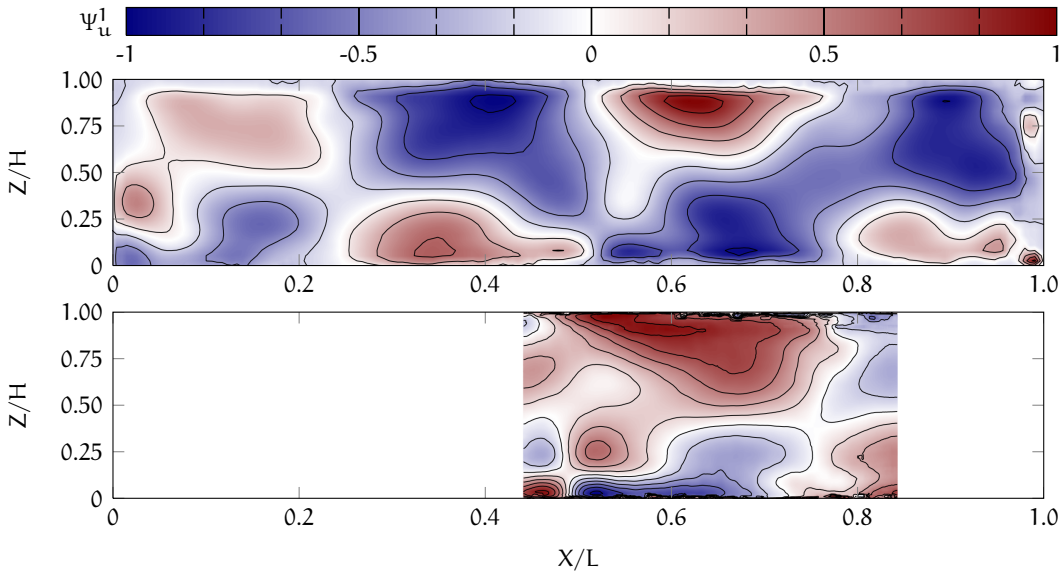

(a)

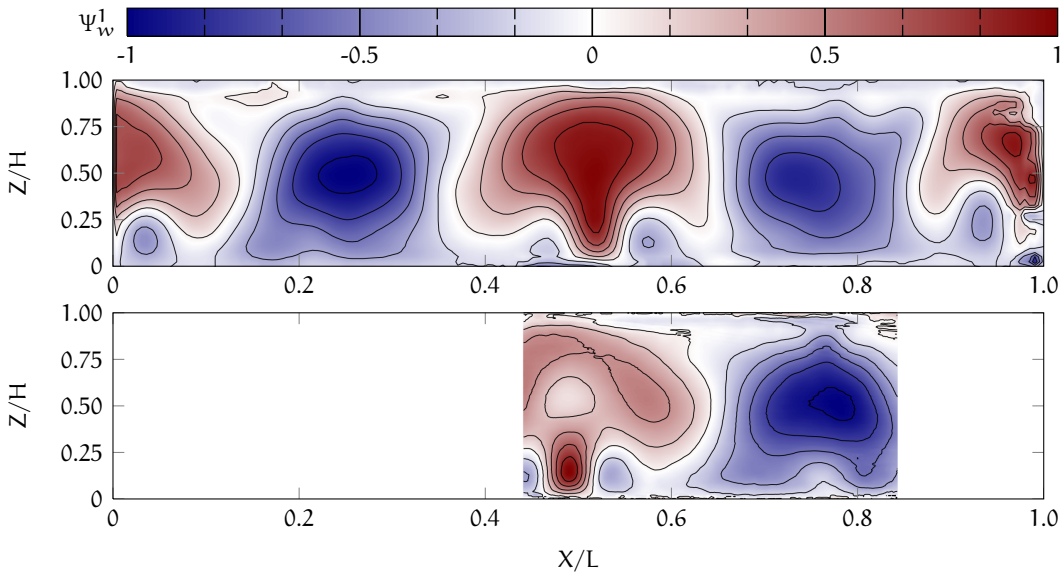

(b)

Figure 46: First mode coherent strcutures Ψ_u^1 (46a) and Ψ_w^1 (46b) at $\mathcal{A}r = 2.23$ (large container) and $\mathcal{A}r = 1.81$ (small container).

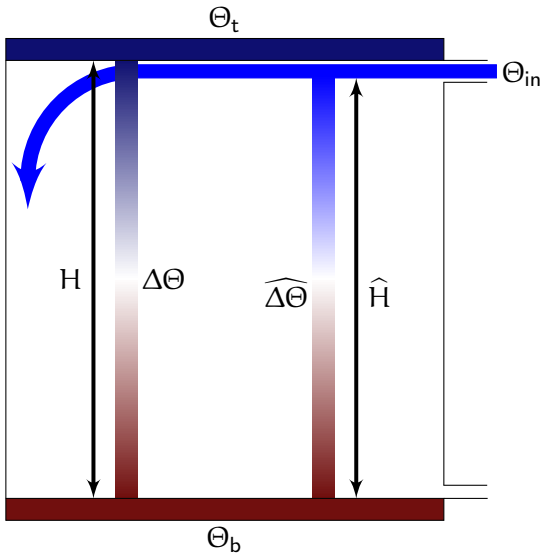

Figure 47: Schematic sketch of the characteritsic height and characteristic temperature difference. H denotes the characteristic height and $\Delta\Theta$ the characteristic temperature difference with respect to the heating and cooling plates. $\widehat{H}$ and $\widehat{\Delta\Theta}$ represents the corresponding characteristic parameters between the heating plate and the bottom edge of the incoming wall jet.

additional non-dimensional parameters. The criteria for the Boussinesq approximation (eq. 2.1) at a pressure of $P \approx 11.6$ are

$$\begin{aligned} g\rho\beta L &\approx 0.042 \\ \tfrac{g\alpha L}{c_P} &\approx 2.6 \cdot 10^{-5} \\ \tfrac{g\alpha L\Theta}{c_P\Delta\Theta} &\approx 3.7 \cdot 10^{-4}. \end{aligned}$$

All values are much smaller than one. Hence, the criteria for the applicability of the Boussinesq approximation are complied at high pressure conditions. Consequently, I assume that the differences are caused by differences in the boundary conditions.

For the large container, the spatial temperature fluctuation at the ceiling is distinctively higher than in the small container (tab. 7). For the small container, the spatial standard deviation is $\sigma_t = 0.04\,K$, while $\sigma_t = 0.25\,K$ in the large container. Although σ_t is higher by a factor six, it is rather too small to impact the flow, leading to such strong differences in the flow structures, in my opinion. Further, the inflow temperature in the large container is nearly $2\,K$ lower than the temperature of the ceiling, whereas the mean temperature of the ceiling and the inflow differs only by a few tenths of Kelvin in the small container.

		$P = 1\,\text{bar}$	$P = 11.553(3)\,\text{bar}$
H	[m]	0.50(1)	0.100(2)
$\mathcal{A}r$		$\mathcal{A}r = 0.53(4)$	$\mathcal{A}r = 0.48(2)$
$\mathcal{R}e$		$2.51(4) \times 10^4$	$2.70(3) \times 10^4$
$\mathcal{R}a$		$2.38(12) \times 10^8$	$2.39(7) \times 10^8$
$\mathcal{P}r$		0.72(1)	0.707(1)
U	[m/s]	0.82(5)	0.377(3)
$\Delta\Theta$	[K]	21.39(38)	21.19(18)
$\overline{\Theta}_b$	[K]	318.98(30)	316.53(17)
$\overline{\Theta}_t$	[K]	297.59(20)	295.35(5)
$\overline{\Theta}_{in}$	[K]	295.22(1)	295.35(1)
$\overline{\Theta}$	[K]	308.28(38)	306.20(18)

Table 8: Measurement parameters and characteristic numbers of PIV in the longitudinal cross-section at $Y = 0.5 \times W$ in the small container in case of $\mathcal{A}r = 0.48$ and in the large container at $\mathcal{A}r = 0.53$.

This clearly lower inflow temperature leads to two conflicting effects, which finally result in weakened buoyancy forces. On the one hand, an increased characteristic temperature difference $\widehat{\Delta\Theta} = \overline{\Theta}_b - \overline{\Theta}_{in} \approx 23.3\ \text{K}$ is developed between the incoming wall jet and the bottom plate (fig. 47), which results in higher buoyancy forces. On the other hand, since the inflow temperature is lower than the temperature of the ceiling, a reduced characteristic height $\widehat{H}$ is presumed between the bottom edge of the incoming wall jet and the bottom plate (fig. 47). Based on an averaged height of the incoming wall jet at the ceiling of approximately $2 \times H_{in}$ (estimated from figure 12 and 16) a reduced characteristic height $\widehat{H} = H - H_{in} = 0.45\,\text{m}$ is obtained. As a consequence, the decreased characteristic height leads to lower buoyancy forces. A re-evaluation of $\mathcal{A}r$ with $\widehat{H}$ and $\widehat{\Delta\Theta}$ as relevant characteristic parameters, results in $\widehat{\mathcal{A}r} \approx 1.78$. This new Archimedes number $\widehat{\mathcal{A}r}$ differs significantly from the Archimedes number $\mathcal{A}r$ and offers an explanation why the coherent structures in the large container at $\mathcal{A}r = 2.23$ are in comparable to those in the small container at $\mathcal{A}r = 1.81$.

Besides the reduced Archimedes number, additional consequences are caused by the lower inflow temperature. For instance, the lower temperature of the incoming air leads to different thermal boundary layers in the small container and large container (particularly at the ceiling), which can further affect the plumes' emission and thus, the topology and dynamics of the *LSC*s. Moreover, the colder air results in a reduced mean system temperature in the large container and a lower temperature difference at the lateral walls between the ambiance and the cavity. As a consequence, a decreased

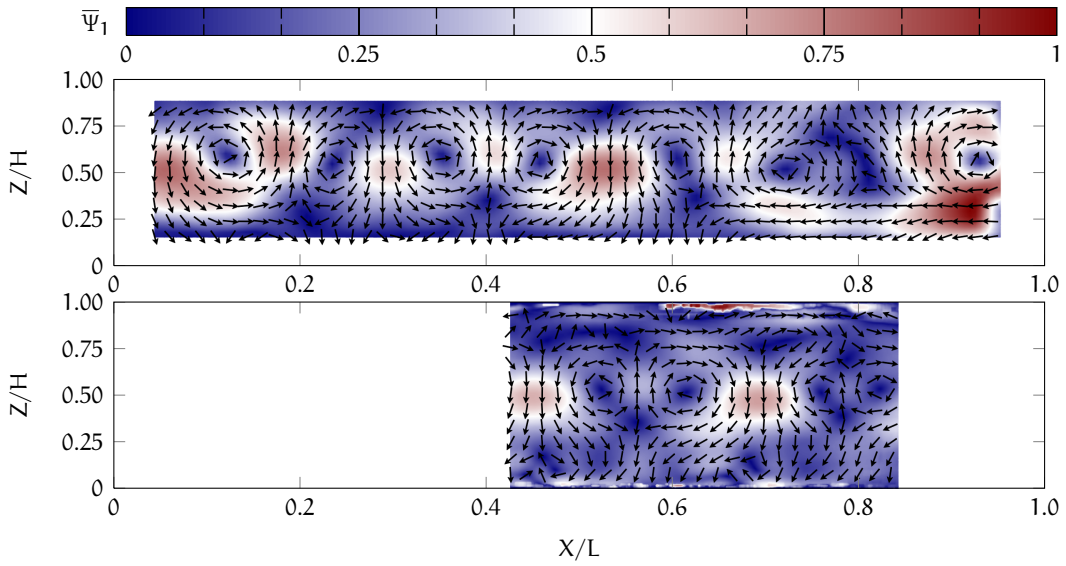

Figure 48: Coherent structure $\overline{\Psi}_1$ in the longitudinal cross-section: small container at $\mathcal{A}r = 0.48$ (top) and in the large container at $\mathcal{A}r = 0.53$ (bottom). The vectors are composed by the eigenfunctions Ψ^1_u and Ψ^1_w and its magnitude is colour-coded. Further, the vectors are scaled to unity and the magnitude is normalised.

heat flux per area unit $\dot{q}$ is obtained. For $\mathcal{A}r \approx 2.25$ the heat flux per area unit amounts $\dot{q} \approx 5.0\,W/m^2$ in the large container and $\dot{q} \approx 5.9\,W/m^2$ in the small container. The mean system temperature is estimated by $(\overline{\Theta}_t + \overline{\Theta}_b + \overline{\Theta}_{in} + \overline{\Theta}_{out})/4$ and the thermal heat transfer coefficient of the lateral walls (sec. 3.1.2) is $h \approx 0.9\,W/m^2\,K$ for both containers.

Another issue, which can lead to a different heat transfer in the containers is the usage of non-similar tracer particles for PIV at atmospheric pressure and high pressure conditions. However, due to the volume ratio of air to tracer particle of 10^{-6}, a significant effect on the transport of heat seems to be negligible.

Taken together, in the intermediate $\mathcal{A}r$-regime, where inertia and buoyancy forces have the same order of magnitude, the flow responses sensitively to changes of the boundary conditions or measurement parameters. As a consequence, it is of utmost importance to provide similar boundary conditions in the full-scale and small-scale configuration to obtain similitude regarding the formation of coherent structures.

At $\mathcal{A}r \approx 0.5$, the first mode eigenfunction, calculated from the measurements in the small container, reveals a coherent structure, which consists of eight counter-rotating rolls (fig. 48, top). The roll structures have a diameter of approximately $H/2$. Due to the restricted measurement plane in the large container the corresponding coherent structure of the first mode (fig. 48, bottom) depicts four rolls only. However, since the rolls have a diameter of approximately $H/2$, it is reasonable to assume that in the

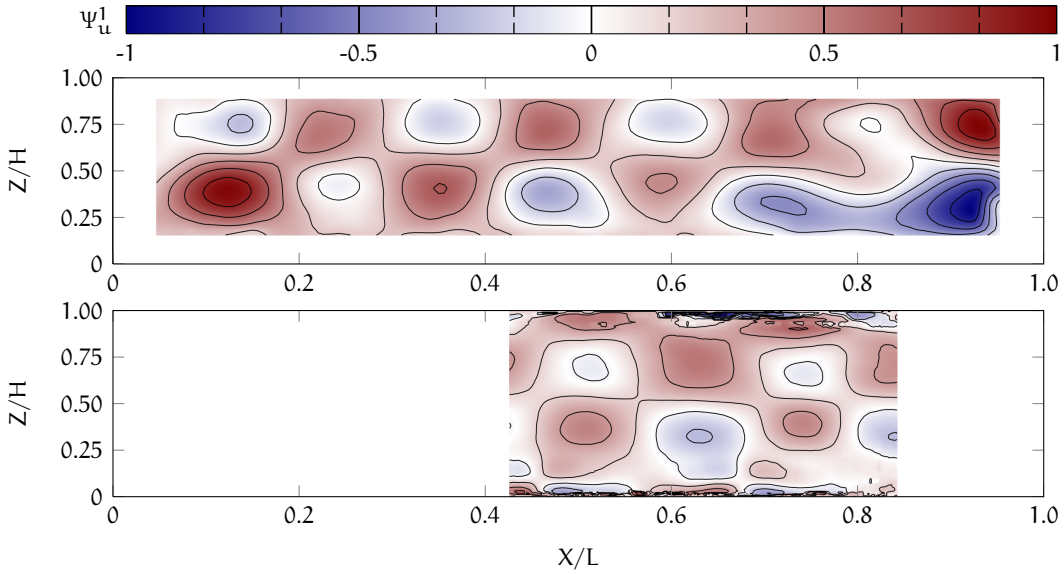

(a)

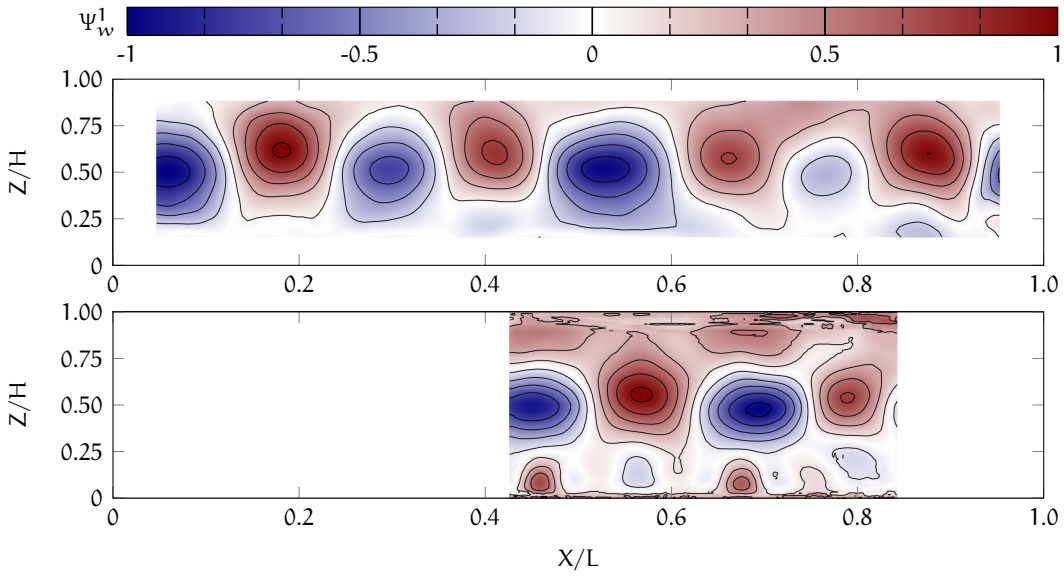

(b)

Figure 49: Coherent structures Ψ_u^1 and Ψ_w^1 at $Ar \approx 0.5$: (49a) Ψ_u^1 small container (top) and large container (bottom) and (49b) Ψ_w^1 small container (top) and large container (bottom).

large container eight counter-rotating *LSC*s are emerged as well. Moreover, in both containers, the roll structures are located in the core region of the forced mean wind.

Nevertheless, in the large container for $\mathcal{A}r = 0.53$ a conspicuous difference of 2.37 K is found between the inflow temperature and the temperature of the ceiling. Based on the same arguments given before, a lower Archimedes number $\widehat{\mathcal{A}r} = 0.43$ is obtained. However, the re-evaluated $\widehat{\mathcal{A}r}$ for the large container is still similar to $\mathcal{A}r$ of the small container. Hence, a direct comparison of the results in the small container and the large container is possible.

A closer inspection of the eigenfunctions calculated from the in-plane velocity components Ψ^1_u (fig. 49a) and Ψ^1_w (fig. 49b) discloses similarities. The topology of the Ψ^1_u (fig. 49a) depicts alternating regions of opposing horizontal flow direction, excluding at the right side of the small container. If the asymmetric structure on the right side represents a flow feature or results from augmented reflections from the laser light is not clear to say. However, due to the high symmetry of the pattern on the left side, it seems reasonable to conclude that the asymmetric structure on the right side is the result of laser light reflections.

For Ψ^1_w (fig. 49b) alternating regions of ascending and descending flow, located in the core region of the forced mean wind, are disclosed for the small and the large container, however, with reversed rotational direction. All in all, it can be stated the predominant coherent structures at $\mathcal{A}r \approx 0.45$ are almost similar. Of course, the topology of structures is not congruent. However, the key features are similar.

6.2 KINEMATIC SIMILITUDE

Due to the finding, that the characteristic length and temperature in the large container have to be adjusted in order to obtain comparable Archimedes numbers, in the following discussion the re-evaluated Archimedes numbers $\widehat{\mathcal{A}r}$ are used.

The frequency analysis of the first mode eigenvectors in section 5.2 reveals time-periodic dynamics of the predominant flow structure at $\mathcal{A}r = 3.33$. In case of the first mode, which consists of four counter-rotating *LSC*s placed side by side in longitudinal direction, two predominant characteristic frequencies $\omega \approx 0.008\,\mathrm{s}^{-1}$ and $\omega \approx 0.62\,\mathrm{s}^{-1}$ are found. The higher frequency is similar to the mean angular velocity of the thermal convection rolls, while the very low frequency seems to be the result of a torsional movement of the *LSC*s. A comparison of the eigenvector ζ_1 for the coherent structures in the longitudinal cross-section (fig. 50) discloses the same very low frequency $\omega = 0.008\,\mathrm{Hz}$ in the small and in the large container. However, because the second mode represents different coherent structures respectively, the *PSD* of the second mode eigenvector (fig. 50d and 50b) reveals no similar characteristic frequencies. In case of the small container, the second mode represents a coherent flow state which consists of three *LSC*s with an eigenvalue of 8.0 % of the total energy. The

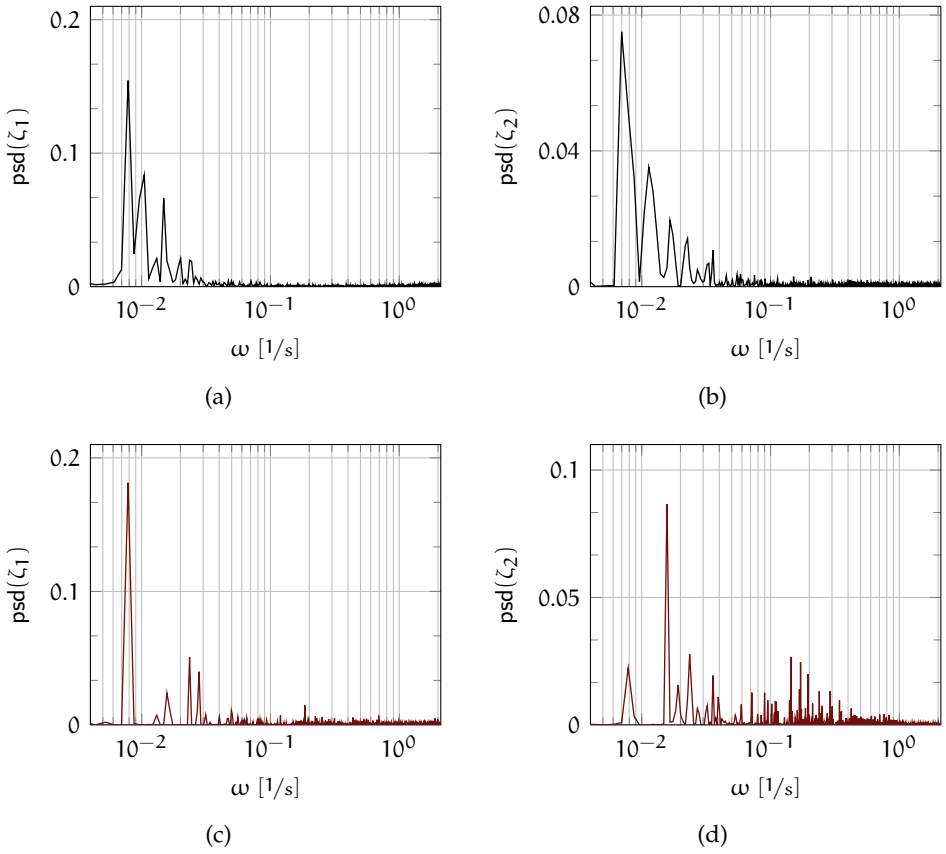

Figure 50: Characteristic frequencies of the first two POD modes in the longitudinal cross-section. (50a) and (50b) *PSD* of the eigenvectors ζ_1 and ζ_2 in the small container at $\mathcal{A}r = 3.33$. (50c) and (50d) *PSD* of the eigenvectors ζ_1 and ζ_2 in the large container at $\mathcal{A}r = 3.31$.

corresponding mode in the large container possesses 0.7 % of the total energy and seems to represent small-scale fluctuations.

The figures 51a and 51c depict the *PSD* of the first mode eigenvectors (vertical cross-section) with respect to the region of preferred ascending air at $X = 0.5 \times L$ in the small container and $X = 0.75 \times L$ in the large container. The *PSD* of ζ_1 reveals a very low frequency of $\omega \approx 0.008\,s^{-1}$ for both containers. The eigenvalue of the first mode is $\lambda_1 = 73$ % in case of the small container and $\lambda_1 = 80$ % for the large container. Further, in the large container the *PSD* of ζ_4 reveals a characteristic frequency of $\omega \approx 0.29\,s^{-1}$ (fig. 51d). This frequency seems to be related to the angular velocity $\omega \approx 0.28\,s^{-1}$ of the thermally induced *LSC*s. The angular velocity of the thermal

convection roll in the large container was calculated from the time-averaged velocity vector field.

Basically, the angular velocity of the thermal convection rolls is a function of the buoyancy velocity $U_B \sim \sqrt{\Delta\Theta g \alpha H}$ and the radius. Hence, the following relation

$$\frac{\omega^{SC}}{\omega^{LC}} = \frac{H^{LC} U_B^{SC}}{H^{SC} U_B^{LC}} \tag{6.1}$$

is obtained. Moreover, within the present measurement range the parameters $\Delta\Theta$, g and α are similar in both containers. Consequently, the angular velocity should scale with

$$\frac{\omega^{SC}}{\omega^{LC}} = \frac{H^{LC}\sqrt{H^{SC}}}{H^{C}\sqrt{H^{LC}}} = \sqrt{s_H}. \tag{6.2}$$

The ratio of the characteristic frequencies, which are releated to the angular velocity is

$$\frac{\omega^{SC}}{\sqrt{s_H}\,\omega^{LC}} = 0.98 \approx 1.$$

On the one hand, this finding substantiates that these characteristic frequencies represent the angular velocity of the thermal *LSC*s. On the other hand, the result shows that the angular velocity of the thermal convection rolls scales in accordence with the concept of spatial scaling.

Nevertheless, an open question is why the same very low characteristic frequencies were found in both containers? In section 5.2.1 these very low frequencies were presumed to be the result of a torsional oscillation of the thermal convection rolls. Suppose that the frequencies are the result of a time-periodic torsional movement of the *LSC*s, the dynamics are certainly determined by the aspect ratio of the container and the interaction of the incoming wall jet and the advective flow of the thermal convection rolls. Consequently, the torsional movement depends on the ratio of buoyancy to inertia forces. Because the buoyancy forces and the inertia forces are almost similar in both containers, the same low-frequency dynamics are obtained. Of course, this is just a very simple explanation. In the end, the present data does not allow a clear statement why these very low frequencies are similar in both containers. Furthermore, studies or publications, which examined the torsional movement in mixed convection for a comparable configuration do not exist as far as I know. Hence, to clarify the origin and the scaling of this very-low frequency additional studies are necessary.

In addition, the analysis of the eigenvectors and the *TTS* reveal further characteristic frequencies, which are associated to the angular velocity of the forced mean wind (sec. 5.2.1 and 5.2.2). Because the forced mean wind is primarily determined by the incoming wall jet, the scaling of the angular velocity is almost proportional to the

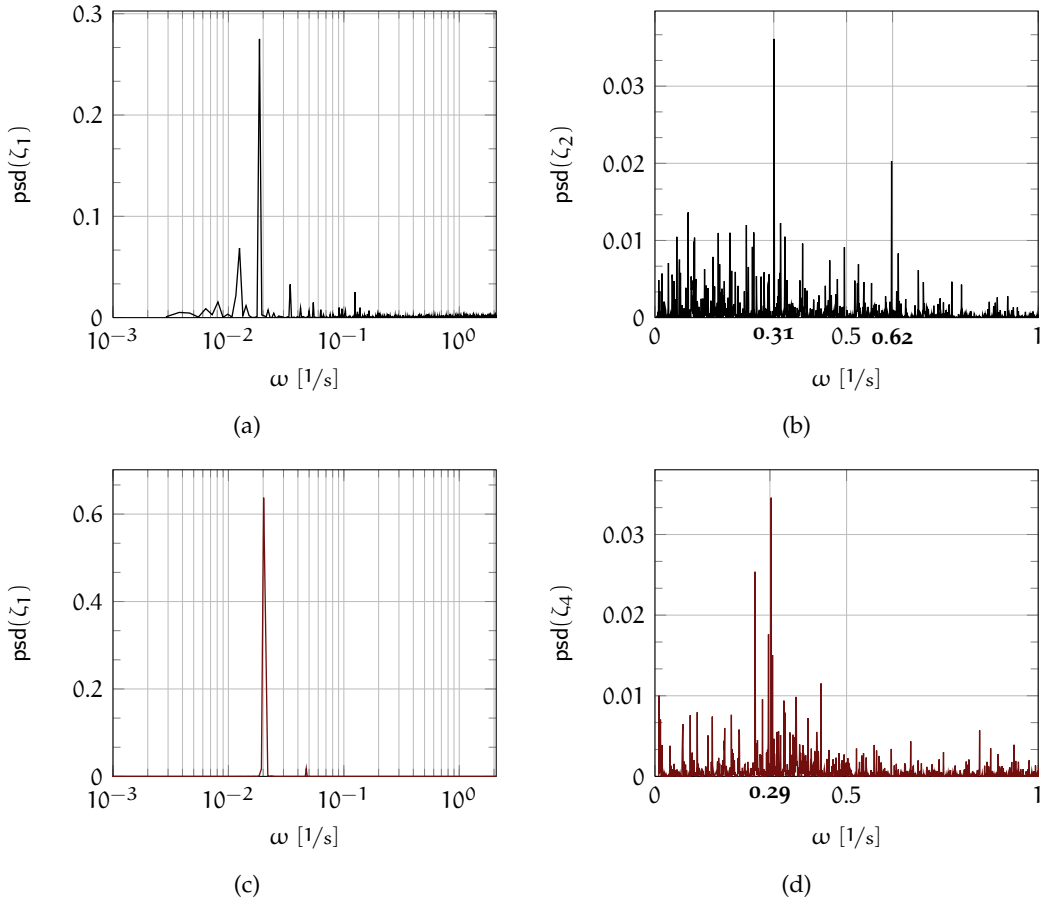

Figure 51: Characteristic frequencies of the first two POD modes eigenvectors in the vertical cross-section. (51a) and (51b) *PSD* of the eigenvectors ζ_1 and ζ_2 in the small container at $Ar = 3.33$. (51c) and (51d) *PSD* of the eigenvectors ζ_1 and ζ_4 in the large container at $Ar = 3.30$.

scaling factor of the inflow velocity $s_U = \sqrt{s_H}$. Moreover, the angular velocity of the forced mean wind is a function of U/R and thus, the angular velocity has to scale with $s_\omega^{FC} = \sqrt{s_H}/s_H$. Accordingly, with the objective to prove the kinematic similitude of the forced mean wind, the following relation is defined

$$\widehat{\omega} = \frac{\omega}{S \cdot \omega_{LSC}} \approx 1, \tag{6.3}$$

where ω_{LSC} denotes the corresponding mean angular velocity of the forced mean wind at *FC*, ω the characteristic frequencies and $S = 1/\sqrt{5}$ the scaling factor for the angular velocity in the large container. As a result, characteristic frequencies, which are related to the rotational dynamics of the forced mean wind, will be close to one.

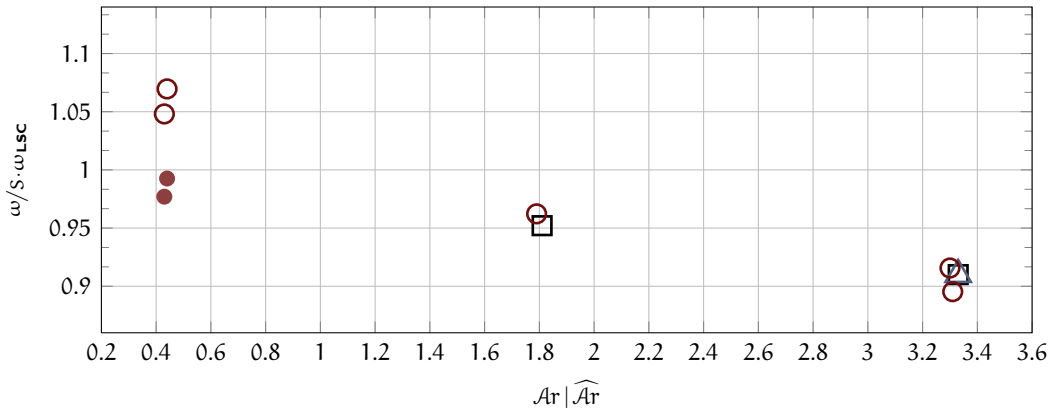

Figure 52: Normalised characteristic frequencies $\omega/s\cdot\omega_{LSC}$ as a function of Ar for both containers. Black squares denote the frequencies determined from the POD eigenvectors and blue triangles reprsent the frequencies found in the *PSD* of the temperature outlet time series (small container). The red circles represent the characteristic frequencies of the eigenvectors regarding the large container.

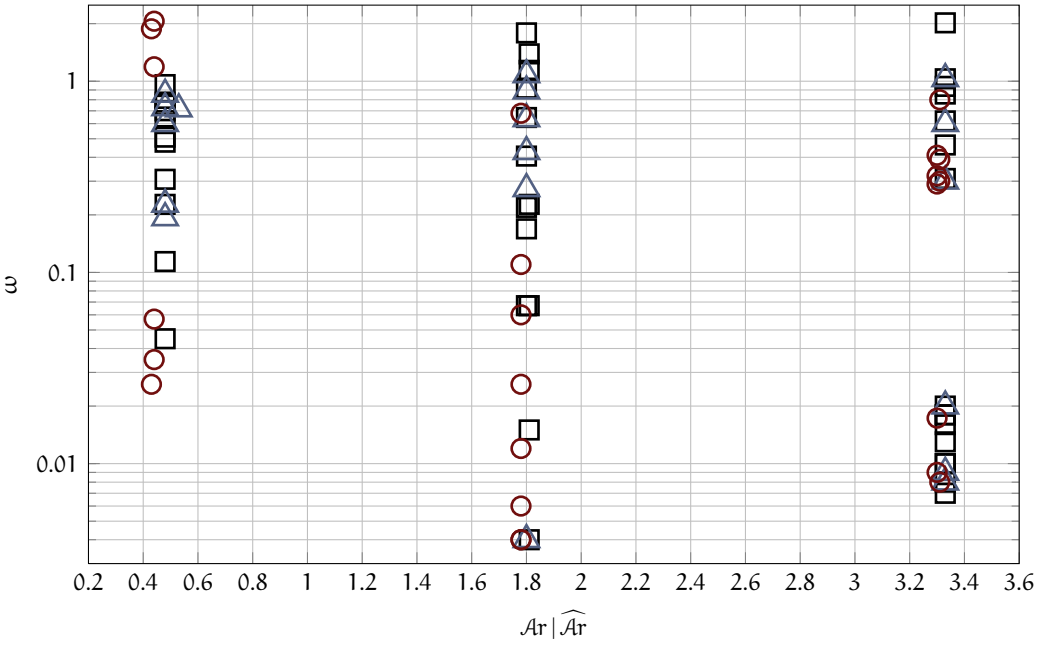

Figure 53: Characteristic frequencies ω as a function of Ar in the large container and the small container.

Figure 52 shows the normalised frequencies $\widehat{\omega} \approx 1$, where black squares and red circles denote frequencies determined from the POD eigenvectors. The blue triangle represents the characteristic frequencies found in *PSD* of the temperature time-series at the outlet regarding the small container. For $\mathcal{A}r \approx 3.3$ and $\mathcal{A}r \approx 1.8$ frequencies of $\widehat{\omega} \approx 1$ (however, clearly below one) are found. Although, the forced convection is strongly affected by the buoyancy flow, characteristic frequencies are uncovered almost similar to the angular velocity of the forced mean wind at *FC*. For $\mathcal{A}r \approx 1.8$ the frequency differs by 5 %, while in case of $\mathcal{A}r \approx 3.3$ the difference is almost 9 %. Moreover, the normalised frequencies are comparable for both containers. The normalised frequencies decrease with increasing $\mathcal{A}r$. With increasing $\mathcal{A}r$ the shear stresses between the incoming wall jet and the thermal convection rolls as well as the interaction with the plumes, leads to a loss of momentum. As a consequence, in comparison to the angular velocity at *FC*, lower angular velocities for the forced mean wind are found at *MC*.

For $\mathcal{A}r = 0.48$ the angular velocity of the forced mean wind in the small container is $\omega \approx 4.0\,s^{-1}$. The PIV sampling rate is $\omega_{PIV} = 4/3\pi$, hence, the *PSD* of the eigenvalues is restricted to $\omega_{PIV}/2 \approx 2.09\,s^{-1}$. As a consequence, figure 52 shows $\widehat{\omega}$ only with respect to the large container. As well the temperature measurements, with a sampling rate of $\omega_{\Theta} = 2/3\pi$, is too slow to capture the angular velocity of the forced mean wind in the small container. Nevertheless, the angular velocity in the large container is small enough to be identified by the POD eigenvectors and the *TTS*.

At $\widehat{\mathcal{A}r} \approx 0.43$ a ratio $\widehat{\omega} > 1$ is found, which would mean that the buoyancy induced flow assists the forced flow. This result contradicts with the other results of this study. As found before, the interaction of the forced mean wind with the thermal convective flow leads to a lower angular velocity of the forced mean wind. Moreover, it was found that in the vertical cross-section at $X = 0.5 \times L$ the time-averaged velocity field at *MC* is similar to the corresponding vector field at *FC* (fig. 12d and 16d). Consequently, $\widehat{\omega}$ has to be almost one. A closer inspection of U_{in} depicts that $U_{in}^{(LC)} > \sqrt{s_H} U^{(SC)}$ although $\mathcal{R}e$ is comparable. An amendment of $\widehat{\omega}$ by the factor $\sqrt{s_H} U^{(SC)}/U^{(LC)}$ leads to more meaningful values of $\widehat{\omega}$ slightly below one. The modified values of $\widehat{\omega}$ are displayed in figure 52 by the filled red circles.

For the sake of completeness, at the end of this paragraph, an overview of the characteristic frequencies (fig. 53) is given, which were determined from both containers. The frequencies represent characteristic peaks, which were found in the *PSD* of the POD eigenvectors of the first six modes and the *TTS* at the outlet. The black squares denote the frequencies determined from the POD eigenvectors and the blue triangles depict the frequencies found in the *PSD* of the temperature outlet time-series of the measurements in the small container. The red circles represent the characteristic frequencies of the eigenvectors regarding the large container.

The figure reveals a fundamental result, which is similar for both containers. In the $\mathcal{A}r$-regime, where the flow is governed by the thermal convective flow, a clear

separation of two intervals of ω is found. Here the lower frequencies seem to represent the torsional oscillation of the thermal convection rolls and the higher frequencies primarily stand for the angular velocity of the forced mean wind and thermal convective roll structures. Within the intermediate $\mathcal{A}r$-regime the frequencies are more homogeneously distributed. Due to the mutual interaction of *FC* and *TC*, several additional characteristic frequencies in the intermediate ω regime are found. In case of $\mathcal{A}r \approx 0.5$ a trend towards higher frequencies is obtained. Due to the predominance of the forced flow frequencies are found, which seems to be mainly related to the dynamics of the forced mean wind.

6.3 HEAT TRANSFER

Proper scaling of *MC* requires similar heat transfer as well. However, the determination of the Nusselt number as a measure for the heat transfer is difficult for the present configuration. Due to the spatial distribution of the temperature at the outlet port, the in-homogeneity of the heat transfer at the lateral walls or at the bottom and the ceiling, makes an exact calculation of the heat flux balance impossible.

Nevertheless, similitude of the heat transfer is examined for the heat flux between the inlet and outlet. The corresponding heat flux of the forced convective flow, which is developed since heated fluid leaves the container through the outlet and cold fluid is entering the container, is

$$\dot{Q}_{FC} = \dot{V}\,\rho\,C_p\,\left|\overline{\Theta}_{out} - \overline{\Theta}_{in}\right|. \tag{6.4}$$

Here $\left|\overline{\Theta}_{out} - \overline{\Theta}_{in}\right|$ represents the mean temperature difference between the inlet and outlet, $\dot{V}$ the mean volume flow, ρ the density and C_p the specific heat capacity. Thereby, the heat flux stands for the amount of heat leaving the container per time unit. The heat flux $\dot{Q}_{FC}$ basically discloses the hot plumes, emitted from the bottom plate, which are convected by the forced flow towards the outlet. Further, $\dot{Q}$ is normalised by the characteristic temperature difference $\Delta\Theta$, the thermal conductivity k and the characteristic height H, which basically corresponds to a Nusselt number of the forced flow

$$\mathcal{N}u_{FC} = \frac{\dot{Q}_{FC} H}{k \Delta\Theta A}, \tag{6.5}$$

where A denotes the area of the inlet port.

It is found that within the parameter range and the $\mathcal{A}r$-regime of this study $\mathcal{N}u_{FC}$ linearly decreases with increasing $\mathcal{A}r$ (fig. 54). Within the parameter space of this study, the heat flux per area unit between the inlet slot and the outlet slot is

$$\dot{q}_{FC} = \frac{\Delta\Theta\, k}{H}\,(a\,\mathcal{A}r + b), \tag{6.6}$$

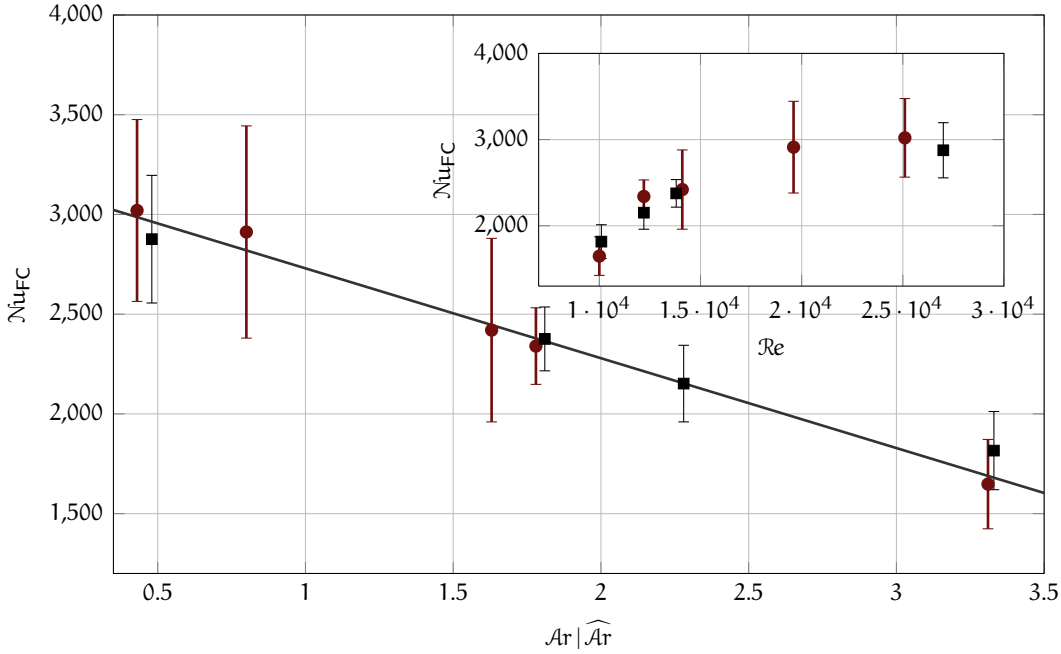

(a)

Figure 54: $\mathcal{N}u_{FC}$ as a function of $\mathcal{A}r$ and $\mathcal{R}e$. The black squares denote the results in the small container and the red circles do so in the large container.

where the slope is $a = -113(9)$ and the ordinate is $b = 3180(76)$. The numbers in brackets denote the standard deviation of the fitting parameters. In the present study, lower $\mathcal{A}r$ means higher $\mathcal{R}e$, because $\mathcal{R}a$ is almost constant for all cases. However, here $\mathcal{R}e$ is primarily a function of U and U is linear in $\dot{V}$, hence, the heat flux and thus, $\mathcal{N}u$ linearly decreases with increasing $\mathcal{A}r$. Regarding the simlitude of the forced heat tranport, a good accordance of $\mathcal{N}u_{FC}$ as a function of $\mathcal{A}r$ is found. Both containers show a comparable linear relation between $\mathcal{A}r$ and $\mathcal{N}u_{FC}$ within the parameter range of the present study. Considering, the unsteady nature of the flow or the re-evaluation of the temperature at the outlet slot and the characteristic numbers for the large container, the results correlate well.

However, this linear relation seems to be valid for a restricted $\mathcal{A}r$-regime. In both containers, the characteristic velocity is more or less the only parameter which was systematically changed. As a result, $\mathcal{N}u_{FC}$ is primarily a function of $\mathcal{R}e$. The subfigure in figure 54a depicts $\mathcal{N}u_{FC}$ as a function of $\mathcal{R}e$. It is clearly found that $\mathcal{N}u_{FC}$ rises with increasing $\mathcal{R}e$. The higher $\mathcal{R}e$ is a result of a higher volume flow and this again results in an enhanced heat flux between the inlet and outlet, which reaches a maximum at $\mathcal{R}e \approx 2.5 \times 10^4$. Moreover, it seems that with increasing $\mathcal{R}e$ a decrease of $\mathcal{N}u_{FC}$ is obtained. As a consequence, an increase of the volume flow would not necessarily

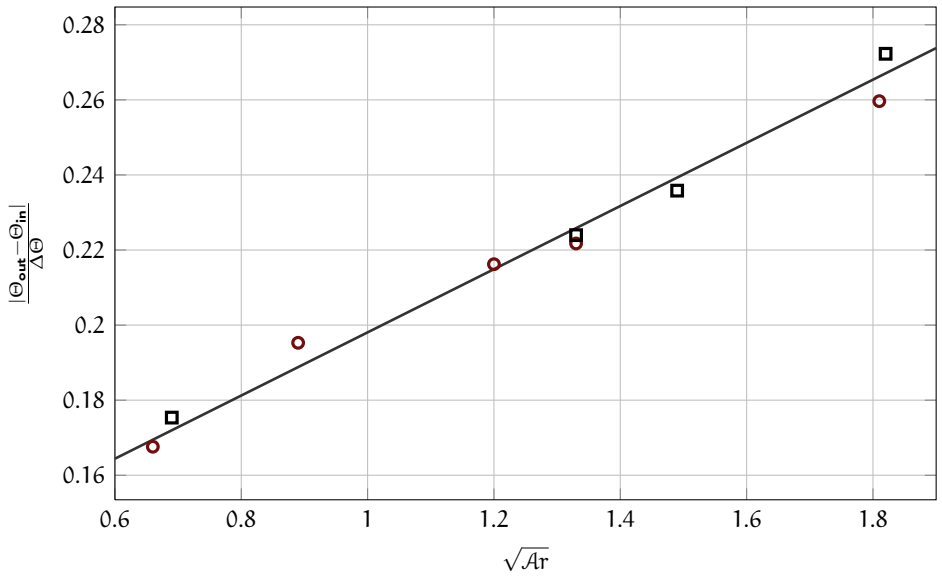

Figure 55: $|\overline{\Theta}_{out}-\overline{\Theta}_{in}|/\Delta\Theta$ as a function of $\sqrt{\mathcal{A}r}$ for the small container (black squares) and large container (red circles).

lead to an increase of the heat flux. Similar results were already reported by Schmeling et al. [110].

Of course, the present data do not allow to draw clear conclusions about the dependency of $\mathcal{N}u_{FC}$ on $\mathcal{R}e$ at lower $\mathcal{A}r$. Nevertheless, the fact that $\mathcal{N}u_{FC}$ decreases for higher $\mathcal{R}e$ can be explained as follows: On the one hand, the heat flux between the heating plate and the fluid grows with increasing volume flow. On the other hand, higher $\mathcal{R}e$ is the result of a higher inflow velocity, leading to an enhanced entrainment of the fluid from the bulk of the container by the wall jet. As a consequence, a higher heat transfer between container core and cooling plate is obtained. However, due to the dominating shear flow at the cooling plate, compared to the heating plate, the latter of the two processes dominates. As a result, the heat flux between inlet and outlet decreases with increasing volume flow. Furthermore, due to the restricted heat transfer from the thermal boundary layer into the flow towards the outlet per time and area, the increase of heat flux is restricted. In conclusion, these effects together lead to a decrease of the heat transfer with increasing volume flow.

In the paragraph above, the forced convective heat transport was discussed. To examine similitude, it is of equal importance that the heat transport by thermal convective flow is similar as well. However, a direct calculation of the thermal convective heat transport is impossible with the present data. Nevertheless, the ratio of the heat flux of the forced convective flow and thermal convective flow can be examined for similitude.

The enthalphy flux of *FC* (per area unit) is

$$\dot{q}_{FC} \sim U_{in}\, \rho\, C_P\, \left|\overline{\Theta}_{out} - \overline{\Theta}_{in}\right| \tag{6.7}$$

and the enthalpy flux of *TC* (per area unit) is

$$\dot{q}_{TC} \sim \langle w \rangle\ \rho\, C_P\, \Delta\Theta, \tag{6.8}$$

where $\langle w \rangle \sim U_b \sim \sqrt{\alpha\, \Delta\Theta\, H\, g}$. Hence, the relation

$$\frac{\dot{q}_{FC}}{\dot{q}_{TC}} \sim \frac{U_{in}}{\sqrt{\alpha\, \Delta\Theta\, H\, g}}\, \frac{\left|\overline{\Theta}_{out} - \overline{\Theta}_{in}\right|}{\Delta\Theta} \tag{6.9}$$

is obtained, where

$$\frac{U_{in}}{\sqrt{\alpha\, \Delta\Theta\, H\, g}} = \frac{1}{\sqrt{\mathcal{A}r}}.$$

As a result the relation

$$\frac{\dot{q}_{FC}}{\dot{q}_{TC}} \sim \frac{1}{\sqrt{\mathcal{A}r}}\, \frac{\left|\overline{\Theta}_{out} - \overline{\Theta}_{in}\right|}{\Delta\Theta} \Rightarrow \frac{\left|\overline{\Theta}_{out} - \overline{\Theta}_{in}\right|}{\Delta\Theta} = f(\sqrt{\mathcal{A}r}) \tag{6.10}$$

is obtained.

Figure 55 shows $|\overline{\Theta}_{out} - \overline{\Theta}_{in}|/\Delta\Theta$ as a function of $\sqrt{\mathcal{A}r}$. It is found that the air which leaves the cell through the outlet becomes warmer with increasing $\mathcal{A}r$. Moreover, within the present parameter space a linear relation between $|\overline{\Theta}_{out} - \overline{\Theta}_{in}|/\Delta\Theta$ and $\sqrt{\mathcal{A}r}$ is found. Based on equation (6.9), this linear relation shows that the ratio $\dot{q}_{FC}/\dot{q}_{TC}$ is constant for the present $\mathcal{A}r$-regime. As a consequence, if $\dot{q}_{FC}$ decreases to the same extent $\dot{q}_{TC}$ have to increase in order to obtain $\dot{q}_{FC}/\dot{q}_{TC} = \text{const}$. Indeed, at first view this result appears contradictorily. However, this phenomenon can be explained as follows. Due to the lower volume flow, less heat per time is convected towards the outlet. As a consequence more heat remains in the container and an increased mean temperature in the bulk and at the outlet is obtained. In addition, less rising warm air is entrained by the incoming wall jet. As a result an increase of hot rising air is obtained and more heat dissipates through the cooling device at the top. Hence, an increased thermal convective heat transport is developed. Moreover, the linear relation, which has been determined for $|\overline{\Theta}_{out} - \overline{\Theta}_{in}|/\Delta\Theta$ as a function of $\sqrt{\mathcal{A}r}$ suggests that the heat dissipation through the ceiling increases to the same extant the inflow velocity decreases.

Regarding the scaling of the heat transfer, the results in both containers are in good accordance. Besides the similar linear behaviour, also comparable values for $|\overline{\Theta}_{out} - \overline{\Theta}_{in}|/\Delta\Theta$ are found at similar $\mathcal{A}r$.

6.4 CONCLUSIONS

Mixed convective air flow was studied in two containers with different size. In conformance with the concept of spatial scaling, the inflow velocity and the ambient pressure condition were adapted with the aim to obtain the same characteristic numbers $\mathcal{R}e$, $\mathcal{R}a$ and $\mathcal{P}r$ in both containers. Three characteristic flow features were analysed and examined for similitude: the topology of the prominent large-scale coherent structures, the time-periodic behaviour of these coherent structures with the highest eigenvalues and the heat transport.

The topology of the prominent coherent structures in the longitudinal cross-section with the highest eigenvalues was examined for similitude as a function of $\mathcal{A}r$. For $\mathcal{A}r \approx 3.3$ the predominant coherent structures in the longitudinal cross-section $Y = 0.5 \times W$ correlates well. Furthermore, line cuts of Ψ_w at characteristic positions of vertical flow were extracted. At the position of ascending air the Ψ_w-profiles of the small and large container are almost congruent. The same picture is drawn for Ψ_w at the position of descending air. However, in the intermediate $\mathcal{A}r$-regime the topology of the predominant coherent structures at similar $\mathcal{A}r$ differs significantly.

For $\mathcal{A}r \approx 2.25$ totally different topologies of the coherent structures in the small and large container are found. In the small container at $\mathcal{A}r = 2.28$ the predominant flow structure in the longitudinal cross-section is almost unaffected by the forced flow, while the corresponding flow case in the larger container discloses already a significant impact of the forced flow. However, an almost similar topology of the first mode coherent structure at $\mathcal{A}r = 1.81$ in the small and at $\mathcal{A}r = 2.23$ in the large container is obtained. A closer inspection of the measurement parameters exposes that in the large container, the temperature of the incoming air was almost 2 K lower than the temperature of the ceiling, while these temperatures are almost the same in the small container. This significant temperature difference leads to two conflicting effects. On the one hand, a higher characteristic temperature difference is developed. On the other hand, a reduced characteristic height is obtained. As a consequence, we achieve a lower $\mathcal{R}a$ and thus an inferior Archimedes number $\widehat{\mathcal{A}r} \approx 1.78$. This re-evaluated Archimedes number is close to $\mathcal{A}r \approx 1.81$ in the small container and explains why the coherent structure of $\mathcal{A}r = 1.81$ and $\mathcal{A}r = 2.23$ correlates.

In the large container, a conspicuous difference between the inflow temperature and the mean temperature of the ceiling is found for $\mathcal{A}r \approx 0.45$ as well. Hence, a re-evaluated Archimedes number $\widehat{\mathcal{A}r} = 0.43$ is obtained. However, the modification of the flow is less distinguished compared to the intermediate $\mathcal{A}r$-regime.

Besides the similarity of the large-scale coherent structures, a proper scaling of mixed convection requires kinematic similitude as well. With the objective to prove the kinematic similitude, the characteristic frequencies, which were found in the *PSD* of the POD eigenvector with the highest energy eigenvalues, were compared. The analysis of the time series shows that the frequencies, which represent the angular

velocity of the forced mean wind and thermal *LSC*s scale in accordance with the concept of spatial scaling. Moreover, in case of $\mathcal{A}r \approx 3.3$, in both containers a very low characteristic frequency $\omega = 0.008 s^{-1}$ was found. Based on the premise that this frequency represents a torsional movement of the *LSC*s and the time periodic dynamics are primarily determined by the ratio of inertia to buoyancy forces as well as by the aspect ratio of the container, the finding of the same frequencies additionally indicates kinematic similitude.

At the end, the heat transfer $\mathcal{N}u_{FC}$ between the inlet and outlet and the enthalpy flux ratio $\dot{q}_{FC}/\dot{q}_{TC}$ were examined for similitude. For both containers, a good conformance of the results is found. In addition, within the regime of $0.48 \leqslant \mathcal{A}r \leqslant 3.33$ an increase of $\mathcal{N}u_{FC}$ with increasing $\mathcal{R}e$ was found. Within the present parameter range, $\mathcal{N}u_{FC}$ seems to be a linear function of $\mathcal{A}r$.

In short, similitude of the coherent structures, their dynamics and the heat transfer was found in the $\mathcal{A}r$-regime of the present study. Hence, spatial scaling of mixed convective air flow is possible by adjusting the ambient pressure and inflow velocity. Moreover, the experiments reveal that, in particular, within the intermediate $\mathcal{A}r$-regime, the formation of large-scale flow structures reacts very sensitively on changes of the boundary conditions. As a consequence, experiments have to be performed with care in order to obtain the same boundary conditions.

7

SUMMARY AND FUTURE WORK

In the present study, the scaling of large-scale structures, their dynamics and heat transport in turbulent mixed convection was examined in order to verify a concept of spatial scaling. To this end, mixed convective air flow was experimentally studied by particle image velocimetry and temperature measurements in two rectangular containers with the same geometry, but dimensions scaled by a factor five. The small container was designed to operate under high pressure conditions and the large container was constructed for the application at atmospheric pressure.

A key result of the previous investigation is that in the present setup and parameter range, mixed convection is far from equilibrium. It comprises a plethora of flow states, depending on the ratio of inertia to buoyancy forces. Hence, the identification and characterisation of the large-scale roll structures need further analysis.

With the aim to examine mixed convection, a proper orthogonal decomposition and a vortex detecting algorithm were subjected to the sets of instantaneous velocity fields. These algorithms provide the determination of the predominant coherent structures and their trajectory in time from a set of vector fields. Furthermore, these methods enable the extraction of the large-scale circulations from the small-scale turbulent background.

To identify and quantify the charateristic flow features, mixed convective air flow was examined under high pressure condition $P = 11.6$. For a better understanding of the mutual interplay between forced convection and thermal convection, the isothermal flow was separately studied for $1.01 \times 10^4 \leqslant \mathcal{R}e \leqslant 2.67 \times 10^4$ and $\mathcal{P}r = 0.7$. As a result of the forced flow, a quasi two-dimensional stationary roll structure is developed in the vertical cross-section with the centre position close to the centre of the cross-section. Moreover, the mean wind behaves like a solid body rotation, however, with different angular velocities for the core region and the outer region of the large-scale circulation.

Mixed convection was examined at $\mathcal{A}r = 3.33$, $\mathcal{A}r = 2.23$, $\mathcal{A}r = 1.81$ and $\mathcal{A}r = 0.48$, where $\mathcal{R}a \approx 2.4 \times 10^8$ was kept constant and $\mathcal{R}e$ varies corresponding to $\mathcal{R}e$ at forced convection. With the onset of buoyancy flow a break-up of the two-dimensional forced mean wind in the vertical cross-section $X = 0.5 \times L$ was observed for $\mathcal{A}r \geqslant 1.81$, while the velocity field is almost unaffected at prevailing forced convection ($\mathcal{A}r = 0.48$). For $\mathcal{A}r \geqslant 2.23$ the POD analysis of the velocity fields in the longitudinal cross-section $Y = 0.5 \times W$ revealed a predominant large-scale flow pattern, which consists of four counter-rotating thermal convection rolls. The four large-scale roll structures with a diameter of the cell height are placed almost side-by-side in longitudinal direction.

Nevertheless, the forced flow has a clear influence on the thermal convection rolls. The impact of the forced flow leads to a tilted orientation of the large-scale circulation. In case of $\mathcal{A}r = 3.33$ an additional pattern in the longitudinal cross-section was found. The pattern consists of three counter-rotating large-scale circulations. However, due to the long-time evolution I cannot discern if this coherent structure represents a transitional or a metastable state.

With decreasing $\mathcal{A}r$ an increased impact of the forced flow on the thermal convection rolls is obtained. At $\mathcal{A}r = 1.81$ the predominant pattern in the longitudinal cross-section still consists of four large-scale roll structures, but the larg-scale roll structures are strongly stretched and tilted. With a further increase of the inertia forces, the thermal convection rolls with a diameter of the cell height break-up. At $\mathcal{A}r = 0.48$, eight smaller circulations are developed in longitudinal direction with a diameter of $H/2$. Furthermore, the rolls are located in the core region of the forced mean wind, where the inertia forces and the buoyancy forces are about the same order of magnitude.

In addition, the temporal evolution of the large-scale coherent structures, the trajectory of the *LSC* centre position and the temperature time series at the outlet were analysed. For $\mathcal{A}r \geqslant 1.81$ the analysis of the *LSC* dynamics discloses sudden break-ups or re-organisations of thermal convection rolls. A closer inspection of the eigenvectors and temperature time series further reveals a time-periodic behaviour of the large-scale coherent structures. Some of these frequencies correlates to the angular velocity of the large-scale circulations, indicating that the thermal convection rolls rotate in a time-periodic manner. Moreover, indications for a torsional oscillation of the large-scale circulations were found.

Based on these features, the scaling of mixed convection was examined for similitude. Regarding the predominant coherent structure, a good conformance is obtained for the flow cases $\mathcal{A}r \approx 3.3$ and $\mathcal{A}r \approx 0.45$. In contrast, for the intermediate $\mathcal{A}r$-regime, where significant differences were disclosed, despite almost similar characteristic numbers. Within this parameter range, the formation of large-scale structures reacts particularly sensitive on differences in the boundary conditions or deviations in the measurement parameters. Nevertheless, a similar topology of the predominant coherent structure was found at $\mathcal{A}r = 1.81$ in case of the small container and at $\mathcal{A}r = 2.23$ in the large container. This similar topology at different $\mathcal{A}r$ is ascribed to the distinctive temperature conditions at the inlet port of the large container and the small container. The finding shows the need of similar boundary conditions for a proper scaling of mixed convection, in particular, within the intermediate $\mathcal{A}r$-regime.

Based on the time-periodic dynamics of the large-scale structures and the corresponding characteristic frequencies were examined for kinematic similitude. The frequencies were determined from the power spectra of the POD eigenvectors and the temperature time series at the container outlet port. With respect to the concept of scaling a good conformance of the predominant characteristic frequencies was found.

In addition, the scaling of the heat transfer was examined for similitude, which develops since heated fluid leaves the container through the outlet. Here, a good conformance was found as well. Moreover, a linear relation in case of the enthalpy flux between in- and outlet ports and the enthalpy flux ratio as a function of $\mathcal{A}r$ were disclosed within $0.48 \leqslant \mathcal{A}r \leqslant 3.33$.

Taken together, the scaling of mixed convective air flow based on the concept of spatial scaling promises a simple method to obtain characteristic numbers of mixed convection on large scales on laboratory scales. In the present study, a good conformance of the large-scale coherent structures, their dynamics and the heat transfer was found for two containers of different size. The results of this investigation reveal that the spatial scaling in turbulent mixed convective air flow is possible by adjusting the ambient pressure and the inflow velocity. However, experiments have to be designed and performed with care regarding the boundary conditions, in particular, within the intermediate $\mathcal{A}r$-regime.

Nevertheless, the three-dimensional structure formation as the result of the mutual interplay of forced and thermal convection, its long-time evolution and the physical mechanisms of mixing are only a few issues, which require further examination. Presently, additional experimental studies are performed to uncover the mechanisms of large-scale structure formation and heat transport in turbulent mixed convection by tomographic PIV [68] and Particle Image Thermography (PIT) [108]. Furthermore, major challenges still remain in the identification of the processes that take place inside the thermal boundary layers at the top and bottom plates.

A

PIV DATA PROCESSING PARAMETERS

In the following tables 9 - 11 the particle image velocimetry data processing parameters are listed.

	$\times 10^4$	$\mathcal{R}e = 1.01$	$\mathcal{R}e = 1.22$	$\mathcal{R}e = 1.40$	$\mathcal{R}e = 2.67$
PIV interrogation window	[px^2]	24×24	24×24	32×32	24×24
step size	[px^2]	8×8	8×8	11×11	8×8
repetition rate	[Hz]	$2/3$	$2/3$	$2/3$	$1/3$
velocity vectors per image		58081	58081	30976	58081
measurement time	[s]	1200	1200	1200	1200

Table 9: PIV data processing parameters for the measurements of forced convective air flow in the small container at $X = 0.5 \times L$. The magnification factor is 19.61 px/mm

		$\mathcal{A}r = 3.33$	$\mathcal{A}r = 2.29$	$\mathcal{A}r = 1.80$	$\mathcal{A}r = 0.48$
PIV interrogation window	[px^2]	24×24	24×24	32×32	24×24
step size	[px^2]	8×8	8×8	11×11	8×8
repetition rate	[Hz]	$2/3$	$2/3$	$2/3$	$1/3$
velocity vectors per image		58081	58081	30976	58081
measurement time	[s]	7200	7200	7200	9000

Table 10: PIV data processing parameters for the measurements of mixed convective air flow in the small container at $X = 0.5 \times L$. The magnification factor is 19.61 px/mm

		$\mathcal{A}r = 3.33$	$\mathcal{A}r = 2.28$	$\mathcal{A}r = 1.81$	$\mathcal{A}r = 0.48$
PIV interrogation window	[px^2]	48×48	48×48	64×64	64×64
step size	[px^2]	16×16	16×16	22×22	22×22
repetition rate	[Hz]	2/3	2/3	2/3	2/3
velocity vectors per image		12700	12700	6845	3630
measurement time	[s]	7200	7200	7200	2400

Table 11: PIV data processing parameters for the measurements of mixed convective air flow in the small container at $Y = 0.5 \times W$. The magnification factor is 8.15 px/mm

		$\mathcal{A}r = 3.31$	$\mathcal{A}r = 2.23$	$\mathcal{A}r = 0.53$
PIV interrogation window	[px^2]	24×24	24×24	64×64
step size	[px^2]	8×8	8×8	22×22
repetition rate	[Hz]	2/3	2/3	2/3
velocity vectors per image		38880	38880	38880
measurement time	[s]	7200	7200	7200

Table 12: PIV data processing parameters for the measurements of mixed convective air flow in the large container at $Y = 0.5 \times W$. The magnification factor is 4.55 px/mm

B

COHERENT STRUCTURES

In the result chapter the time behaviour of the POD eigenfunctions was discussed without showing the topology of all coherent structures. Hence, in the following the coherent structures of the first four POD modes in the longitudinal cross-section $Y = 0.5 \times W$ and vertical cross-section $X = 0.5 \times L$ of the measurements in the small container are plotted (insofar as they have not shown before). The eigenfunctions $\Psi_i^{(n)}$ and the magnitude Ψ_n of the eigenfunctions are normalised. Here n denotes the mode number and i indicates the velocity component u, v and w. The vectors are scaled to unity and consist of the corresponding eigenfunctions $\Psi_i^{(n)}$. The corresponding normalised eigenvalues are listed in table 13 and 14. All eigenvalues are normalised by the sum of all eigenvalues.

	$Ar = 3.33$	$Ar = 2.28$	$Ar = 1.81$	$Ar = 0.48$
λ_1 [%]	46.09	45.95	40.06	17.62
λ_2 [%]	8.03	8.68	6.75	1.45
λ_3 [%]	4.65	2.20	2.46	1.45
λ_4 [%]	4.29	1.07	1.10	1.3

Table 13: Normalised eigenvalues of the first four POD modes of the PIV measurement in the longitudinal cross-section $Y = 0.5 \times W$.

	$Ar = 3.31$	$Ar = 2.23$	$Ar = 0.48$
λ_1 [%]	72.62	60.19	92.88
λ_2 [%]	3.69	4.67	0.41
λ_3 [%]	2.23	1.97	0.30
λ_4 [%]	1.13	1.58	0.23

Table 14: Normalised eigenvalues of the first four POD modes of the PIV measurement in the vertical cross-section $X = 0.5 \times L$.

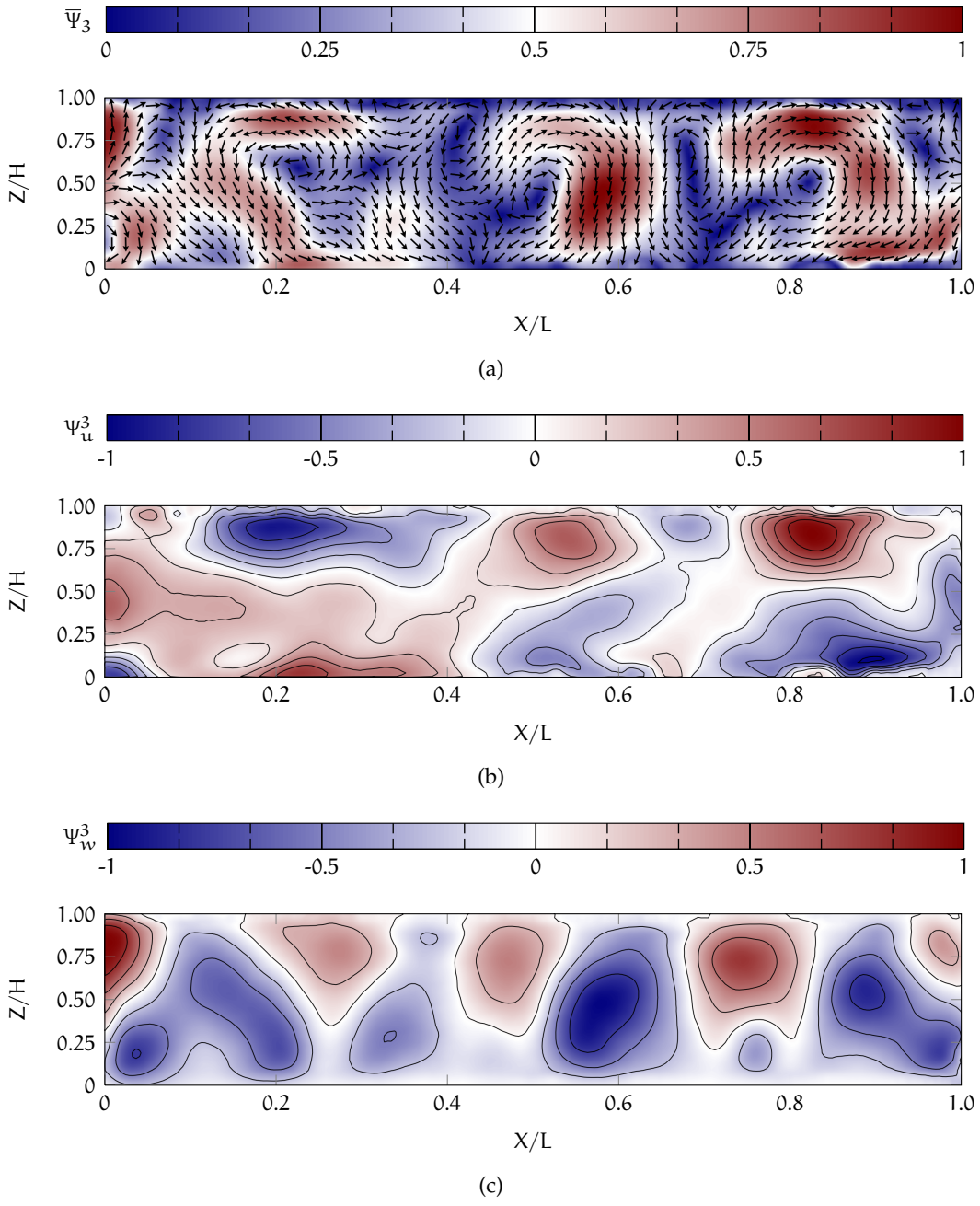

Figure 56: Coherent structures of the third POD mode at $Y = 0.5 \times W$ for $Ar = 3.33$. Figures (56a), (56b) and (56c): coherent structures of the eigenfunctions $\overline{\Psi}_3$, Ψ^3_u and Ψ^3_w respectively.

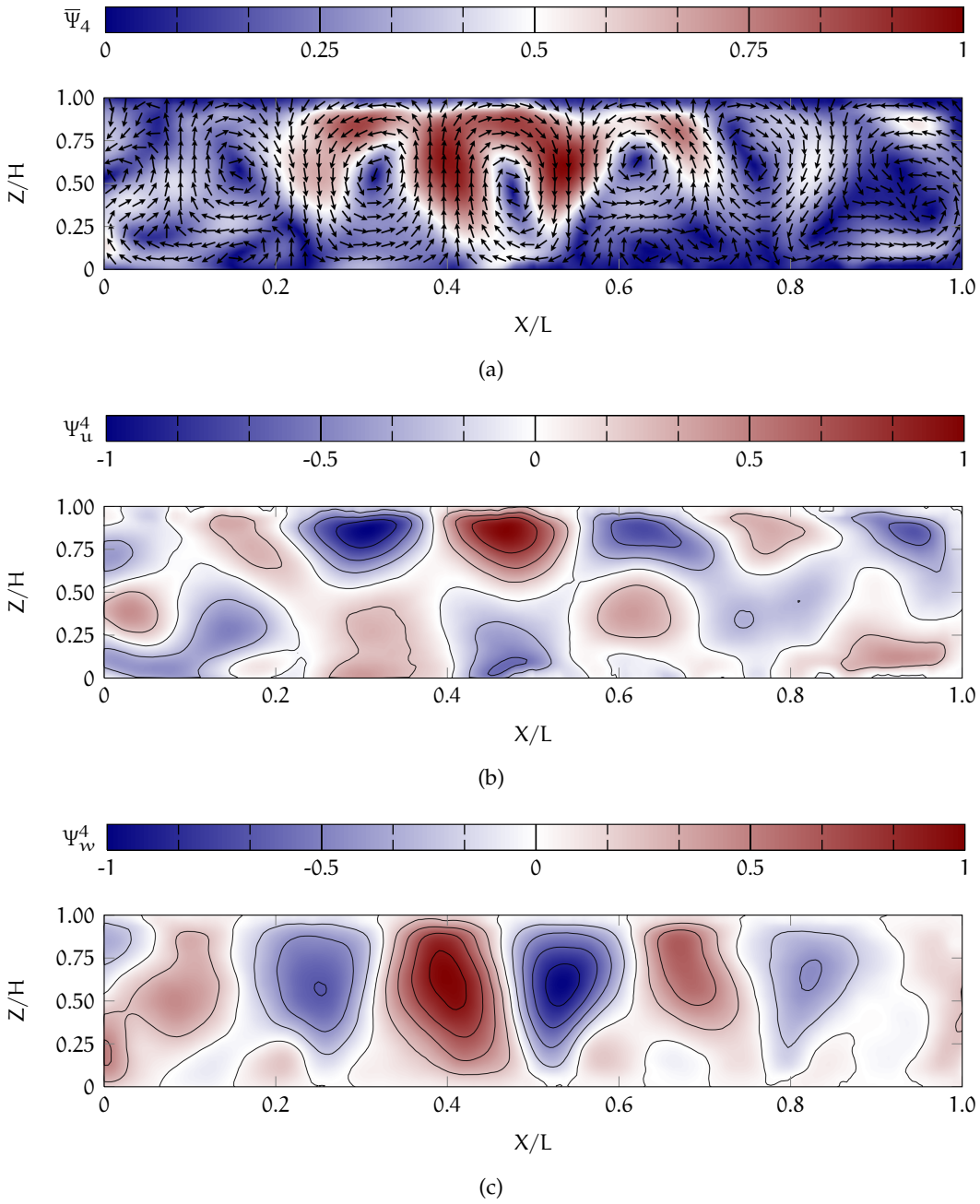

Figure 57: Coherent structures of the third POD mode at $Y = 0.5 \times W$ for $Ar = 3.33$. Figures (57a), (57b) and (57c): coherent structures of the eigenfunctions $\overline{\Psi}_4$, Ψ^4_u and Ψ^4_w respectively.

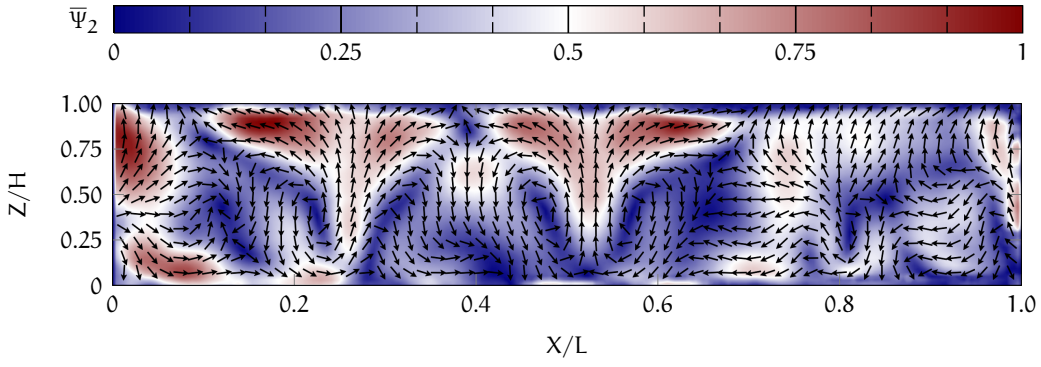

(a)

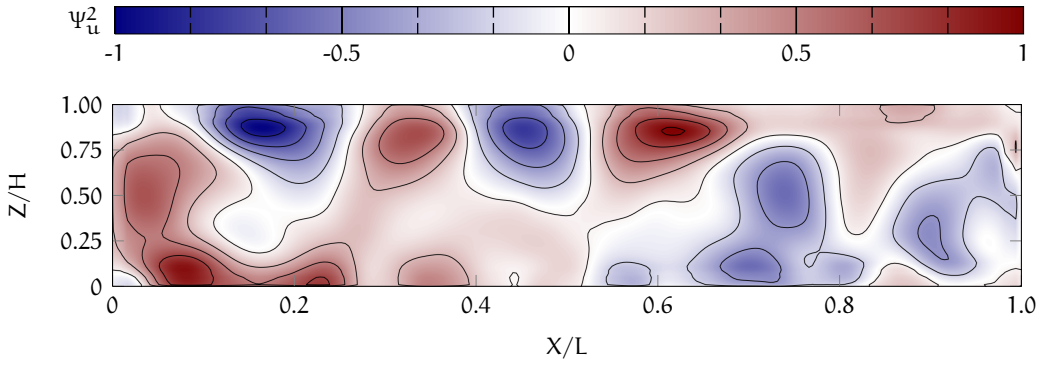

(b)

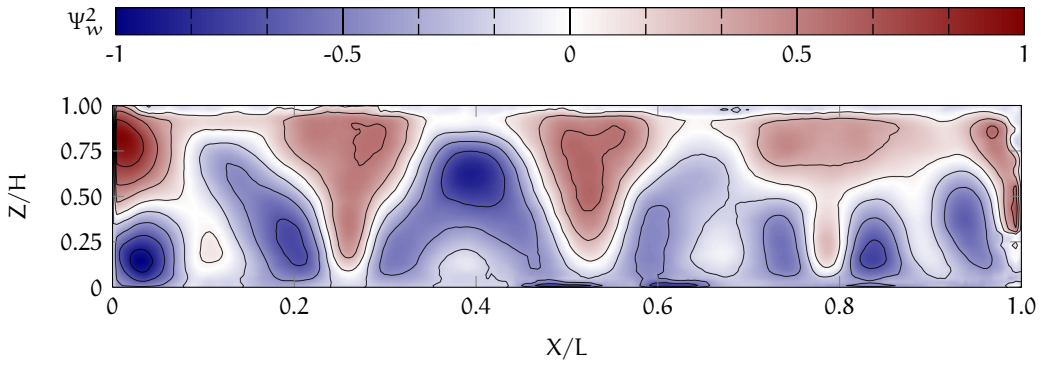

(c)

Figure 58: Coherent structures of the second POD mode at $Y = 0.5 \times W$ for $\mathcal{A}r = 2.28$. Figures (58a), (58b) and (58c): coherent structures of the eigenfunctions $\overline{\Psi}_2$, Ψ_u^2 and Ψ_w^2 respectively.

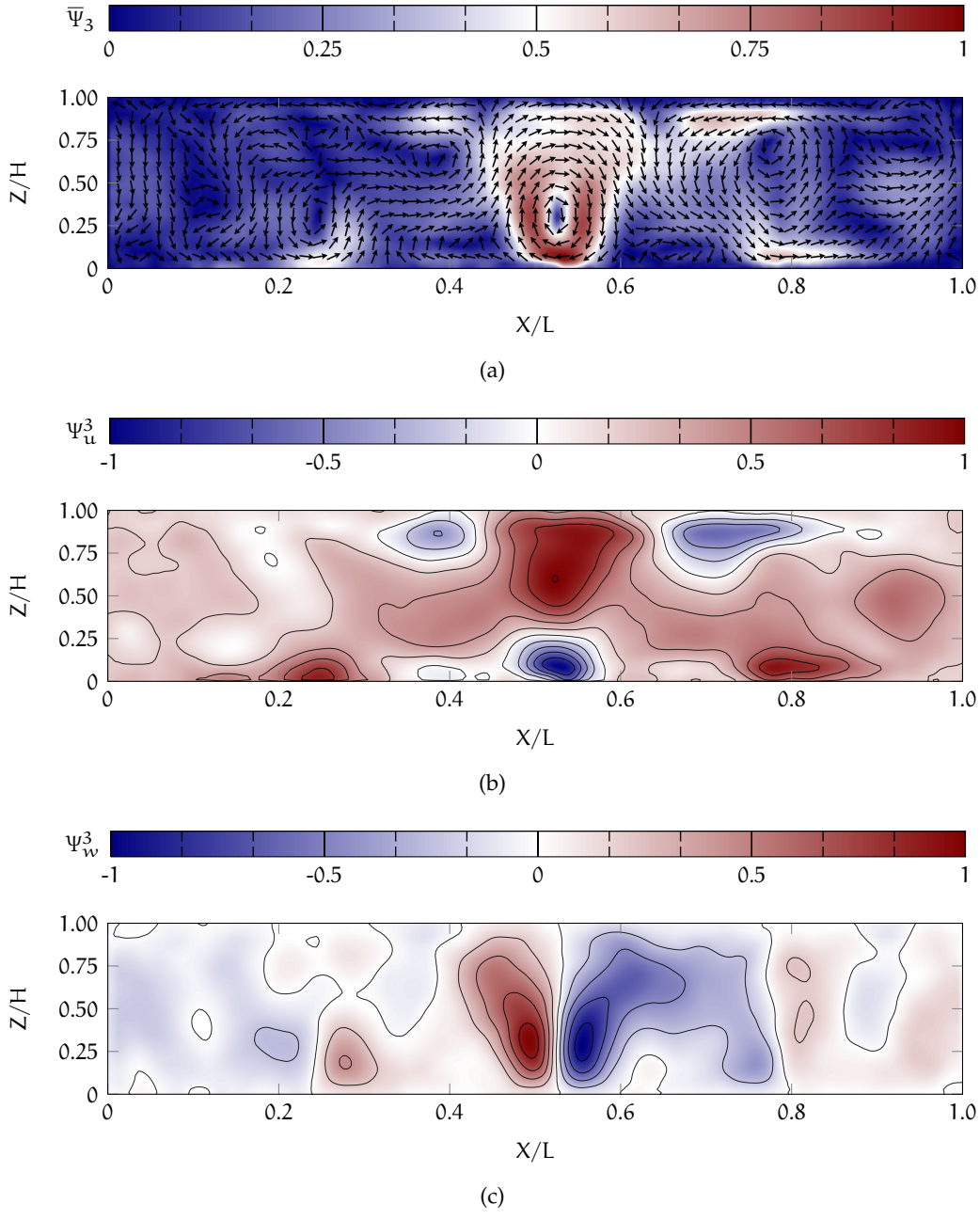

Figure 59: Coherent structures of the third POD mode at $Y = 0.5 \times W$ for $\mathcal{A}r = 2.28$. Figures (59a), (59b) and (59c): coherent structures of the eigenfunctions $\overline{\Psi}_3$, Ψ^3_u and Ψ^3_w respectively.

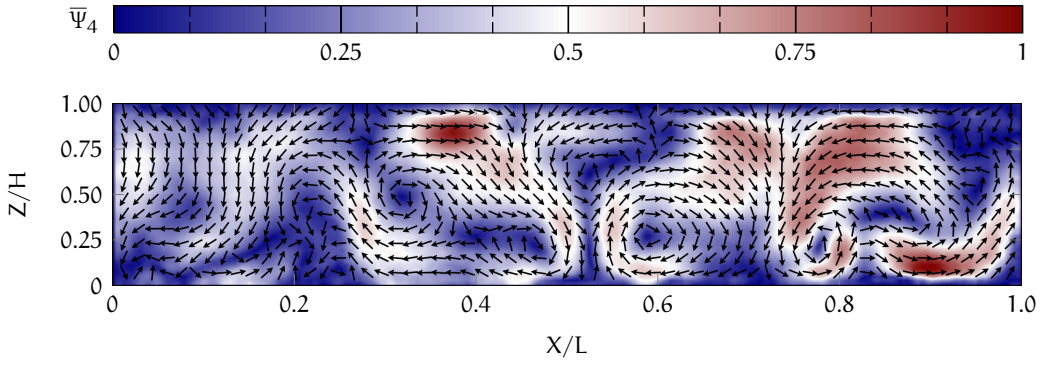

(a)

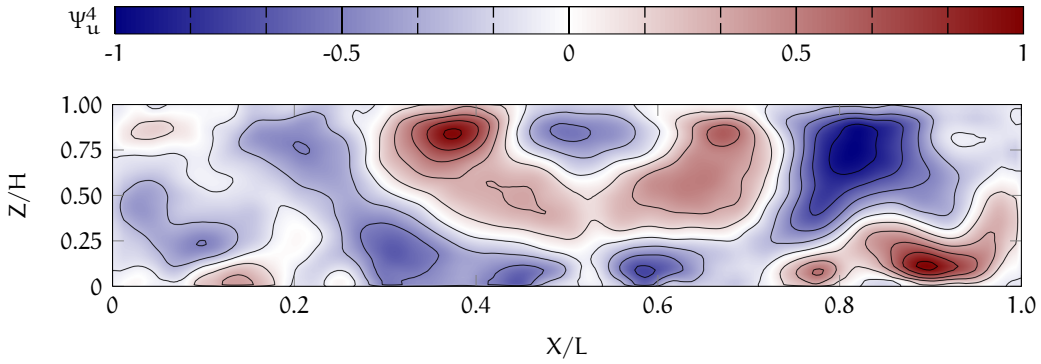

(b)

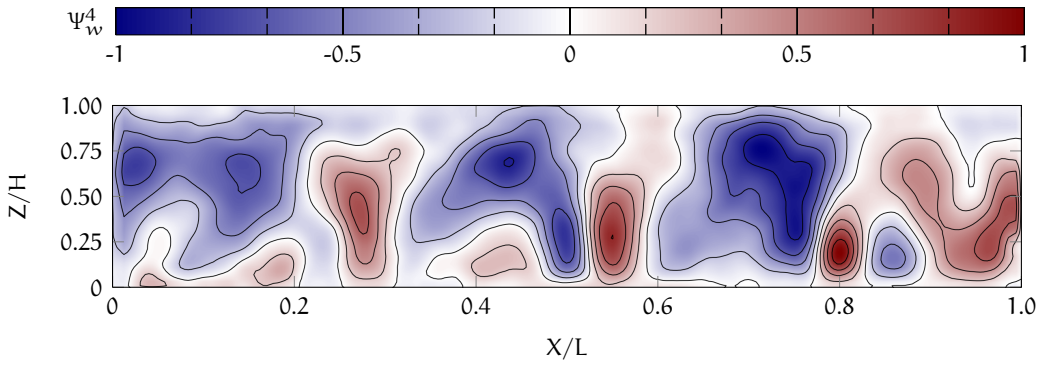

(c)

Figure 6o: Coherent structures of the fourth POD mode at $Y = 0.5 \times W$ for $\mathcal{A}r = 2.28$. Figures (6oa), (6ob) and (6oc): coherent structures of the eigenfunctions $\overline{\Psi}_4$, Ψ^4_u and Ψ^4_w respectively.

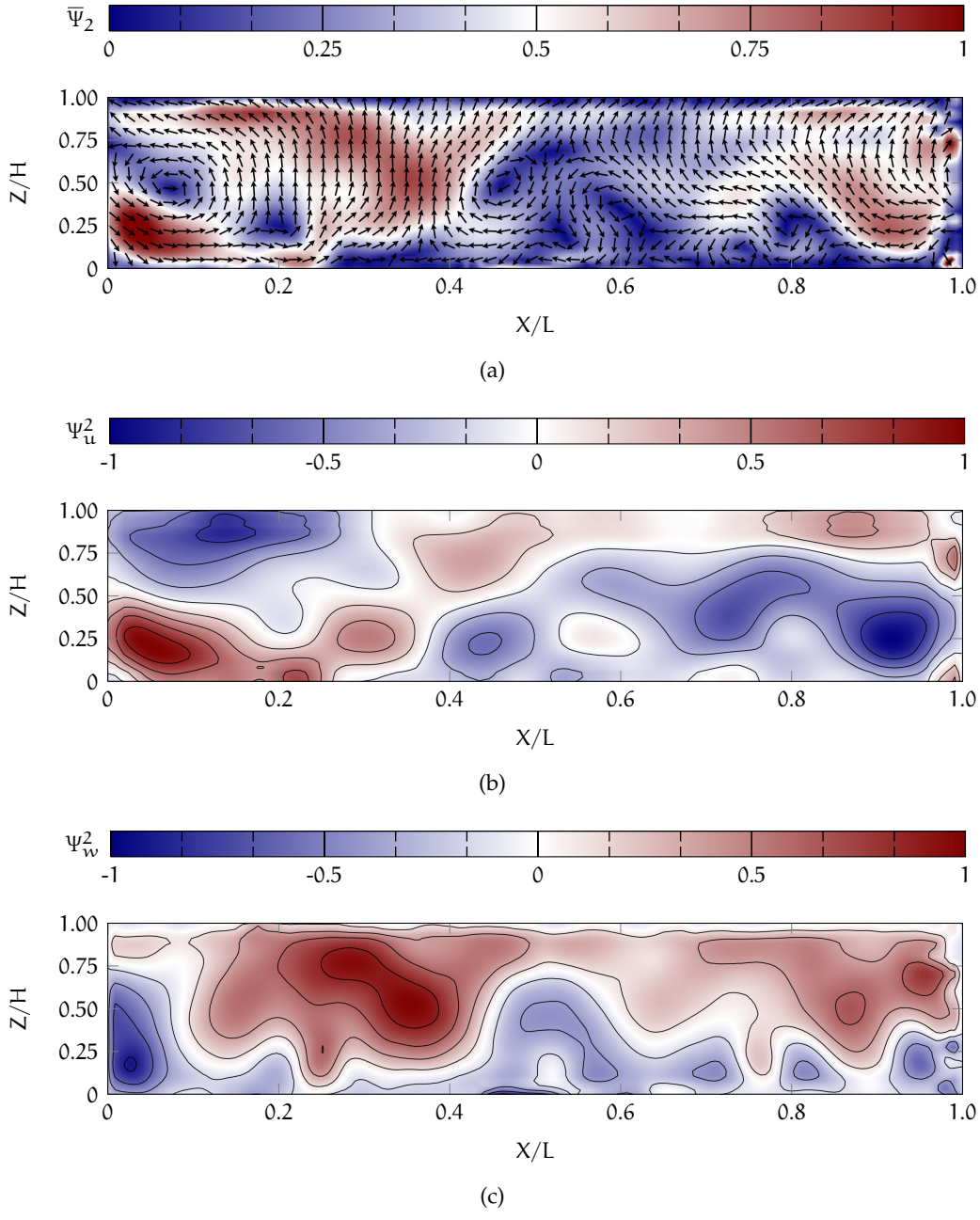

Figure 61: Coherent structures of the second POD mode at $Y = 0.5 \times W$ for $\mathcal{A}r = 1.81$. Figures (61a), (61b) and (61c): coherent structures of the eigenfunctions $\overline{\Psi}_2$, Ψ^2_u and Ψ^2_w respectively.

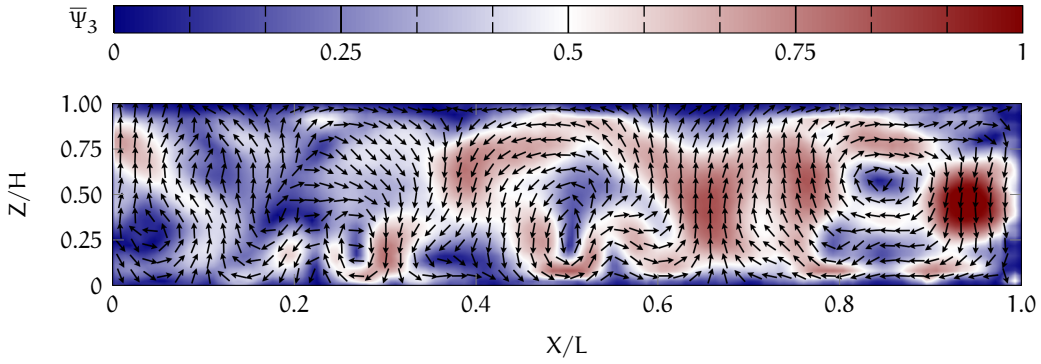

(a)

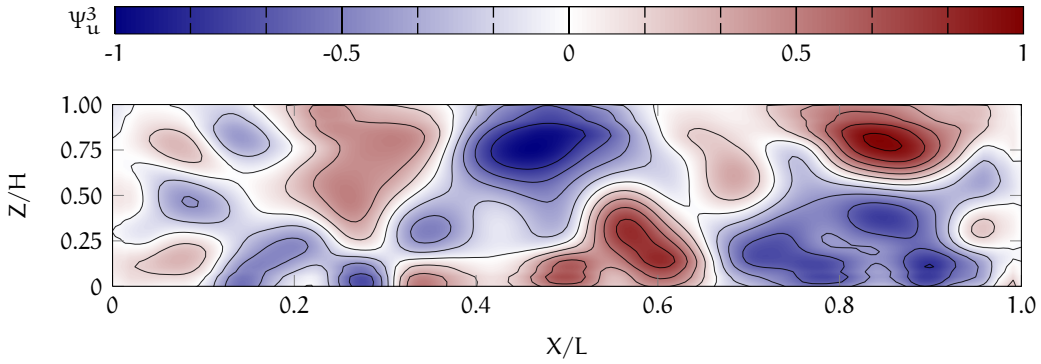

(b)

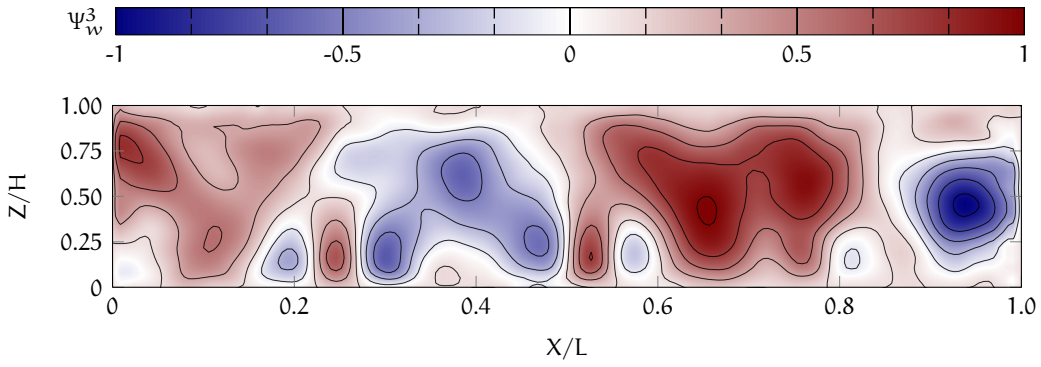

(c)

Figure 62: Coherent structures of the third POD mode at $Y = 0.5 \times W$ for $\mathcal{A}r = 1.81$. Figures (62a), (62b) and (62c): coherent structures of the eigenfunctions $\overline{\Psi}_3$, Ψ_u^3 and Ψ_w^3 respectively.

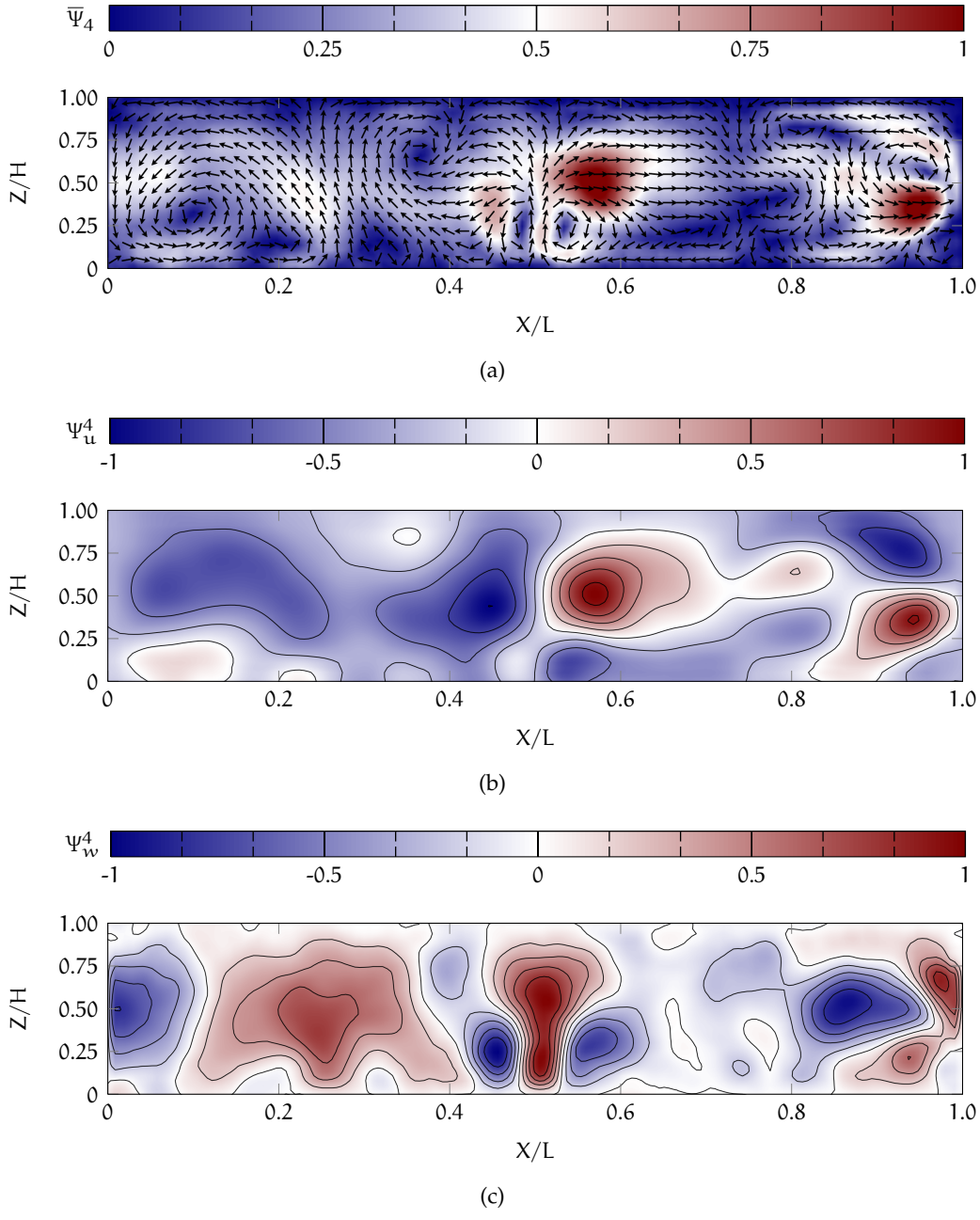

Figure 63: Coherent structures of the fourth POD mode at $Y = 0.5 \times W$ for $\mathcal{A}r = 1.81$. Figures (63a), (63b) and (63c): coherent structures of the eigenfunctions $\overline{\Psi}_4$, Ψ^4_u and Ψ^4_w respectively.

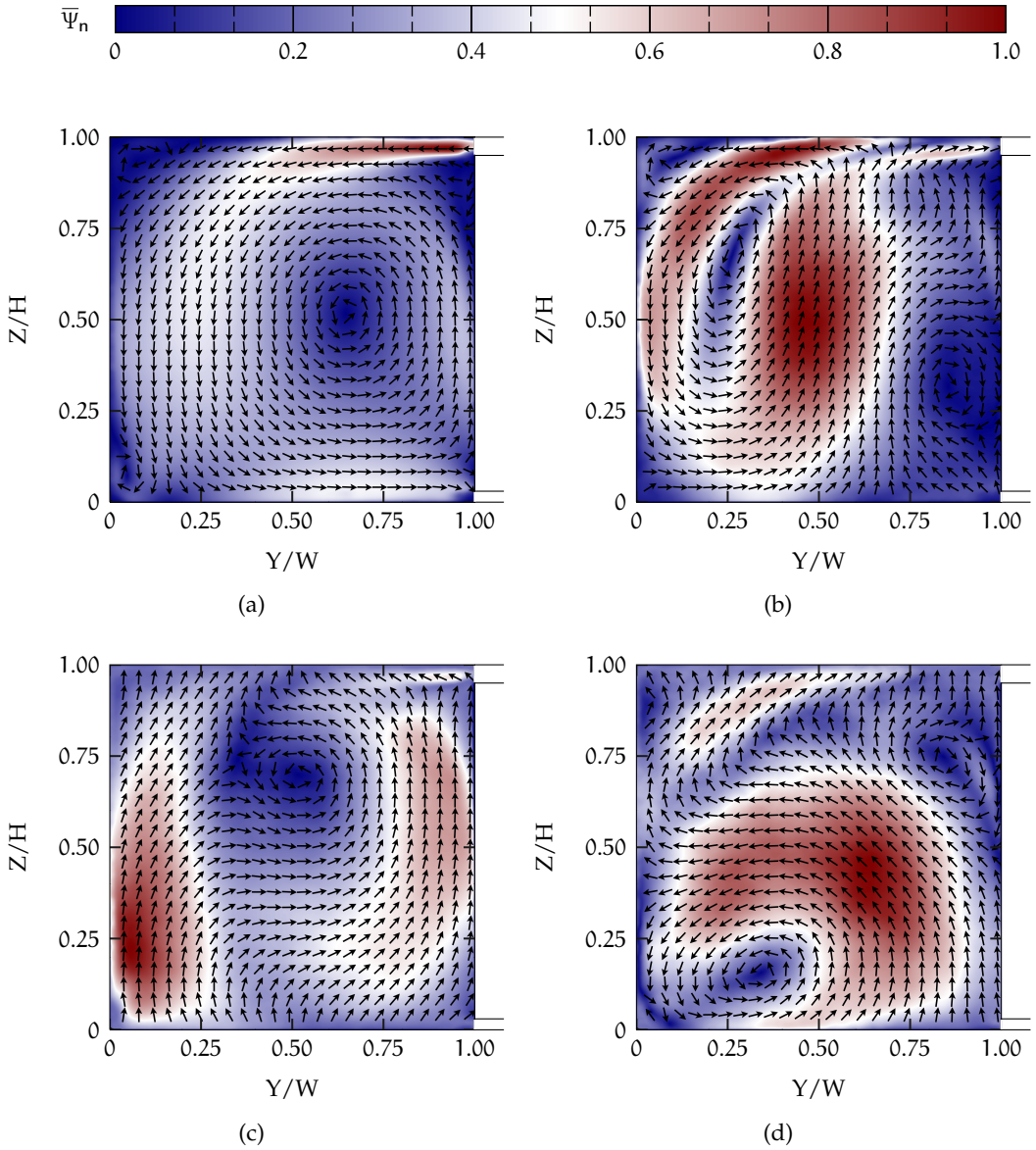

Figure 64: Coherent structures of the first four POD modes at X = 0.5 × L for $Ar = 3.33$. Figures (64a), (64b), (64c) and (64d): coherent structures of the eigenfunctions $\overline{\Psi}_1$, $\overline{\Psi}_2$, $\overline{\Psi}_3$ and $\overline{\Psi}_4$ respectively.

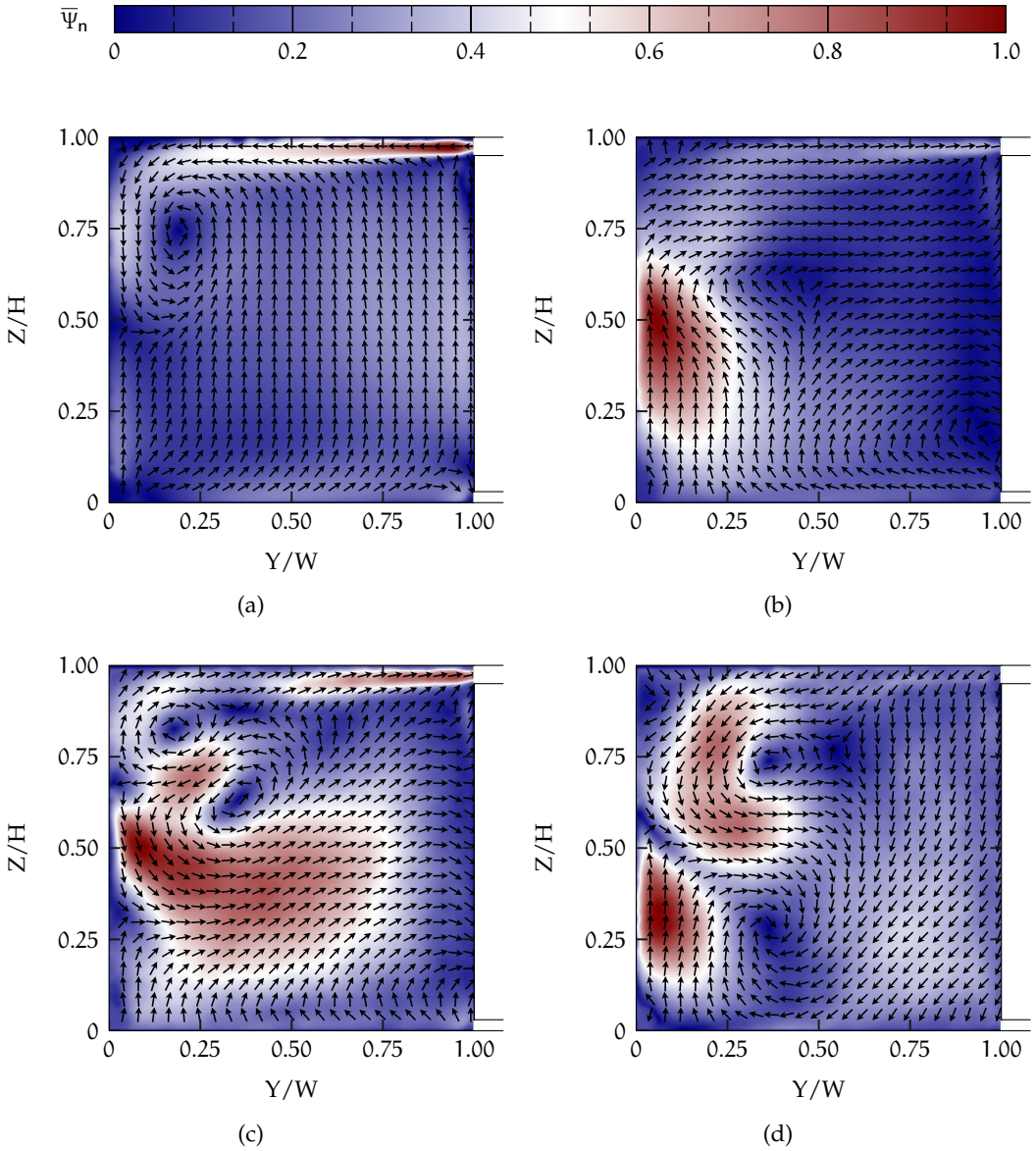

Figure 65: Coherent structures of the first four POD modes at $X = 0.5 \times L$ for $Ar = 2.29$. Figures (65a), (65b), (65c) and (65d): coherent structures of the eigenfunctions $\overline{\Psi}_1$, $\overline{\Psi}_2$, $\overline{\Psi}_3$ and $\overline{\Psi}_4$ respectively.

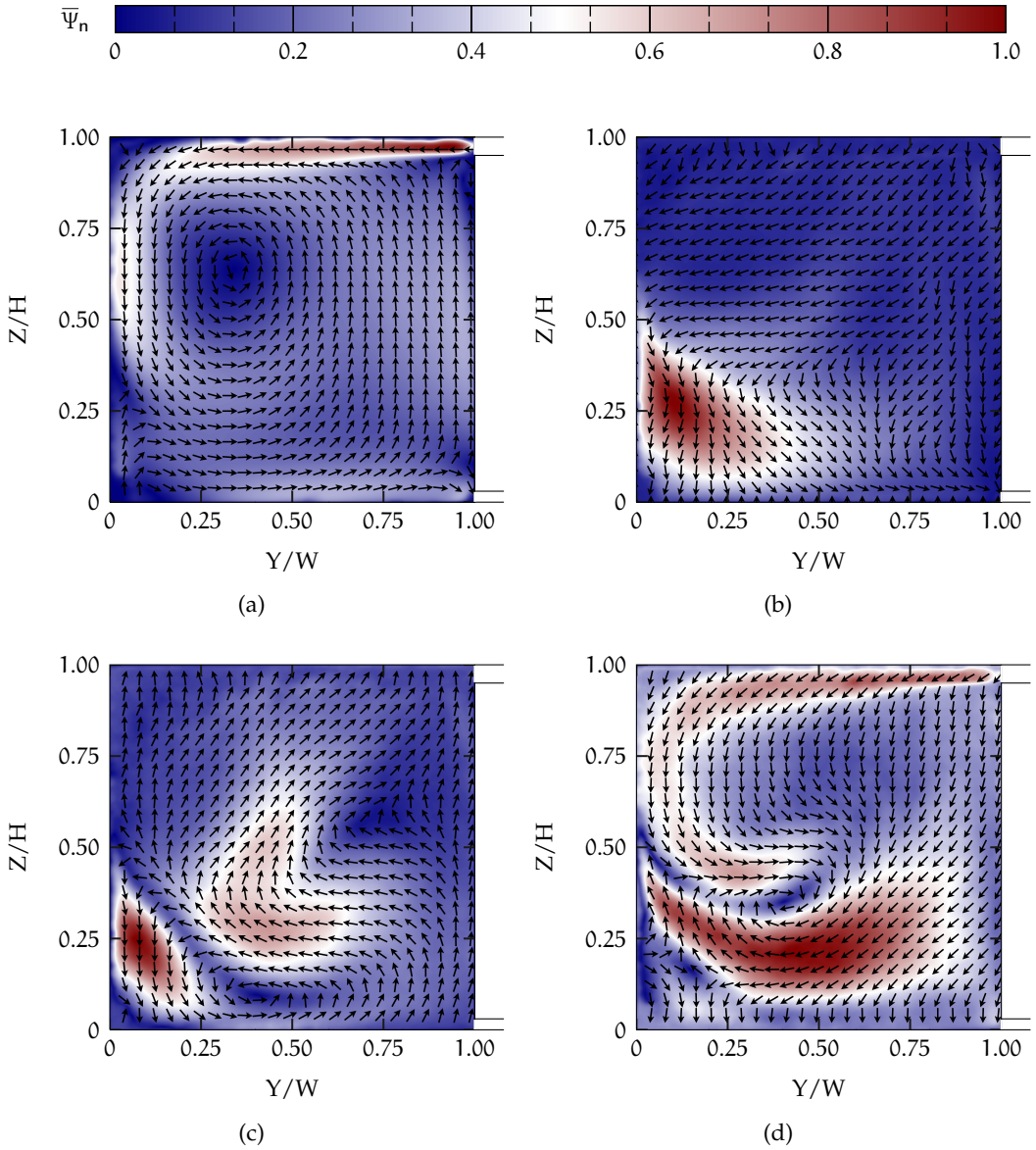

Figure 66: Coherent structures of the first four POD modes at $X = 0.5 \times L$ for $Ar = 1.81$. Figures (66a), (66b), (66c) and (66d): coherent structures of the eigenfunctions $\overline{\Psi}_1$, $\overline{\Psi}_2$, $\overline{\Psi}_3$ and $\overline{\Psi}_4$ respectively.

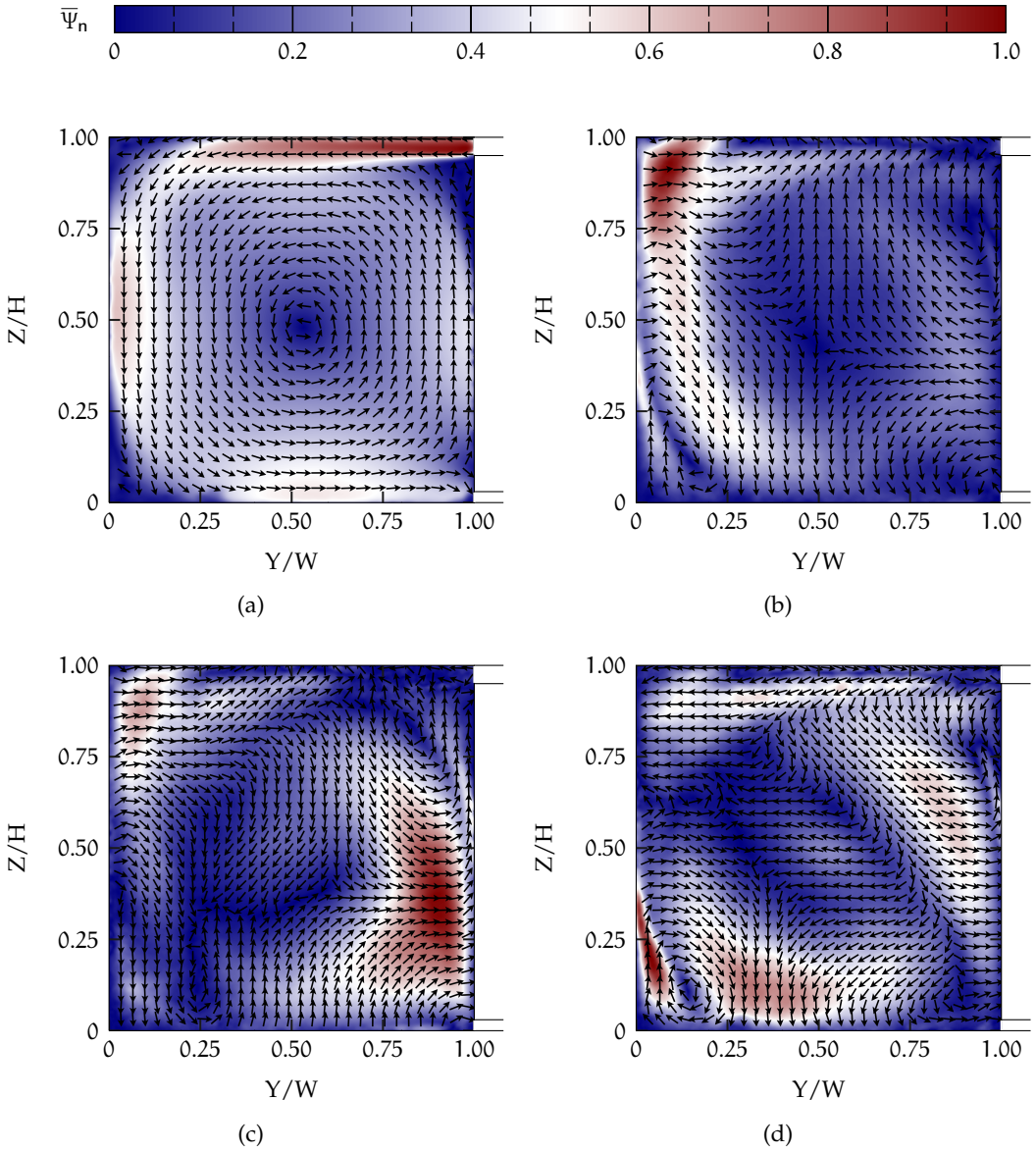

Figure 67: Coherent structures of the first four POD modes at $X = 0.5 \times L$ for $Ar = 0.48$. Figures (67a), (67b), (67c) and (67d): coherent structures of the eigenfunctions $\overline{\Psi}_1$, $\overline{\Psi}_2$, $\overline{\Psi}_3$ and $\overline{\Psi}_4$ respectively.

C

DYNAMICS OF THERMAL CONVECTION ROLLS

A key feature in mixed convective air flows for the present configuration at higher $\mathcal{A}r$ is the development of thermal convection rolls arranged in longitudinal direction. The structure and dynamics of these large-scale circulations were analysed with the help of a vortex detecting algorithm (sec. 4.1).

With the aim to give a deeper insight to the dynamics of the themal convection rolls additional statistics are presented. In the following the time series and spatial distribution of the centre positions for the flow cases $\mathcal{A}r = 3.33$, $\mathcal{A}r = 2.28$ and $\mathcal{A}r = 1.81$ are illustrated, insofar, they have not shown before.

Regarding the time series of the thermal convective roll structures centre position, the bold y-tick labels denote the normalised time averaged centre positions. Further, the rotational direction of the roll structures is colour coded: blue signifies clockwise and red counter-clockwise rotating *LSC*.

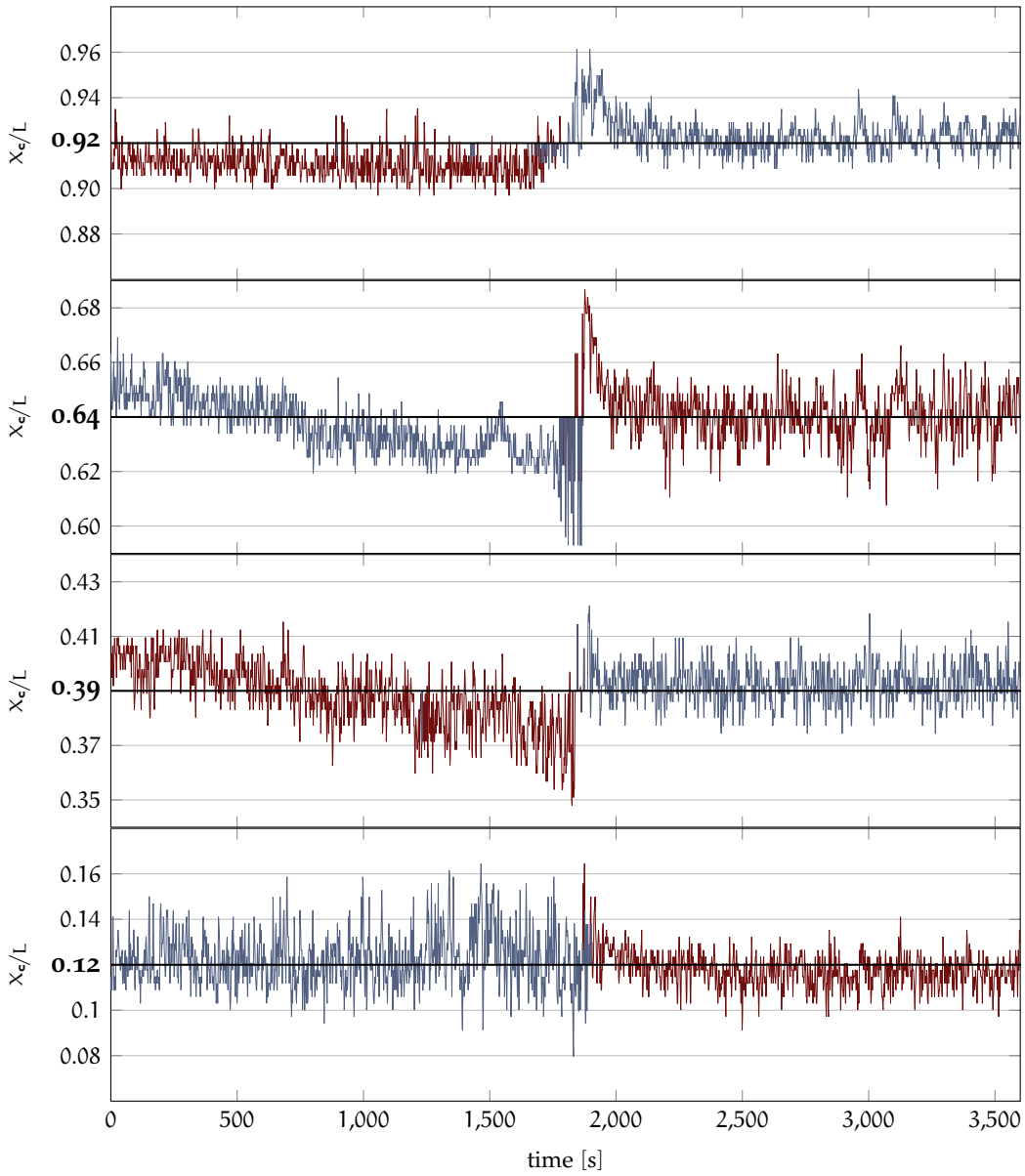

Figure 68: Centre position X_c/L of the four longitudinal arranged thermal convection rolls as a function of time at $Ar = 2.28$.

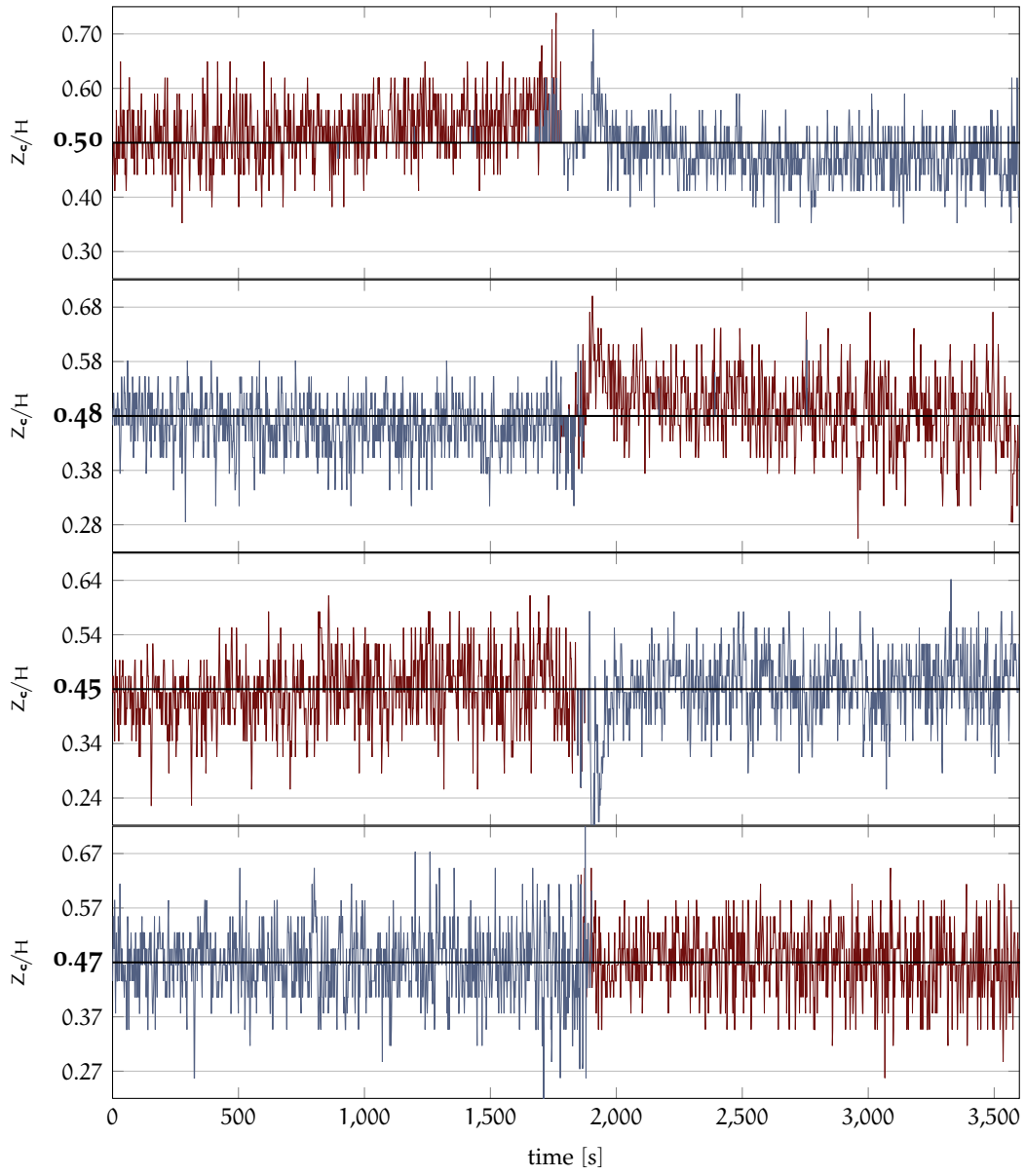

Figure 69: Centre position Z_c/H of the four longitudinal arranged thermal convection rolls as a function of time at $Ar = 2.28$.

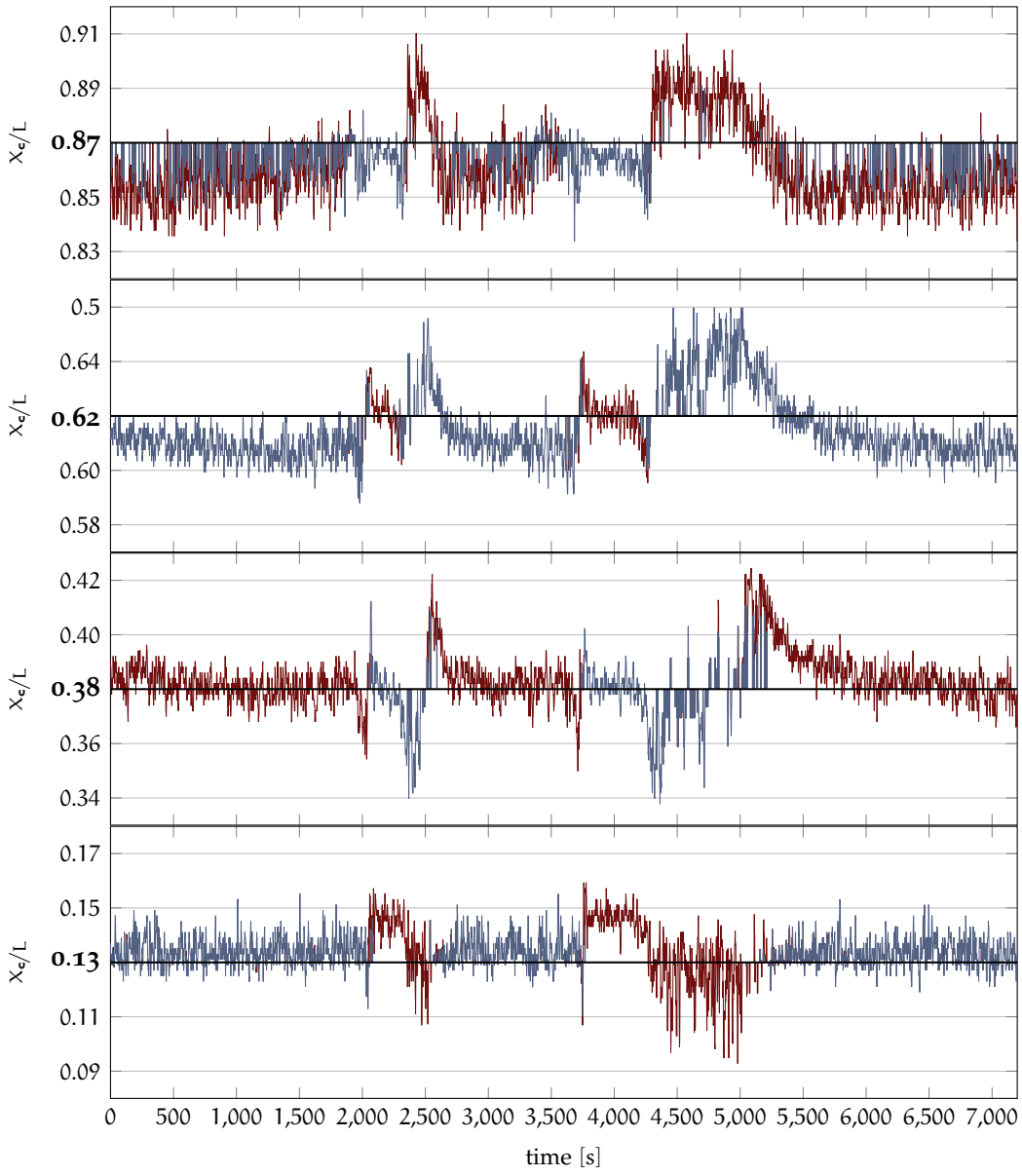

Figure 70: Centre position X_c/L of the four longitudinal arranged thermal convection rolls as a function of time at $\mathcal{A}r = 1.81$.

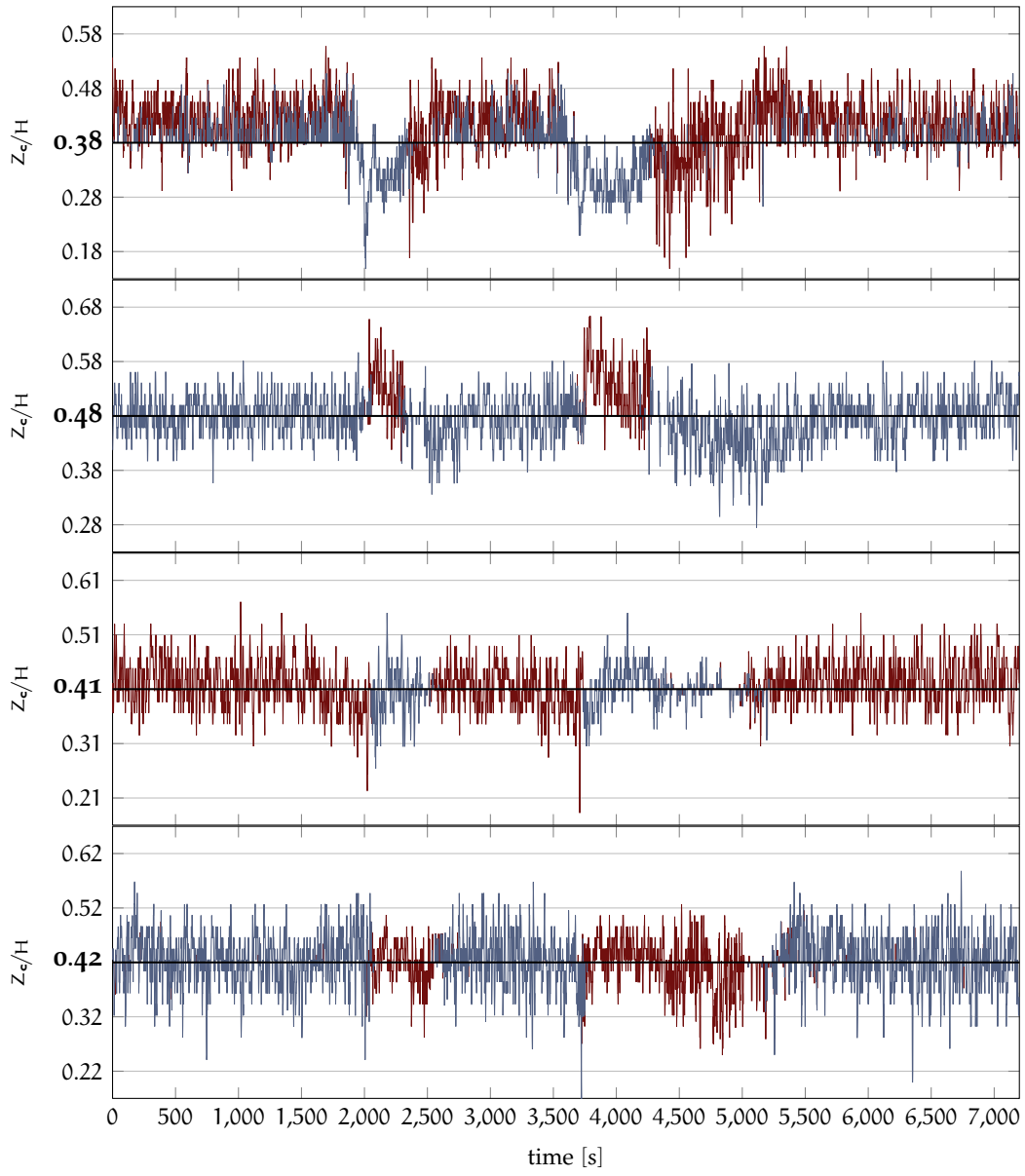

Figure 71: Centre position Z_c/H of the four longitudinal arranged thermal convection rolls as a function of time at $Ar = 1.81$.

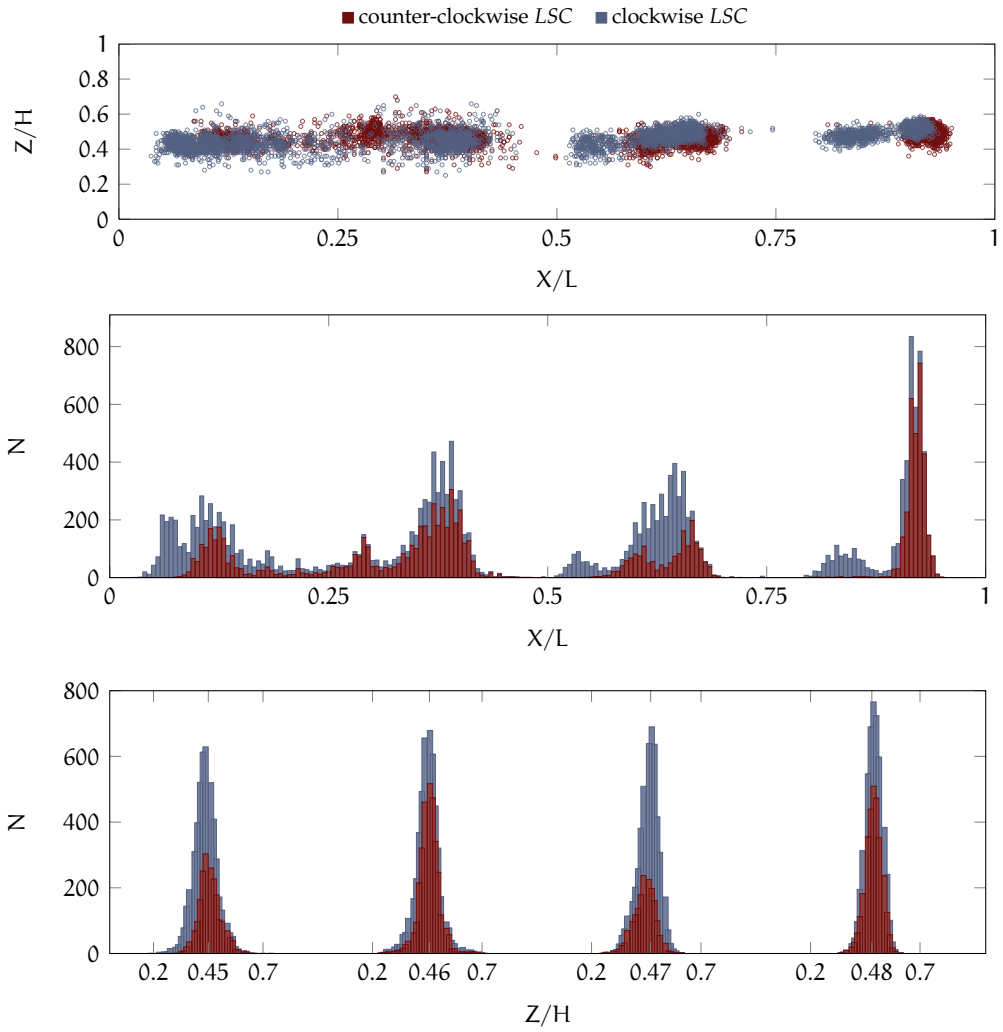

Figure 72: Spatial distribution and probability of the centre positions at $Ar = 3.33$. Top-down: the spatial distribution of the centre positions in the measurement plane $Y = 0.5 \times W$, corresponding probability of the X-centre positions and the Z-centre positions.

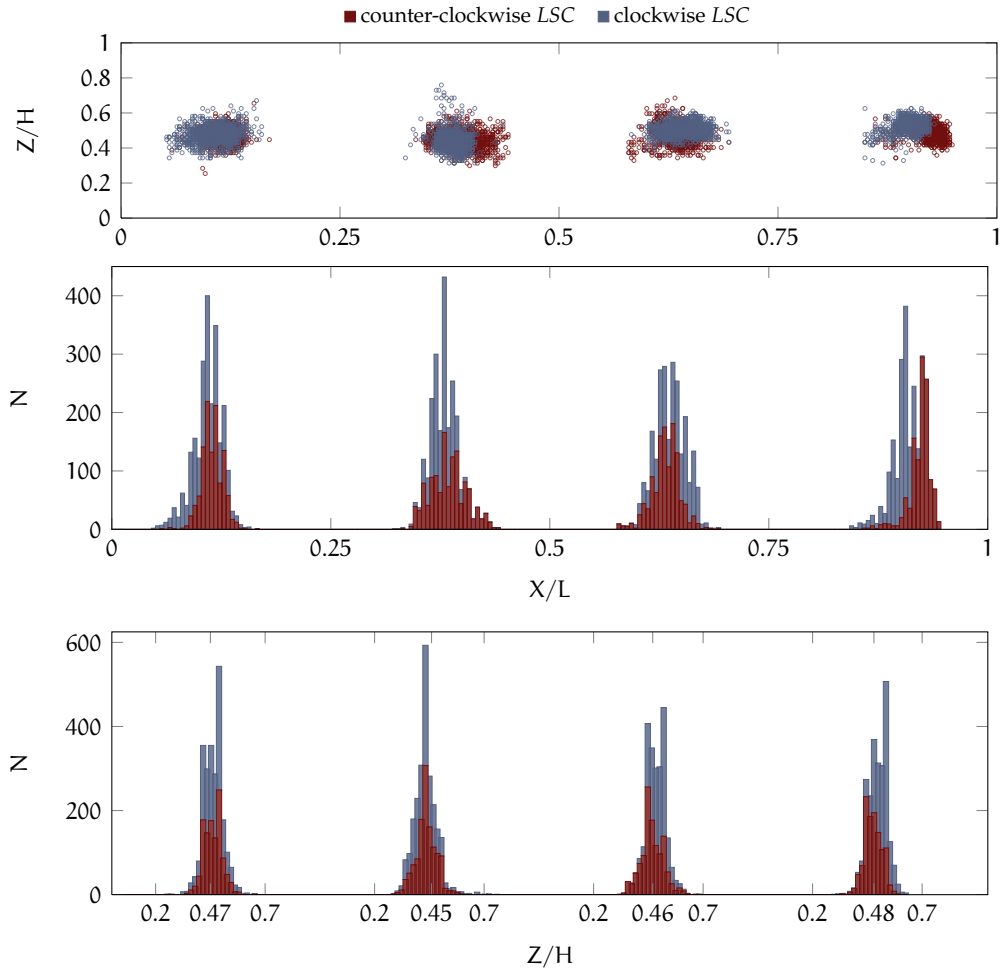

Figure 73: Spatial distribution and probability of the centre positions at $\mathcal{A}r = 2.28$. Top-down: the spatial distribution of the centre positions in the measurement plane $Y = 0.5 \times W$, corresponding probability of the X-centre positions and the Z-centre positions.

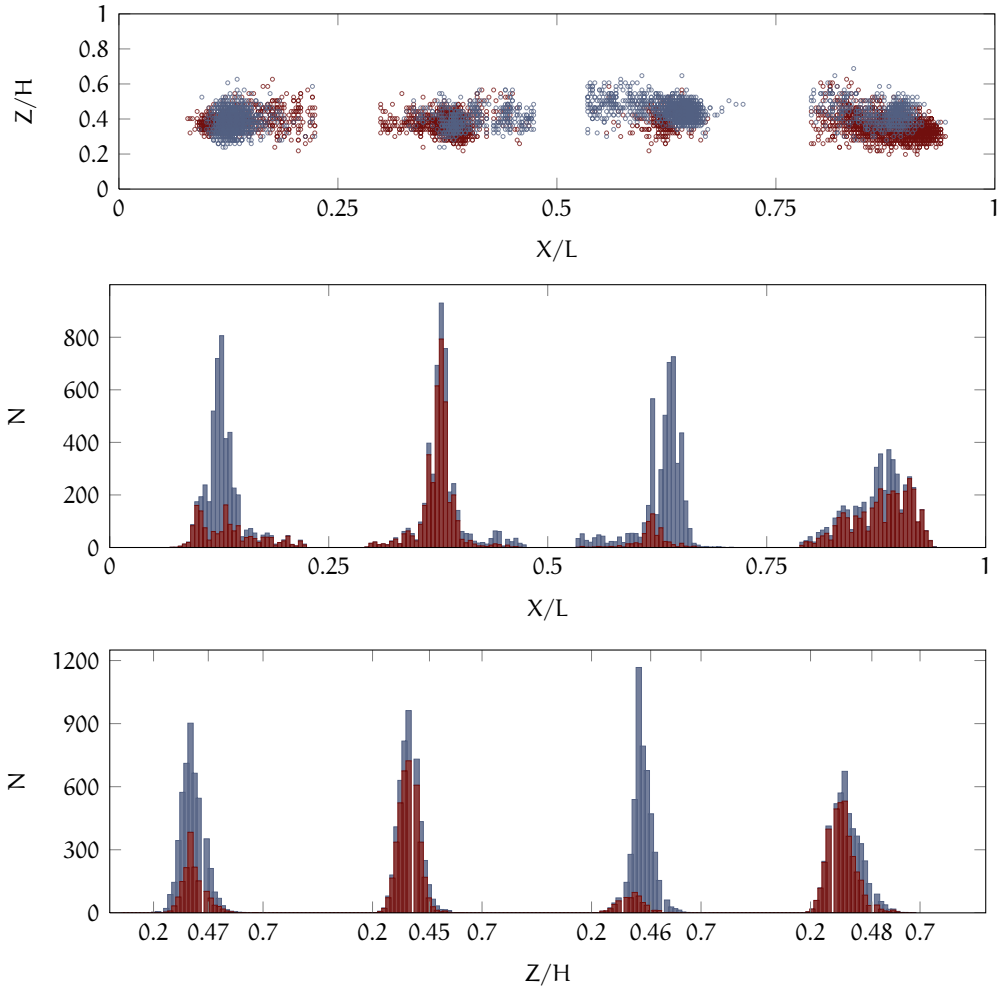

Figure 74: Spatial distribution and probability of the centre positions at $Ar = 1.81$. Top-down: the spatial distribution of the centre positions in the measurement plane $Y = 0.5 \times W$, corresponding probability of the X-centre positions and the Z-centre positions.

BIBLIOGRAPHY

[1] G. Ahlers. Effect of sidewall conductance on heat-transport measurements for turbulent Rayleigh-Bénard convection. *Phys. Rev. E*, 63:015303, 2000.

[2] G. Ahlers, S. Grossmann, and D. Lohse. Hochpräzision im Kochtopf: Neues zur turbulenten Konvektion. *Physik Journal*, 1(2):31–37, 2002.

[3] G. Ahlers, S. Grossmann, and D. Lohse. Heat transfer and large scale dynamics in turbulent Rayleigh-Bénard convection. *Rev. Mod. Phys.*, 81(2):503–537, 2008.

[4] T. Ahmad, I. Hassan, and A. Megahed. Experimental investigation of turbulent heat transfer in the entrance region of microchannels. *J. Thermophysics and Heat Transfer*, 24(2):388, 2010.

[5] V. R. Algazi and D. J. Sakrison. Adaptive data compression. *Proc. IEEE*, 55:267–277, 1967.

[6] V. R. Algazi and D. J. Sakrison. On the optimality of Karhunen-Loève expansion. *IEEE Trans. Inform. Theory*, 15:319–321, 1969.

[7] S. Ashkenazi and V. Steinberg. High rayleigh number turbulent convection in a gas near the gas-liquid critical point. *Phys. Rev. Lett.*, 83:3641–3644, Nov 1999.

[8] M. Asplund, A. Nordlund, R. Trampedach, C. Allende Prieto, and R. F. Stein. Line formation in solar granulation. *Astronomy and astrophysics*, 359:729–742, 2000.

[9] N. Aubry. On the hidden beauty of proper orthogonal decomposition. *Theoret. Comput. Fluid Dynamics*, 2:339–352, 1991.

[10] O. Aydem. Aiding and opposing mechanisms of mixed convection in a shear- and buoyancy-driven cavity. *Int. Comm. Heat Mass Transfer*, 26:1019–1028, 1999.

[11] H. D. Baehr and K. Stephan. *Wärme- und Stoffübertragung*. Springer Verlag Berlin Heidelberg New York, 1998.

[12] A. Baïri. Nusselt-Rayleigh correlations for design of industrial elements: Experimental and numerical investigations of natural convection in tilted square air filled enclosure. *Heat Mass Transfer*, 42:56–63, 2008.

[13] N. Baker and P. F. Linden. Physical modelling of airflows. *Atrium Buildings Architecture & Engineering*, pages 13–22, 1991.

[14] G. I. Barenblatt. *Scaling, Self-Similarity, and intermediate Asymptotics*. Cambridge University Press, 1996.

[15] R. Benzi. Flow reversal in a simple dynamical model of turbulence. *Phys. Rev. Lett.*, 95:024502, 2005.

[16] G. Berkooz, P. Holmes, and L. J. Lumley. The proper orthogonal decomposition in the analysis of turbulent flows. *Annu. Rev. Fluid Mech.*, 25:539–575, 1993.

[17] G. Biswas, N. K. Mitra, and M. Fiebig. Heat transfer enhancement in fin-tube heat exchangers by winglet type vortex generators. *Heat Mass Transfer*, 37(2):283–291, 1994.

[18] D. Bolster, A. Maillard, and P. Linden. The response of natural displacement ventilation to time-varying heat sources. *Energy and Buildings*, 40(12):2099 – 2110, 2008.

[19] E. Brown and G. Ahlers. Effect of the earth's coriolis force on large-scale circulation of turbulent Rayleigh-Bénard convection. *Phys. Fluids*, 18:125108, 2006.

[20] E. Brown and G. Ahlers. Rotations and cessations of the large-scale circulation in turbulent Rayleigh-Bénard convection. *J. Fluid Mech.*, 568:351–386, 2006.

[21] E. Brown and G. Ahlers. Large-Scale Circulation model for turbulent Rayleigh-Bénard convection. *Phys. Rev. Lett.*, 98:134501, 2007.

[22] E. Brown and G. Ahlers. Azimuthal asymmetries of the large-scale circulation in turbulent Rayleigh-Bénard convection. *Physics of Fluids*, 20:105105, 2008.

[23] E. Brown and G. Ahlers. A model of diffusion in a potential well for the dynamics of the large-scale circulation in turbulent Rayleigh-Bénard convection. *Physics of Fluids*, 20:075101, 2008.

[24] E. Brown, A. Nikolaenko, and G. Ahlers. Reorientation of the large-scale circulation in turbulent Rayleigh-Bénard convection. *Phy. Rev. Lett*, 95:084503, 2005.

[25] E. Brown, A. Nikolaenko, D. Funfschilling, and G. Ahlers. Heat transport in turbulent Rayleigh-Bénard convection: Effect of finite top- and bottom-plate conductivities. *Physics of Fluids*, 17:075108, 2005.

[26] E. Buckingham. On physically similar systems; illustrations of the use of dimensional equations. *Phys. Rev.*, 96:345–376, 1914.

[27] E. Buckingham. The principle of similitude. *Nature*, 4(4):396–397, 1915.

[28] B. Castaing, G. Gunaratne, F. Heslot, L. Kadanoff, A. Libchaber, S. Thomae, S. Xiao-Zhong Wu, S. Zaleski, and G. Zanetti. Scaling of hard thermal turbulence in Rayleigh-Bénard convection. . *Fluid Mech.*, 204:1–30, 1989.

[29] B. D. G. Chandran. Convection in galaxy-cluster plasmas driven by active galatic nuclei and cosmic-ray buoyancy. *The Astrophyical Journal*, 616:169–177, 2004.

[30] D. Chatterjee, G. Biswas, and S. Amiroudine. Numerical investigation of forced convection heat transfer in unsteady flow past a row square cylinders. *Int. J. Heat and Fluid flow*, 30:1114–1128, 2009.

[31] K.-C. Chiu, J. Ouazzani, and F. Rosenberger. Mixed convection between horizontal plates - II. Fully developed flow. *Int. J. Heat and Mass Transfer*, 30(8):1655–1662, 1987.

[32] K.-C. Chiu and F. Rosenberger. Mixed convection between horizontal plates - I. Entrance effects. *Int. J. Heat and Mass Transfer*, 30(8):1645–1654, 1987.

[33] S. Cioni, S. Ciliberto, and J. Sommeria. Strongly turbulent Rayleigh–Bénard convection in mercury: comparison with results at moderate prandtl number. *J. Fluid Mech.*, 335:111–140, 1997.

[34] E. Covas, R. Tavakol, D. Moss, and A. Andrew Tworkowski. Torsional oscillations in the solar convection zone. *Astronomy and astrophysics Lett.*, 360:21–24, 2000.

[35] M. Cross. Pattern formation outside of equilibrium. *Reviews of Modern Physics*, 65:851–1112, 1993.

[36] E. de St. Q. Isaacson and M. d. S. Q. de St. Q. Isaacson. *Dimensional Methods in Engineering and Physics*. Arnold, London, 1975.

[37] A. Dogan, M. Sivrioglu, and S. Baskaya. Experimental investigation of mixed convection heat transfer in a rectangular channel with discrete heat sources at the top and the bottom. *Int. Communications in Heat and Mass Transfer*, 32(9):1244–1252, 2005.

[38] P. Drazin and W. H. Reid. *Hydrodynamic stability*. Cambridge University Press, 1981.

[39] Evonik Industries. Produktbeschreibung plexiglas (datasheet). `http://www.plexiglas.de/product/plexiglas/de/produkte/massivplatten/standardsorten/pages/downloads.aspx`.

[40] H. S. Fernando. Fluid dynamics of urban atmosphere in complex terrain. *Annu. Rev. Fluid Mech.*, 42:365–389, 2010.

[41] A. S. Fleischer and R. J. Goldstein. High-Rayleigh-number convection of pressurized gases in a horizontal enclosure. *J. Fluid Mech.*, 469:1–12, 2002.

[42] F. Fontenele Araujo, S. Grossmann, and D. Lohse. Wind reversals in turbulent Rayleigh-Bénard convection. *Phys. Rev. Lett.*, 95:084502, 2005.

[43] D. Funfschilling and G. Ahlers. Plume motion and large-scale circulation in a cylindrical Rayleigh-Bénard cell. *Phys. Rev. Lett.*, 92(19):194502, 2004.

[44] D. Funfschilling, E. Brown, and G. Ahlers. Torsional oscillations of the large-scale circulation in turbulent Rayleigh-Bénard convection. *J. Fluid Mech.*, 607:119–139, 2008.

[45] German-Dutch wind tunnels (DNW). High pressure wind tunnel göttingen. `http://www.dnw.aero/`.

[46] A. V. Gimbitskii and A. G. Dezider'ev, S. G. andKarimova. Heat transfer at various methods of thermal protection in the systems of power-driven gas turbine plants (gtp). *Russian Aeronautics (Iz.VUZ)*, 54(3):322–327, 2011.

[47] G. A. Glatzmaier, R. S. Coe, L. Hongre, and P. H. Roberts. The role of the earth's mantle in controlling the frequency of geomagnetic reversals. *Nature*, 401:885–890, 1999.

[48] L. Graftiaux, M. Michard, and N. Grosjean. Combining piv, pod and vortex identification algorithms for the study of unsteady turbulent swirling flows. *Meas. Sci. Technol.*, 12:1422–1429, 2001.

[49] G. Günther, J. Bosbach, J. Pennecot, C. Wagner, T. Lerche, and I. Gores. Experimental and numerical simulations of idealized aircraft cabin flows. *Aerospace Science and Technology*, 10(7):563 – 573, 2006.

[50] Harke. Bènard cells inside a flat enclosure containing air. `http://de.wikipedia.org/w/index.php?title=Datei:BenardConvection.png&filetimestamp=20081003163231`, May 2008.

[51] D. L. Hartmann, L. A. Moy, and Q. Fu. Tropical convection and the energy balance at the top of the atmosphere. *J. Climate*, 14:4495–4511, 2001.

[52] M. Henze, J. von Wolfersdorf, B. Weigand, C. Dietz, and S. Neumann. Flow and heat transfer characteristics behind vortex generator - a benchmark dataset. *Int. J. Heat and Fluid Flow*, 32:318–328, 2011.

[53] F. Heslot, B. Castaing, and A. Libchaber. Transitions to turbulence in helium gas. *Phys. Rev. A*, 36(12):5870–5873, 1987.

[54] P. Holmes, J. L. Lumley, and G. Berkooz. *Turbulence, coherent structures, dynamical systems and symmetry*. Cambridge University Press, 2008.

[55] K. Hooman. A superposition approach to study slip-low forced convection in straight microchannels of uniform but arbitrary cross-section. *Int. J. Heat and Mass Transfer*, 51:3753–3762, 2008.

[56] C. C. Huang and T. F. Lin. Buoyancy induced flow transition in mixed convective flow of air through a bottom heated horizontal rectangular duct. *Int. J. Heat Mass Transfer*, 37(8):1235–1255, 1994.

[57] G. R. Hunt and P. F. Linden. Displacement and mixing ventilation driven by opposing wind and buoyancy. *Building and Environment*, 34:707–720, 1999.

[58] G. R. Hunt and P. F. Linden. The fluid mechanics of natural ventilation - displacement ventilation by buoyancy-driven flows assisted by wind. *J. Fluid Mech.*, 527:27–55, 2004.

[59] F. P. Incropera, J. S. Kerby, D. F. Moffatt, and S. Ramadhyani. Convection heat transfer from discrete heat sources in a rectangular channel. *Int. J. Heat and Mass Transfer*, 29:1051–1058, 1986.

[60] J. D. Jackson, M. A. Cotton, and B. P. Axcell. Studies of mixed convection in vertical tubes. *Int. J. Heat and Fluid Flow*, 10(1):2–15, 1988.

[61] J.-Y. Jung, H.-S. Oh, and H.-Y. Kwak. Forced convection heat transfer of nanofluids in microchannels. *Int. J. Heat and Mass Transfer*, 52:466–472, 2009.

[62] C. J. Kähler. General design and operating rules for seeding atomisers. *5th Int. Sym. on Particel Image Velocimetry*, (3207), 2003.

[63] M. Kalteh, A. Abbassi, M. Saffar-Avval, and J. Harting. Eulerian-Eulerian two-phase numerical simulations of nano fluid laminar forced convection in a microchannel. *Int. F. of Heat and Fluid Flow*, 32:107–116, 2011.

[64] Keithley Instruments GmbH. Model 3706 six-slot system switch with high performance dmm. `http://www.keithley.de/products/dcac/sensitive/acdc/?mn=3706`.

[65] M. Konstantinov, M. Rütten, M. Lambert, and C. Wagner. Strahlung als wesentlicher Faktor der numerischen Simulation von Flugzeugkabineninnenströmungen für Komfortvorhersagen. *Deutscher Luft- und Raumfahrtkongress*, (121285), 2009.

[66] R. Krishnamurty and L. N. Howard. Large-scale flow generation in turbulent convection. *Proc. Nat. Acad. Sci. USA*, 78:1981–1985, 1981.

[67] H. Kuchling. *Nachschlagebücher für Grundlagenfächer - Physik*. VEB Fachbuchverlag Leipzig, 1987.

[68] M. Kühn, K. Ehrenfried, J. Bosbach, and C. Wagner. Large-scale tomographic particle image velocimetry using helium-filled soap bubbles. *Exp. Fluids*, page 929–948, 2011.

[69] F. Kupka. Convection in stars. *Proc. Int. Astronomical Union Symposium*, 50:119–129, 2004.

[70] M. Kühn, J. Bosbach, and C. Wagner. Experimental parametric study of forced and mixed convection in a passenger aircraft cabin mock-up. *Building and Environment*, 44(5):961 – 970, 2009.

[71] G. Labonia and G. Guj. Natural convection in a horizontal concentric cylindrical annulus: oscillatory flow and transition to chaos. *J. Fluid Mech.*, 375:179–202, 1998.

[72] G. Lane-Serff. Heat flow and air movement in buildings. *PhD Thesis, Cambridge Univ., UK*, 1989.

[73] R. L. Larson and O. Peter. Mantle plumes control magnetic reversal frequency. *Earth and Planetary Science Lett.*, 107:437–447, 1991.

[74] W. L. Lin and T. Lin. Experimental study of unstable mixed convection of air in a bottom heated horizontal retangular duct. *Int. J. Heat Mass Transfer*, 39(8):1649–1663, 1996.

[75] P. F. Linden. The fluid mechanics of natural ventilation. *Annu. Rev. Fluid Mech.*, 31:201–238, 1999.

[76] P. F. Linden, G. Lane-Serff, and D. A. Smeed. Emptying filling boxes: the fluid mechanics of natural ventilation. *J. Fluid Mech.*, 212:309–335, 1990.

[77] J. L. Lumely and H. A. Panofsky. *The structure of atmospheric turbulence*. Interscience publishers, Inc., New York, 1964.

[78] J. L. Lumley. *Stochastic tools in turbulence*. Academic press New York and London, 1970.

[79] J. L. Lymley. The structures of inhomogeneous turbulent flows. *Atmospheric Turbulence and Radio Wave Propagation*, pages 166–178, 1967.

[80] C. Maalouf, E. Wurtz, L. Mora, and F. Allard. Optimization and study of an autonomous solar desiccant cooling system. In *International Conference Passive and Low Energy Cooling for the Bulit Environment*, pages 663–668, May 2005.

[81] J. Marshall and F. Schott. Open-ocean convection: Observation, theory and models. *Rev. Geophysics*, 37:1–64, 1999.

[82] W. V. R. Marshall. The heat transport and spectrum of thermal turbulence. *Proc. R. Soc. Lond. A 31*, 225(1161):196–212, 1954.

[83] Martinswerk Albemarle. Specifications and safety data sheets matroxid mr-70. `http://www.martinswerk.de/allproducts_e.aspx`.

[84] M. Michard, L. Graftieaux, L. Lolline, and N. Grosjean. Identification of vortical structures by a non local criterion - application to PIV measurements and DNS-LES results of turbulent rotating flows. *Proc 11th Symposium on Turbulent Shear Flows, Grenoble, France*, 1998.

[85] W. J. Morgan. Convection plumes in the lower mantle. *Nature*, 230:42–43, 1971.

[86] B. Nacke and O. Irretier. *Taschenbuch Industrielle Wärmetechnik*. Vulkan, 2007.

[87] NASA. Satellite image of a hurricane named «fran». `http://geology.com/hurricanes/hurricane-names.shtml`, Sep 1996.

[88] J. J. Niemela, L. Skrbek, K. R. Sreenivasan, and R. Donnelly. Turbulent convection at very high Rayleigh numbers. *Nature*, 404:837–840, 2000.

[89] J. J. Niemela, L. Skrbek, K. R. Sreenivasan, and R. Donnelly. The wind in confined turbulent convection. *J. Fluid Mech.*, 449:169–178, 2001.

[90] Y. Ogura and N. A. Phillips. Scale analysis of deep and shallow convection in atmosphere. *J. Atmospheric Sciences*, 19(2):173–179, 1962.

[91] D. G. Osborne and F. P. Incropera. Laminar, mixed convection heat transfer for flow between horizontal parallel plates with asymmetric heating. *Int. J. Heat Mass Transfer*, 28(1):207–217, 1985.

[92] S. Paolucci and D. R. Chenoweth. Transition to chaos in a differentially heated vertical cavity. *J. Fluid Mech.*, 201:379–410, 1989.

[93] S. Park, R. T. Hellwig, G. Grün, and A. Holm. Local and overall thermal comfort in an aircraft cabin and their interrelations. *Building and Environment*, 46(5):1056 – 1064, 2011.

[94] PCO AG. pco.4000 cooled digital 14 bit ccd camera system. `http://www.pco.de/sensitive-cameras/pco4000/`.

[95] X. F. Peng and G. P. Peterson. Convective heat transfer and flow friction for water flow in microchannel structures. *Int. J. Heat and Mass Transfer*, 39(12):2599–2608, 1996.

[96] PIVTEC GmbH. Pivview 2.46 linux 32 bit. http://www.pivtec.de/.

[97] R. W. Preisendorfer and C. D. Mobley. Principal component analysis in meteorology and oceanography. *Development in atmospheric science*, 27:425, 1988.

[98] D. Prvulovic, S.and Tolmac and M. Lambic. Convection drying in the food industry. *Agricultural Engineering International: the CIGR Ejournal*, 9(9):1–13, 2007.

[99] X.-L. Qiu, X.-D. Shang, P. Tong, and K.-Q. Xia. Velocity oscillations in turbulent Rayleigh–Bénard convection. *Phys. Fluids*, 16(2):412–423, 2004.

[100] X.-L. Qiu and P. Tong. Large-scale velocity structures in turbulent thermal convection. *Phys. Rev. E*, 64:036304, 2001.

[101] X.-L. Qiu and P. Tong. Onset of coherent oscillations in turbulent Rayleigh-Bénard convection. *Phys. Rev. Lett.*, 87(9):094501, 2001.

[102] M. Raffel, C. E. Willert, and J. Kompenhans. *Particle image velocimetry*. Springer Verlag, 1997.

[103] L. Rayleigh. On convection currents in a horizontal layer of fluid, when the higher temperature is on the under side. *Phil. Mag. and J. of science*, 32(192):530–546, 1916.

[104] W.-H. Reid and D. Harris. Some further results on the Bénard problem. *Phys. of Fluids*, 1(2):102–110, 1958.

[105] P.-E. Roche, B. Castaing, B. Chabaud, B. Hébral, and J. Sommeria. Side wall effects in Rayleigh Bénard experiments. *Eur. Phys. J. B*, 24:405–408, 2001.

[106] A. Rosenfeld and A. C. Kak. *Digital picture processing*. New York : Academic, 1982.

[107] S. M. Saeidi and J. M. Khodadadi. Forced convection in a square cavity with inlet and oulet ports. *Int. J. Heat and Mass Transfer*, 49:1896–1906, 2006.

[108] D. Schmeling, J. Bosbach, and C. Wagner. Feasibility of combined pit and piv in mixed convective air flows. *9TH INTERNATIONAL SYMPOSIUM ON PARTICLE IMAGE VELOCIMETRY - PIV11*, 2011.

[109] D. Schmeling, J. Bosbach, and C. Wagner. Oscillations of the large-scale circulation in turbulent mixed convection in a closed rectangular cavity. *Exp. Fluids*, in review, 2012.

[110] D. Schmeling, A. Westhoff, M. Kühn, J. Bosbach, and C. Wagner. Large-scale flow structures and heat transport of turbulent forced and mixed convection in a closed rectangular cavity. *Int. J. Heat and Fluid Flow*, 32:889–900, 2011.

[111] A. Sergent and P. Le Quéré. Long time evolution of large-scale patterns in a rectangular Rayleigh-Bénard cell. 2011.

[112] R. Seydel. *Practical Bifurcation and Stability Analysis 3rd edition*. Springer New York Dordrecht Heidelberg Londen, 2010.

[113] X.-D. Shang, X.-L. Qiu, P. Tong, and K.-Q. Xia. Measured local heat transport in turbulent Rayleigh-Bènard convection. *Phy. Rev. Let.*, 90(7):074501, 2003.

[114] P. L. Silva Dias, W. H. Schubert, and D. M. Large-scale response of the tropical atmosphere to transient convection. *J. atmospheric sciences*, 32(9):1244–1252, 1983.

[115] L. Sirovich. Turbulence and the dynamics of coherent structures part I: Coherent structures. *Quarterly of Applied Mathematics*, 45(3):561–571, 1987.

[116] L. Sirovich. Turbulence and the dynamics of coherent structures part II: Symmetries and transformation. *Quarterly of Applied Mathematics*, 45(3):573–582, 1987.

[117] L. Sirovich. Chaotic dynamics of coherent structures. *Physica D*, 37:126–145, 1989.

[118] A. J. Smits and M. V. Zagarola. Applications of dense gases to model testing for aeronautical and hydrodynamic applications. *Meas. Sci. Technology*, 16:1710–1715, 2005.

[119] S. R. Sreenivasan, A. Bershadskii, and J. J. Niemela. Mean wind and its reversal in thermal convection. *Phys. Rev. Lett.*, 65:056306, 2005.

[120] S. R. Sreenivasan and R. J. Donnelly. Role of cryogenic helium in classical fluid dynamics: Basic research and model testing. *Adv. Appl. Mech.*, 37:239–276, 2001.

[121] C. Sun and K.-Q. Xia. Three-dimensional flow stuctures and dynamics of turbulent convection in a cylindrical cell. *Phys. Rev. E*, 72:026302, 2005.

[122] R. Verzicco. Sideall finite-conductivity effects in confined turbulent thermal convection. *J. Fluid Mech.*, 72:026302, 2002.

[123] P. J. Webster. The role of hydrological processes in ocean-atmosphere interactions. *Rev. of Geophysics*, 32:427–476, 1994.

[124] A. Westhoff, J. Bosbach, D. Schmeling, and C. Wagner. Experimental study of low-frequency oscillations and large-scale circulations in turbulent mixed convection. *Int. J. Heat Fluid Flow*, 31(5):794 – 804, 2010.

[125] A. Westhoff, J. Bosbach, and C. Wagner. Scaling of mixed convection in aircraft cabins. *26th International Congress of the Aeronautical Sciences*, 2008.

[126] S. Whitaker. Forced convection heat transfer correlations for flow in pipes, past flat plates, single cylinders, single spheres, and for flow in packed beds and tube bundles. *AIchE Journal*, 18(2):361–371, 1972.

[127] C. Willert and M. Jarius. Planar flow field measurements in atmosheric and pressurized combustion chambers. *Exp. Fluids*, 33:931–939, 2002.

[128] H.-D. Xi, Q. Zhou, and K.-Q. Xia. Azimuthal motion of the mean wind in turbulent thermal convection. *Phys. Rev. E*, 73:056312, 2006.

[129] K.-Q. Xia, C. Sun, and S.-Q. Zhou. Particle image velocimetry measurements of the velocity field in turbulent thermal convection. *Physical Review E*, 68:066303, 2003.

[130] X. Xu, K. M. S. Bajaj, and G. Ahlers. Heat transport in turbulent Rayleigh-Bènard convection. *Phys. Rev. Lett.*, 84(19):4357–4360, 2000.

[131] R. Yao, B. Li, and K. Steemers. Energy policy and standard for built environment in china. *Renewable Energy*, 30(13):1973 – 1988, 2005.

[132] H. Zhang, L.Dai, G. Xu, Y. Li, W. Chen, and W.-Q. Tao. Studies of air-flow and temperature fields inside a passenger compartment for improving thermal comfort and saving energy. part i: Test/numerical model and validation. *Applied Thermal Engineering*, 29(10):2022 – 2027, 2009.